



UNIVERSIDADE ESTADUAL DE CAMPINAS

INSTITUTO DE QUÍMICA

LANOUSSE PETIOTE

**SYNTHESIS AND CHARACTERIZATION OF LANTHANIDE COORDINATION
POLYMERS AS LUMINESCENT TEMPERATURE PROBES**

**SÍNTESE E CARACTERIZAÇÃO DE POLÍMEROS DE COORDENAÇÃO DE ÍONS
LANTANÍDEOS COMO SONDAS LUMINESCENTES DE TEMPERATURA**

**CAMPINAS
2019**

LANOUSSE PETIOTE

**SYNTHESIS AND CHARACTERIZATION OF LANTHANIDE COORDINATION
POLYMERS AS LUMINESCENT TEMPERATURE PROBES**

**SÍNTESE E CARACTERIZAÇÃO DE POLÍMEROS DE COORDENAÇÃO DE
ÍONS LANTANÍDEOS COMO SONDAS LUMINESCENTES DE TEMPERATURA**

Tese de Doutorado apresentada ao Instituto de Química da
Universidade Estadual de Campinas como parte dos requisitos
exigidos para a obtenção do título de Doutor em Ciências

Doctor's Thesis presented to the Institute of Chemistry of the
University of Campinas as part of the requirements to obtain the title
of Doctor in Sciences.

Supervisor: Prof. Dr. Fernando Aparecido Sigoli

-

**O arquivo digital corresponde à versão final da Tese defendida pelo aluno
Lanousse Petiote e orientada pelo Prof. Dr. Fernando Aparecido Sigoli.**

**CAMPINAS
2019**

Ficha catalográfica
Universidade Estadual de Campinas
Biblioteca do Instituto de Química
Camila Barleta Fullin - CRB 8462

Petiotte, Lanousse, 1985-
P445s Synthesis and characterization of lanthanide coordination polymers as
luminescent temperature probes / Lanousse Petiotte. – Campinas, SP : s.n.],
2019.

Orientador: Fernando Aparecido Sigoli.
Tese (doutorado) – Universidade Estadual de Campinas, Instituto
de Química.

1. Química de coordenação. 2. Lantanídeos. 3. Fotoluminescência. 4.
Termometria. I. Sigoli, Fernando Aparecido, 1972-. II. Universidade
Estadual de Campinas. Instituto de Química. III. Título.

Informações para Biblioteca Digital

Título em outro idioma: Síntese e caracterização de polímeros de coordenação de íons
lantanídeos como sondas luminescentes de temperatura

Palavras-chave em inglês:

Coordination chemistry

Lanthanides

Photoluminescence

Thermometry

Área de concentração: Química Inorgânica

Titulação: Doutor em Ciências

Banca examinadora:

Fernando Aparecido Sigoli [Orientador]

Andréa Simone Stucchi de Carmargo Alvarez Bernardez

Regina Célia Galvão Frem

Rene Alfonso Nome Silva

Andre Luiz Barboza Formiga

Data de defesa: 13-09-2019

Programa de Pós-Graduação: Química

Identificação e informações acadêmicas do(a) aluno(a)

- ORCID do autor: <https://orcid.org/0000-0002-1475-0967>

- Currículo Lattes do autor: <http://lattes.cnpq.br/4099318989419310>

BANCA EXAMINADORA

Prof. Dr. Fernando Aparecido Sigoli (Orientador)

Profa. Dra. Regina Célia Galvão Frem (Instituto de Química de Araraquara - Universidade Estadual Paulista)

Profa. Dra. Andréa Simone Stucchi de Camargo Alvarez Bernadez (Instituto de Física de São Carlos - Universidade de São Paulo)

Prof. Dr. Andre Luiz Barboza Formiga (Instituto de Química - Universidade Estadual de Campinas)

Prof. Dr. Rene Alfonso Nome Silva (Instituto de Química - Universidade Estadual de Campinas)

A Ata da defesa assinada pelos membros da Comissão Examinadora, consta no SIGA/Sistema de Fluxo de Dissertação/Tese e na Secretaria do Programa da Unidade.

Este exemplar corresponde à redação final da Tese de Doutorado defendida pelo aluno **Lanousse Petiote**, aprovada pela Comissão Julgadora em 13 de setembro de 2019.

Dedication

PROUDLY DEDICATED TO MY MOTHER, MARIE ADELINE LUXAMAR. A POSITIVE MODEL MOTHER WHO, IN THE FACE OF ADVERSITY AND NUMEROUS DIFFICULT CHALLENGES YEAR AFTER YEAR, HAS NEVER GIVEN UP WORKING HARD TO CARE AND INSTRUCT HIS CHILDREN. I WILL ALWAYS BE GRATEFUL TO HER FOR HIS ENDLESS LOVE, PRAYERS, SACRIFICES, AND ADVICE.

Acknowledgment

These last few years should have been a very difficult life-experience for me without the great and precious support, motivation and encouragement received from many people within and especially outside the university.

Foremost, I gratefully acknowledge the funding (Process: 141691/2015-8) received from the Brazilian National Council for Scientific and Technological Development (CNPq in Portuguese).

I am also indebted to FAPESP (Fundação de Amparo à Pesquisa do Estado de São Paulo), for the financial support given to develop and maintain the great quality of scientific infrastructure and material conditions to perform high-impact studies.

I would like to express my deep and sincere gratitude to my advisor professor Fernando A. Sigoli for accepting me in his research group since 2013, giving me the opportunity to learn and providing me invaluable guidance during these last six years throughout my master and doctoral researches. In addition to his very high competence as an advisor for me and the other students of the LMF, professor Sigoli has many important many personal characteristics such as friendship, empathy, critic, acceptance, and patience during our academic discussion. It was a great privilege and honor to work and study under his guidance and I am extremely grateful for what he has offered me. My sincere thanks also go to professor Ítalo Odone Mazali for the tireless acting to keep the laboratory running, maintain the members integrated and for offering valuable advice in each opportunity. My deep gratitude to the laboratory technicians of the chemistry institute for their constant assistance in the experimental measurements.

To my friends and research colleagues at the LMF, I would like to say thanks for the friendship, the birthday cakes, and interesting dialogues.

I am extremely grateful to my parents for their love, prayers, caring and sacrifices for educating and preparing me for my future. I am very much thankful to my girlfriend Lucimara for her love, the partnership, and the psychoanalysis teachings. I thank his family also the memorable moments lived together.

Finally, my thanks go to all the people who have supported me directly or indirectly to complete this study period.

This study was financed in part by the Coordenação de Aperfeiçoamento de Pessoal de Nível Superior - Brasil (CAPES) - Finance Code 001.

Resumo

A limitação intrínseca das sondas convencionais no monitoramento de temperatura nas escalas micro e nanométrica tem impulsionado a pesquisa visando o desenvolvimento de novos termômetros não invasivos, autoreferenciados e que apresentem sensibilidade térmica elevada e melhor resolução espacial. Para alcançar tal objetivo, os polímeros de coordenação contendo íons lantanídeos constituem alternativa promissora devido às propriedades espectroscópicas dos íons lantanídeos e pelo fato das estruturas dos polímeros de coordenação permitirem a inserção simultânea de dois ou mais íons opticamente ativos. Essa tese apresenta uma série de compostos de coordenação homo e heterolépticos contendo uma mistura dos íons Gd^{III} , Tb^{III} e Eu^{III} amplamente caracterizados usando as técnicas de difração de raios X de monocristal e de pó, espectroscopias de refletância difusa e vibracional na região do infravermelho, análises elementar e termogravimétrica, e finalmente testados como sondas óticas ratiométricas para aplicação na nano termometria óptica. Inicialmente, os ligantes 1,3,5-tris(4-caboxifenoximetil)benzeno (H_3TCPMB) e 1,3,5-tris(2,6-dicarboxipiridina-4-oximetil)benzeno ($H_6TDCPMB$) foram preparados e usados na preparação dos compostos homolépticos os quais são representados pelas fórmulas gerais $Tb_{0.95}Eu_{0.05}-TCPMB$ e $Gd_{1.6-x}Tb_{0.4}Eu_x-TDCPMB$ ($x = 0.1, 0.2, 0.3, 0.4, 0.5$), respectivamente. Em seguida, os polímeros de coordenação heterolépticos representados por $Tb_xEu_{1-x}-BDC-AC$ ($x = 0.93, 0.993$) e $Tb_xEu_{1-x}acac_xBDC_{1.5-x/2}$ ($x = 0.99, 0.95, 0.90, 0.85, 0.75$) baseados nas misturas dos ligantes ácido 1,4-benzendicarboxílico (H_2BDC) / ácido antracenocarboxílico (HAC) e ácido 1,4-benzendicarboxílico (H_2BDC) / acetilcetona ($Hacac$), respectivamente, foram preparados e investigados. Monitorando a variação da razão de intensidade I_{Tb} / I_{Eu} , os sistemas co-dopados $Gd_{1.6-x}Tb_{0.4}Eu_x-TDCPMB$ apresentaram respostas lineares em amplas faixas de temperatura. Por exemplo, os compostos $Gd_{1.5}Tb_{0.4}Eu_{0.1}-TDCPMB$ e $Gd_{1.3}Tb_{0.4}Eu_{0.3}-TDCPMB$ são potencialmente aplicáveis como sondas de temperatura nas faixas de 273 – 373 K e de 100 - 300 K, respectivamente. Além disso, o composto $Gd_{1.5}Tb_{0.4}Eu_{0.1}-TDCPMB$ apresenta uma sensibilidade absoluta de $4,9\%K^{-1}$ que é um valor consideravelmente alto em comparação aos resultados reportados na literatura para compostos de íons lantanídeos. Os compostos heterolépticos também apresentaram resultados promissores com destaque para o

composto $\text{Tb}_{0.90}\text{Eu}_{0.1}\text{acac}_{0.90}\text{BDC}_{1.05}$ que apresenta uma faixa operacional entre 80 e 280 K com uma sensibilidade térmica absoluta de $45\ \%K^{-1}$ fazendo desse composto, portanto, um candidato potencial para ser utilizado como sonda ótica na termometria baseada na luminescência. Os dados sugerem que, a partir de uma otimização das frações dos íons lantanídeos, melhores resultados podem ser alcançados.

Abstract

The intrinsic limitation of the conventional temperature sensors in the remote temperature sensing at micro and nanoscale has put forward the research aiming for the development of non-contact, self-referenced thermometers and high temperature-sensitive nanothermometers. To achieve this goal, the lanthanide-based coordination polymers (Ln-CPs) represent one a very promising approach due to the peculiar spectroscopic properties of the trivalent lanthanides (mainly the narrow emission band long-lived emission) and the fact that the CPs structure facilitates the simultaneous insertion of two or more optically active ions in the same matrix. This thesis presents a series of homo and heteroleptic CPs containing the mixed- Gd^{III} , Tb^{III} and Eu^{III} ions which have been successfully synthesized by solvothermal and precipitation methodologies, fully characterized by single-crystal X-ray diffraction (XRD), powder X-ray diffraction, diffuse reflection spectroscopy, FT-IR spectroscopy, elemental analyses and thermogravimetric analysis, and targeted as ratiometric optical probes for applications in luminescence-based thermometry. Primarily, the ligands 1,3,5-tris(4-carboxyphen-oxymethyl)benzene (H_3TCPMB) and 1,3,5-tris(2,6-dicarboxypyridine-4-oxy methyl)-benzene ($H_6TDCPMB$) were prepared and used to prepare the homoleptic co-doped CPs represented by the general formulas $Tb_{0.95}Eu_{0.05}-TCPMB$ and $Gd_{1.6-x}Tb_{0.4}Eu_x-TDCPMB$ ($x = 0.1, 0.2, 0.3, 0.4, 0.5$), respectively. Secondly, the heteroleptic Tb/Eu containing CPs represented by $Tb_xEu_{1-x}-BDC-AC$ ($x = 0.93, 0.993$) and $Tb_xEu_{1-x}acac_xBDC_{1.5-x/2}$ ($x = 0.99, 0.95, 0.90, 0.85$ and 0.75) based on the mixed-ligands 1,4-benzene dicarboxylic acid (H_2BDC) / 9-anthracenecarboxylic acid (HAC) and 1,4-benzene dicarboxylic acid (H_2BDC) / acetylacetone ($Hacac$), respectively, were prepared and investigated. Monitoring the variation of the I_{Tb} / I_{Eu} intensity ratio, the co-doped systems $Gd_{1.6-x}Tb_{0.4}Eu_x-TDCPMB$ show linear responses in wide temperature ranges. For instance, $Gd_{1.5}Tb_{0.4}Eu_{0.1}-TDCPMB$ and $Gd_{1.3}Tb_{0.4}Eu_{0.3}-TDCPMB$ may potentially operate in the ranges 273 – 373 K and 100 - 300 K, respectively. Interestingly, $Gd_{1.5}Tb_{0.4}Eu_{0.1}-TDCPMB$ displays an interesting high absolute thermal sensitivity of $4.9 \%K^{-1}$. Also, promising results were obtained with the heteroleptic CPs highlighting $Tb_{0.90}Eu_{0.1}acac_{0.90}BDC_{1.05}$ which shows the operating range of 80 – 280 K with an absolute thermal sensitivity of $45 \%K^{-1}$ making it suitable for applications as ratiometric optical probes for luminescence-based thermometry. Furthermore, it's was

observed that by virtue of adjusting the composition of lanthanide ions, better results should be obtained.

List of Figures

Fig. 1: Radial distribution plot of the s, p, d, and f valence orbitals in the hydrogen-like Lanthanide ions	34
Fig. 2: Energy diagrams of the trivalent lanthanide ions and radiative transitions between different levels. Adapted from [27].	35
Fig. 3: Diagram representing the interactions leading to the splitting of the electronic energy levels of a Eu^{III} ion inserted in a solid [29].	36
Fig. 4: Schematic representations of energy absorption, energy migration and emission processes in lanthanide complexes: ISC = intersystem crossing; ET = energy transfer; IC = internal conversion. Adapted from [46].	39
Fig. 5: Diagrams illustrating the (A) Forster resonant energy transfer and (B) Dexter energy transfer mechanisms	40
Fig. 6: Examples of secondary building units in coordination polymers [52].	41
Fig. 7: Schematic summaries of three different electronic structures leading to dual emission system. (a) Two independent luminescent centers where one, at least, shows a response to temperature. (b) Two luminophores interacting through energy transfer. (c) Two luminescent excited states in fast thermal equilibrium. Adapted from [19]. ..	44
Fig. 8: Schematic representation of energy absorption, migration, emission, and processes in luminescent mixed lanthanide coordination polymers thermometers. Abbreviations: S = singlet; T= triplet, A = absorption probability; ISC = intersystem crossing; k = radiative transition probability. The solid arrows represent singlet-singlet absorption and radiative transitions; dotted arrows indicate non-radiative transitions [76].	47
Fig. 9: Matt illustration of the molecular structure of the ligand 1,3,5-tris(4-carboxyphenoxy methyl)benzene (H_3TCPMB). The dark dots and the dotted line between aromatic rings represent the centroids and distance between them, respectively.	62
Fig. 10: Hydrogen bonded self-assembly of the ligand 1,3,5-tris(4-carboxyphenoxy methyl)benzene (H_3TCPMB) in its single-crystal structure.	62
Fig. 11: The 400-MHz ^1H -nuclear magnetic resonance spectrum of H_3TCPMB in DMSO-d_6 . Inset: magnification of the range 6.91-7.99 ppm and chemical structure of the ligand H_3TCPMB . see spectrum conditions in the appendix A 7.	64

Fig. 12: The 400-MHz ^1H -nuclear magnetic resonance spectrum of Na_6TDCPMB in $\text{H}_2\text{O}-d_2$ containing (3-(trimethylsilyl)-2,2,3,3-tetradeuteropropionic acid (TMPS)- d_4 as standard reference. Inset: chemical structure of the salt Na_6TDCPMB . see spectrum conditions in the appendix A 18.....	65
Fig. 13: The 400-MHz ^{13}C -nuclear magnetic resonance spectrum of Na_6TDCPMB in $\text{H}_2\text{O}-d_2$ containing (3-(trimethylsilyl)-2,2,3,3-tetradeuteropropionic acid (TMPS)- d_4 as standard reference. Inset: chemical structure of the salt Na_6TDCPMB . see spectrum conditions in the appendix A 19.....	66
Fig. 14: Solid-state vibrational spectra in the infrared region of H_3TCPMB and H_6TDCPMB collected in the attenuated total reflection (ATR) mode.....	67
Fig. 15: Recorded absorption spectra, at room temperature of 4-hydroxybenzoic acid, H_3TDCPMB and 1,3,5-tris(bromomethyl)benzene as acetonitrile solutions, and Na_6TDCPMB as aqueous solution (a). Thermogravimetric curves (TG) of the protonated ligand H_3TCPMB and H_6TDCPMB (b).....	69
Fig. 16: (a) Matt drawing of the asymmetric unit of Eu-TCPMB . (b) The coordination geometries of Eu^{III} ions in Eu-TCPMB resulting in a C_1 symmetry site for the central ion. (c) The connection mode of Eu^{III} ions in a binuclear unit. (d) View of the 1D chain as the infinite secondary building units (SBUs) along the crystallographic b-axis obtained from binuclear units linked through carboxylate group. H atoms and free solvent molecules were omitted for clarity.....	71
Fig. 17: (a) Each TCPMB^{3-} ligand connects three binuclear $\text{Eu}_2(\mu_2\text{-COO})_2$ units in Eu-TCPMB . (b) Number of TCPMB^{3-} ligands around the binuclear unit $\text{Eu}_2(\mu_2\text{-COO})_2$. H atoms were omitted for clarity.....	72
Fig. 18: View of the 3D supramolecular structure of the coordination network Eu-TCPMB along the crystallographic b-axis.....	72
Fig. 19: (a) Calculated P-XRD patterns from the CIF files of the compounds obtained from the ligand H_3TCPMB . (b) Experimental P-XRD patterns of the compounds Eu-TCPMB , Gd-TCPMB , Tb-TCPMB and $\text{Tb}_{0.95}\text{Eu}_{0.05}\text{-TCPMB}$ and calculated P-XRD pattern of Eu-TCPMB	74
Fig. 20: (a) Experimental P-XRD patterns of the compounds La-TCPMB and $\text{La}_{0.95}\text{Eu}_{0.05}\text{-TCPMB}$. (b) FT-IR spectra of free ligand H_3TCPMB and the as-synthesized compounds Eu-TCPMB , Tb-TCPMB , Gd-TCPMB , $\text{Tb}_{0.95}\text{Eu}_{0.05}\text{-TCPMB}$ and La-TCPMB	75

Fig. 21: Thermograms of Eu-TCPMB, Tb-TCPMB, Eu-TCPMB-tppo and Eu-TCPMB-phen obtained in synthetic air flow.	77
Fig. 22: (a) P-XRD patterns of Eu-TDCPMB obtained by solvothermal synthesis in DMF at 120 °C (1), 150 °C (2), 180 °C (3) and by hydrothermal at 120 °C (4), 150 °C (5), 180 °C (6). (b) P-XRD patterns of Eu-TDCPMB, Gd-TDCPMB, Tb-TDCPMB, Gd _{1.9} Eu _{0.1} -TDCPMB, Gd _{1.9} Tb _{0.1} -TDCPMB obtained by precipitation. (d) P-XRD patterns of Eu-TDCPMB obtained in DMF (black) or water (red) with the addition of NaOH to the reaction mixture. (d) TG and DTA curves of thermal decomposition of Eu-TDCPMB, Gd-TDCPMB and Tb-TDCPMB.....	78
Fig. 23: Infrared spectra of the salt Na ₆ TDCPMB and the compounds represented by Ln-TDCPMB (Ln = Eu ^{III} , Gd ^{III} , Tb ^{III}) and Gd _{1.9} Ln _{0.1} -TDCPMB (Ln = Eu ^{III} , Tb ^{III}).....	79
Fig. 24: (a) Powder XRD diffraction patterns of Eu-AC, Eu-BDC, Eu-AC-BDC and Tb-AC-BDC (b) FT-IR spectra of the free ligand HAC, H ₂ BDC, the salts NaAC, Na ₂ BDC and the compounds Eu-AC, Eu-BDC and Eu-AC-BDC.	82
Fig. 25: Thermogravimetric curves of Eu-AC, Eu-BDC and Eu-AC-BDC	83
Fig. 26: P-XRD patterns (a) and FT-IR spectra (b) of the compounds represented by Tb _x Eu _{1-x} acac _x BDC _{1.5-x/2} (x = 0.99, 0.95, 0.93, 0.9, 0.85 and 0.75).....	85
Fig. 27: Thermograms of the compounds represented by Tb _x Eu _{1-x} (acac) _x (BDC) _{1.5-x/2} (x = 0.99, 0.95, 0.93 and 0.9).	86
Fig. 28: Representative UV-vis DRS spectra of the compounds synthesized from the ligands H ₃ TCPMB (a), H ₆ TDCPMB (b), HAC & H ₂ BDC (c) and Hacac & H ₂ BDC (d). 87	
Fig. 29: (a) Excitation (dark) and emission (red) spectra of the free ligand H ₃ TCPMB at 77 K monitored at λ _{em} = 338 nm and λ _{ex} = 283 nm respectively. (b) Excitation (dark) and emission (red) spectra of Gd-TCPMB at 77 K monitored at λ _{em} = 416 nm and λ _{ex} = 286 nm respectively.	89
Fig. 30: (a) Photoluminescence study of La-TCPMB at 295 K. Excitation spectrum monitored at λ _{em} = 430 nm (dark) and emission spectra monitored at λ _{ex} = 270 nm (red) and at λ _{ex} = 295 nm (blue). (b) Prompted and delayed emission of La-TCPMB upon excitation at λ _{ex} = 270 nm and T = 77 K.	90
Fig. 31: Normalized excitation spectra obtained at 77 K (dark), 110 K (red) and 300 K (blue) of Eu-TCPMB monitoring at 616 nm (a). Normalized emission spectra of Eu-TCPMB upon excitation at 290 nm (dark) and at 393 nm (red) collected at 77 K (b), 110 K (c) and 300 K (d). Emission spectra of Eu-TCPMB at 77 upon excitation at 290	

nm and 393 nm. The Insets show the $^5D_0 \rightarrow F_1$ and $^5D_0 \rightarrow F_2$ regions magnified (e). High-resolution $^5D_0 \rightarrow ^7F_0$ emission band of the Eu-TCPMB coordination network obtained at 77 K upon excitation at 290 and 393 nm (f).....	92
Fig. 32: Normalized excitation and emission spectra monitored at 614 nm and at 280 nm respectively of Eu-TCPMB-tpo (a) and at 614 nm and 300 nm of Eu-TCPMB-phen (b) collected at ca. 293 K.....	93
Fig. 33: Normalized excitation (a) and emission (b) spectra of Tb-TCPMB monitored at 543 nm and 280 nm respectively and collected at 77 K (dark) and at 300 K (red). ...	94
Fig. 34: (a) Normalized excitation of Tb _{0.95} Eu _{0.05} -TCPMB monitored at 616 nm and 543 nm at the temperatures of 77 K and 300 K. (b) normalized emission spectra of Tb _{0.95} Eu _{0.05} -TCPMB excited at 283 nm and at 393 nm at the temperatures of 77 K and 300 K.....	95
Fig. 35: Luminescence decay curves of Eu-TCPMB and Tb-TCPMB monitored at 616 nm and 543 nm respectively upon excitation at 290 nm and 393 nm for Eu-TCPMB and at 280 nm for Tb-TCPMB at the temperatures of 77K, 110 K and 300 K.	97
Fig. 36: Emission decay curves of Eu-TCPMB-tpo excited at 393 nm (a) and at 290 nm (b) monitored at 616nm at the temperatures of 77 K, 110 K and 300 K.	98
Fig. 37: Emission decay curves of Eu-TCPMB-phen excited at 393 nm (a) and at 290 nm (b) monitored at 616nm at the temperatures of 77 K (black), 110 K (red) and 300 K (green).	98
Fig. 38: Emission decay curves of Tb _{0.95} Eu _{0.05} -TCPMB monitored at 543 nm and 616 nm upon excitation at 283 nm at the temperatures of 77K, 110 K and 300 K	99
Fig. 39: Time-resolved photoluminescence of Gd-TDCPMB at 77 K excited at 310 nm (a) and triplet energy estimation for H ₆ TDCPMB using both tangent and deconvolution methodologies (b).....	100
Fig. 40: Excitation (a) and emission (b) spectra of Gd-TDCPMB, Eu-TDCPMB and Tb-TDCPMB measured at 295 K.....	100
Fig. 41: Excitation and emission spectra of Gd _{1.1} Tb _{0.4} Eu _{0.5} -TDCPMB obtained at room temperature (293 K).	102
Fig. 42: Luminescence decay profiles of the compounds Tb-TDCPMB and Eu-TDCPMB(a), Gd _{1.9} Tb _{0.1} -TDCPMB and Gd _{1.9} Eu _{0.1} -TDCPMB(b), Gd _{1.5} Tb _{0.4} Eu _{0.1} -TDCPMB(c) and Gd _{1.3} Tb _{0.4} Eu _{0.3} -TDCPMB(d) excited at 275 nm and monitored at 543 nm (Tb ^{III}) and at 616 nm (Eu ^{III}).	103

Fig. 43: (a) Excitation spectrum monitored at 616 nm (black) and emission spectrum monitored at 324 nm (red) of Eu-BDC at 295 K. (b) (a) excitation spectrum monitored at 545 nm (black) and emission spectrum monitored at 320 nm (red) of Tb-BDC at 295K.	104
Fig. 44: (a) Excitation spectra of the free ligand HAC and the compounds Eu-AC and Tb-AC monitored at 504, 441 and 524 nm respectively. (b) emission spectra of HAC excited at 284 nm (dark) and 370 nm (red), of Eu-AC excited at 257 nm (green) and 366 nm (blue) and of Tb-AC excited at 257 nm (cyan) and 364 nm (orange). The spectra were recorded at 293 K.	105
Fig. 45: (a) Excitation spectrum monitored at 615 nm (black) and emission spectrum monitored at 304 nm (red) of Eu-BDC-AC at 295K. (b) (a) excitation spectrum monitored at 546 nm (black) and emission spectrum monitored at 304 nm (red) of Tb-BDC-AC at 295K.	105
Fig. 46: (a) Normalized emission spectra of Tb _{0.93} Eu _{0.07} -BDC-AC monitored at 303 nm obtained at 80 K (black) and 300 K (red). (b) Normalized emission spectra of Tb _{0.993} Eu _{0.007} -BDC-AC at 80 K (dark) and at 305 (red) upon excitation at 303 nm. .	106
Fig. 47: (a) Emission decay curves of Eu-BDC (black) and Eu-BDC-AC (red) exciting at 324 nm and 304 nm respectively and monitoring at 616 nm and 615 nm respectively. (b) Photoluminescence decay curves of Tb-BDC (black) and Tb-BDC-AC (red) exciting at 320 nm and 304 nm respectively and monitoring at 545 nm and 546 nm respectively.	107
Fig. 48: (a) Emission decay curves of Tb _{0.93} Eu _{0.07} -BDC-AC upon excitation at 303 nm and monitoring at 698 and 545 nm at the temperature of 80 and 300 K. (b) Photoluminescence decay curves of Tb _{0.993} Eu _{0.007} -BDC-AC upon excitation at 304 nm and monitoring at 698 and 545 nm at the temperature of 80 and 300 K.	108
Fig. 49: Excitation spectra monitored at 545 nm (a), at 615 nm (b) and at 698 nm and emission spectra upon excitation at 325 nm (c) of the compound Tb _x Eu _{1-x} acac _x BDC _{1.5-x/2} collected at room temperature (x = 0.99, 0.95, 0.93, 0.9, 0.85 and 0.75).	110
Fig. 50: Emission decay profiles of the compounds Tb _x Eu _{1-x} acac _x BDC _{1.5-x/2} (x = 0.99, 0.95, 0.90, 0.85, 0.75) at 295 K upon excitation at 320 nm and monitored the Eu ^{III} emission at 698 nm (a) and the Tb ^{III} emission at 545 nm (b).	110
Fig. 51: (a) Solid-state emission spectra of Eu-TCPMB recorded between 80 and 300 K upon excitation at 280 nm. (b) Temperature-dependent area of the band assigned	

to $^5D_0 \rightarrow ^7F_2$ transition of Eu-TCPMB (dark dot), the linear fit of the area of $^5D_0 \rightarrow ^7F_2$ transition versus temperature in the temperature of 90-220 K, relative sensitivity versus temperature (blue).....	112
Fig. 52: (a) Solid-state emission spectra of Tb-TCPMB recorded between 80 and 300 K upon excitation at 280 nm. (b) Temperature-dependent area of the band assigned to $^5D_4 \rightarrow ^7F_5$ transition of Tb-TCPMB (dark dot), relative sensitivity versus temperature (blue).....	113
Fig. 53: (a) Solid-state emission spectra of Tb _{0.95} Eu _{0.05} -TCPMB recorded between 80 and 300 K upon excitation at 280 nm. (b) Temperature-dependent area of the band assigned to $^5D_4 \rightarrow ^7F_5$ transition of Tb-TCPMB (dark dot), relative sensitivity versus temperature (blue).....	114
Fig. 54: (a) Temperature-dependent of Tb _{0.95} Eu _{0.05} -TCPMB recorded between 278 and 348 K with the excitation wavelength fixed at 280 nm. (b) Corresponding temperature dependence of normalized I_{Tb} and I_{Eu} . (c) and (d) Corresponding temperature dependence of I_{Tb} / I_{Eu}	115
Fig. 55: (a) Temperature-dependent of Tb _{0.95} Eu _{0.05} -TCPMB recorded between 298 and 393 K with the excitation wavelength fixed at 283 nm. (b) Corresponding temperature dependence of normalized I_{Tb} and I_{Eu} . (c) and (d) Corresponding temperature dependence of I_{Tb} / I_{Eu}	115
Fig. 56: (a) Temperature-dependent of Tb _{0.95} Eu _{0.05} -TCPMB recorded between 80 and 320 K with upon laser excitation at 488 nm. (b) Corresponding temperature dependence of normalized I_{Tb} and I_{Eu} . (c) and (d) Corresponding temperature dependence of I_{Tb} / I_{Eu}	116
Fig. 57: (a) Temperature-dependent of Gd-TCPMB recorded between 80 and 210 K with the excitation wavelength fixed at 286 nm. (b) Temperature dependence of the integrated intensities in the spectral range of the triplet and the $^5D_4 \rightarrow ^7F_5$ and $^5D_0 \rightarrow ^7F_2$ emissions. Temperature dependence of the $I_{triplet} / I_{Eu}$ (c), $I_{triplet} / I_{Tb}$ (d) and I_{Tb} / I_{Eu} (e).	118
Fig. 58: Emission spectra of Gd _{1.9} Eu _{0.1} -TDCPMB (a) and Gd _{1.9} Tb _{0.1} -TDCPMB (b) recorded between 77 K and 300 K upon excitation at 275 nm and 280 nm, respectively.	119

Fig. 59: Relative thermal sensitivities and temperature-dependent of the areas of the bands assigned to the $^5D_0 \rightarrow ^7F_2$ and $^5D_4 \rightarrow ^7F_5$ transitions for Gd _{1.9} Eu _{0.1} -TDCPMB (a) and Gd _{1.9} Tb _{0.1} -TDCPMB (b) between 77 and 300 K.....	120
Fig. 60: (a) Temperature-dependent of Gd _{1.5} Tb _{0.4} Eu _{0.1} -TDCPMB recorded between 77 and 300 K with the excitation wavelength at 330 nm. (b) Corresponding temperature dependence of normalized I_{Tb} and I_{Eu}	121
Fig. 61: (a) Temperature-dependent of Gd _{1.5} Tb _{0.4} Eu _{0.1} -TDCPMB recorded between 77 and 300 K with the excitation wavelength at 275 nm. (b) Corresponding temperature dependence of normalized I_{Tb} and I_{Eu} . (c e d) Corresponding temperature dependence of I_{Tb} / I_{Eu}	122
Fig. 62: (a) Temperature-dependent of Gd _{1.5} Tb _{0.4} Eu _{0.1} -TDCPMB recorded between 273 and 373 K with the excitation wavelength at 275 nm. (b) Corresponding temperature dependence of normalized I_{Tb} and I_{Eu} . (c and d) Corresponding temperature dependence of I_{Tb} / I_{Eu}	123
Fig. 63: Emission decay curves of Gd _{1.5} Tb _{0.4} Eu _{0.1} -TDCPMB excited at 275 nm and monitoring at 615 nm (a) and 543 nm (b) and variation profile of the luminescence lifetime values (c) between 80 and 300 K.....	124
Fig. 64: Emission decay curves of Gd _{1.5} Tb _{0.4} Eu _{0.1} -TDCPMB upon excitation at 275 nm and monitoring at 615 nm (a) and 543 nm (b) and variation profile of the luminescence lifetime values (c) between 273 and 373 K.....	126
Fig. 65: (a) Temperature-dependent of Gd _{1.3} Tb _{0.4} Eu _{0.3} -TDCPMB recorded between 77 and 300 K with the excitation wavelength at 275 nm. (b) Corresponding temperature dependence of normalized I_{Tb} and I_{Eu} . (c) Corresponding temperature dependence of I_{Tb} / I_{Eu}	128
Fig. 66: (a) Temperature-dependent of Gd _{1.3} Tb _{0.4} Eu _{0.3} -TDCPMB recorded between 278 and 373 K with the excitation wavelength at 275 nm. (b) Corresponding temperature dependence of normalized I_{Tb} and I_{Eu} . (c) Corresponding temperature dependence of I_{Tb} / I_{Eu}	128
Fig. 67: (a) Temperature-dependent of Gd _{1.2} Tb _{0.4} Eu _{0.4} -TDCPMB recorded between 77 and 320 K with the excitation wavelength at 275 nm. (b) Corresponding temperature dependence of normalized I_{Tb} and I_{Eu} . (c) Corresponding temperature dependence of I_{Tb} / I_{Eu}	129

Fig. 68: (a) Temperature-dependent of Gd _{1.1} Tb _{0.4} Eu _{0.5} -TDCPMB recorded between 77 and 320 K with the excitation wavelength at 275 nm. (b) Corresponding temperature dependence of normalized I_{Tb} and I_{Eu} . (c) and (d)Corresponding temperature dependence of I_{Tb} / I_{Eu} .	129
Fig. 69: (a) Temperature-dependent of Gd _{1.2} Tb _{0.4} Eu _{0.4} -TDCPMB recorded between 278 and 348 K with the excitation wavelength at 275 nm. (b) Corresponding temperature dependence of normalized I_{Tb} and I_{Eu} . (c) and (d)Corresponding temperature dependence of I_{Tb} / I_{Eu}	130
Fig. 70: (a) Temperature-dependent of Gd _{1.1} Tb _{0.4} Eu _{0.5} -TDCPMB recorded between 278 and 345 K with the excitation wavelength at 280 nm. (b) Corresponding temperature dependence of normalized I_{Tb} and I_{Eu} . (c) and (d)Corresponding temperature dependence of I_{Tb} / I_{Eu}	130
Fig. 71: (a) Solid-state emission spectra of Tb _{0.93} Eu _{0.07} -BDC-AC recorded between 80 -300 K. (b) Temperature-dependent areas of the $^5D_0 \rightarrow ^7F_2$, $^5D_0 \rightarrow ^7F_4$ and $^5D_4 \rightarrow ^7F_5$ transitions. (c and d) Temperature-dependent intensity ratio $^5D_4 \rightarrow ^7F_5 / ^5D_0 \rightarrow ^7F_2$ and $^5D_4 \rightarrow ^7F_5 / ^5D_0 \rightarrow ^7F_4$ between 80 and 300 K.....	131
Fig. 72: (a) Solid-state emission spectra of Tb _{0.993} Eu _{0.007} -BDC-AC recorded between 80 -305 K. (b) Temperature-dependent areas of the $^5D_0 \rightarrow ^7F_2$, $^5D_0 \rightarrow ^7F_4$ and $^5D_4 \rightarrow ^7F_5$ transitions. (c and d) Temperature-dependent intensity ratio $^5D_4 \rightarrow ^7F_5 / ^5D_0 \rightarrow ^7F_2$ and $^5D_4 \rightarrow ^7F_5 / ^5D_0 \rightarrow ^7F_4$ between 80 and 305 K.....	132
Fig. 73: (a) Emission spectra of Tb _{0.99} Eu _{0.01} acac _{0.99} BDC _{1.005} recorded between 80 and 300 K upon excitation at 320 nm. (b) temperature dependence of the normalized integrated intensities of the $^5D_4 \rightarrow ^7F_5$, $^5D_0 \rightarrow ^7F_2$ and $^5D_0 \rightarrow ^7F_4$ (c) and (d) Temperature dependence of the integrated intensity ratio of Tb ^{III} and Eu ^{III} . The green and the blue curves represent the linear fitting of the intensity ratios and the relative sensitivities respectively.	134
Fig. 74: (a) Emission spectra of Tb _{0.95} Eu _{0.05} acac _{0.95} BDC _{1.025} recorded between 80 and 300 K upon excitation at 320 nm. (b) temperature dependence of the normalized integrated intensities of the $^5D_4 \rightarrow ^7F_5$, $^5D_0 \rightarrow ^7F_2$ and $^5D_0 \rightarrow ^7F_4$ (c) and (d) Temperature dependence of the integrated intensity ratio of Tb ^{III} and Eu ^{III} . The green and the blue curves represent the linear fitting of the intensity ratios and the relative sensitivities respectively.	134

Fig. 75: (a) Emission spectra of $\text{Tb}_{0.90}\text{Eu}_{0.10}\text{acac}_{0.90}\text{BDC}_{1.05}$ recorded between 80 and 300 K upon excitation at 320 nm. (b) temperature dependence of the normalized integrated intensities of the $^5\text{D}_4 \rightarrow ^7\text{F}_5$, $^5\text{D}_0 \rightarrow ^7\text{F}_2$ and $^5\text{D}_0 \rightarrow ^7\text{F}_4$ (c) and (d) Temperature dependence of the integrated intensity ratio of Tb^{III} and Eu^{III} . The green and the blue curves represent the linear fitting of the intensity ratios and the relative sensitivities respectively. 135

Fig. 76: (a) Emission spectra of $\text{Tb}_{0.85}\text{Eu}_{0.15}\text{acac}_{0.90}\text{BDC}_{1.05}$ recorded between 80 and 300 K upon excitation at 320 nm. (b) temperature dependence of the normalized integrated intensities of the $^5\text{D}_4 \rightarrow ^7\text{F}_5$, $^5\text{D}_0 \rightarrow ^7\text{F}_2$ and $^5\text{D}_0 \rightarrow ^7\text{F}_4$ (c) and (d) Temperature dependence of the integrated intensity ratio of Tb^{III} and Eu^{III} . The green and the blue curves represent the linear fitting of the intensity ratios and the relative sensitivities respectively. 135

Fig. 77: (a) Emission spectra of $\text{Tb}_{0.75}\text{Eu}_{0.25}\text{acac}_{0.75}\text{BDC}_{1.125}$ recorded between 80 and 300 K upon excitation at 320 nm. (b) temperature dependence of the normalized integrated intensities of the $^5\text{D}_4 \rightarrow ^7\text{F}_5$, $^5\text{D}_0 \rightarrow ^7\text{F}_2$ and $^5\text{D}_0 \rightarrow ^7\text{F}_4$ (c) and (d) Temperature dependence of the integrated intensity ratio of Tb^{III} and Eu^{III} . The green and the blue curves represent the linear fitting of the intensity ratios and the relative sensitivities respectively. 136

List of Tables

Table 1: Electronic Configurations of the lanthanides trivalent Lanthanide Ions in the Ground State.....	33
Table 2: Average lengths of the bonds between trivalent metal ions Ln and the coordinated oxygen atoms and the Ln···Ln internuclear distances (Å) in the binuclear units of Eu-TCPMB, Gd-TCPMB, Tb-TCPMB, Tb _{0.95} Eu _{0.05} -TCPMB ^a	72
Table 3: Crystal data of the free ligand (H ₃ TCPMB) and the lanthanides-based coordination polymers	73
Table 4: Observed emission-lifetime values of the compounds prepared from ligand H ₃ TCPMB.....	97
Table 5: Emission lifetime values of the compounds Tb _x Eu _{1-x} acac _x BDC _{1.5-x/2} (x = 0.99, 0.95, 0.90, 0.85, 0.75) at 295 K.....	111
Table 6: Temperature-dependence luminescent decay times (τ) of Gd _{1.5} Tb _{0.4} Eu _{0.1} monitored at 543 nm and 615 nm in the temperature range of 77 - 300 K.	125
Table 7: Temperature-dependence emission lifetimes (τ) of Gd _{1.5} Tb _{0.4} Eu _{0.1} -TDCPMBmonitored at 543 nm and 614 nm in the temperature range of 273 to 373 K	127
Table 8: Composition, working ranges, absolute sensitivity values (S _a) and maximum relative sensitivity values (max S _r) of the CPs studied as ratiometric thermal probes.	138

List of acronyms

BDCF ₄	: 2,3,5,6-Tetrafluoro-1,4-benzenedicarboxylate
BPYDC	: 2,2'-bipyridine-5,5'-dicarboxylic acid
BTC	: 1,3,5-benzenetricarboxylate
CPDA	: 5-(4-carboxyphenyl)-2,6-pyridinedicarboxylate
CPNA	: 4-carboxyphenyl)nicotinic acid
CPs	: Coordination polymers
D-H ₂ cam	: D-camphoric acid
DMBDC	: 2,5-dimethoxy-1,4-Benzenedicarboxylate
DRS	: Diffuse reflectance Spectroscopy
DSB	: 3,5-disulfobenzoate
EDTA	: Disodium ethylenediaminetetraacetic acid
FT-IR	: Fourier-transform infrared
H ₂ BDC	: 1,4-benzene dicarboxylic acid
H ₂ DSTP	: 2,4-(2,2':6',2''-terpyridin-4'-yl)-benzenedisulfonic acid
H ₃ imdc	: 4,5-imidazole dicarboxylic acid
H ₃ TCPMB	: 1,3,5-tris(4-carboxyphenoxy methyl)benzene
H ₆ TDCPMB	: 1,3,5-tris(2,6-dicarboxypyridine-4-oxy methyl)benzene
HAC	: 9-anthracenecarboxylic
Hacac	: acetylacetone
IC	: Internal conversion
ISC	: Intersystem crossing
IUPAC	: International Union of Pure and Applied Chemistry
K _{nr}	: Non-radiative decay rates
K _r	: Radiative decay rates
LEDs	: Light-emitting devices
Ln	: Lanthanide
Ln-Cps	: Lanthanide Coordination polymers
MOF	: Metal-Organic Framework
OA	: oxalic acid
PBU	: Primary building unit
PDC	: Pyridine-3,5-dicarboxylate

PES	: Potential energy surface
phen	: Phenanthroline
PIA	: 5-(Pyridin-4-yl)isophthalate)
P-XRD	: Powder X-ray diffraction
QPTCA	: 1,1', 4',1'',4'',1'''-quaterphenyl-3,3'',5,5'''-tetracarboxylate
RTDs	: Resistance temperature detectors
SBU	: Secondary building unit
TCSPC	: Time-correlated single photon counting
TMSP-d ₄	: 3-(trimethylsilyl)-2,2,3,3-tetradeuteropropionic acid
tppo	: triphenylphosphine oxide

Summary

1. General Introduction.....	27
1.1. The concept of temperature	27
1.2. Types of temperature sensors.....	28
1.3. The luminescence-based thermometry	30
1.4. Characteristics of a luminescence-based temperature sensor.....	31
1.5. The trivalent lanthanide and their luminescence properties	32
1.6. Lanthanide coordination polymers and temperature sensing	40
1.7. Examples of luminescent ratiometric thermometers based on lanthanide coordination polymers.....	48
2. Objectives and motivation	51
3. Experimental section	53
3.1. Materials and methods	53
3.2. Synthesis of 1,3,5-tris(4-carboxyphenoxy)methyl)benzene (H ₃ TCPMB)	55
3.3. Synthesis of the 4-hydroxy-2,6-dimethoxycarbonylpyridine	55
3.4. Synthesis of 1,3,5-tris(2,6-dicarboxypyridine-4-oxy methyl)benzene (H ₆ TDCPMB)	56
3.5. Synthesis of the coordination polymers based on the ligand H ₃ TCPMB	56
3.6. Synthesis of the coordination polymers based on the ligand H ₆ TDCPMB....	57
3.6.1. Syntheses of Ln-TDCPMB (Ln = Eu ^{III} , Gd ^{III} , Tb ^{III})	57
3.6.2. Syntheses of the mixed Ln-TDCPMB (Ln = Eu ^{III} , Gd ^{III} , Tb ^{III}).....	57
3.6.3. Synthesis of the compounds represented by Ln-AC (Ln = Tb ^{III} , Eu ^{III})....	58
3.6.4. Synthesis of the compounds represented by Ln-BDC (Ln = Tb ^{III} , Eu ^{III}) .	58
3.6.5. Synthesis of the compounds represented by Ln-BDC-AC (Ln = Tb ^{III} , Eu ^{III}) and containing the mixed of lanthanide ions	58
3.6.6. Synthesis of the compounds represented by Tb _x Eu _{1-x} acac _x BDC _{1.5-x/2} ...	58
4. Results and discussion.....	60

4.1. Characterization of the synthesized ligands 1,3,5-tris(4-carboxyphenoxy methyl)benzene (H ₃ TCPMB) and 1,3,5-tris(2,6-dicarboxypyridine4oxy methyl)benzene (H ₆ TDCPMB).....	60
4.1.1. Synthesis and structural description of the ligand H ₃ TCPMB	60
4.1.2. Synthesis of the ligand H ₆ TDCPMB.....	62
4.2. Nuclear Magnetic Resonance (NMR) spectroscopy.....	64
4.2.1. Fourier-transform infrared spectroscopy.....	66
4.2.2. Ultraviolet-visible spectroscopy and thermal stability.....	67
4.3. Syntheses and characterization of the compounds based on H ₃ TCPMB.....	70
4.3.1. Syntheses and structural description	70
4.3.2. Powder X-ray Diffraction and FT-IR spectroscopy.....	74
4.3.3. Thermal stability.....	76
4.4. Synthesis and characterization of the compounds based on H ₆ TDCPMB ...	77
4.4.1. Synthesis, P-XRD, and FT-infrared spectroscopy	77
4.4.2. Thermal stability.....	80
4.5. Characterization of the compounds based on H ₂ BDC and HAC	80
4.5.1. Powder x-ray diffraction and Infrared spectroscopy.....	80
4.5.2. Thermal stability.....	83
4.6. Characterization of the compounds based on H ₂ BDC and Hacac.....	84
4.6.1. P-XRD and FT-IR spectroscopy studies	84
4.6.2. Thermal stability.....	86
4.6.3. Electronic properties: Diffuse reflectance UV-vis spectroscopy	86
4.7. Solid-state photophysical properties.....	88
4.7.1. Compounds based on the ligand H ₃ TCPMB.....	88
4.7.2. Compounds based on the H ₆ TDCPMB ligand	100
4.7.3. Compounds based on the ligand H ₂ BDC and HAC	104
4.7.4. Compounds based on the ligand H ₂ BDC and Hacac.....	109

4.8. Temperature-dependent photoluminescence properties	111
4.8.1. Compounds based on the ligand (H ₃ TCPMB)	111
4.8.2. Compounds based on the ligand (H ₆ TDCPMB).....	119
4.8.3. Compounds based on the ligand H ₂ BDC and HAC	131
4.8.4. Compounds based on the ligand H ₂ BDC and Hacac.....	133
5. Conclusions.....	139
References	141
6. Appendix	151

1. General Introduction

1.1. The concept of temperature

Temperature is one of the most important if not the most fundamental physical parameter, that describe and may affect the dynamics and viability of natural and engineered systems, hence its great importance as an informative parameter in many fields of natural science, medicine, and technology [1,2]. For global climate patterns temperature is a major determining factor; a tiny change in average temperature may exert formidable effects on the environment worldwide. A temperature variation by just a few degrees may affect the plant yield, induces the apparition of invasive species, unbalances the aquatic life by varying the oxygen content for example. Consequently, the temperature is one of the most measured physical parameters, behind time and length, and probably that is one reason why thermal probes account for 80% of the total sensor worldwide market with a capital estimated to USD 5.13 billion in 2016 [2,3].

In a first approximation, the temperature may be defined as a measurement of the tendency of an object to spontaneously give up energy to its surroundings. The movement of molecules or atoms produces heat (kinetic energy) and the greater the movement, more heat is generated and consequently higher the temperature of the system. However, this definition in terms of molecular kinetic energy is applicable basically only in a monoatomic ideal gas system. In that case, the equilibrium reached is one of maximum entropy, and the rate of approach to that state will be proportional to the difference in temperature between the two parts of the system. Considering the same ideal gas system, the equilibrium state will be the state of greatest entropy indicating that temperature (T) can be defined as the inverse of the rate of change of entropy* (S) with energy †(U), with volume V and number of particles N held constant. This concept can be mathematically expressed by Eq.1 [4].

$$T^{-1} = (\partial S / \partial U)_{V,N} \quad (\text{Eq. 1})$$

* Measure of the disorder of a system.

† Energy associated with the random, disordered motion of atoms or atoms groups.

Understanding the fundamental role of the temperature in the physical and chemical properties of materials, accurate and precise measurements of temperature, and sometimes its mapping in real-time are vital in many industrial areas such as automotive, aerospace and defense, metrology, climate and marine research, chemistry, medicine, biology, military technology, air conditioning, practically in all devices for heating and cooling, in the production of plants and storage of food making the thermal probes as leader in the sensors world's market [5]. By using a temperature sensor, one can measure the amount of heat energy or even coldness that is generated by an object or system, allowing the detection of possible physical change. With the arrival of the nanotechnology and the miniaturization of the devices, an increasing challenge to develop novel approaches in temperature sensing based on accurate and self-referenced Nano-thermometers operating according to non-invasive principle has gained importance.

1.2. Types of temperature sensors

There are many different types of temperature sensors which, according to the operation principle, can be classified into two main groups: The contact and non-contact thermometers [6]. The contact thermometers enable invasive measurement, where the monitoring device is installed in the medium of interest resulting in physical contact of the probe with the object being sensed and use conduction to monitor the temperature changes. In the non-contact thermometry, the measurement is noninvasive carrying out remotely usually by correlating the temperature changes to variations in some electromagnetic radiation. There are also the semi-invasive techniques where the medium of interest is treated in some manner to enable remote observation, for instance, surface coatings whose color changes with temperature [5]. In temperature sensing based on contact thermometers such as the liquid-filled glasses, the bimetallic, the thermocouples, the resistance temperature detectors (RTDs) and the thermistors, the temperature is correlated to the variations of the thermal expansion of the liquid, the electric potential, the Seebeck effect intensity [7], Ohmic resistance and the electric conductance respectively [5]. Consequently, as suggested by the proper name, the temperature measurement using the contact thermometers requires heat transfer to reach the thermal equilibrium between sample and probe making them not suitable for temperature mapping in the presence of fast-

moving objects (pistons in engines or rotors in gas turbines, for example), corrosive medium, in the fabrication of microsystems such as: microfluidics, microelectronics integrated photonic devices, and the Nano-medicine (intracellular temperature probing) where the temperature measurement is revealed to be fundamental. Only to justify using some examples, in the fabrication process of micro and Nano-metric devices, the reduction of the dimensions of the electrical conduction channels lead to relevant resistances in such a way that the Joule heating effect becomes non-negligible [8]. Thus, small geometry variations in the conduction wire can result in “hot-spots” which can catalyze performance deterioration, affect the durability or / and cause an irreversible failure of the device. Knowledge of these “hot-spots” should ease and increase the development and reliability of the microelectronics and allow to understand the low-scale thermal behavior. In integrated photonic devices, the refraction index is the main parameter used for light manipulation. Strongly temperature-dependence makes the devices performance temperature-sensitive. Therefore, novel methods are needed for obtaining knowledge of the temperature distribution in micro-photonic and nanophotonic devices. Finally, in biomedicine, the detection of small temperature variations in biosystems can help in early diagnostic and treatment of many diseases because of the difference in the metabolic rates involving pathological and normal cells [9–11]. In biosystems, all chemical and biological processes such as; cell division, gene expression, enzyme reaction and protein denaturation, besides being directly affected by the ambient temperature, usually involve heat change implying that intracellular temperature distribution may be a good parameter to evaluate the thermodynamics and cell functions [12–14]. When dealing with these very small objects, contact thermometry methods are completely inadequate. Pursuing new alternatives to measure temperature in the mentioned areas encouraged scientists to develop new noninvasive and accurate thermal probe based on optical methods such as infrared thermography, thermal reflection, the Rayleigh and Raman scattering and the luminescence spectroscopy [6,8,15].

Based on the black body radiation[‡], the infrared thermography was the first kind of optical thermometer and has been widely used in medical and industrial areas to monitor surface distribution of temperature thus, it is unsuitable for surface with low

[‡] Thermal electromagnetic radiation surrounding a body in thermodynamic equilibrium with its environment.

emissivity beyond the low-spatial resolution [2]. Furthermore, the infrared-based thermometer cannot be used in most microfluidics systems once water and glass absorb the infrared radiation. The thermal reflection technique, limited by the requirement of an optical surface or interface, utilizes the temperature dependence of the reflection coefficient of a material. Rayleigh and Raman scatterings[§] are the elastic and inelastic scattering of light by molecules or very small particles, respectively [5]. The use of Rayleigh and Raman scattering to sense temperature is substantiated by the fact that vibrational modes are affected by temperature changes. Because the low thermal sensitivity, these techniques are applicable only to those materials showing large Rayleigh and Raman scattering efficiencies. The luminescence-based thermometry has been emerged as a superior technique to overcome problems and limitations of the methods listed above.

1.3. The luminescence-based thermometry

Luminescence, including the phosphorescence^{**} and fluorescence^{††}, can be defined as the emission of photons occurred after an appropriate material has been electronically excited by an external source such as chemical reaction, electron beams, electromagnetic radiation, and so on [16]. In general, the return to the ground state of an excited specie can occur via radiative or/and non-radiative processes with the decay rates K_r and K_{nr} , respectively. The decay rates are temperature-dependent, at least, due to the Boltzmann distribution of the electrons between the vibrational levels within the electronic levels [2]. When exposed to changes in temperature, one or more luminescent properties of a material phosphor, such as bandwidth, band shape, polarization, emission lifetime, emission intensity, usually undergo some changes. If these changes are reproducible over successive cycling temperatures, the phosphor material can be characterized as a thermographic phosphor [3].

The luminescence thermometry is the optical technique for temperature measurement exploring the temperature dependence of the luminescence of a thermographic material. Such new luminescent thermometers have distinct advantages over other conventional thermometers because of their fast-response,

[§] Scattering in this context is the absorption and re-emission of electromagnetic radiation by atoms and molecules.

^{**} radiative deactivation process via electronic transitions involving change in spin multiplicity.

^{††} radiative deactivation process via electronic transitions without change in spin multiplicity.

high sensitivity, noninvasive operation, and inertness to strong electric fields opening routes for temperature mapping in reduced scale regions where contact thermometers are unsuitable. Indeed, the design and development of thermographic materials has been a very active research field in recent years.

Since Demas and De Graff have reported the first luminescent ruthenium complexes having thermographic properties in 1988 [17], many compounds were investigated for applications as optical thermal probes. Between the classes of compounds susceptible to be used as luminescent probes, one can mention the organic dyes, polymers dots, chelate complexes, up-conversion nanoparticles, semiconductor nanocrystals and trivalent lanthanides incorporated into inorganic, organic or hybrid hosts, where the temperature sensing is in general based on the decrease of their emission intensity with increasing temperature, due to the thermal activation of non-radiative relaxation pathways [18–21]. The lanthanide-based materials have attracted attention due to the uniqueness of the photophysical properties of the trivalent lanthanide ions. More recently, a step forward was made by the introduction of multi-center lanthanide luminescent thermal probes containing at least two optically active ions. If the emission of each luminescent center follows different thermal behaviors, the corresponding emission intensity ratio can be strongly correlated to the temperature changes. In this context, the coordination polymers have attracted much attention by making easy the insertion of diverse ions in the same matrix.

1.4. Characteristics of a luminescence-based temperature sensor

As for any sensor, the performance of a luminescence thermometer can be judged from a series of characteristics that define its figure of merit. Such parameters can be divided into two categories: the static characteristics which are measured after all transient effects have been stabilized to their final or steady-state values and the dynamic characteristics which are employed to describe the sensing system's transient properties [22]. These characteristics deal with issues such as the rate and the accuracy at which the output changes in response to a measurand alteration and how these changes occur. Among the parameters that compose the static characteristics are: accuracy, precision, repeatability, reproducibility, stability, error, noise, drift, resolution, minimum detectable signal, calibration curve, intrinsic sensitivity, linearity,

selectivity, hysteresis, measurement range, response and recovery Time [22]. In the literature of luminescence-based thermometry, the thermal sensitivity (S) is the most frequently reported parameter used as figure of merit. Defined as the quotient of an observed optical parameter Q (peak energy, luminescence lifetime, emission intensity, luminescence quantum yield or ratio between band intensities) and the change in the temperature (T), the thermal sensitivity is given by (Eq. 2).

$$S = \partial Q / \partial T \quad (\text{Eq. 2})$$

Temperature sensors showing large absolute changes in Q with small changes in temperature will be the most sensitive. In practice, however, a quantitative comparison of temperature sensors operating by different mechanisms or in different temperature ranges has proven challenging. In order to make this comparison possible, it was suggested a normalization of the internal thermal sensitivity introducing the relative thermal sensitivity (S_r) defined as presented in (Eq. 3).

$$S_r = \frac{\partial Q / \partial T}{Q} \quad (\text{Eq. 3})$$

From the absolute sensitivity and the measurement uncertainty σ which depends on the instrument, one can estimate the temperature ΔT_{min} and spatial Δx_{min} resolutions according to Eq. 4 and Eq. 5, respectively.

$$\Delta T_{min} = \frac{\sigma}{S} \quad (\text{Eq. 4})$$

$$\Delta x_{min} = \left| \frac{dx}{dT} \right| \Delta T_{min} \quad (\text{Eq. 5})$$

1.5. The trivalent lanthanide ions and their luminescence properties

The lanthanides represent the group of 14 elements from Ce ($Z = 58$) to Lu ($Z = 71$). By including the group-prototype (La) and the d-elements Sc ($Z = 21$) and Y ($Z = 39$) due to their similarity, the group is named as rare-earth elements. The lanthanum and the lanthanides exhibit the electronic configuration of $[\text{Xe}]4f^n 6s^2$ where $n = 1-15$ with notable exceptions for lanthanum, cerium, gadolinium, and lutetium which

also may be found in the $[\text{Xe}]4f^{n-1}5d^16s^2$ configuration resulting in a higher spin multiplicity (Table 1). The trivalent lanthanides (Ln^{III}) are their most stable oxidation state with the electronic configurations being $[\text{Xe}]4f^n$ (Table 1) thus, the trivalent lanthanide ions have in common an open 4f shell. Because of the largest radial extension of the filled 5s and 5p orbitals regarding the 4f shell, the 4f electrons are found to be shielded from the coordination environment (Fig. 1). As a result, lanthanides bind mostly through non-directional electrostatic interactions. Trivalent lanthanide ions have a wide range of coordination numbers, typically ranging from 6 to 12 (most commonly 8 and 9) with coordination geometries being determined by ligand steric considerations rather than crystal field effects.

Table 1: Electronic Configurations of the trivalent Lanthanide ions in the Ground State.

Element	Symbol	Electronic configuration	
		Ln	Ln^{III}
Lanthanum	La	$[\text{Xe}]4f^05d^16s^2$	$[\text{Xe}]4f^0$
Cerium	Ce	$[\text{Xe}]4f^26s^2$	$[\text{Xe}]4f^1$
Praseodymium	Pr	$[\text{Xe}]4f^36s^2$	$[\text{Xe}]4f^2$
Neodymium	Nd	$[\text{Xe}]4f^46s^2$	$[\text{Xe}]4f^3$
Promethium	Pm	$[\text{Xe}]4f^56s^2$	$[\text{Xe}]4f^4$
Samarium	Sm	$[\text{Xe}]4f^66s^2$	$[\text{Xe}]4f^5$
Europium	Eu	$[\text{Xe}]4f^76s^2$	$[\text{Xe}]4f^6$
Gadolinium	Gd	$[\text{Xe}]4f^75d^16s^2$	$[\text{Xe}]4f^7$
Terbium	Tb	$[\text{Xe}]4f^96s^2$	$[\text{Xe}]4f^8$
Dysprosium	Dy	$[\text{Xe}]4f^{10}6s^2$	$[\text{Xe}]4f^9$
Holmium	Ho	$[\text{Xe}]4f^{11}6s^2$	$[\text{Xe}]4f^{10}$
Erbium	Er	$[\text{Xe}]4f^{12}6s^2$	$[\text{Xe}]4f^{11}$
Thulium	Tm	$[\text{Xe}]4f^{13}6s^2$	$[\text{Xe}]4f^{12}$
Ytterbium	Yb	$[\text{Xe}]4f^{14}6s^2$	$[\text{Xe}]4f^{13}$
Lutetium	Lu	$[\text{Xe}]4f^{14}5d^16s^2$	$[\text{Xe}]4f^{14}$

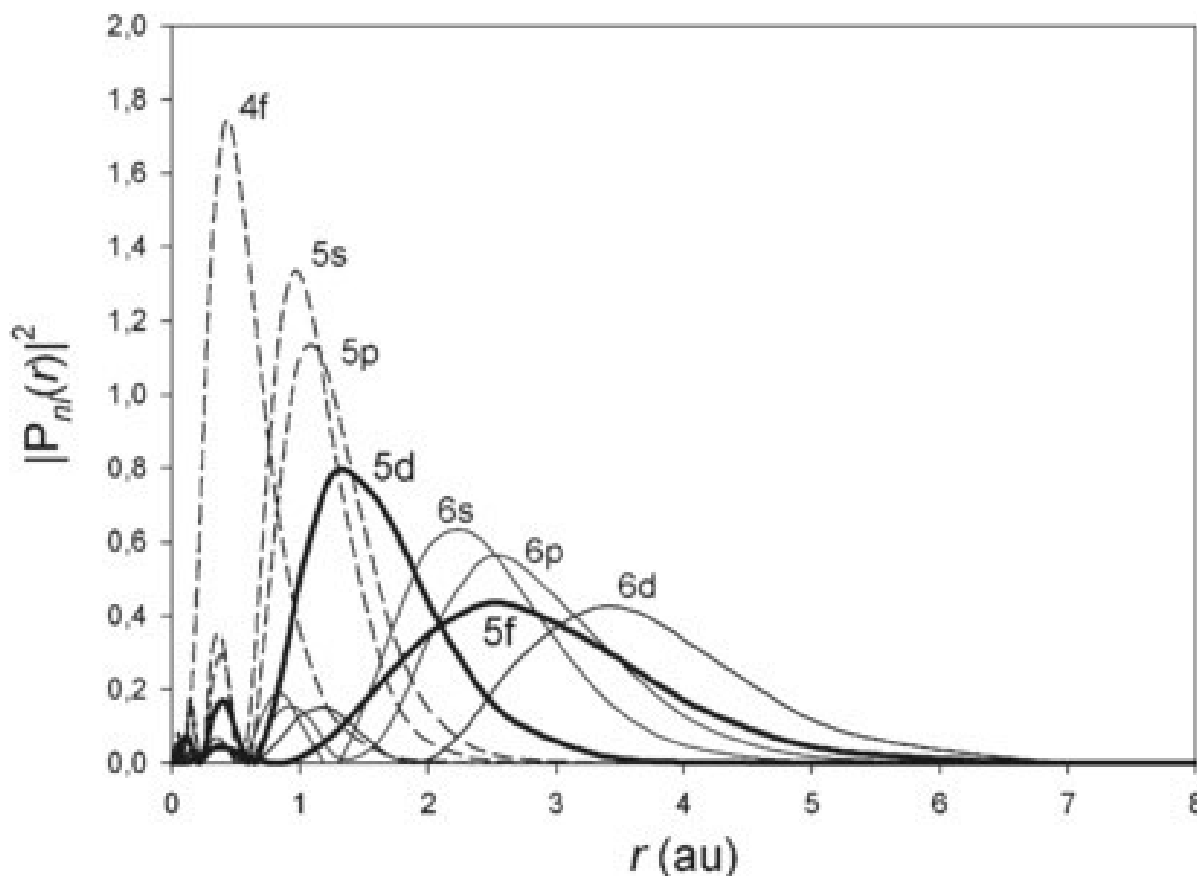


Fig. 1: Radial distribution plot of the s, p, d, and f valence orbitals in the hydrogen-like Lanthanide ions.

Because of the incomplete 4f shells, the electronic configurations $[\text{Xe}]4f^n$ generate many electronic states responsible for their magnetic and spectroscopic properties. In comparison with other types of metal ions, lanthanide ions exhibit a large atomic magnetic moment, strong spin-orbital coupling, high coordination number, and abundant coordination modes. These peculiar properties imply many technological applications for trivalent lanthanide ions containing systems such as light-emitting diodes and display devices [23], optoelectronic devices [24], lasers, biological imaging applications [25], light-emitting sensors for hetero and homogeneous fluoro-immunoassays [26]. In lanthanide compounds, the metal-centered luminescence is due to intra-configurational f–f electronic transitions. Due to the shielding of the 4f electrons from the external environment by the filled 5s and 5p orbitals, the spectral properties of lanthanide ions are minimally perturbed by the external field generated by their chemical ambient. Consequently, the shapes of the potential energy surfaces (PES) retain most of their atomic characters. In other words, in a configurational coordinate diagram, the electronics levels owing from the $4f^n$ configurations can be

considered matrix-independent and represented as parallel parabolas. Therefore, the relative energies of the electronic states ($^{2S+1}L_J$ where L represented by S, P, D, F, G, H, I, K, L, M,... for L = 0, 1, 2, 3, 4, 5, 6, 7, 8, 9, ..., S and J are the orbital, spin and total angular momenta respectively as shown in the well-known Dieke diagram given in Fig. 2) due to the fact that the $4f^n$ configuration is practically independent of the chemical environment of the trivalent ion. The total momentum J is given by the sum $J = L - S$ and $L + S$ when the number of 4f electrons is smaller and larger than 7 respectively.

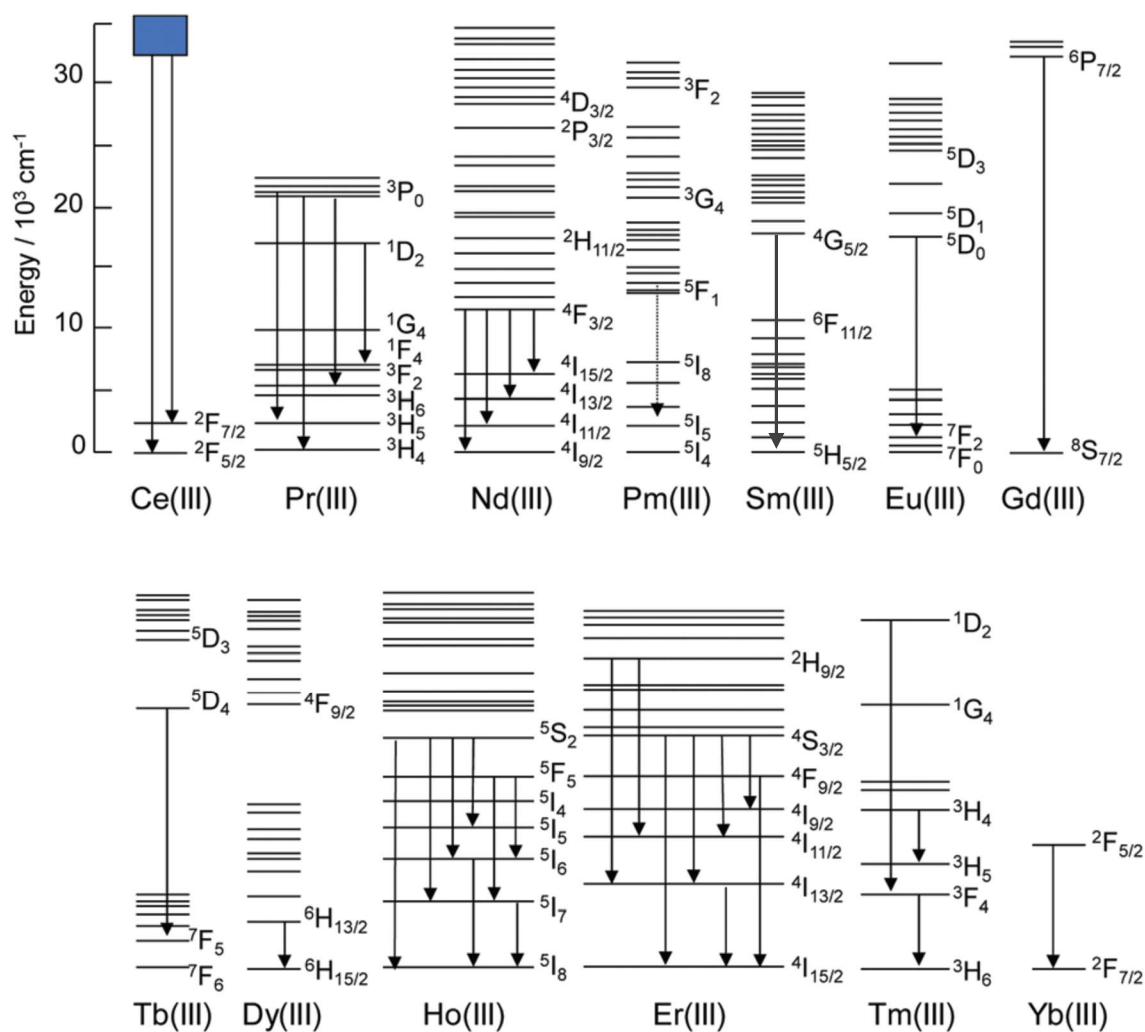


Fig. 2: Energy diagrams of the trivalent lanthanide ions and radiative transitions between different levels. Adapted from [27].

As a consequence of the 4f electrons shielding, in lanthanide compounds, the interaction with the ligand crystal field in the order of 10^2 cm^{-1} is considerably smaller

than the spin-orbit interaction which is in the order of 10^3 cm^{-1} . The crystal field only perturbs splitting them into the so-called Stark sublevels [28]. The number of Stark components depending on the crystal field symmetry and selection rules can reach $2J + 1$ when J is an integer number or $J + \frac{1}{2}$ when J is a half-integer number. Fig. 3 shows an illustration of the influence of principal physical interactions on the development of the energy level structure of a trivalent europium ion when introduced into a solid.

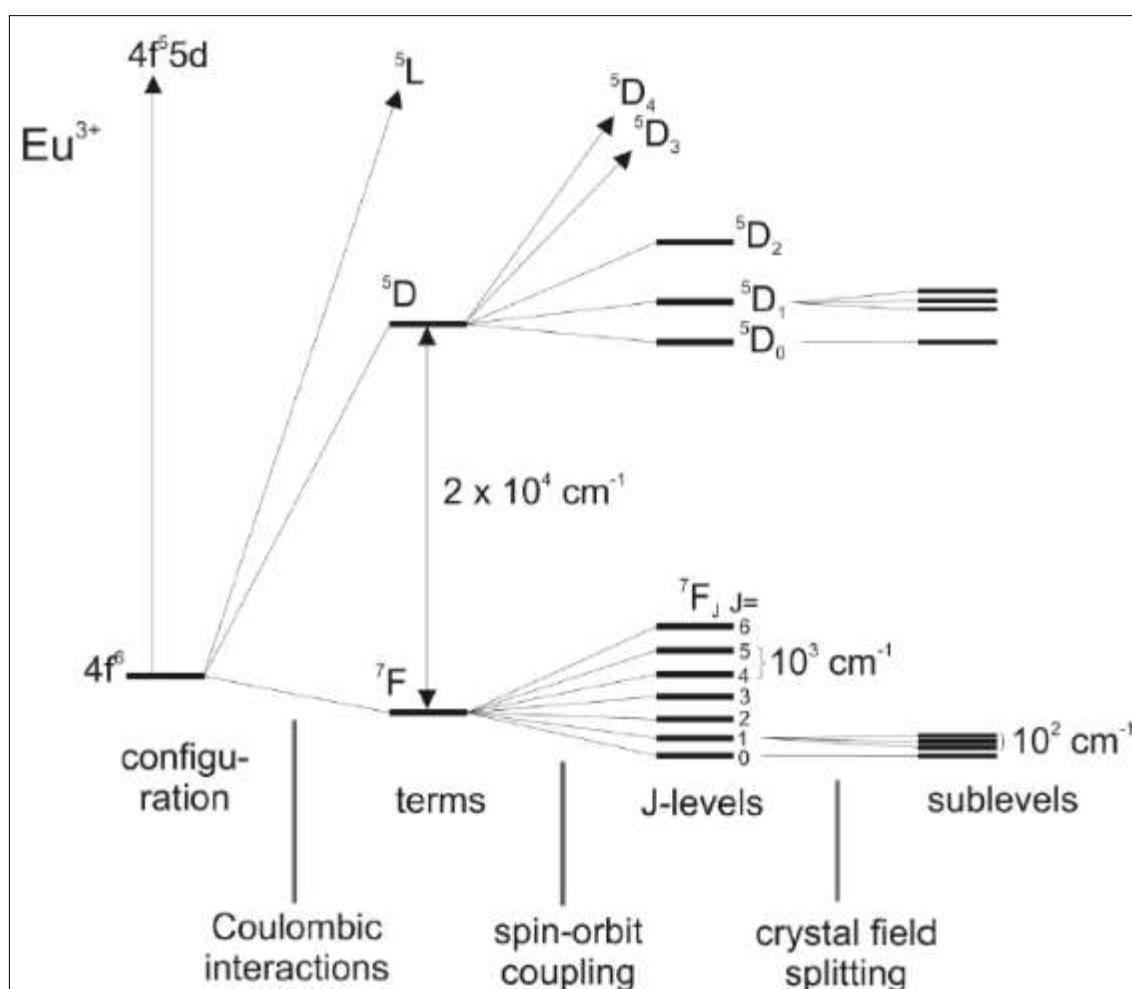


Fig. 3: Diagram representing the interactions leading to the splitting of the electronic energy levels of a Eu^{III} ion inserted in a solid [29].

With the exception of La^{III} and Lu^{III} , the luminescence is specific for each trivalent lanthanide ion and characterized by narrow and well-separated emission bands covering the whole spectrum range from the UV (Gd^{III}) to the visible (Pr^{III} , Sm^{III} ,

Eu^{III}, Tb^{III}, Dy^{III} and Tm^{III}) and further into the NIR region (Pr^{III}, Nd^{III}, Ho^{III}, Er^{III} and Yb^{III}) making them excellent candidates as luminescence-based probes [30–32]. Such narrow emission bands in the visible range enable the construction of solid-state light materials and devices with high color purity. Furthermore, their relatively long-lived luminescence falling in the range of micro to milliseconds is an attractive feature from an analytical viewpoint, as it allows the implementation of time-gating procedures so that the lanthanide luminescence is readily distinguished from the shorter-lived (sub-microseconds) background of biomolecules avoiding thus, autofluorescence and Rayleigh scattering in measurements involving biological systems [33]. Due to the almost independence of the 4fⁿ electronic configuration regarding the chemical environment, the spectral energies of the absorption and emission lines of a trivalent lanthanide (excepted Ce^{III} whose emission spectrum may exhibit f-d bands) are slightly dependent of the matrix where it is inserted while the profile and band intensities are symmetry-dependent. However, their emission intensities are very sensitive to structural details of the coordination environment providing thus, an effective platform for specific chemical sensing.

In a free Ln^{III}, electronic transitions are allowed by magnetic dipole ($\Delta J = 0, 1$ except for $0 \leftrightarrow 0$) and completely forbidden by electric dipole. By inserting them in an environment site without inversion center can result in mixing of the opposite parity configurations [Xe]4fⁿ⁻¹d and [Xe]4fⁿ allowing, to the transition, a small electric dipole component which becomes the main component due to its magnitude. These transitions are governed by specific selection rules established simultaneously by the scientist G. S. Ofelt [34] and B. R. Judd [35] as $\Delta J, \Delta L \leq 6$ and $\Delta S = 0$. It's also demonstrated that for trivalent lanthanide with even electron numbers, the electronic transitions from $J = 0$ to $J' = 0$, an odd number and 2, 4 or 6 are forbidden, weak and strong respectively due to J-mixing [36].

Although their photoluminescence is an efficient process, direct excitation of the trivalent lanthanides is a very inefficient process due to the fact that electronic transitions within the f manifold are forbidden by odd parity also known as Laporte rule since there is no change in the angular momentum quantum number between the excited and ground state. In some cases, the 4f-4f electron transitions are also spin-forbidden [37]. As a consequence, the absorption lines of these ions are very weak

and characterized by low molar absorption coefficient (smaller than $10 \text{ L mol}^{-1} \text{ cm}^{-1}$) rendering very inefficient the direct excitation which is only practicable with lasers [38,39]. Accordingly, the emission lines of the free lanthanide ions are very weak. This limitation may be circumvented by the so-called antennae effect also known as photosensitization [40]. It was observed for the first time, in 1942, by Weissman who studied the luminescence of Eu^{III} based complexes upon UV excitation [40,41]. The Antennae effect consists of an intramolecular energy transfer [42] from an adjacent strongly absorbing chromophore to the Ln^{III} stimulating its luminescence [43]. Good candidates as photosensitizers include both organic molecules and inorganic matrices [44]. To achieve this indirect excitation of the lanthanide ions, some conditions should be fulfilled such as photostability of the matrix, high absorptivity mainly in the blue region and the energy transfer to the lanthanide ion should be efficient compared with other energy decay processes of the ligand excited state. In general, the energy of the lowest triplet and the first singlet electronic levels of the ligand also play a crucial role. According to Latva and collaborators ([45]) who investigated the intramolecular energy-transfer processes from the triplet energy level of the ligand to the resonance levels of the Ln^{III} ions in more than 40 different Eu^{III} and Tb^{III} compounds, when the lanthanide ion is coordinated by the chromophore ligand, luminescence optimal sensitization requires an energy gap in gate $2100 - 4500 \text{ cm}^{-1}$ between the ligand triplet state and acceptor level of the lanthanide [45]. A very small energy gap between ligand triplet and lanthanide accepting state enables thermally activated energy-back transfer re-populating the triplet state resulting in a dramatic decrease in the luminescence quantum yield [45]. On the other hand, if the energy gap is too great, then the efficiency of the energy transfer step is compromised so a balance needs to be reach between these opposing factors [39]. An accepted scheme for the energy transfer from organic ligands to a lanthanide ion can be described as shown in Fig. 4 [46]. The ligand absorbs radiation and is excited to a vibrational level of a singlet state represented here by S_1 . The molecule undergoes fast internal conversion to lower vibrational levels for instance through interactions with solvent molecules. The excited singlet state undergoes non-radiative intersystem crossing (ISC) to the triplet state. Subsequently, the system undergoes an intramolecular energy transfer from the triplet state to a level of the lanthanide ion which emits its characteristic emission via f-f electronic transitions after the internal conversion (IC). The rate and efficiency of the

ligand triplet to the trivalent lanthanide is maximized when there is a short distance between the chromophore and the lanthanide ion, a relatively small energy gap and no competing back-energy transfer. As represented in the figure, in some cases, the energy transfer can occur also directly from the singlet state. There are a series of undesirable decay processes including the ligand fluorescence and phosphorescence and interaction of the triplet level with other molecules which can reduce the efficiency of the sensitization phenomena.

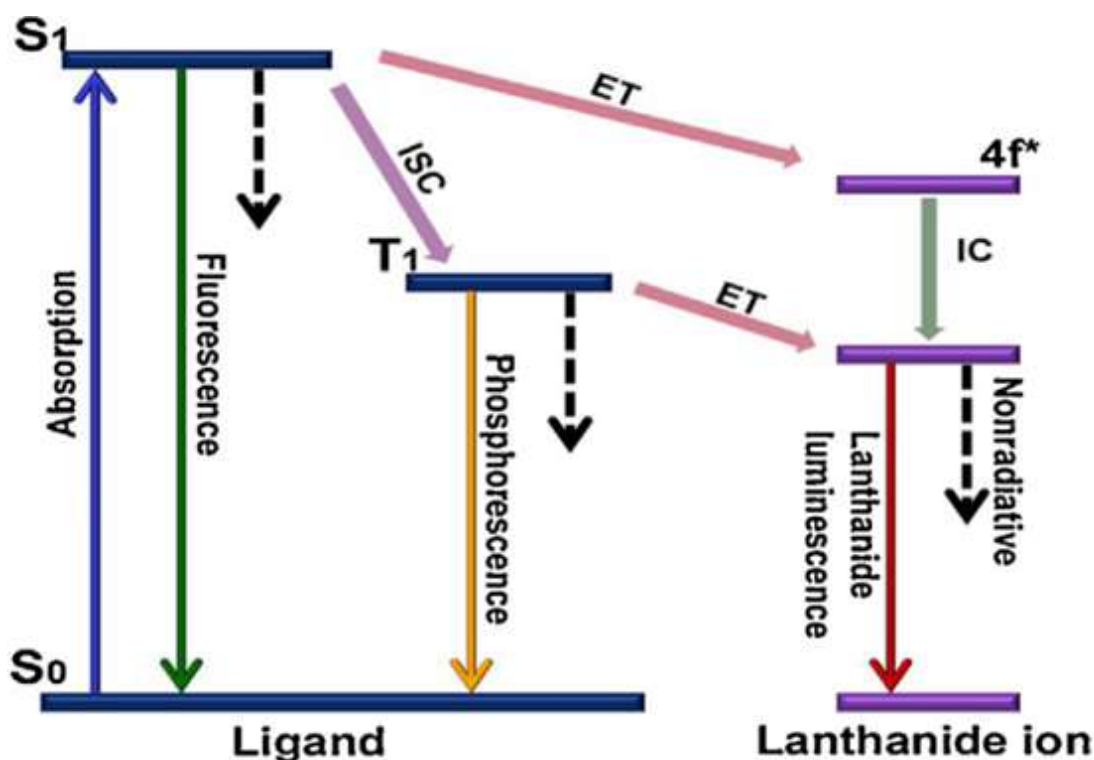


Fig. 4: Schematic representations of energy absorption, energy migration and emission processes in lanthanide complexes: ISC = intersystem crossing; ET = energy transfer; IC = internal conversion. Adapted from [46].

The energy-transfer process from ligand excited states to the energy levels of the lanthanide ions can proceed via Förster and/or Dexter mechanisms [33,47]. Both mechanisms are schematized in Fig. 5. The Dexter mechanism involves an electron-transfer from the excited state of the donor to the unoccupied excited state of the acceptor. Simultaneously, an electron of the electronic ground state of the acceptor migrates to the poorly occupied electronic ground state of the donor. To occur this electron exchange mechanism, the system needs to present an overlap between the

wavefunctions of the donor and the acceptor. In this context, a good orbital overlap and a short distance between the Ln^{III} ion and the ligand are required. In the Förster mechanism, electronic multipolar interactions between the donor excited state and the acceptor ground state enabling an energy transfer, in which absorption and emission of the energy occur simultaneously. A large oscillator strength is required for efficient energy transfer by the Förster mechanism. Finally, the average performance of all processes together may be quantified by the average luminescence quantum yield defined as the ratio of the number of emitted photons to the number of absorbed photons per time unit.

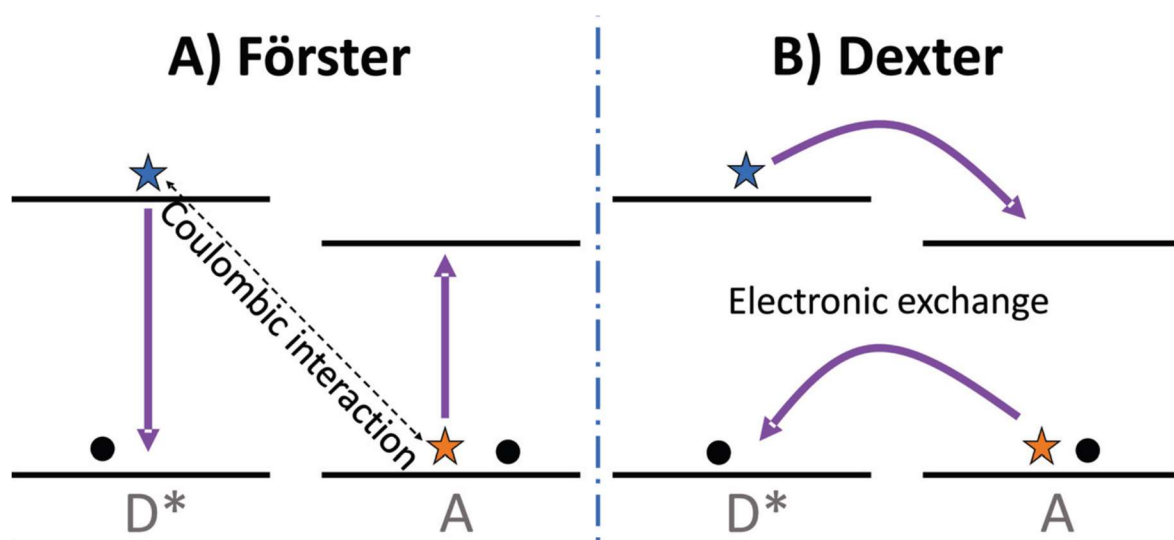


Fig. 5: Diagrams illustrating the (A) Förster resonant energy transfer and (B) Dexter energy transfer mechanisms.

Once the limitation regarding the direct excitation is solved, luminescent lanthanide materials have been extensively prepared and applied in displays, lighting apparatus [48], LASER devices and photo isolators^{‡‡} [25,49] and as no-contact molecular probes for diverse applications including the measurement of temperature.

1.6. Lanthanide coordination polymers and temperature sensing

Denomination used, for the first time, by Y. Shibata in 1916 to describe dimers and trimers of various cobalt(II) ammine nitrates [50], the coordination polymers are,

^{‡‡} Electronic component that transfers electrical signals between two isolated circuits by using light.

according to the International Union of Pure and Applied Chemistry (IUPAC), all inorganic-organic materials composed of repeating coordination entities forming an extended array in one, two or three dimensions via metal coordination bonds [51]. In this context, an entity is defined as an ion or a neutral molecule composed of a central metal ion to which is attached a surrounding array of atoms or groups of atoms known as ligands. The crystalline coordination polymers are known as coordination network and metal-organic framework (MOF) when the coordination network exhibits a tridimensional structure and are potentially porous [51]. Due to the porosity, the MOFs constitute a sub-class of CPs that are attractive for scientific and industrial applications as porous materials owing to the large surface areas, and relatively good chemical and thermal stabilities. From the structural point of view, a crystalline coordination polymer consists of the central ion center and the linker. The ion and the first coordination sphere form the primary building unit (PBU) or coordination polyhedron^{§§}. PBUs units can edge or face share defining a secondary building unit (SBU) which can propagate into zero-dimensional dimer, trimer, tetramer, chain and sheet as shown in Fig. 6.

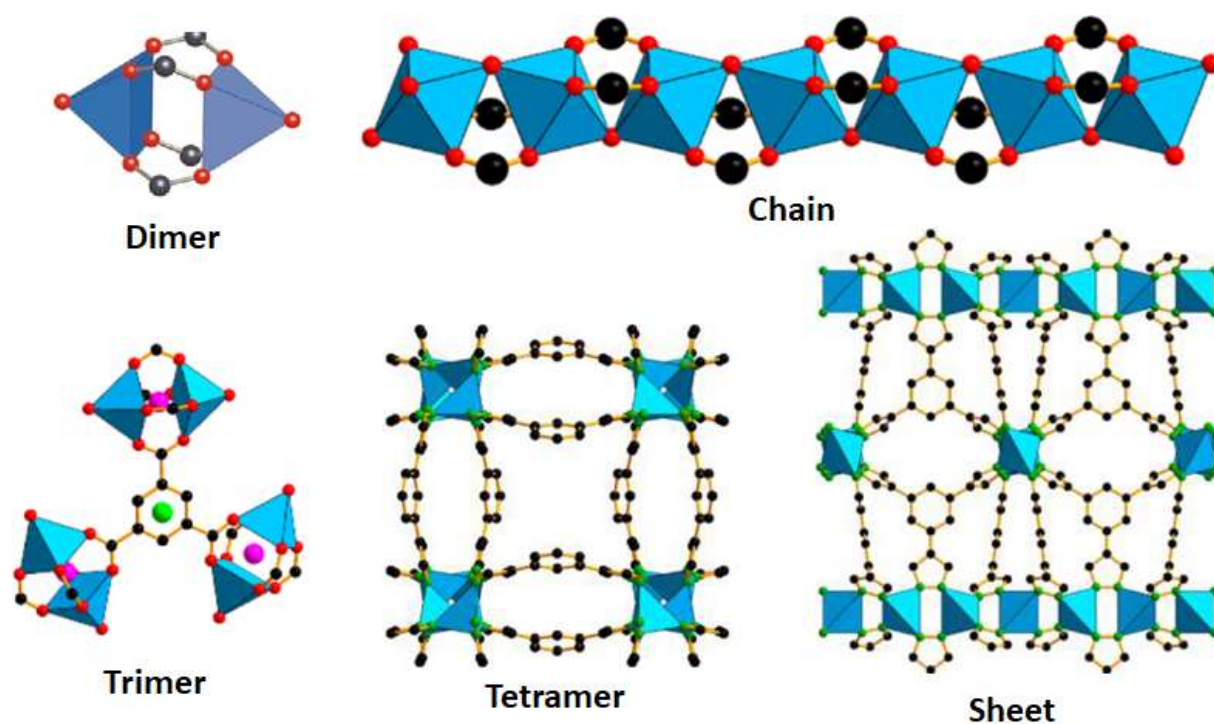


Fig. 6: Examples of secondary building units in coordination polymers [52–54].

^{§§} In a coordination entity, the solid figure defined by the positions of the ligand atoms directly attached to the central atom.

In general, single crystal of coordination polymers are obtained under mild solvothermal conditions. Taking advantage of the nearly limitless choices of metal ions and organic linkers, one can design and create MOFs with predictable structures and porosities, nanoscale processability, and collaborative properties to develop luminescent multifunctional materials for applications in many important areas such as heterogeneous catalysis, separations, gas storage, light-emitting devices, display, metal ions and small molecules probing based on the host-guest chemistry [55–62]. Furthermore, the dimensional cavities can enable the encapsulation of guest species by post-synthetic modification without change in the crystalline structure [63].

Among the coordination polymers, the lanthanide-based ones, self-assembled from organic ligands and trivalent lanthanides ions, have emerged as a very promising sub-group and gained attention in the polymers and materials science. In comparison to the d-block metal ions, the lanthanide ions establish chemical bonds mainly via nondirectional electrostatic interactions and, have higher coordination numbers and connectivity (in the range 6-13 [64]) favorable for the structure stabilization, thermal and chemical stability. Consequently, the topology of the lanthanide-based coordination polymers is not largely predictable. This group of coordination polymers combine the attractive structural advantages of the coordination polymers and the intrinsic magnetic and the spectroscopic properties of the optically active trivalent lanthanides, such as the well-defined line emissions, relative high quantum yields, large ligand-induced Stokes, also known as pseudo-Stokes shifts and long emission lifetimes providing a bright promise to develop novel multifunctional luminescent materials with enhanced targeted functionalities and high added values for specific applications [32,65]. In the lanthanide-containing coordination polymers, furthermore the optically active central ion, luminescence may derive from the organic moieties and also guest molecules within the Ln-CPs may luminesce or induce luminescence. Compared with the traditional molecular approach, by making use of molecular organic and coordination compounds to explore functional luminescent materials, the coordination polymer approach also has the advantage to collaboratively interplay/interact with each other among the periodically located luminescent centers directing new functionalities making them multi-functional materials that can be used in various applications [66]. In fact, over the past two decades, a variety of luminescent coordination polymers have

been realized for their diverse applications on chemical sensing, light-emitting devices such LEDs technologies, and biomedical imaging and the monitoring of drug delivery and treatment [9,67,68]. The polycarboxylate binders bearing aromatic sensitizing chromophores are the main class of ligands used in the design and construction of lanthanide coordination polymers due to the oxophilic nature of the trivalent lanthanides which are hard acid species (according to the Pearson's Hard/Soft Acid/Base Theory) and preferably bind to ligands with hard electron donor atoms such as N and O [69]. Due to the high coordination numbers, the flexibility of the trivalent lanthanide coordination spheres and the character mostly ionic of the bonds, it is generally rather difficult to obtain high-quality crystals of Ln-based CPs and the establishment of permanent porosity is more difficult in comparison to d metal-containing coordination polymers [61]. Many Ln-CPs has been evaluated for use in gas storage and separation, proton conduction, heterogeneous catalysis and as probes in the sensing of small organic molecules, cations, anions, vapor and temperature where the changes in analyte concentrations or temperature can be reflected by the changes of luminescence intensity and lifetime [2,57,70]. In 2008, Chen and Quian reported the selectivity of the coordination polymer Eu(PDC) (PDC is the pyridine-3,5-dicarboxylate) for Cu^{II} sensing [71]. By exploring the high-sensitive character of the emission intensity of Eu^{III} regarding its first coordination sphere, the same authors showed the potential of the Eu-based coordination polymer Eu(BTC) (BTC = 1,3,5-benzenetricarboxylate) for dimethylformamide and acetone sensing [72].

Despite the relatively high number of luminescent parameters susceptible to be used as metrics in luminescence-based sensing, most of the works reported deal with the changes of a temperature-dependent emission intensity [63]. When established between the temperature and the variations of the intensity of only one emission band, the correlation may lead to erroneous conclusions due to the fact that, beyond the temperature, the emission intensity can be heavily affected by the excitation power, inhomogeneity of the luminophore, drifts within the optoelectronic devices and possible variation in the scatter cross section changing the sample [56,63,73]. Although overall quantum yield and emission lifetimes are independent of these factors, their measurements require a relatively long experimental time and computational treatment. To avoid these drawbacks of the single intensity-based methods, the self-calibrating technique using as parameter the intensity ratio of a dual emitting system

has been introduced as a superior technique. To be applicable, the dual-emitting sensor must show resolvable luminescence from two different excited states. When the temperature changes affect the luminescence intensities of two distinct species, its effect is become measurable from relative instead of absolute luminescence intensities, reducing the impact of the extrinsic factors.

Exploring the platform of a coordination polymer, dual emitting sensor may be designed basically in three different ways regarding the extent of population migration between the two optically active excited states as schematized in Fig. 7.

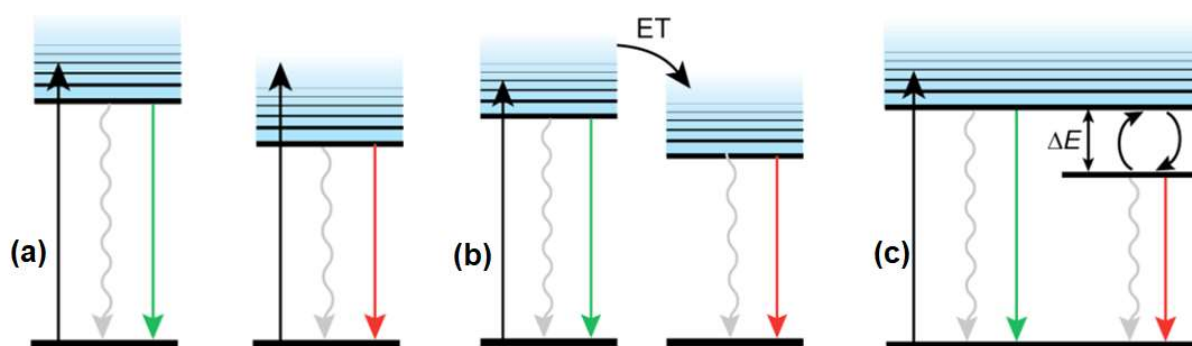


Fig. 7: Schematic summaries of three different electronic structures leading to dual emission system. (a) Two independent luminescent centers where one, at least, shows a response to temperature. (b) Two luminophores interacting through energy transfer. (c) Two luminescent excited states in fast thermal equilibrium. Adapted from [19].

In the first case (a), two electronically independent optically active centers (metal ions or guest molecules) are mixed and incorporated in the same matrix. There is no energy migration between them on the time scale of their luminescence and the temperature dependence of both luminescence occurs only due to the different quenching behavior of each luminescent center. The key point in this approach is the temperature dependence of the radiative and nonradiative deactivation rates of both excited states. To achieve high thermal sensitivity values, it is desirable that one of the centers has a strong temperature-dependent emission while the other shows a temperature-independent emission or has its emission intensity varying in opposite direction. In a second way (b), the dual-emitting system is obtained by using two electronically coupled emitters allowing energy migration between them such as between ligands and lanthanide ions. Finally, the third scenario (c) involves a unique luminescent specie with two thermally coupled emitting states. In this scenario, temperature controls the population distribution, and therefore the relative

luminescence intensities from the two excited states. Two excited levels 1 and 2 are considered as thermally coupled when the energy gap between them is less than 2000 cm^{-1} [3]. In this case, assuming a Boltzmann distribution of the electrons between the states, the electronic population ($P_{i=1,2}$) of each of them may be expressed in the form of Eq. 6 [74].

$$P_{i=1,2} = \alpha_i e^{-E_i/K_B T} \quad (\text{Eq. 6})$$

Where α_i and E_i represent the level degeneracy and the energy of the state i . $K_B = 0.695 \text{ (cm K)}^{-1}$ and T are the Boltzmann's constant and thermodynamic temperature. Therefore, the ratio of probabilities of the two states known as Boltzmann factor [75] depends only on the energy gap of the states and is given by Eq.7.

$$\frac{P_2}{P_1} = \frac{\alpha_2}{\alpha_1} e^{\frac{E_1 - E_2}{K_B T}} \quad (\text{Eq. 7})$$

Since the emission intensity (I_i) owing from the radiative deactivation of the state i to the fundamental level is given by Eq.8.

$$I_i = h\nu_i A_i P_i \quad (\text{Eq. 8})$$

Where h , ν_i , A_i , are the Plank constant, the barycenter of the band and radiative transition probability, respectively. Therefore, the intensity ratio of the emission intensities owing from two excited thermally levels can be deduced to be (Eq.9):

$$\frac{I_2}{I_1} = B e^{\frac{E_1 - E_2}{K_B T}} \quad (\text{Eq. 9})$$

With B being given by Eq.10.

$$B = \frac{\nu_2 A_2 \alpha_2}{\nu_1 A_1 \alpha_1} \quad (\text{Eq. 10})$$

As expected, Eq.9 shows an increase in the intensity ratio with the temperature.

Recently, taking advantage of the thermal coupling of the 5D_0 and 5D_1 Eu^{III} excited states, Aleksandar and collaborators published a paper about an investigation of the luminescent thermometer based on a Eu^{III} doped YVO_4 matrix studied on the range from room temperature to 733 K [3]. The thermographic parameters were

defined as the intensity ratios between the bands assigned to the $^5D_1 \rightarrow ^7F_1$ and $^5D_0 \rightarrow ^7F_{2,4}$ electronic transitions.

The coordination polymers represent a very easy way to insert an infinity of optically active centers in the same sensitizer matrix obtaining isostructural compounds where energy migration between the building ligands and the central ions may be modulated by modifications in nature and the molar ratios between ligands and lanthanide ions. By using this approach, mixed-lanthanide coordination polymers may be easily achieved, which are very interesting in white light generation and ratiometric probing. The richness of organic linkers to tune their different triplet excited state energy and thus to sensitize different combination of lanthanide ions in their luminescent mixed-lanthanide coordination polymers enables the construction of diverse structures optimizing the energy transfer among the lanthanide ions to obtain highly sensitive luminescent thermometers with tunable response range. In such systems, the luminescence intensity, emission lifetime and overall quantum yield are usually higher due to the decrease of the concentration quenching effect. Although the thermally coupled energy levels in diverse trivalent lanthanide such as Er^{III} , Dy^{III} , and Nd^{III} which should result in excellent thermal probes, most of the lanthanide mixed coordination polymers for ratiometric thermometers refer to $\text{Tb}^{\text{III}} / \text{Eu}^{\text{III}}$ or $\text{Gd}^{\text{III}} / \text{Tb}^{\text{III}} / \text{Eu}^{\text{III}}$ embedded into organic-inorganic hybrid matrices. The rarity of the infrared emitting Ln-CPs may be due to the small energy gaps between the resonance level and the ground state of these ions making very easy the non-radiative deactivation of their excited states by the vibrations of the groups C=C, O-H, N-H and C-H present in organic binders. The temperature dependence of the $\text{Tb}^{\text{III}} / \text{Eu}^{\text{III}}$ relative intensity arises from thermally driven phonon-assisted energy migration mechanism. The Gd^{III} ions do not participate in the emission process but reduce the amount of Eu^{III} and Tb^{III} centers preventing the effect of concentration quenching [76]. The $\text{Gd}^{\text{III}} / \text{Tb}^{\text{III}} / \text{Eu}^{\text{III}}$ ternary system is currently tested also as white light-emitting materials. The Tb^{III} and Eu^{III} ions exhibit green and red luminescence, respectively, whereas the ligands emit the blue fraction of the light. By careful tuning of the $\text{Tb}^{\text{III}} / \text{Eu}^{\text{III}} / \text{Gd}^{\text{III}}$ ratio, the emission color can be changed gradually, and white light emission can be achieved [55,68,77].

Fig. 8 exhibits a simplified scheme of the energy migration processes susceptible to occur in a $\text{Tb}^{\text{III}} / \text{Eu}^{\text{III}}$ mixed-lanthanide coordination polymer. After triplet state generation (T_1) following the excitation of the ligand to a singlet state (S_1), energy can

tune to both optically active ions with the rates K_{Tb}^1 and K_{Eu}^1 . Energy back-transfer may take place mainly from the emitting levels 5D_4 (K_{Tb}^{Tb}) and 5D_0 (K_{Eu}^{Eu}) to the ligand affecting negatively the radiative decay rates K_{DF}^{Tb} and K_{DF}^{Eu} of the lanthanide ions.

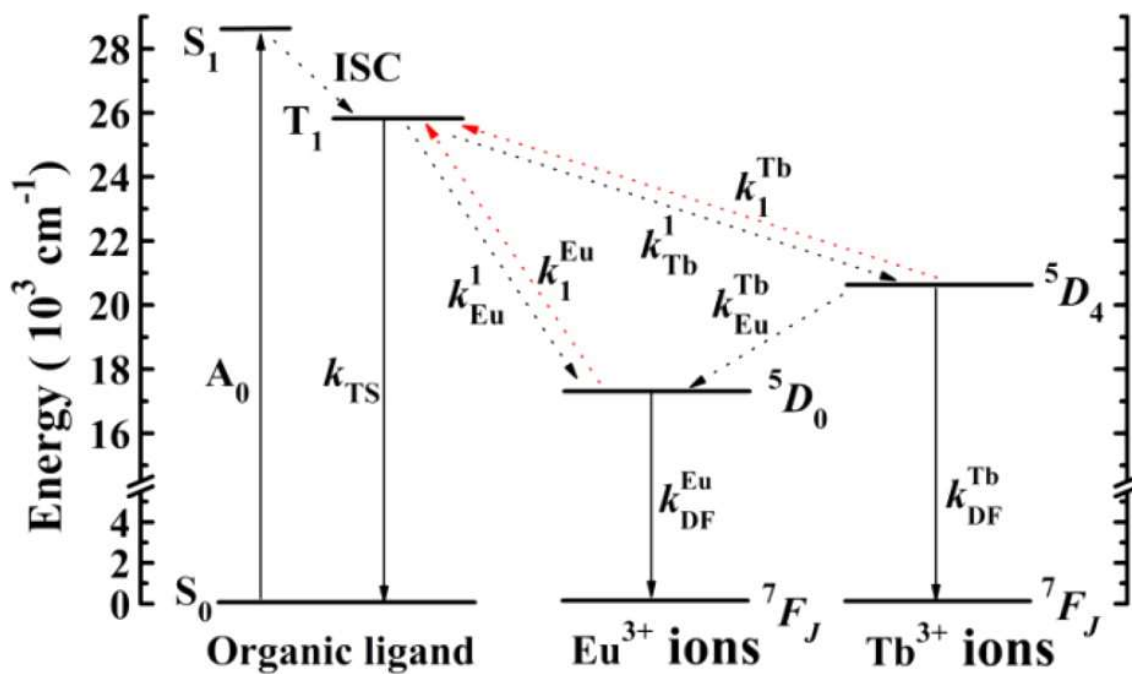


Fig. 8: Schematic representation of energy absorption, migration, emission, and processes in luminescent mixed lanthanide coordination polymers thermometers. Abbreviations: S = singlet; T= triplet, A = absorption probability; ISC = intersystem crossing; k = radiative transition probability. The solid arrows represent singlet-singlet absorption and radiative transitions; dotted arrows indicate non-radiative transitions [78].

The performance of a co-doped lanthanide coordination polymer is closely dependent on these different energy transfer rates which may be modulated in different ways such as: By using ligands with different triplet energy, mixing of ligands and post-synthetic modifications to attempt more sensitive thermometers operating in wider temperature ranges. Especially for Eu^{III} / Tb^{III} -based thermometer, the organic linkers need to have the triplet level energies ranging between 22,000 and 27,000 cm^{-1} to assure the simultaneous sensitization of both ions when the temperature dependence of the thermometric parameter is dominated by host-to-metal energy transfer or metal-to-host back transfer mechanisms [79].

1.7. Examples of luminescent ratiometric thermometers based on lanthanide coordination polymers

The high similarity between the ionic radii of the trivalent lanthanide makes possible the preparation of lanthanide-mixed CPs where the ions occupy the same chemical ambient. By rational definition of the ratio between the lanthanide salt precursors, emission can be realized from two individual emitting centers in one Ln-based CP. These dual emission Ln-CPs have been proved to be promising materials as ratiometric probe for temperature sensing in different temperature regimes including cryogenic ($T < 100$ K), medium ($100 < T < 300$ K), physiological ($293 < T < 323$ K) and high temperatures ($T > 323$ K) [80]. The first ratiometric thermometer based on luminescent lanthanide coordination polymer was the mixed-MOF $\text{Tb}_{0.9931}\text{Eu}_{0.0069}$ -DMBDC (DMBDC = 2,5-dimethoxy-1,4-Benzenedicarboxylate dianion) reported by Qian and co-authors in 2011. The triplet state energy of the ligand DMBDC was estimated to be 23300 cm^{-1} [81]. Intense photoluminescence owing from both Eu^{III} and Tb^{III} was observed upon excitation at 381 nm. To realize the temperature sensing, the intensity ratio between the most intense emission bands of Tb^{III} and Eu^{III} assigned to the $^5\text{D}_4 \rightarrow ^7\text{F}_5$ and $^5\text{D}_0 \rightarrow ^7\text{F}_2$ was used as the ratiometric thermographic parameter. It was found that the temperature and the intensity ratio are linearly correlated from 50 to 200 K with an absolute sensitivity of $0.38\% \text{ K}^{-1}$. The maximum relative thermal sensitivity was found to be $1.5\% \text{ K}^{-1}$ at 200 K. By varying the molar ratios of the lanthanide salts, the authors have prepared and studied two isostructural mixed-MOFs $\text{Tb}_{0.9989}\text{Eu}_{0.0011}$ -DMBDC and $\text{Tb}_{0.9954}\text{Eu}_{0.0046}$ -DMBDC which have similar thermal-dependent luminescence behavior and present the maxima relative sensitivities of 0.61 and $0.53\% \text{ K}^{-1}$, respectively at 200 K. Such results suggest that for isostructural coordination polymers, the molar ratios of the ions can be optimized to achieve probe with better performance which is quantified by the thermal sensitivity value. One year after, considering that the sensing range could be further expanded by tuning the energy transfer between organic linkers and lanthanides, the same group published two mixed MOFs represented by $\text{Tb}_{0.957}\text{Eu}_{0.043}$ -CPDA and $\text{Tb}_{0.9}\text{Eu}_{0.1}$ -PIA. CPDA and PIA are the ligands 5-(4-carboxyphenyl)-2,6-pyridinedicarboxylate and 5-(Pyridin-4-yl)isophthalate) anions. These ligands are characterized, in comparison with DMBDC, by the highest triplet excited state energies of $27,027$ and $25,866\text{ cm}^{-1}$, respectively. The good linear relationship between the $I_{\text{Tb}} / I_{\text{Eu}}$ ratio and the temperature was within

the ranges 40 – 300 K with the thermal sensitivity of 0.37% K⁻¹ and 100 - 300 K with the thermal sensitivity of 3.53% K⁻¹ for Tb_{0.957}Eu_{0.043}cpda and Tb_{0.9}Eu_{0.1}PIA, respectively. According to Dian Zhao and collaborators, the relative thermal sensitivities for Tb_{0.957}Eu_{0.043}cpda and Tb_{0.9}Eu_{0.1}PIA were calculated to be 3.27% K⁻¹ at 300 K and 16.03% K⁻¹ at 300K [63]. Those interesting results were attributed to the fact that the higher triplet and Ln^{III} energy gap restricting the competitive energy-back transfer enabling more temperature-sensitive the Tb^{III} to Eu^{III} energy transfer. By choosing the 2,4-(2,2':6',2''-terpyridin-4'-yl)-benzenedisulfonic acid (H₂DSTP) as the first and the oxalic acid (OA) or 1,4-benzene dicarboxylic acid (BDC) as ancillary ligands, the MOF represented by [Tb_{0.98}Eu_{0.02}(OA)_{0.5}(DSTP)]·3H₂O successfully developed by Wei and collaborators in 2015 [82]. By substituting the coordinated solvent molecules, the auxiliary ligand enables better luminescence efficiency and higher thermal stability. It was found that the temperature measurement can be linearly correlated to the experimental parameter I_{Tb} / I_{Eu} in the temperature range 77–275 K with a sensitivity of 0.5% K⁻¹ and a maximum relative sensitivity of 2.75% K⁻¹. The MOF Eu_{0.7}Tb_{0.3}(D-cam)(Himdc)₂(H₂O)₂ (D-H₂cam = D-camphoric acid, H₃imdc = 4,5-imidazole dicarboxylic acid) reported by Yun and collaborators was investigated as thermal probe in the large temperature range 100 – 450 K and the thermometric parameter (I_{Tb} / I_{Eu}) was linearly related to the temperature in the whole temperature range [83]. However, the system offered a very small sensitivity due to the simultaneous decrease in the intensities of Tb^{III} and Eu^{III} ions. The maximum value of the relative sensitivity was estimated to be only 0.11% K⁻¹ at 450 K. Monge and collaborators constructed the ratiometric thermal probes Gd_{0.98}Ln_{0.02}-DSB where Ln = Eu^{III} or Tb^{III} and DSB = 3,5-disulfobenzoate). The thermometric parameters were defined as the ligand phosphorescence which decreases quickly with temperature increasing and Tb^{III} or Eu^{III} emission intensity ratios, which remain almost constant in the studied temperature range 70 – 240 K yielding interesting values of relative sensitivity [55]. The MOF Tb_{0.99}Eu_{0.01}(DBC)_{1.5}(H₂O) obtained from a shape control micro-emulsion technique was suspended in water and evaluated in the range of physiological temperatures (300 – 320 K) by Rocha and collaborators [84]. By using the spray-drying methodology, the same group constructed the thermometer based on the ligand 1,4-phenylenediacetic acid and mixing of Tb^{III} and Eu^{III} ions a the 11:1 ratio. The authors showed that the nanothermometer operates in the range 10–325 K upon

excitation at 370 nm, with a high sensitivity of 6% K⁻¹ and low-temperature uncertainty at 25 K [85]. Attempting to construct stable luminescence-based thermometer operating in the physiological range, Zhou and collaborators developed a straightforward post-synthetic lanthanide functionalization strategy consisting of soaking the nano-MOF In(OH)(BPYDC) (BPYDC = 2,2'-bipyridine-5,5'-dicarboxylic acid) in DMF solutions containing the chloride salts of Tb^{III} and Eu^{III} in a 0.995:0.005 ratio. The resulting Tb/Eu-doped MOF was tested as ratiometric thermal probe between 10 and 60 °C showing a very good linear relationship of the intensity ratio to the temperature characterized by the very high absolute sensitivity of 5.0% °C⁻¹ and the maximum relative sensitivity of 2.53% K⁻¹ at 333 K [11]. Taking advantage of the pores in the MOF ZJU-88* $\equiv [\text{Eu}_2(\text{QPTCA})(\text{NO}_3)_2 (\text{DMF})_4] \cdot (\text{CH}_3\text{CH}_2\text{OH})_3$ (QPTCA = 1,1', 4',1'',4'',1'''-quaterphenyl-3,3'',5,5'''-tetracarboxylate) anion, Cui and collaborators proposed a different approach for ratiometric luminescent thermometers [11]. By encapsulating the luminescent perylene dye into the pores, they developed a novel probe where the thermographic parameter was the intensity ratio of the perylene and Eu^{III} emission. It was found a very good linear relationship between the thermographic parameters and the temperature in the range 20 - 80 °C with an absolute sensitivity of 1.3% °C⁻¹ making it an interesting option to realize physiological temperature probing. Further studies have demonstrated that apart from energy transfer of the ligand QPTCA to the Eu^{III} ion, energy transfer from a perylene excited state to Eu^{III} also occurs in the post-synthetic modified compound. More recently, Dian and collaborators reported the MOFs Tb_{0.95}Eu_{0.05}-CPNA and Tb_{0.95}Eu_{0.05}-BPYDC where CPNA and BPYDC are the dianions of (4-carboxyphenyl)nicotinic acid and [2,2'-bipyridine]-5,5'-dicarboxylic acid respectively [80]. The maxima relative sensitivities of the two systems were evaluated to be 2.55 % K⁻¹ at 131 K and 2.59% K⁻¹ at 179 K for Tb_{0.95}Eu_{0.05}-CPNA and Tb_{0.95}Eu_{0.05}-BPYDC respectively in the operating range 25 – 200 K. Quian and collaborators developed an thermometer Nd_{0.577}Yb_{0.423}-BDCF₄ (BDCF₄ = 2,3,5,6-tetrafluoro-1,4-benzenedicarboxylate dianion) which emits in the infrared range. Under laser excitation at 808 nm, the system emits both emission bands assigned to the ⁴F_{3/2} → ⁴I_{11/2} Nd^{III} and ²F_{5/2} → ²F_{11/2} Yb^{III} transitions centered at around 1060 and 980 nm respectively whose ratio shows a linear relationship with temperature in the range of 293–313 K [86].

2. Objectives and motivation

As justified above, the advantages of ratiometric thermo-sensing analysis using mixed-trivalent lanthanide ions systems with small full widths at half maximum emission bands provide precise temperature-sensing on a material body without requiring any standard reference sample of temperature-sensitive luminophores.

In this context, this thesis proposed to prepare a series of new lanthanide-based coordination polymers and evaluate their potential as ratiometric probes for applications in luminescence-based thermometry.

The principal objectives were:

- Preparation and characterization of the polydentate ligands 1,3,5-tris(2,6-dicarboxypyridine-4-oxy methyl)benzene ($H_6TDCPMB$) and 1,3,5-tris(4-carboxyphenoxy methyl)benzene (H_3TCPMB).
- Syntheses and characterization of homonuclear and co-doped lanthanide-containing coordination polymers from $H_6TDCPMB$ and H_3TCPMB .
- Syntheses and characterization of heteroleptic homonuclear and co-doped lanthanide-containing coordination polymers from the ligands 1,4-benzene dicarboxylic acid (H_2BDC) and 9-anthracenecarboxylic acid (HAC).
- Syntheses and characterization of heteroleptic homonuclear and co-doped lanthanide-containing coordination polymers from the ligands and 1,4-benzene dicarboxylic acid (H_2BDC) / acetylacetone (Hacac).
- Evaluation of the obtained coordination polymers as ratiometric luminescent thermometers in terms of emission intensity ratios.

The linkers H_3TCPMB and $H_6TDCPMB$ were chosen due to the strong lanthanide coordination offered through oxygen and (also nitrogen for $H_6TDCPMB$) donor atoms, and the delocalized aromatic system, which allowed the molecule to absorb energy to be transferred to the lanthanide ions. Furthermore, until now, lanthanide coordination polymers constructed from them have not been reported. The choose of the acetylacetone ligand was based on the fact that It is a very Tb^{III} luminescence sensitizer contrary to the Eu^{III} . Thus, in the systems constructed from the mixing $H_2BDC/Hacac$, we expected that both ions should show very different profiles of the emission versus temperature. Finally, due to its triplet energy state at around 20,000

cm^{-1} , the ligand HAC was used in order to obtain opposite effect where the Eu^{III} luminescence should be sensitized while the Tb^{III} being quenched at the same time. The Eu^{III} and Tb^{III} ions were selected as optically active center due to their attractive visible light, narrow emission profiles and the possibility of the used ligands sensitize their luminescence simultaneously and the possibility of energy migration from Tb^{III} to Eu^{III} due to the good resonance between the $^5\text{D}_1$ Eu^{III} and $^5\text{D}_4$ Tb^{III} states located at 19,000 and 20,500 cm^{-1} , respectively. In fact, in some cases the organic ligand may effectively sensitize the luminescence of Tb^{III} rather than Eu^{III} due to the superior match of the triplet and accepting states making the Eu^{III} luminescence strongly dependent of energy transfer owing from the Tb^{III} . According to the effect of the temperature on the rate of this process, high-sensitive thermometers can be obtained. The structures of the ligands are shown in the appendix A 36.

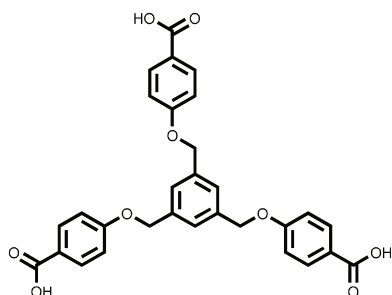
3. Experimental section

3.1. Materials and methods

The two ligands were prepared in one pot synthesis following an adapted literature methodology [87]. The ^1H and ^{13}C -NMR spectra were obtained using an advance spectrometer from Bruker Analytische Messtechnik GmbH. Aqueous solutions of lanthanide nitrate salts were prepared by dissolving lanthanide oxide in hot concentrated nitric acid. For the terbium oxide (Tb_4O_7) which contains both ions Tb^{III} and Tb^{IV} in the 1:1 ratio, total dissolution was obtained by adding drops of 30% hydrogen peroxide (H_2O_2) reducing the Tb^{IV} to Tb^{III} according to the equation: $2\text{Tb}^{\text{IV}} + \text{H}_2\text{O}_2 \rightarrow \text{O}_2 + 2\text{Tb}^{\text{III}} + 2\text{H}^+$. It is worthwhile to note that the efficiency of H_2O_2 to reduce Tb^{IV} is pH dependent. Despite $E_{\text{Tb}^{\text{IV}}/\text{Tb}^{\text{III}}}^0$ (3.1 V) [88] being positive and relatively large, in a very concentrated acidic solution, more H_2O_2 will be needed to offset the reaction equilibrium. Furthermore, H_2O_2 may react with H^+ generating water. After elimination of the excess of acid by many water addition /evaporation cycles, the Ln^{III} ion concentration determination was performed by complexometric titration with disodium ethylenediaminetetraacetic acid (EDTA) salt [89] using Xylenol orange (5 w% in KBr) as indicator and acetic / acetate (pH \approx 6) as buffer. All other reagents and solvents were purchased and used as received without further purification. Single-crystal X-ray diffraction data were collected on a Bruker Apex Duo diffractometer equipped with a graphite-monochromatized Mo $\text{K}\alpha$ radiation ($\lambda = 0.71073 \text{ \AA}$) at 150 K. All structures were solved and refined by direct methods with full-matrix least-squares refinements based on F^2 using SHELXS-97 and SHELXL-97 program packages [90]. All non-hydrogen atoms were refined anisotropically and hydrogen atoms were placed in geometrically calculated positions. The R_1 and wR_2 values are defined as $R_1 = \sum(|F_0| - |F_c|) / \sum|F_0|$ and $wR_2 = \{\sum[w(F_0^2 - F_c^2)^2] / \sum[w(F_0^2)^2]\}^{1/2}$, respectively. CCDC 1875767 (TbL), CCDC 1875768 (EuL) and CCDC 1875769 (GdL) contain the crystallographic data in CIF format. Powder X-ray diffraction measurements were performed on a Bruker D8 ADVANCE X-ray powder diffractometer using a Cu- $\text{K}\alpha$ radiation (1.5418 \AA) beam at room temperature with 2θ ranging from 5° to 50° . Thermogravimetric analysis was conducted under synthetic air on a Universal V2.6 DTA system by heating up from 30 to 900°C with a heating rate of 10°Cmin^{-1} . FT-IR

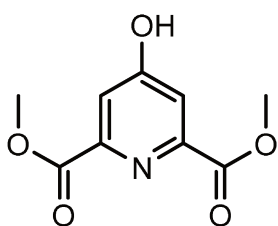
spectra were recorded on an Agilent FTIR spectrometer (model CARY 630) in ATR mode using a diamond crystal in the range of 4000–400 cm^{-1} . Elemental analyses (C, H, N) were determined using an elemental analyzer Perkin Elmer (model CHN 2400). The absorbance in solution was measured in CH_3CN or H_2O using a Cary 50 UV-vis spectrophotometer from Agilent. The diffuse reflectance spectra (DRS) of the free ligand and the as-synthesized compounds were recorded on a Shimadzu, UV-2450 spectrophotometer using BaSO_4 as the standard. The spectra are presented in the absorption mode. The photoluminescence data were obtained on a Fluorolog-3 spectrofluorometer (Horiba FL3-22-iHR320), with double-gratings (1200 g mm^{-1} , 330 nm blaze) in the excitation monochromator and double-gratings (1200 g mm^{-1} , 500 nm blaze) in the emission monochromator using an ozone-free xenon lamp of 450 W (Ushio) radiation source. All of them were corrected according to the optical system of the emission monochromator and the photomultiplier response (Hamamatsu R928P). Time-resolved phosphorescence emission spectra of the analogous gadolinium(III) complex were obtained at $\sim 77 \text{ K}$ using a time-correlated single-photon counting (TCSPC) system with successive delay increments, in order to get only emission bands from triplet levels of the ligand. The emission decay curves were obtained with a flash 150 W xenon lamp using a time-correlated single photon counting (TCSPC) system. The temperature-dependence emission spectra and lifetime measurements were achieved by holding the samples in a cryostat (Janis Research Company VNF-100), a F-3004 Peltier Sample Cooler, a Linkam THMS600 / HFS600 temperature controller operating in the temperature ranges of 77–320 K, 273 – 373 K and 77 – 873 K, respectively using as excitation sources the ozone-free xenon lamp of 450 W, the flash 150 W xenon lamp and a 488 nm sapphire laser, Model: SAPPHIRE 488-75 SF CDRH from COHERENT. Temperature-dependent photoluminescence behaviors were measured with steps of 10 or 20 K after equilibrium of ca. 10 min.

3.2. Synthesis of 1,3,5-tris(4-carboxyphenoxy)methylbenzene (H₃TCPMB)



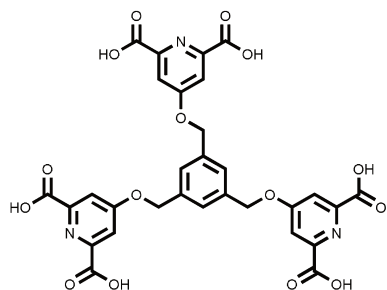
A stirred mixture of 1,3,5-tris(bromomethyl)benzene (1.5 g; 4.2 mmol), ethyl 4-hydroxybenzoate (2.1 g, 12.6 mmol), sodium carbonate (2 g, 18.9 mmol) in dimethylformamide (DMF) (20 mL) contained in a 1-neck round-bottom flask was heated at 80 °C for 72 h. After cooling to room temperature, the solvent was removed at 60 °C by vacuum-assisted rotary evaporation to obtain a white powder that was subsequently dissolved in acetone (20 mL). This acetone solution was combined to NaOH (1.0 g) dissolved in water (20 mL) and the stirred mixture heated 80 °C for 24 h. After cooling to room temperature, the acetone was eliminated, and the solution acidified (pH ~1) by addition of concentrated hydrochloric acid resulting in a gelatinous precipitate which was collected by vacuum filtration and washed several times with water. After drying off, 1.85 g (yield = 83%) the protonated ligand was isolated as a colorless solid. ¹H-NMR (400 MHz, DMSO): δ / ppm = 5.23 (s, 6 H, CH₂), 7.13 (d, J_{HH} = 8.9 Hz, 6 H, Ar-H), 7.55 (s, 3 H, Ar-H), 7.90 (d, J_{HH} = 8.9 Hz, 6 H, Ar-H), 12.66 (s, 3 H, COOH). Elemental analysis (%) - found (calculated) for C₃₀H₂₄O₉ C = 68.10 (68.18); H = 4.60 (4.58).

3.3. Synthesis of the 4-hydroxy-2,6-dimethoxycarbonylpyridine



To a stirred suspension of 1,4-Dihydro-4-oxo-2,6-pyridine-dicarboxylic acid hydrate (3.0 g, 16.4 mmol (anhydrous basis)) in 20 mL of methanol at room temperature, were added chloride thionyl (2.8 mL) dropwise following a reported procedure [91]. After stirring the reaction mixture for 24 h, the methanol was removed by evaporation resulting in a white precipitate, which was dried at 50 °C under reduced pressure. ¹H-NMR (500 MHz, DMSO): δ / ppm = 3.88 (s, 6 H, CH₃), 7.60 (s, 2 H, Ar-H).

3.4. Synthesis of 1,3,5-tris(2,6-dicarboxypyridine-4-oxy methyl)benzene (H₆TDCPMB)



The synthesis of the ligand H₆TDCPMB was carried out similarly to the synthesis of the ligand H₃TCPMB using 1.00 g of the 4-hydroxy-2,6-dimethoxycarbonylpyridine. The ester 1,3,5-tris(2,6-dimethoxycarbonyl-pyridine-4-oxy methyl)benzene was hydrolyzed using only the NaOH solution without acetone. The dried sample weighed 2.30 g corresponding to a yield of 73 % for the reaction. ¹H-NMR of the corresponding sodium salt (400 MHz, D₂O:0,75% TSP): δ / ppm = 5.34 (s, 6 H, CH₂), 5.63 (s, 6 H, Ar-H), 7.71 (s, 3 H, Ar-H). Elemental analysis (%) - found (calculated) for C₃₀H₂₁N₃O₁₅ C = 54.31 (54.31); H = 3.66 (3.19); N = 5.85 (6.33). To obtain its sodium salt, the H₆TDCPMB was suspended in water and treating with an aqueous solution of NaOH 6 mol L⁻¹ stirring magnetically at room temperature for 6 h. The product was precipitated using ethanol, isolated by vacuum filtration washed several times with ethanol and dried at 50 °C under reduced pressure for 12 h approbatively. Thermogravimetric analysis suggests the molar ratio of 1:3.8 between Na₆TDCPMB and hydration molecules.

3.5. Synthesis of the coordination polymers based on the ligand H₃TCPMB

The four CPs build from H₃TCPMB, named as Ln-TCPMB (Ln = Eu^{III}, Ln = Gd^{III}, Ln = Tb^{III}) and Tb_{0.95}Eu_{0.05}-TCPMB, were obtained following a modified solvothermal method described in the literature [92]. (60.00 mg, 0.14 mmol) of H₃TCPMB were dissolved in 10 mL of DMF in a 40 mL Teflon-lined stainless-steel vessel. Then 100 μ L of concentrated HCl were added following by 0.14 mol of Ln(NO₃)₃ dissolved in ca. 2 mL of deionized water. The reaction mixture was sealed in a stainless-steel autoclave and heated at 120 °C for 72 hours under autogenous pressure and then cooled to 30 °C spontaneously keeping the oven closed. Accordingly, the synthesis of Tb^{III} /Eu^{III} mixed CP represented by the formula Tb_{0.95}Eu_{0.05}-TCPMB follows exactly the same route using an aqueous solution containing 0.133 mmol of Tb(NO₃)₃ and 7 μ mol of Eu(NO₃)₃. The resulting yellow crystals were isolated by microcentrifugation washed

with DMF and water and dried at 50 °C under reduced pressure during 12 h approximatively yielding ca. 50 % based on the lanthanide ions. The compounds were characterized by X-ray crystallography, elemental and thermogravimetric analyses, FT-IR, DRS, and photoluminescence spectroscopy.

Eu-TCPMB $\equiv \{[\text{Eu}_2(\text{L})_2(\text{DMF})_2(\text{H}_2\text{O})_2]\cdot\text{DMF}\}_n$. Yield 54 %. Elemental analysis (%) - found (calculated) for $\text{Eu}_2\text{C}_{69}\text{H}_{67}\text{N}_3\text{O}_{23}$ (MW = 1610.22 g.mol⁻¹), C = 51.10 (51.47); H = 4.23 (4.19); N = 2.65 (2.61). Gd-TCPMB $\equiv \{[\text{Gd}_2(\text{L})_2(\text{DMF})_2(\text{H}_2\text{O})_2]\cdot\text{DMF}\}_n$. Yield 55 %. Elemental analysis (%) - found (calculated) for $\text{Gd}_2\text{C}_{69}\text{H}_{67}\text{N}_3\text{O}_{23}$ (MW = 1620,79g.mol⁻¹), C = 51.10 (51.13); H = 4.27 (4.17); N = 2.61 (2.59). Tb-TCPMB $\equiv \{[\text{Tb}_2(\text{L})_2(\text{DMF})_2(\text{H}_2\text{O})_2]\cdot\text{DMF}\}_n$. Yield 49 %. Elemental analysis (%) - found (calculated) for $\text{Tb}_2\text{C}_{69}\text{H}_{67}\text{N}_3\text{O}_{23}$ (MW = 1624,14 g.mol⁻¹), C = 50.89 (51.03); H = 4.20 (4.16); N = 2.62 (2.59).

3.6. Synthesis of the coordination polymers based on the ligand H₆TDCPMB

3.6.1. Syntheses of Ln-TDCPMB (Ln = Eu^{III}, Gd^{III}, Tb^{III})

70 mg (0.081 mmol) of Na₆TDCPMB were dissolved in 20 mL of deionized water and heated at 60 °C. The aqueous solution containing 0.162 mmol of the lanthanide nitrate salt (Ln(NO₃)₃) was added dropwise resulting in the formation of a white suspension which was magnetically stirred for 3 h at 60 °C. The precipitate was isolated by vacuum filtration, washed several times with deionized water and dried at 50 °C for 12 h approximatively.

3.6.2. Syntheses of the mixed Ln-TDCPMB (Ln = Eu^{III}, Gd^{III}, Tb^{III})

The synthesis of the binary and trinary compounds of the general formulas Gd_{1.9}Ln_{0.1}-TDCPMB and (Ln = Eu^{III}, Tb^{III}) and Gd_xTb_{0.4}Eu_{1.6-x}-TDCPMB followed the same route only for the use of a mixture of the salts of interest as starting materials varying their molar ratios. In all cases, the compounds were isolated in amorphous phase yielding around 90% based on the ligand. The characterization was carried out by TG-DTA analysis, P-XRD, FT-IR, DRS, and photoluminescence spectroscopy.

3.6.3. Synthesis of the compounds represented by Ln-AC (Ln = Tb^{III}, Eu^{III})

The compounds Ln-AC were prepared by direct precipitation, at room temperature, from lanthanide nitrate salt ((Ln(NO₃)₃) in aqueous solution and anthracene-9-carboxylic acid (HAC) using deionized water as solvent. 100,0 mg (0.45 mmol) of HAC were suspended in 20 mL of water following by an addition of 0.45 mmol of NaOH. After complete dissolution, 0.45 mmol of Ln(NO₃)₃ was added to the organic linker solution under continuous stirring forming a yellow precipitate within a few minutes. The suspension remained under stirring at room temperature for 24 h to complete precipitation has been performed. The precipitate was then filtered, centrifuge-washed repeatedly with water and dried overnight at 80 °C under atmospheric pressure, yielding ca. 98 % of the anhydrous compounds Ln-AC. The characterization was carried out by TG-DTA analysis, P-XRD, FT-IR, DRS, and photoluminescence spectroscopy.

3.6.4. Synthesis of the compounds represented by Ln-BDC (Ln = Tb^{III}, Eu^{III})

The syntheses of the compounds Ln-BDC followed the same route of the Ln-AC syntheses only changing HAC by H₂BDC. The 100.0 g (0.60 mmol) of H₂BDC was deprotonated by using 1.20 mmol of NaOH following by addition of 0.40 mmol of Ln(NO₃)₃. The yields were 106 % and 108 % for Eu-BDC and Tb-BDC respectively. The characterization was carried out by TG-DTA analysis, P-XRD, FT-IR, DRS, and photoluminescence spectroscopy.

3.6.5. Synthesis of the compounds represented by Ln-BDC-AC (Ln = Tb^{III}, Eu^{III}) and containing the mixed of lanthanide ions

The syntheses of the compounds with the mixing ligands follow a similar using the mixture of HAC and H₂BDC in a 2:1 ratio, in other words, 50 % of the carboxylate ions derive from each ligand.

3.6.6. Synthesis of the compounds represented by Tb_xEu_{1-x}acac_xBDC_{1.5-x/2}

The compounds obtaining from Hacac and H₂BDC were designed so they can be represented by the general formula Tb_xEu_{1-x}acac_xBDC_{1.5-x/2} where x = 0.99, 0.95, 0.93, 0.85, 0.75. in each synthesis, the sum of both Eu(NO₃)₃ and Tb(NO₃)₃ was 0.5

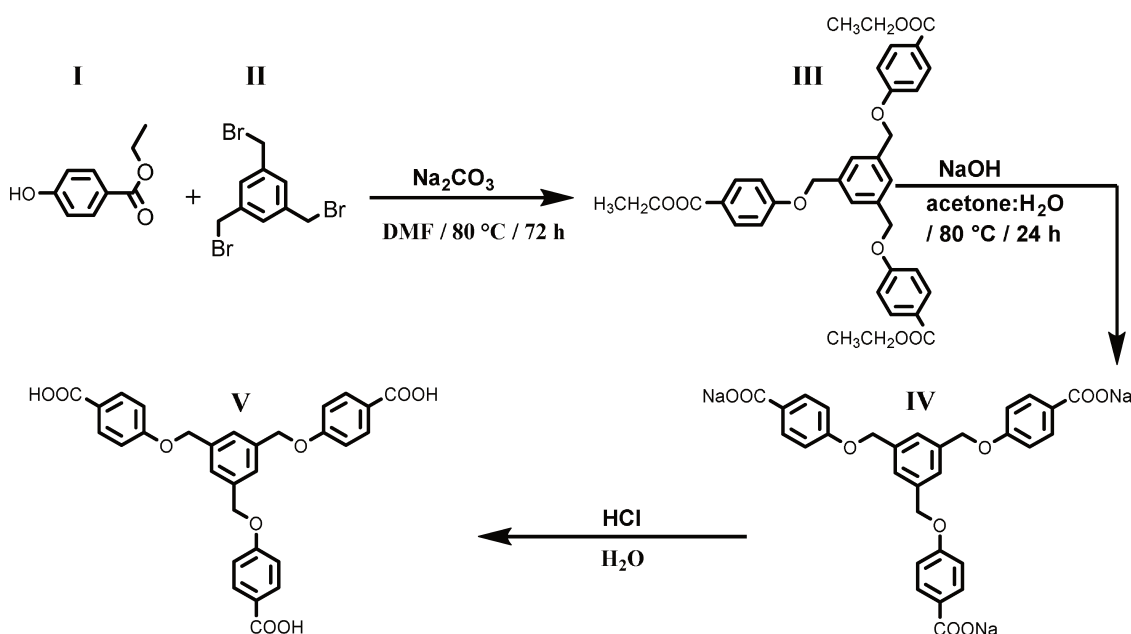
mmol. To an aqueous solution of the $\text{Tb}(\text{NO}_3)_3$ in 20 mL under magnetic stirring at 60 °C was added dropwise 10 mL of ethanolic solution the Naacac. After 1 h, the aqueous solution of the $\text{Eu}(\text{NO}_3)_3$ was added following by dripping the aqueous solution of Na_2BDC maintaining the stirring for 4 h. The resulting white precipitate was isolated by vacuum filtration, washed several times with water and dried for 12 h approximatively.

4. Results and discussion

4.1. Characterization of the synthesized ligands 1,3,5-tris(4-carboxyphenoxy methyl)benzene (H₃TCPMB) and 1,3,5-tris(2,6-dicarboxypyridine-4-oxy methyl)benzene (H₆TDCPMB).

4.1.1. Synthesis and structural description of the ligand H₃TCPMB

The ligand 1,3,5-tris(4-carboxyphenoxy methyl)benzene (H₃TCPMB) was prepared using a one-pot synthesis based on a modified procedure [87] according to the scheme S1.



Scheme S1: Preparation scheme of the ligand 1,3,5-tris(4-carboxyphenoxy methyl)benzene (H₃TCPMB).

Firstly, the 1,3,5-tris(4-ethoxycarbonylphenoxy methyl)benzene (**III**) was obtained by reaction of 1,3,5-tris(bromomethyl)benzene (**II**) with the 4-hydroxy(ethoxycarbonyl)benzene (**I**) (both commercially acquired) in the presence of sodium carbonate DMF for 72 hours. After the reaction time, the solvent was removed, and the white crude precipitate was dissolved in the mixture of acetone and an aqueous solution of NaOH to obtain the ligand as its sodium salt (**IV**) after 24 hours. It is noteworthy mentioning that the use of the mixture of solvents was important to guarantee that the reaction was carried out in the liquid state, once the ester (**III**) is not

water-soluble. After the elimination of the acetone, concentrated chloride acid was added to precipitate the acid (**V**), which was isolated, washed and dried to yield 83 % of the expected mass. The synthesis of the intermediary product triethyl 1,3,5-tris(4-ethoxycarbonylphenoxy-methyl)benzene was confirmed by ^1H -NMR spectroscopy. Its ^1H -NMR spectrum is shown in the appendix A 5. The peaks assignment was carried out basing on the ^1H -NMR of the precursors 1,3,5- tris(bromomethyl)benzene and 4-hydroxy(ethoxycarbonyl-benzene) shown in the appendices A 1 and A 3, respectively. The peak assigned to protons of the methylene groups appears at 4.7 ppm and at 5.2 ppm for the 1,3,5- tris(bromomethyl)benzene and 1,3,5-tris(4-ethoxycarbonylphenoxy-methyl) benzene due the higher electronegativity of the oxygen element regarding the bromine. NMR signal of the proton in ortho position considering the hydroxyl group shifts from 6.8 (appendix A 1) ppm to 7.1 ppm (appendix A 5) due the acidity of the phenolic hydrogen.

Single crystals were obtained on slow vapor diffusion into a diluted solution of the ligand H_3TCPMB in DMF. As reported by Sebastian et. al. [87], It crystallizes in the triclinic space $P\bar{1}$ with an asymmetric unit consisting of one molecule (Fig. 9). Its molecular geometry differs completely from the trigonal one. Two of the molecular branches are arranged in a pincer-like fashion stabilized by an intra-molecular π - π interaction between two aromatic rings that are 4.013 Å apart. The third molecular arm is oriented in the opposite direction conferring an elongated conformation of the molecule in the crystal. Each ligand molecule was found to be associated with two neighboring ligand molecules via $\text{O}\cdots\text{H}$ hydrogen bonding between the pincer-like branches ($\text{O}\cdots\text{H} = 1.742$ Å and 1.868 Å) and between the branches in opposite direction ($\text{O}\cdots\text{H} = 1.823$ Å) resulting in infinite 1D chains. Such chains are packed to form the three-dimensional network which is appeared to be stabilized by van der Waals interactions (Fig. 10). Crystallographic data, experimental parameters and selected details of the refinements are summarized in Table 1.



Fig. 9: Mett illustration of the molecular structure of the ligand 1,3,5-tris(4-carboxyphenoxy methyl)benzene (H_3TCPMB). The dark dots and the dotted line between aromatic rings represent the centroids and distance between them, respectively.

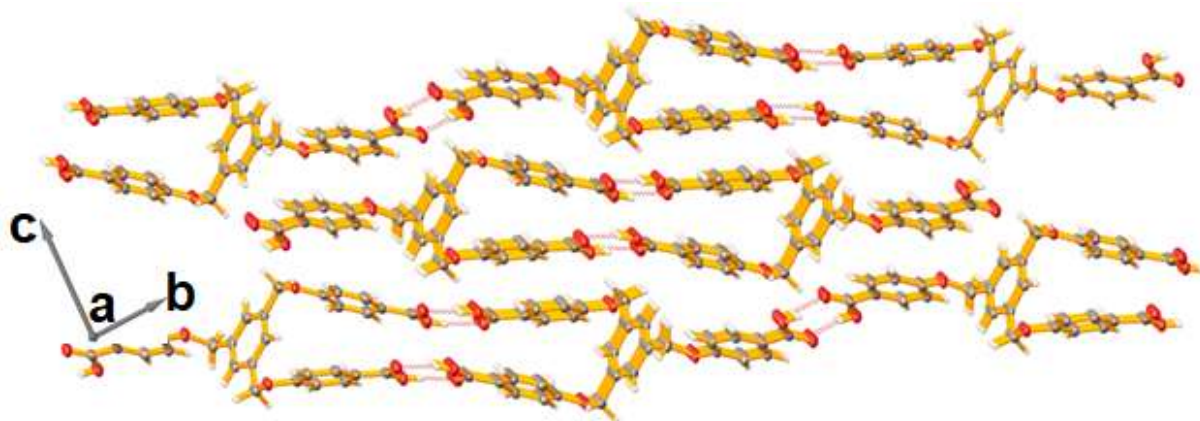
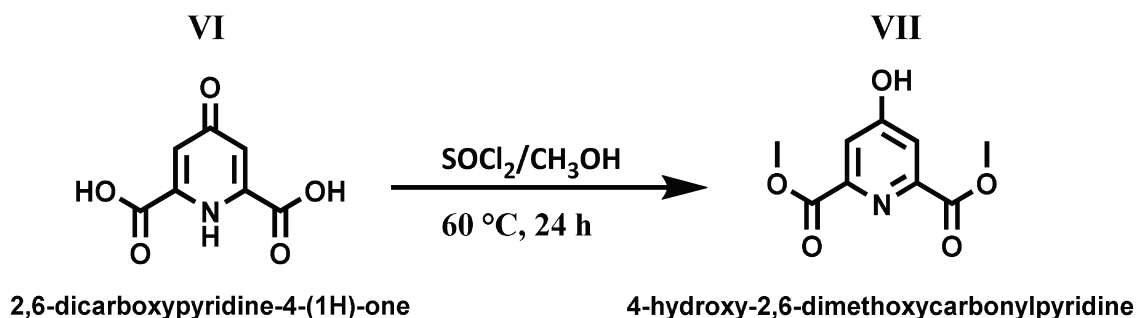


Fig. 10: Hydrogen bonded self-assembly of the ligand 1,3,5-tris(4-carboxyphenoxy methyl)benzene (H_3TCPMB) in its single-crystal structure.

4.1.2. Synthesis of the ligand $H_6TDCPMB$

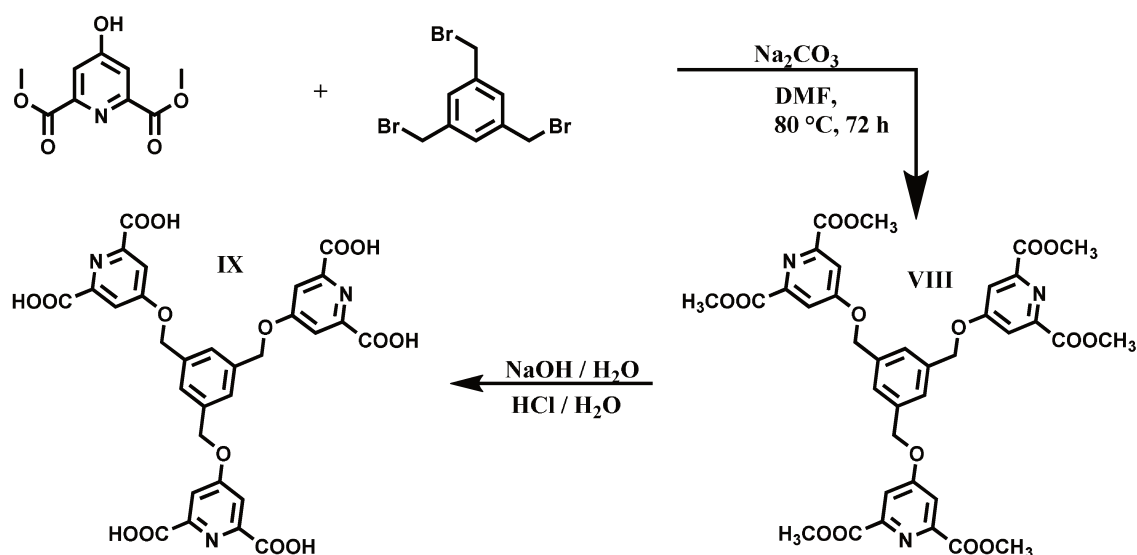
The ligand 1,3,5-tris(2,6-dicarboxypyridine-4-oxy methyl)benzene ($H_6TDCPMB$) was synthesized in two steps schematized in the schemes S2 and S3, respectively. Firstly, the carboxylic groups of the 2,6-dicarboxypyridine-4-(1H)-one H_2DCP (**VI**) (commercially known as hydrate chelidamic acid) were protected from a methylation reaction in anhydrous methanol intermediated by chloride thionyl ($SOCl_2$) to obtain the 4-hydroxy-2,6-dimethoxycarbonylpyridine (**VII**) as schematized in the scheme S2. The success of the reaction was confirmed using the NMR spectroscopy. The appendix A 12 exhibits the 1H -NMR spectrum of the product with two signals at 3.88 ppm and at 7.60 ppm assigned to the protons of the methyl groups and belonging to the ring

respectively. The O-H proton appears as a broad signal between 10.2 and 12.8 ppm, thus indicating the occurrence of proton exchange in the solution.



Scheme S 2: Methylation reaction of 2,6-dicarboxypyridine-4-(1H)-one (H₂DCP)

In the second step, the dimethyl 4-hydroxypyridine-2,6-dicarboxylate was coupled to the tris(bromomethyl)benzene to obtain the 1,3,5-tris(2,6-dimethoxycarbonyl-pyridine-4-oxy methyl)benzene (VIII) in the scheme S3 which was subsequently hydrolyzed by reacting with NaOH. The targeted acid (IX) was precipitated by addition of an aqueous solution of hydrochloric acid. The obtention of VIII was also confirmed using the ^1H -NMR spectroscopy. The peaks exhibited in its ^1H -NMR spectrum are relatively broad due to the low solubility in DMSO.



Scheme S 3: Preparation of the ligand 1,3,5-tris(2,6-dicarboxypyridine-4-oxy methyl)benzene

4.2. Nuclear Magnetic Resonance (NMR) spectroscopy

The ^1H -NMR spectrum of the target Ligand H_3TCPMB is shown in Fig. 11 and the experimental conditions are presented in the appendix A 7. The peak chemical shifts were obtained relative to the peak position at 2.50 ppm of the residual solvent resonance signal. As can be seen in the figure, the spectrum shows that the ligand H_3TCPMB was obtained in high purity degree exhibiting only resonance signals assigned to the residual solvents at 2.50 ppm (DMSO) and at 3.34 (H₂O) and the five proton groups chemically nonequivalent of the ligand, thus, corroborating the results obtained in the elemental analysis. The singlet peak at 5.22 ppm integrated to six was assigned to the methylene protons (4). The two doublets at 7.09 -7.12 ppm and at 7.88 – 7.92 ppm, each one integrated to six can be assigned to the protons (3) and (2), respectively. The singlet at 7.54 ppm assigned to the protons (5) of the central ring is integrated into three. As expected, the resonance signal attributed to the protons of the carboxylic groups appears in the lower field region at 12.60 ppm due to the fact that the chemical environment removes electron density around them.

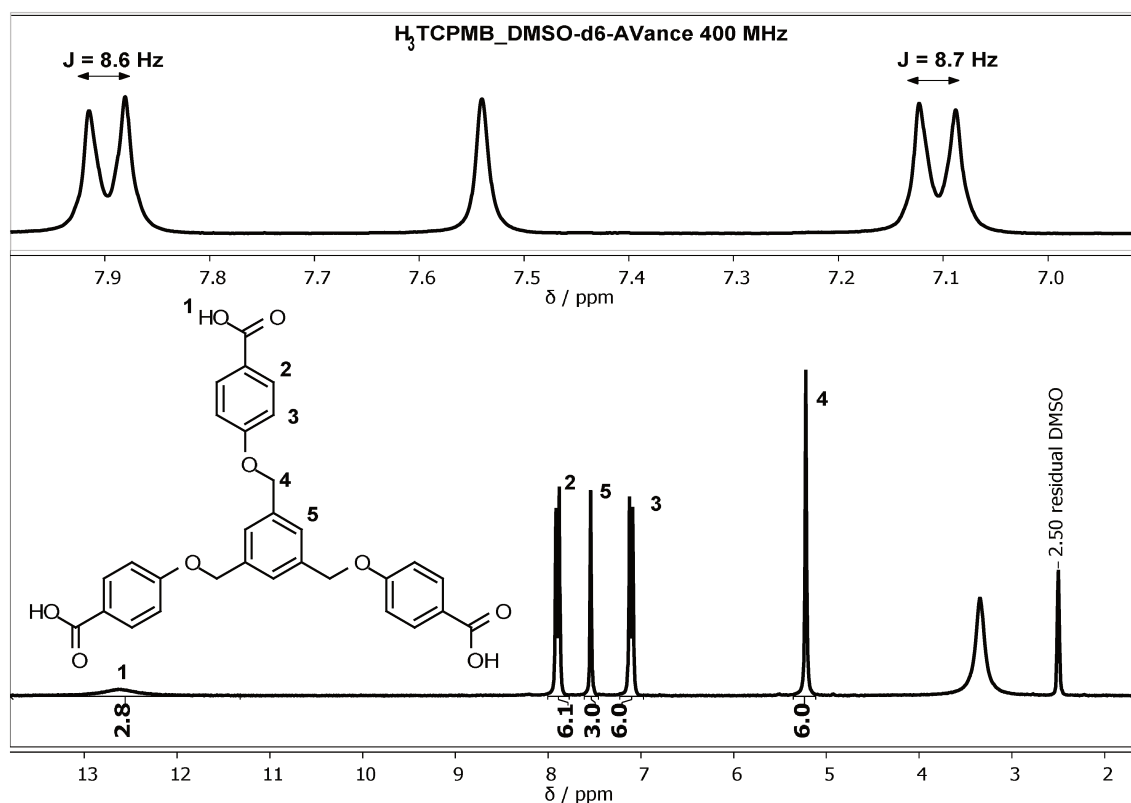


Fig. 11: The 400-MHz ^1H -nuclear magnetic resonance spectrum of H_3TCPMB in DMSO-d_6 . Inset: magnification of the range 6.91-7.99 ppm and chemical structure of the ligand H_3TCPMB . see spectrum conditions in the appendix A 7.

To overcome the problem relative to its insolubility in the common solvents, the ^1H -NMR spectroscopy study of the ligand H_6TDCPMB was carried out using the equivalent sodium salt (Na_6TDCPMB) prepared by treating an aqueous suspension of the protonated ligand with an aqueous solution of sodium hydroxide ($\sim 1 \text{ mol L}^{-1}$). As expected, the ^1H -NMR spectrum exhibits as singlets the three resonance signals assigned to the three magnetically equivalent proton groups of TDCPMB^{6-} and two extra singlets at 0 ppm and at 4.8 ppm assigned to the internal reference (3-(trimethylsilyl)-2,2,3,3-tetradeuteriopropionic acid (TMSP- d_4) and the residual water, respectively. The resonance signals were assigned as shown in Fig. 12. Due to the lone interaction after deprotonation, the protons belonging to the central ring and in ortho position with respect to the carboxylate group show a variation in the relative chemical shifts compared to 1,3,5-tris(2,6-dimethoxycarbonyl-pyridine-4-oxy methyl)benzene (appendix A 16).

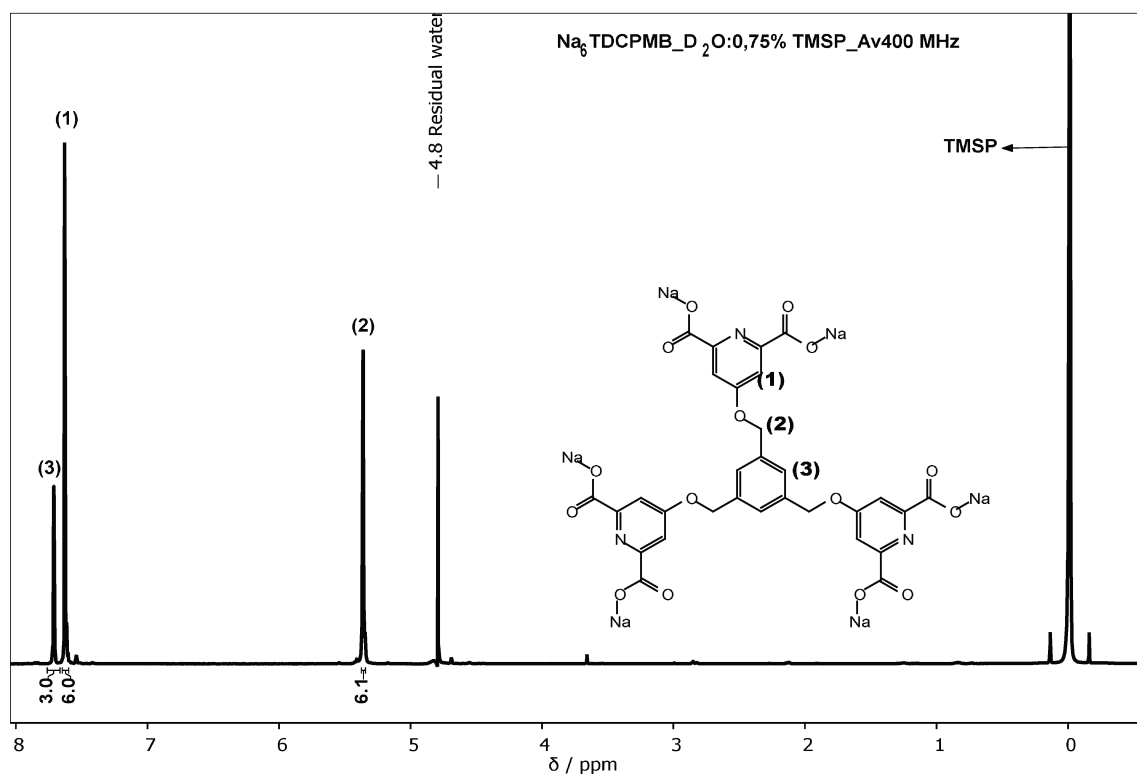


Fig. 12: The 400-MHz ^1H -nuclear magnetic resonance spectrum of Na_6TDCPMB in $\text{H}_2\text{O}-\text{d}_2$ containing (3-(trimethylsilyl)-2,2,3,3-tetradeuteriopropionic acid (TMSP)- d_4 as standard reference. Inset: chemical structure of the salt Na_6TDCPMB . see spectrum conditions in the appendix A 18.

The ^1H -NMR result is validated by the ^{13}C -NMR spectrum which exhibits seven resonance signals at 72.8 ppm, 114.5 ppm, 130.6 ppm, 139.7 ppm, 157.7 ppm, 169.3 ppm, 175.5 ppm assigned the seven types of magnetically distinct carbons as expected by symmetry. The eighth at 188.6 ppm may be attributed to the carbon of carboxylic group evidencing thus, a COO^-/COOH equilibrium in the aqueous solution.

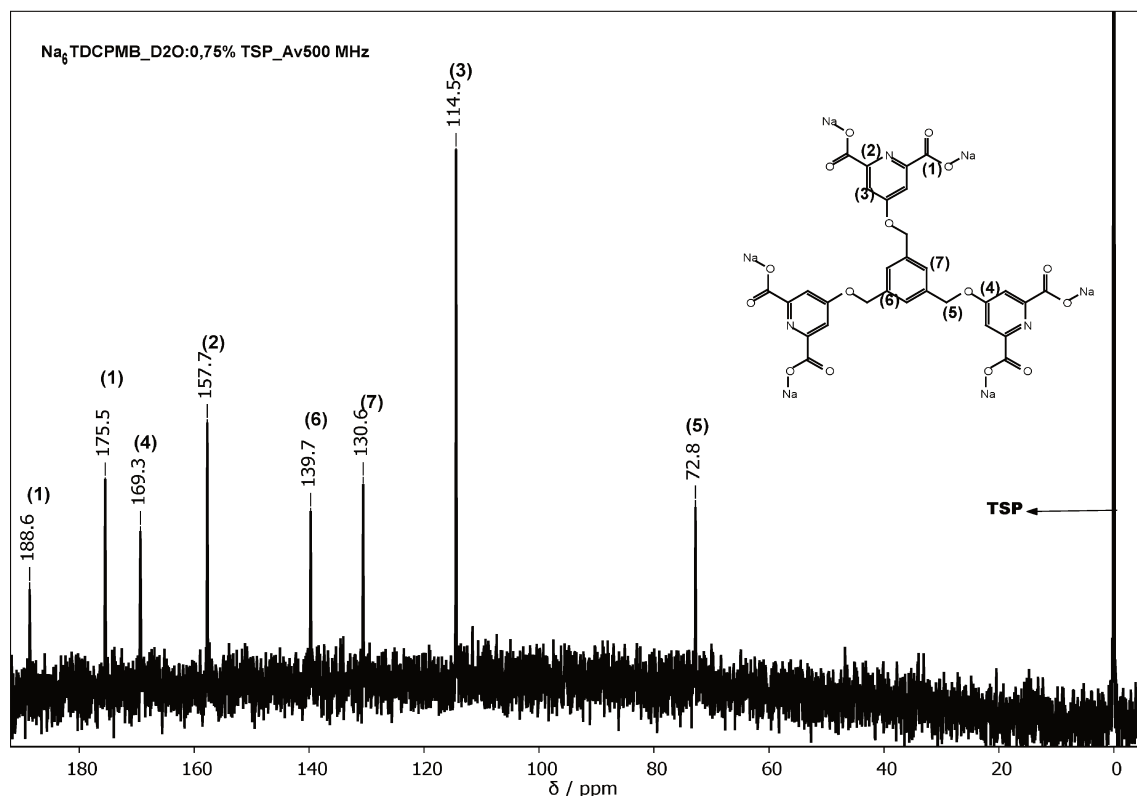


Fig. 13: The 400-MHz ^{13}C -nuclear magnetic resonance spectrum of Na_6TDCPMB in $\text{H}_2\text{O}-\text{d}_2$ containing (3-(trimethylsilyl)-2,2,3,3-tetraduteropropionic acid (TMPS)- d_4 as standard reference. Inset: chemical structure of the salt Na_6TDCPMB . see spectrum conditions in the appendix A 19.

4.2.1. Fourier-transform infrared spectroscopy

The vibrational spectra in the mid-infrared region of both free ligands are shown in Fig. 14. They exhibit the carboxylic acid O–H stretch as broad band, superimposed on the sharp $=\text{C}-\text{H}$ stretching in the aromatic rings and the antisymmetric and symmetric stretching bands of the $-\text{CH}_2$ groups extending from 2500 cm^{-1} to 3400 cm^{-1} [93]. The reason that the O–H stretch band of carboxylic acids is so broad is that carboxylic acids usually exist as hydrogen-bonded dimers as seen in the single-crystal structure of H_3TCPMB [94]. The carbonyl stretch $\text{C}=\text{O}$ of the carboxylic acid groups

appears as an intense band centered at 1672 cm^{-1} for H_6TCPMB and at 1734 cm^{-1} for H_3TCDPMB [95]. Based on the molecular structures of the two ligands, one expects that the C=O stretch band of H_6TCDPMB , due to the presence of the N atoms, should appear in higher energy comparing to H_3TCPMB . The unexpected result indicates that H_6TDCPMB shows less intermolecular hydrogen bonding than H_3TCPMB . Both spectra show the carbon-carbon stretching vibrations in the aromatic rings bands centered at ca. 1600 cm^{-1} and 1510 cm^{-1} [96]. The region $1450 - 1000\text{ cm}^{-1}$ exhibits many absorption bands due to C–H in-plane bending, C–O stretching, $-\text{CH}_2$ rocking and wagging vibrations [93].

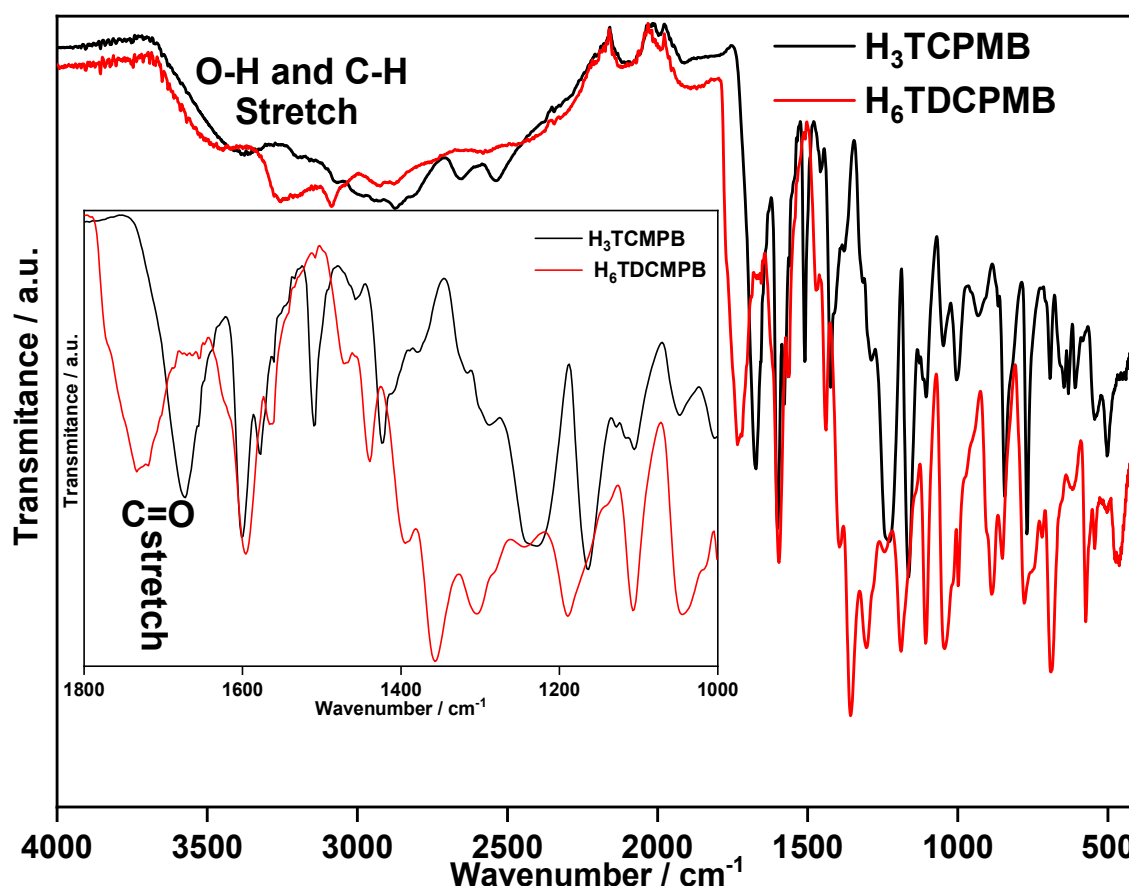


Fig. 14: Solid-state vibrational spectra in the infrared region of H_3TCPMB and H_6TDCPMB collected in the attenuated total reflection (ATR) mode.

4.2.2. Ultraviolet-visible spectroscopy and thermal stability

The light absorption spectra between 200 nm and 500 nm of H_3TCPMB dissolved in acetonitrile and of Na_6TDCPMB dissolved in water, were measured at

room temperature ($\sim 25^\circ\text{C}$). The spectra of 4-hydroxybenzoic acid and 1,3,5-tris(bromo-methyl)benzene were also collected by comparison effect. As shown in Fig. 15a, 1,3,5-tris(bromomethyl)benzene spectrum exhibits a unique band with an absorption maximum at 216 nm which can be attributed to $(\pi^* \leftarrow \pi)$ electronic transitions in the aromatic rings. 4-hydroxybenzoic acid, H_3TCPMB and H_6TDCPMB display two absorption bands in the ultra-violet region with a bathochromic shift in the case of Na_6TDCPMB as result of an important solvent effect. The first band, more intense, is attributed to $(\pi^* \leftarrow \pi)$ electronic transitions in the aromatic rings. The blue-shift regarding the $(\pi^* \leftarrow \pi)$ band in 1,3,5-tris(bromomethyl)benzene suggests an effective actuation of the heavy atom effect due to the Bromine [97]. The second one may be attributed to electronic transitions from nonbonding orbital of the oxygen atom to antibonding orbital in the $\text{C}=\text{O}$ group.

The thermal stability was investigated through thermogravimetric studies (TG and DTA). The thermogravimetric curves (Fig. 15b) show that both ligands are thermally stable up to 200°C (T_{onset}^{***}) where starts the degradation process until 600°C ($T_{\text{enset}}^{\dagger\dagger\dagger}$) remaining in a residue amount of 0.3 %. The slight weight loss at the beginning of the thermogram may be ascribed to some water molecules solvating the carboxylic group. The DTA of H_3TCPMB and H_6TDCPMB (appendix A 20) show one and two $T_{\text{peaks}}^{\ddagger\ddagger\ddagger}$ indicating the degradation of the benzenic and pyridinic ring respectively. The thermogram of the salt Na_6TDCPMB is also shown in appendix A 20. The weight loss of 8% observed in the temperature range of $30 - 150^\circ\text{C}$ may be assigned to the water of hydration (4 molecules per Na_6TDCPMB). Based on the agreement of the experimental residue (35%) and the expected (36.8%), it was possible to conclude that the decomposition of the salt results in sodium carbonate (Na_2CO_3). The endothermal event at 750°C and the slight weight loss at around the same temperature may be assigned to the fusion of the Sodium carbonate and the beginning of its decomposition in sodium oxide (Na_2O) and carbon dioxide (CO_2) thus, corroborating the fact that the expected value for the residue be slightly higher than found.

*** Temperature at which the degradation begins [135].

$\dagger\dagger\dagger$ Temperature at which the degradation ends

$\ddagger\ddagger\ddagger$ Temperature at which the degradation rate reaches a maximum value

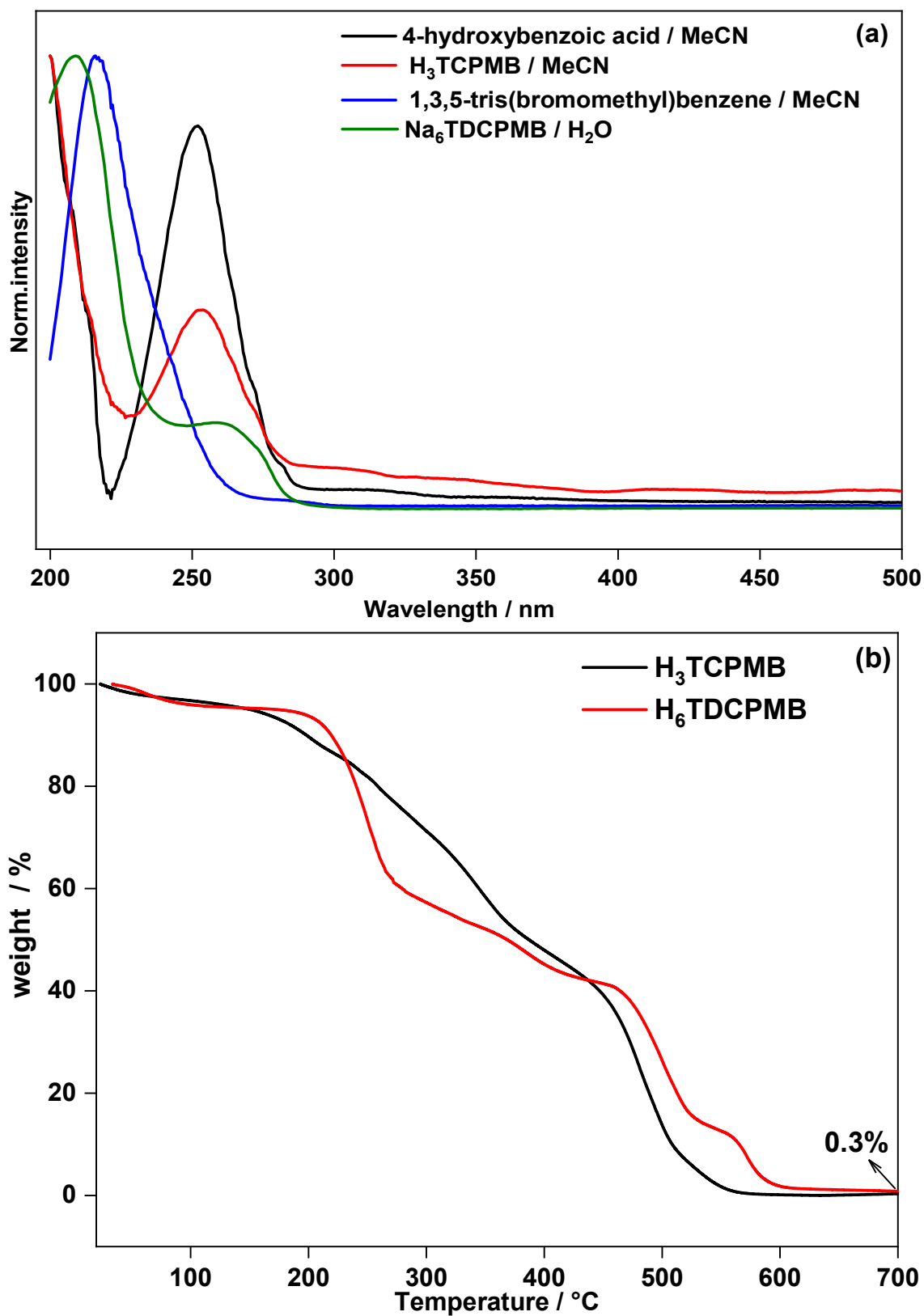


Fig. 15: Recorded absorption spectra, at room temperature of 4-hydroxybenzoic acid, H₃TDCPMB and 1,3,5-tris(bromomethyl)benzene as acetonitrile solutions, and Na₆TDCPMB as aqueous solution (a). Thermogravimetric curves (TG) of the protonated ligand H₃TCPMB and H₆TDCPMB (b).

4.3. Syntheses and characterization of the compounds based on H₃TCPMB

4.3.1. Syntheses and structural description

Solvothermal conditions have been proven to be a useful methodology to obtain crystalline coordination networks. As the ligand is soluble in DMF, the hydrochloric acid was used to reduce the coordination rates, and consequently, potentialize the growth of high-quality single crystals [98]. As the acid slows down the deprotonation of the carboxylic group and, consequently, the binding of the linkers to the metal centers, it promotes the growth of larger crystals and preventing the formation of amorphous and polycrystalline phases, which may be formed if the reaction is allowed to proceed with no acid added [99]. X-ray single-crystal structure analyses reveal that the four synthesized compounds Eu-TCPMB, Gd-TCPMB, Tb-TCPMB, and Tb_{0.95}Eu_{0.05}-TCPMB are isostructural as confirmed by the crystal data in Table 3 and the simulated powder X-ray diffraction pattern (Fig. 19a). They crystallize in the triclinic space group crystal system $P\bar{1}$ and feature an extended isolated 1D structure. Thus, the representative structure description and discussion will be restricted to the europium compound Eu-TCPMB. As can be seen in Fig. 16a, the asymmetric unit of Eu-TCPMB contains one Eu^{III} ion, one TCPMB³⁻ tri-anion, one DMF molecule and one water molecule coordinated to the metal center and one lattice DMF molecule. Each europium ion is eight-coordinated and binds two oxygen atoms from one DMF and one H₂O molecule (average bond length of 2.415 and 3.093 Å, respectively) and carboxylate oxygen atoms belonging to three different TCPMB³⁻ trianions that coordinate to the metal ion in the bridging and the chelating bis-dentate modes (average Eu-O bond length of 2.292 and 2.461 Å, respectively). The coordination geometry of the Eu^{III} ion (Fig. 16b) can be viewed as a distorted square antiprism, basal planes made by O4, O5, O6, O10, and O7, O8, O9 O11 atoms, respectively leading to a distorted D_{4d} coordination sphere around the metal center. Each ligand TCPMB³⁻ binds to three metal ions through two chelating and one bidentate carboxylate groups (Fig. 17a). Two non-centrosymmetric Eu atoms bridged through the same carboxylate group to generate a binuclear Eu₂(μ₂-COO)₂ unit where the distance between the metal ions is 4.816 Å (Fig. 17b) and Table 2. The binuclear units are linked along the b axis in the infinite 1D chains (Fig. 16d), which are further packed in a 3D

network (Fig. 18). Each binuclear unit is surrounded by four TCPMB³⁻ ligands (Fig. 17b) and each ligand connects two binuclear units. The 1D chain of Eu-TCPMB is defined as a 2,4-connected network. The asymmetric units, first coordination spheres, and binuclear units for the four compounds Eu-TCPMB, Tb-TCPMB, Gd-TCPMB, and Tb_{0.95}Eu_{0.005}-TCPMB are shown in the appendix (A 22, A 23, A 24) by comparison effect. As can be conferred in Table 2, the Ln–O bond lengths and Ln···Ln internuclear distances in the binuclear units decreases slightly from the Eu-TCPMB to Tb-TCPMB. Such fact can be ascribed to the lanthanide contraction effect [100]. It is worth mentioning that the free DMF molecule shows an identical special position and orientation in the asymmetric units of Tb-TCPMB and Tb_{0.95}Eu_{0.05}-TCPMB and different for Eu-TCPMB and Gd-TCPMB suggesting a dependence with the nature of the central ion.

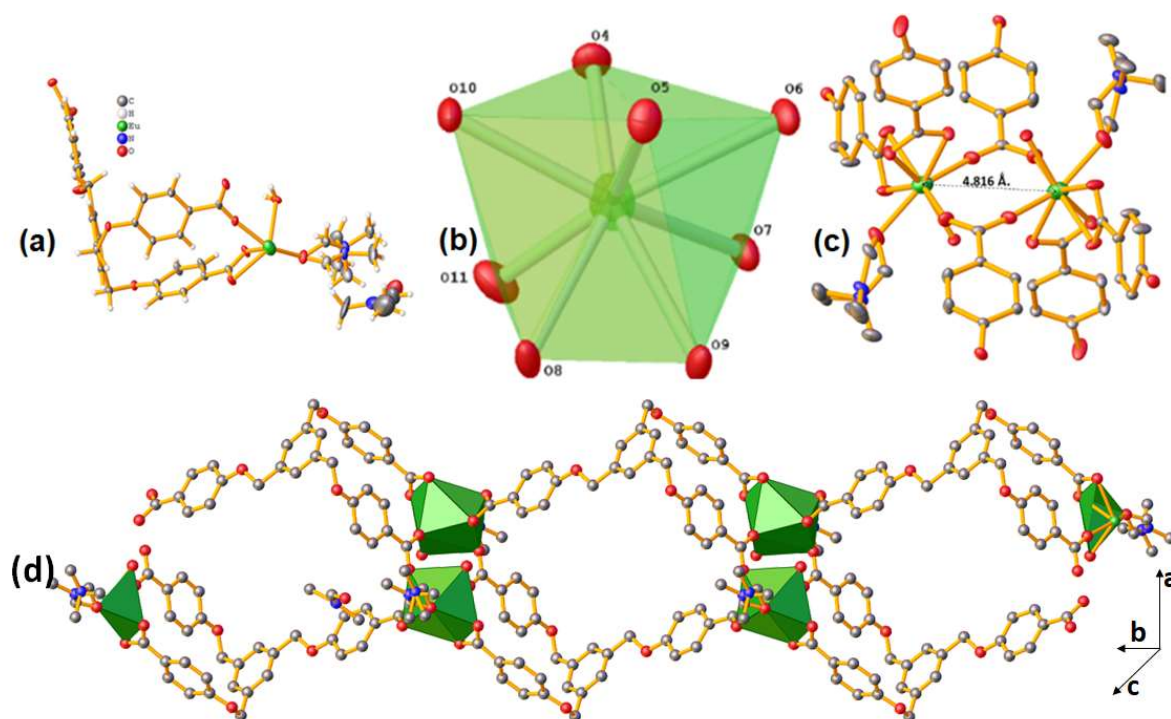


Fig. 16: (a) ORTEP drawing of the asymmetric unit of Eu-TCPMB. (b) The coordination geometries of Eu^{III} ions in Eu-TCPMB resulting in a C₁ symmetry site for the central ion. (c) The connection mode of Eu^{III} ions in a binuclear unit. (d) View of the 1D chain as the infinite secondary building units (SBUs) along the crystallographic b-axis obtained from binuclear units linked through carboxylate group. H atoms and free solvent molecules were omitted for clarity.

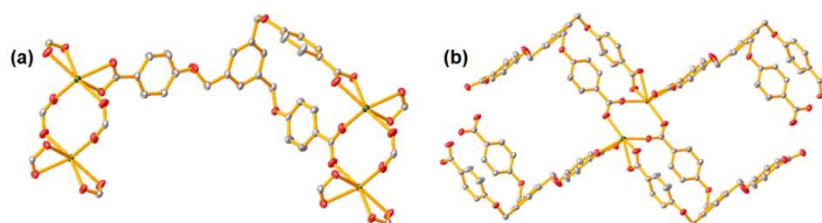


Fig. 17: (a) Each TCPMB^{3-} ligand connects three binuclear $\text{Eu}_2(\mu_2\text{-COO})_2$ units in Eu-TCPMB. (b) Number of TCPMB^{3-} ligands around the binuclear unit $\text{Eu}_2(\mu_2\text{-COO})_2$. H atoms were omitted for clarity.

Table 2: Average lengths of the bonds between trivalent metal ions Ln and the coordinated oxygen atoms and the $\text{Ln}\cdots\text{Ln}$ internuclear distances (Å) in the binuclear units of Eu-TCPMB, Gd-TCPMB, Tb-TCPMB, $\text{Tb}_{0.95}\text{Eu}_{0.05}\text{-TCPMB}^a$.

	Eu-TCPMB	Gd-TCPMB	Tb-TCPMB	$\text{Tb}_{0.95}\text{Eu}_{0.05}\text{-TCPMB}$
Ln-O_w	2.415	2.401	2.385	2.387
Ln-O_D	2.415	2.401	2.383	2.375
$\text{Ln-O}_{C(\text{br})}$	2.330	2.313	2.302	2.300
$\text{Ln-O}_{C(\text{bi})}$	2.455	2.445	2.432	2.433
$\text{Ln}\cdots\text{Ln}$	4.816	4.808	4.785	4.776

^a O_w , O_D , $\text{O}_{C(\text{br})}$, $\text{O}_{C(\text{bi})}$: oxygen atoms of the water molecule, DMF molecule, carboxylate group in bridging and bidentate coordination mode respectively.

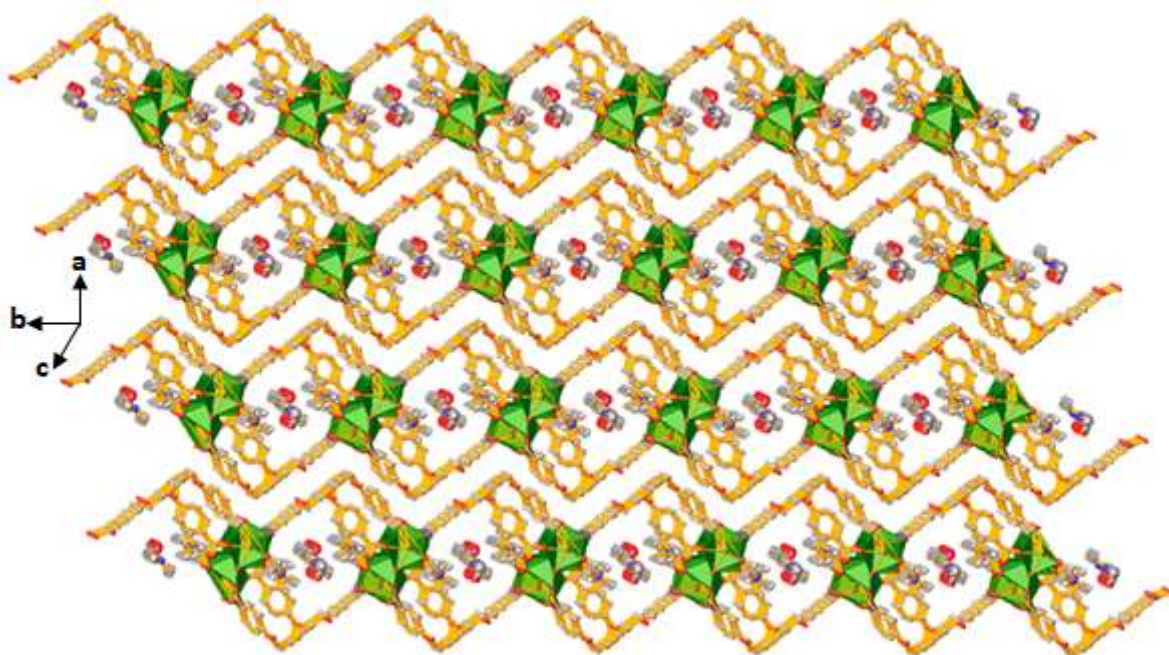


Fig. 18: View of the 3D supramolecular structure of the coordination network Eu-TCPMB along the crystallographic b-axis.

Table 3: Crystal data of the free ligand (H₃TCPMB) and the lanthanides-based coordination polymers

compound	H ₃ TCPMB	Tb-TCPMB	Gd-TCPMB	Eu-TCPMB	Tb _{0.95} Eu _{0.05} -TCPMB
Emp. Form.	C ₃₀ H ₂₄ O ₉	Tb ₂ C ₆₉ H ₆₇ N ₃ O ₂₃	Gd ₂ C ₆₉ H ₆₇ N ₃ O ₂₃	Eu ₂ C ₆₉ H ₆₇ N ₃ O ₂₃	Ln ₂ C ₆₇ H ₆₃ N ₃ O ₂₃
MW	528.49	1624.09	1620.79	1610.17	1589.32
T/K	150	150	150	150	150
$\lambda/\text{\AA}$	Cu K α	Mo K α	Mo K α	Mo K α	Mo K α
Crystal Syst.	Triclinic	Triclinic	Triclinic	Triclinic	Triclinic
Space group	P $\bar{1}$	P $\bar{1}$	P $\bar{1}$	P $\bar{1}$	P $\bar{1}$
a/ \AA	6.3171(5)	8.5108 (5)	8.5212 (12)	8.5361 (6)	8.5183(16)
b/ \AA	10.6482(7)	14.2208 (9)	14.186 (2)	14.2116(10)	14.248(3)
c/ \AA	18.1883 (1)	14.3990 (9)	14.434 (2)	14.4375(10)	14.380(3)
$\alpha/^\circ$	86.360 (3)	98.265 (2)	98.010 (3)	98.093 (1)	98.401(8)
$\beta/^\circ$	88.548 (3)	106.718 (1)	106.609 (3)	106.628 (1)	106.971(8)
$\gamma/^\circ$	79.326 (3)	96.164 (1)	96.382 (4)	96.329 (1)	96.266(8)
V/ \AA^3	1199.74 (15)	1631.26 (17)	1634.6 (4)	1640.4 (2)	1630.0(5)
Z	2	1	1	1	1
Z'	1	0.5	0.5	0.5	0.5
D/Mgm ⁻³	1.463	1.653	1.646	1.630	1.619
μ/mm^{-1}	0.91	2.23	2.10	1.98	2.23
F(000)	552	816	814	812	796
θ range/ $^\circ$	4.2–68.8	2.7–28.2	2.5–28.2	2.7–30.4	2.3–27.6
^a R ₁ /%	3.19	3.08	2.98	1.70	3.38
^b wR ₂ /%	8.60	7.08	6.70	4.61	8.51
R _{int} /%	1.51	2.95	5.17	1.51	7.27
GooF	1.050	1.054	1.035	1.084	1.030

$$^a R_1 = \sum(|F_0| - |F_c|) / \sum|F_0| \quad ^b wR_2 = \{\sum[w(F_0^2 - F_c^2)^2] / \sum[w(F_0^2)^2]\}^{1/2}$$

4.3.2. Powder X-ray Diffraction and FT-IR spectroscopy

In order to check the phase purity of the crystalline compounds, the X-ray powder diffraction (P-XRD) patterns were recorded at room temperature and compared to the simulated ones [101]. As shown in Fig. 19b, the peak positions in the simulated diffractogram of Eu-TCPMB and the experimental P-XRD patterns of the as-synthesized compounds are in agreement with each other indicating the high phase purity of the four structures. The diffractograms of La-TCPMB and La_{0.95}Eu_{0.05}-TCPMB (Fig. 20a) show a profile completely different and suggest the formation of a cubic structure. The slight peak shifting towards a higher angle in the diffractogram of La_{0.95}Eu_{0.05}-TCPMB may be interpreted as a decrease in the lattice parameter due to the presence of the Eu^{III} ions. Both other compounds (Eu-TCPMB-phen and Eu-TCPMB-tppo) synthesized with the intention to substitute the solvent molecules by the ligand phenanthroline (phen) or triphenylphosphine oxide (tppo) were obtained as amorphous powders as confirmed by their P-DRX patterns (appendix A 25).

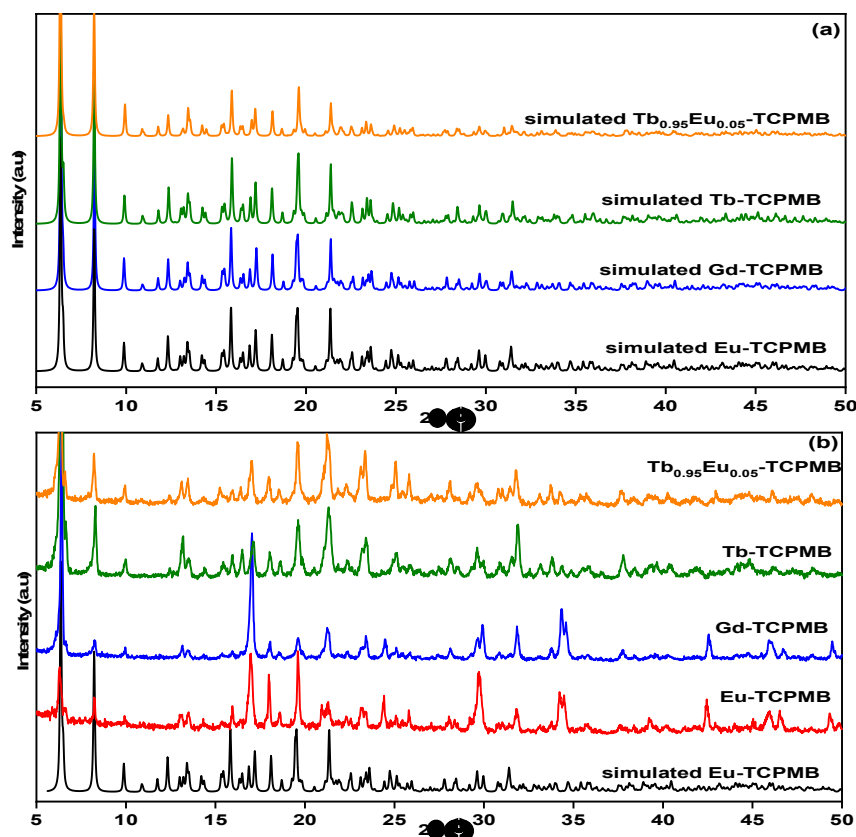


Fig. 19: (a) Simulated P-XRD patterns from the CIF files of the compounds obtained from the ligand H₃TCPMB. (b) Experimental P-XRD patterns of the compounds Eu-TCPMB, Gd-TCPMB, Tb-TCPMB and Tb_{0.95}Eu_{0.05}-TCPMB and simulated P-XRD pattern of Eu-TCPMB.

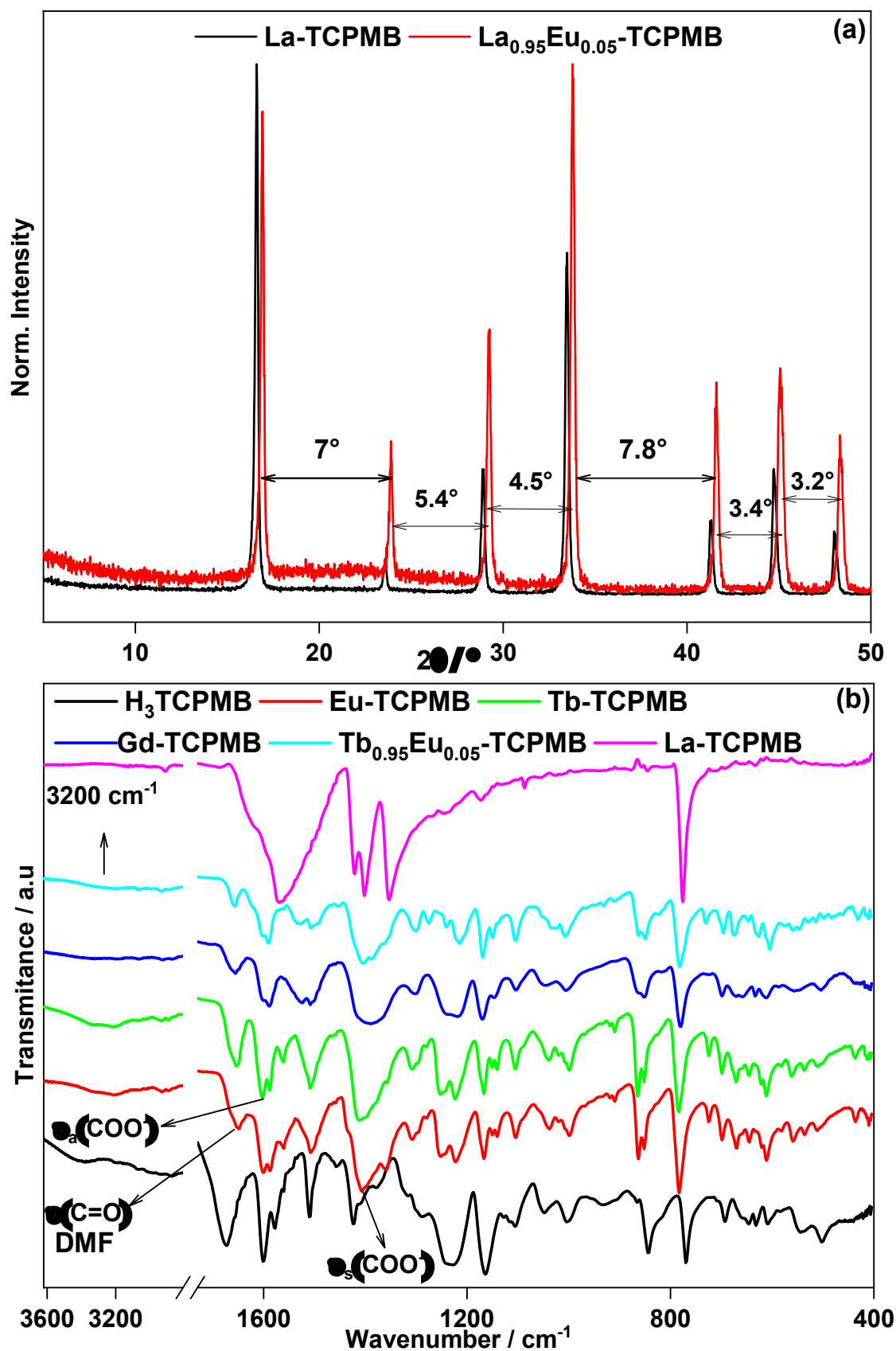


Fig. 20: (a) Experimental P-XRD patterns of the compounds La-TCPMB and La_{0.95}Eu_{0.05}-TCPMB. (b) FT-IR spectra of free ligand H₃TCPMB and the as-synthesized compounds Eu-TCPMB, Tb-TCPMB, Gd-TCPMB, Tb_{0.95}Eu_{0.05}-TCPMB, and La-TCPMB.

The Fourier transform infrared (FT-IR) spectroscopy is commonly used for structural characterization of hybrid materials because it can provide information about changes in bonds containing in coordinating chemical functional groups and they may suggest the nature of the coordination modes. The infrared spectra of all compounds were collected between 4000 and 400 cm^{-1} (Fig. 20b). The spectra of Eu-TCPMB, Gd-TCPMB, Tb-TCPMB and $\text{Tb}_{0.95}\text{Eu}_{0.05}$ -TCPMB exhibit the same spectral profile, thus, corroborating the fact that there are isostructural. The broad absorption bands in the range of 3000–3500 cm^{-1} may be assigned to the stretching of O–H bonds of the coordinated water molecules [38]. The spectra show a band at around 1655 cm^{-1} assigned to the C=O stretching of the DMF molecules [102,103]. The bands of carboxylates occur around 1590 cm^{-1} for antisymmetric stretching and around 1400 cm^{-1} for symmetric stretching [104]. The IR spectrum of La-TCPMB shows a profile completely different compared to the compounds obtained as single crystal corroborating the crystal data. The shoulder at around 1620 cm^{-1} may be probably interpreted as an indication of the presence of DMF molecules in the structure. The fact that the spectrum of La-TCPMB does not show absorption band at 1670 cm^{-1} indicates that the ligand is completely deprotonated.

4.3.3. Thermal stability

The study of thermal stability was performed for Eu-TCPMB, Tb-TCPMB, Eu-TCPMB-tpo and Eu-TCPMB-phen in the temperature range of 20 – 800 °C in a synthetic air atmosphere at a heating rate of 10 °C / min. The thermograms are presented in Fig. 21. TG curves of Eu-TCPMB and Tb-TCPMB show similar thermal behavior undergo weight loss in three steps. The first and second weight losses up to 240 °C correspond to two water and two DMF molecules. The further heating leads to the structural collapse which reaches the maximum rates at 414 °C (appendices A 26 a-b). The final residue of 24% may be identified as Ln_2O_3 . It is very close to the calculated values of 23% and 24% expected for Eu-TCPMB and Tb-TCPMB, respectively. TG of Eu-TCPMB-tpo and Eu-TCPMB-phen also reveal a weight loss until 325 °C evidencing, thus the presence of free or coordinated solvent molecules. The collapse of the structures results in two endothermal events as can be seen in the appendices A 26 c-d. This difference in the profile of the degradation of the ligand may be considered as a confirmation of the presence of the auxiliary ligands in the

structures. The fact that the final residue values coincide with ones obtained for Ln-TCPMB suggests that only a few solvents molecules were substituted.

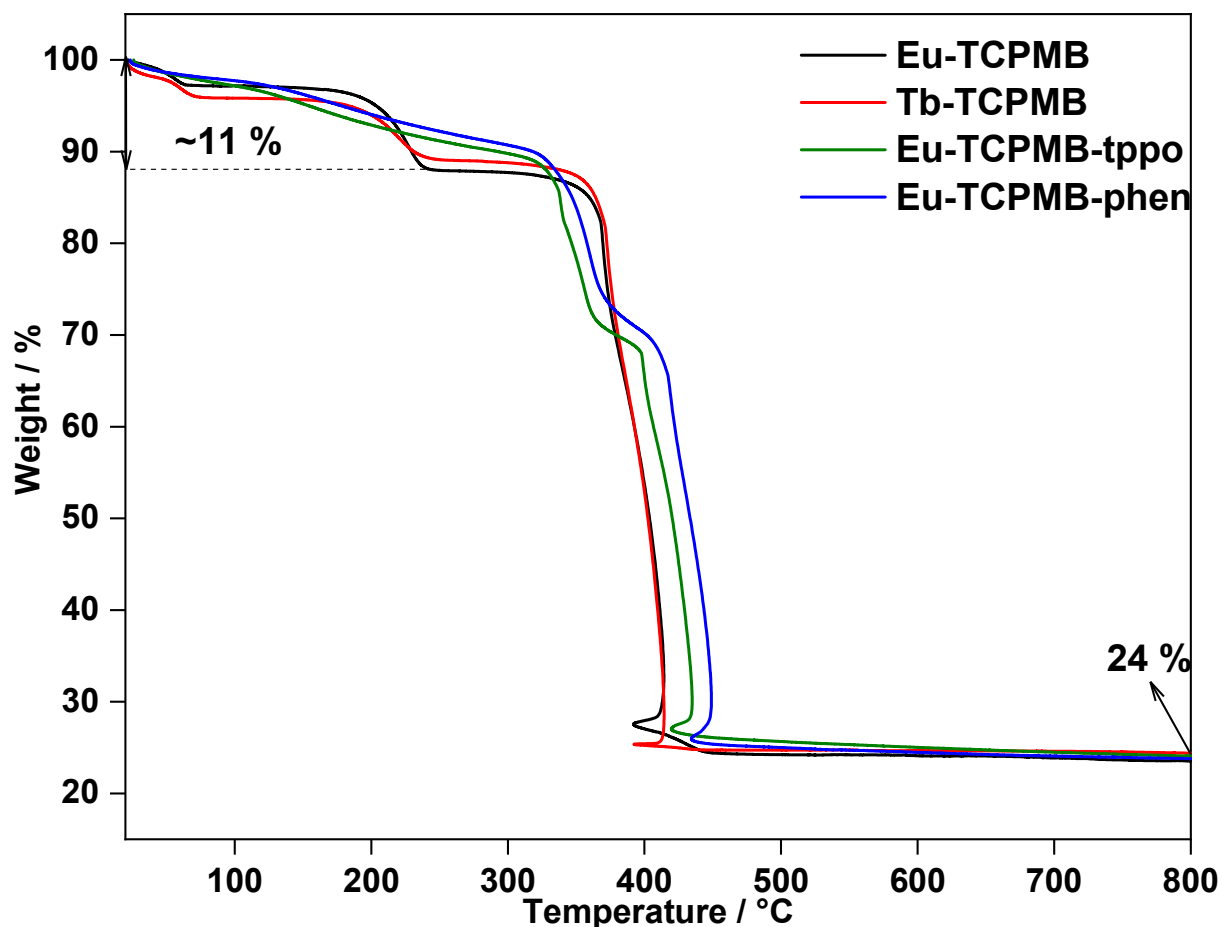


Fig. 21: Thermograms of Eu-TCPMB, Tb-TCPMB, Eu-TCPMB-tppo and Eu-TCPMB-phen obtained in synthetic air flow.

4.4. Synthesis and characterization of the compounds based on $H_6TDCPMB$

4.4.1. Synthesis, P-XRD, and FT-infrared spectroscopy

In order to obtain in a crystalline phase, the solvothermal procedure was tested using water or DMF as the solvent and the temperatures of 120, 150, and 180 °C. The weight of ligand, time of reaction and volume of solvent were fixed to, 60 mg, 72 h and 15 mL (37.5 % of the Teflon vessel). The use of chloride acid has not been tested considering very slight solubility of $H_6TDCPMB$ in DMF. Unfortunately, we have not been successful as shown by the P-XRD patterns of a series of Eu^{III} containing compounds obtained in the attempts (Fig. 22a). Therefore, the compounds were

synthesized by precipitation in aqueous solution which, as expected, result in amorphous powder (Fig. 22b). Besides the shorter time required, in this methodology, the purification of the compounds was facilitated by washing with water. Another last attempt was done pursuing the obtention of single crystal. In this case, the reaction mixture consisted of 60 mg of $H_6TDCPMB$, 15 mL of water or DMF, 0.5 mmol of NaOH was sealed and heated at 120 °C for 5 days. The diffractograms (Fig. 22d) suggest that by adding NaOH and adjusting other parameters, crystalline structure should be obtained. Probably the presence of hydroxide ions results in the formation of insoluble lanthanide-hydroxide species, which may initiate the crystal growth processes.

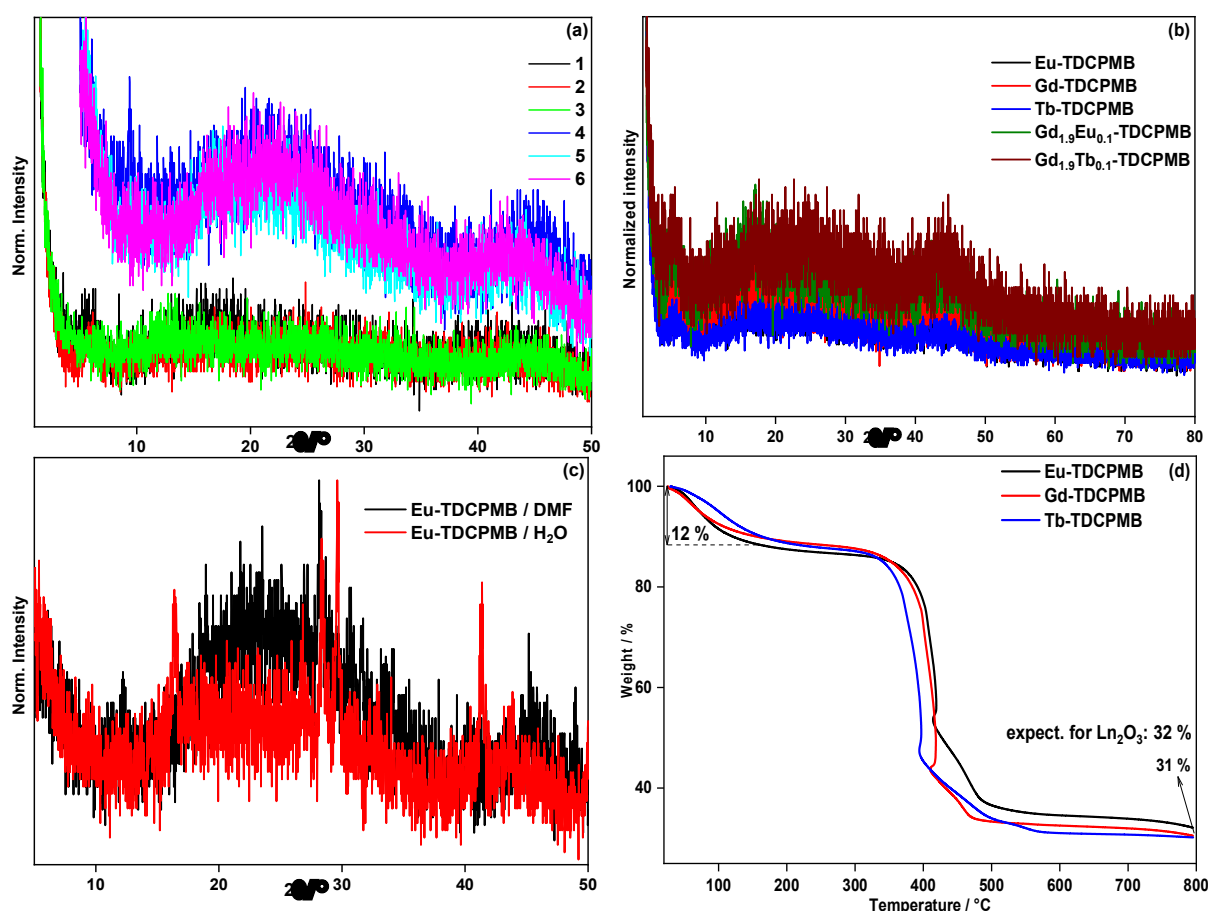


Fig. 22: (a) P-XRD patterns of Eu-TDCPMB obtained by solvothermal synthesis in DMF at 120 °C (1), 150 °C (2), 180 °C (3) and by hydrothermal at 120 °C (4), 150 °C (5), 180 °C (6). (b) P-XRD patterns of Eu-TDCPMB, Gd-TDCPMB, Tb-TDCPMB, Gd_{1.9}Eu_{0.1}-TDCPMB, Gd_{1.9}Tb_{0.1}-TDCPMB obtained by precipitation. (c) P-XRD patterns of Eu-TDCPMB obtained in DMF (black) or water (red) with the addition of NaOH to the reaction mixture. (d) TG and DTA curves of thermal decomposition of Eu-TDCPMB, Gd-TDCPMB, and Tb-TDCPMB.

The FT-IR spectroscopy study was performed for the compounds represented by the general formulas Ln-TDCPMB (Ln = Eu^{III}, Gd^{III}, Tb^{III}) and Gd_{1.9}Ln_{0.1}-TDCPMB

(Ln = Eu^{III}, Tb^{III}). The IR spectrum of the salt Na₆TDCPMB was also collected by comparison effect. The strong and broad absorption bands in the range of 3650 – 2900 cm⁻¹ attributable to the O-H stretching vibrations of the free water molecules. The antisymmetric and symmetric stretching of the CH₂ appear as very low-intensity bands at around 2950 cm⁻¹ and 2920 cm⁻¹, respectively. The strong bands appearing around 1590 and 1360 cm⁻¹ correspond to the antisymmetric and symmetric stretching of the carboxylate group, respectively. The absence of strong absorption bands around 1730 cm⁻¹ indicates that the ligands are totally deprotonated. It is worth noting that the COO⁻ antisymmetric and symmetric show practically no red-shift after coordination to the Ln^{III} indicating coordination of Ln^{III} mainly from an electrostatic interaction. The middle and narrow bands in the range of 1000-1470 cm⁻¹ are attributed to C-N and C-C vibrations, C-H in-plane bending, C-O stretching, -CH₂ rocking and wagging [105].

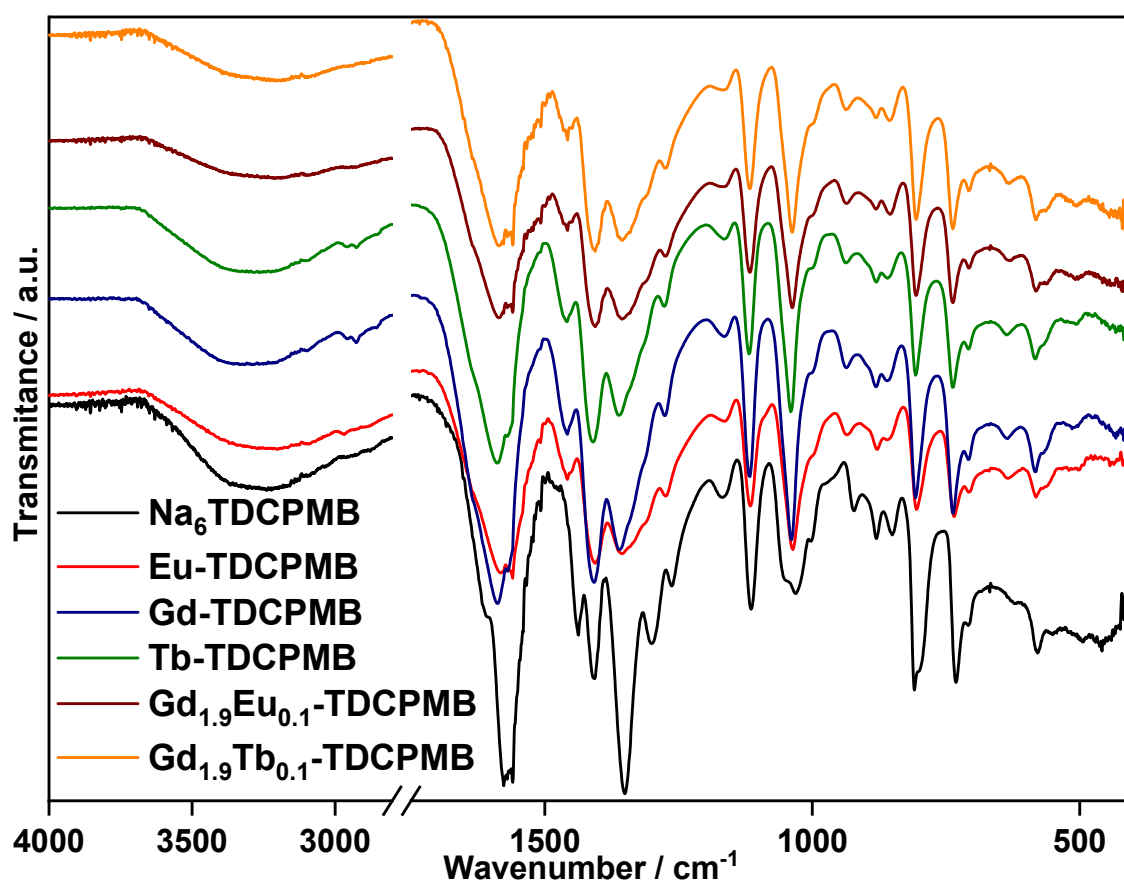


Fig. 23: Infrared spectra of the salt Na₆TDCPMB and the compounds represented by Ln-TDCPMB (Ln = Eu^{III}, Gd^{III}, Tb^{III}) and Gd_{1.9}Ln_{0.1}-TDCPMB (Ln = Eu^{III}, Tb^{III}).

4.4.2. Thermal stability

Thermogravimetric analyses were performed for Eu-TDCPMB, Gd-TDCPMB and Tb-TDCPMB as dried and powdered samples in the range of 30 – 800 °C under N₂ atmosphere. The thermograms are shown in Fig. 22d. They exhibit basically two mass losses in the temperature ranges 30 – 160 °C and 340 – 600 °C which may be probably attributed to the loss of water molecules and burning of the organic ligands, respectively. The process of involving the water molecules observed in the TG curves, characterized by a total mass loss of ~12% corresponding to a ratio of 7 water moles per mol of Ln-TDCPMB. Such result suggests that the water molecules are not coordinated to central ion as expected. In fact, the pyridine-2, 6-dicarboxylic acid moiety is an efficient tridentate N, O-chelating ligand able to coordinate with the lanthanide ion in a 3:1 ratio through six oxygens of carboxyl groups and three nitrogen atoms of the pyridine units saturating the first coordination sphere, thus leaving no coordination site for water molecules. After dehydration, the anhydrous compounds are stable up to about 340 °C where further heating leads to the degradation of the organic part and formation of lanthanide oxycarbonate (Ln₂O₂(CO₃)₂) which is posteriorly decomposed in Ln₂O₃ and CO₂ as indicated by an exothermic event at around 460 °C [106]. The found value for ca. 31 % for the final residue agrees with the expected 32% based on the stoichiometry of the reaction between Ln^{III} and TDCPMB⁶⁻. Thus, the molecular formula of the compounds Ln-TDCPMB can be represented by Ln₂TDCPMB.7H₂O.

4.5. Characterization of the compounds based on H₂BDC and HAC

4.5.1. Powder x-ray diffraction and Infrared spectroscopy

The powder X-ray diffraction (P-XRD) has been carried to compare the crystalline structure of the compounds. Fig. 24a shows that independently using one or a mixture of ligands, the compounds were obtained as crystalline powder and the diffractograms of the Eu-AC-BDC and TB-AC-BDC exhibit all diffraction peaks found in the diffractograms of Eu-AC and Eu-BDC. As can be seen in A 28, The diffractograms show that the two compounds containing only one ligand and the two compounds build using the mixing ligands are isomorphous one to each other.

Therefore, the infrared spectroscopy study was carried only for the Eu^{III} containing compounds.

The vibrational spectra in the infrared range of the free ligand H_2DBC , HAC , their sodium salts Na_2BDC , NaAC and the compounds Eu-AC , Eu-BDC , and Eu-AC-BDC are presented in Fig. 24b. The spectra of both protonated ligands show a broad band (due to hydrogen bonding) in the range $2250\text{--}3120\text{ cm}^{-1}$ assigned to the stretching of the O-H of the COOH groups overlapping to the ring C-H stretching (A 29). The strong band centralized at 1675 cm^{-1} , which can be assigned to the stretching mode of the C=O groups. The band assigned to the C-O stretching appears at 1275 cm^{-1} and 1253 cm^{-1} for H_2BDC and HAC , respectively [107]. The spectra of their sodium salts Na_2BDC and NaAC exhibit strong absorption bands owing from the antisymmetric (ν_a) and symmetric (ν_s) stretching of the carboxylate groups centered at 1553 and 1379 cm^{-1} , respectively for Na_2BDC ($\nu_a - \nu_s = 174\text{ cm}^{-1}$) and at 1558 and 1318 cm^{-1} for NaAC ($\nu_a - \nu_s = 240\text{ cm}^{-1}$). The spectrum of NaAC shows three absorption bands centralized at 1618 , 3337 , 3042 and 3654 cm^{-1} which may be attributed to the aromatic ring vibrations, O-H stretching in solvation water, ring C-H stretching and stretching of O-H bond in residual NaOH [108], respectively. In the Na_2BDC spectrum, the ring C-C stretching is coupling with the COO^- antisymmetric vibration mode and the ring C-H appears as a low-intensity band centered at 3068 cm^{-1} . Upon coordination to the trivalent Ln resulting in the compounds Ln-BDC and Ln-AC , the antisymmetric and symmetric bands of the COO^- red-shifts and blue-shifts, respectively to 1536 and 1396 cm^{-1} ($\nu_a - \nu_s = 140\text{ cm}^{-1}$) for Ln-BDC and both red-shifts to 1528 and 1308 cm^{-1} respectively ($\nu_a - \nu_s = 220\text{ cm}^{-1}$) for Ln-AC . By using a series of acetate salts, Deacon and Phillips [109], have examined the structures and vibrational frequencies observed for a number of carboxylate salts in the solid-state and have found an empirical rule for the correlation between the frequency separation between the COO^- antisymmetric and symmetric stretching ($\nu_a - \nu_s$) and the Kinds of coordination of the COO^- group to a metal cation. The rule is expressed as: ($\nu_a - \nu_s$) for unidentate $>$ ($\nu_a - \nu_s$) for ionic \sim ($\nu_a - \nu_s$) for bridging $>$ ($\nu_a - \nu_s$) for bidentate. Thus, based on the values of ($\nu_a - \nu_s$) obtained of the salts and the compounds, one may conclude that both ligands coordinate the trivalent ions mainly as a bidentate mode. The spectra exhibit the broad band assigned to O-H stretching vibrations of coordinated and uncoordinated water molecules centered at around 3440 cm^{-1} and indicate that compounds obtained from

H₂DC contain more water molecules in their structures. The absorption bands centered 447 cm⁻¹ for Ln-BDC and 425 cm⁻¹ for Ln-AC may be attributed to Ln-O stretching. The presence of these bands indicates a strong interaction between Ln and the carboxylate groups. The spectrum of Eu-AC-BDC is identical to the spectrum of Eu-AC probably due to the fact that HAC was used in higher quantity.

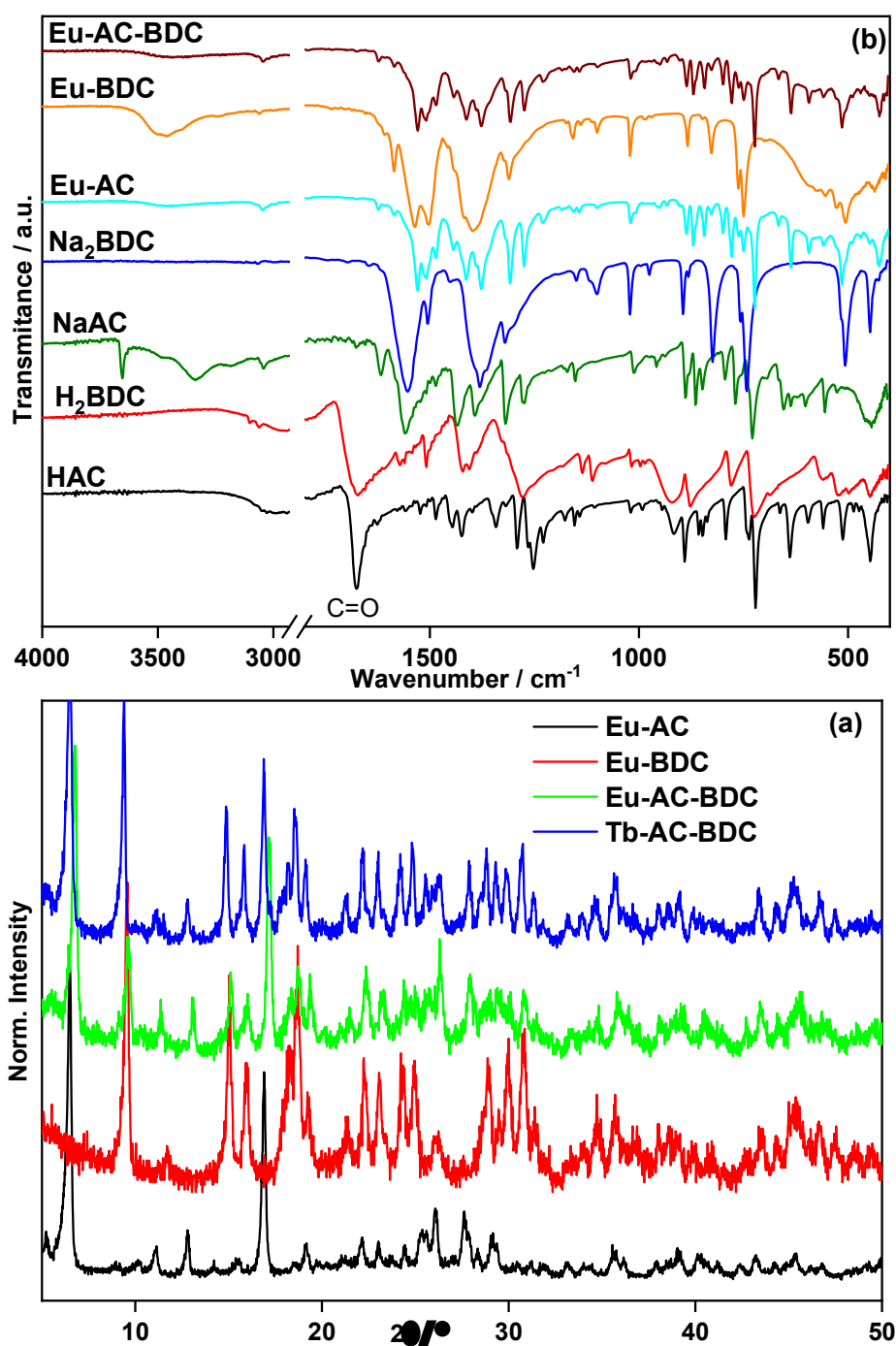


Fig. 24: (a) Powder XRD diffraction patterns of Eu-AC, Eu-BDC, Eu-AC-BDC and Tb-AC-BDC (b) FT-IR spectra of the free ligand HAC, H₂BDC, the salts NaAC, Na₂BDC and the compounds Eu-AC, Eu-BDC and Eu-AC-BDC.

4.5.2. Thermal stability

As the P-XRD patterns confirm that the compounds containing one ligand or the mixing of both are isomorphous one to each other respectively, the thermal degradation profile and the thermal differential analysis curves were performed only for Eu-AC, Eu-BDC and Eu-AC-BDC in synthetic air atmosphere from ambient temperature (ca. 30 °C) to 740 °C. The TG and DTA curves are shown in Fig. 25. The thermogram profile of Eu-AC indicates good thermal stability up to 350 °C. Its DTA curves show no endothermic peak that should be assigned to coordinated water molecules suggesting $\text{Ln}(\text{AC})_3$ as the molecular formula for the compounds represented by Ln-AC. The decomposition of the complex occurs in one thermal event, observed by the one exothermic peak centered at 425 °C in the DTA curve (A 31), resulting in a plateau corresponding to the formation of Eu_2O_3 . The agreement between the found value (22 %) and the expected (22%) confirms the purity of the compounds.

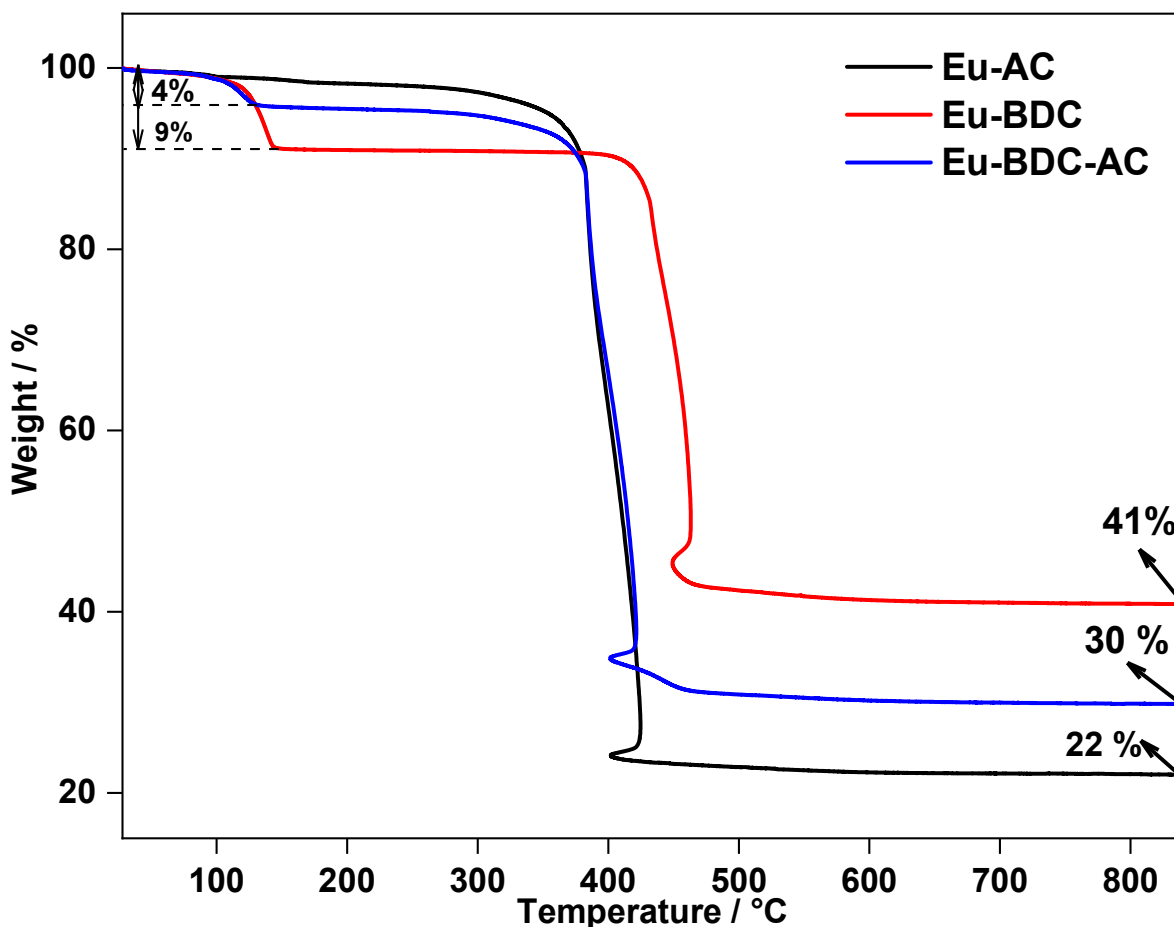


Fig. 25: Thermogravimetric curves of Eu-AC, Eu-BDC, and Eu-AC-BDC

The TG of Eu-DBC is characterized by a plateau up to 110 °C where starts a mass loss of 8.7 % until 142 °C accompanied by an exothermal event (appendix A 31) corresponding to 4 coordinated molecules. The resulting anhydrous structure is thermally stable until 410 °C where begins the degradation of the ligand. The complete collapse happens 463 °C resulting in Eu_2O_3 as residue. The expected value (41 %) matches the found experimentally (41 %) (appendix A 31). Thus, the molecular formula of the compounds Ln-DBC was determined to be $\text{Ln}_2(\text{BDC})_3(\text{H}_2\text{O})_4$. The loss weight and the final residue in the Eu-AC-BDC's thermogram show values intermediary compared to the ones obtained on the thermograms of Eu-AC and Eu-BDC. The bound water molecules correspond to 4.3 % (half of the value (8.7 %) in Eu-BDC) of the molecular weight and the final residue corresponds to 30 % which is in good agreement to the mean (31.9 %) of final residues found for Eu-AC and Eu-BDC. Such results confirm the ligand ratio used in the synthesis. The residue calculated based on the formula $\text{Eu}_2(\text{AC})_3(\text{BDC})_{1.5}(\text{H}_2\text{O})_3$ was 28%. The temperature drop at the end of the ligand decomposition indicates that the thermal decomposition occurred in high speed and involves a high quantity of heat.

4.6. Characterization of the compounds based on H_2BDC and Hacac

4.6.1. P-XRD and FT-IR spectroscopy studies

The X-ray powder diffraction patterns of the compounds represented by $\text{Tb}_x\text{Eu}_{1-x}(\text{acac})_x(\text{BDC})_{1.5-x/2}$ are displayed in Fig. 26a together with the P-XRD pattern of Tb-BDC by effect comparison. They indicate that, except for $x = 0.95$, the compounds are isostructural with each other and with Tb-BDC. It is important to note the decrease in crystallinity with increasing of acac⁻ fraction. The vibrational spectra in the infrared range were recorded and compared to the infrared spectra of Eu-BDC and $\text{Tb}(\text{acac})_3(\text{H}_2\text{O})_2$. As can be seen in Fig. 26b, the spectra show no vibrational bands which should be assigned to the acac ligand. Such observation may be due to the low acac / BDC mass ratio which varies between 0.4 and 0.6 for $x = 0.75$ and 0.99 respectively.

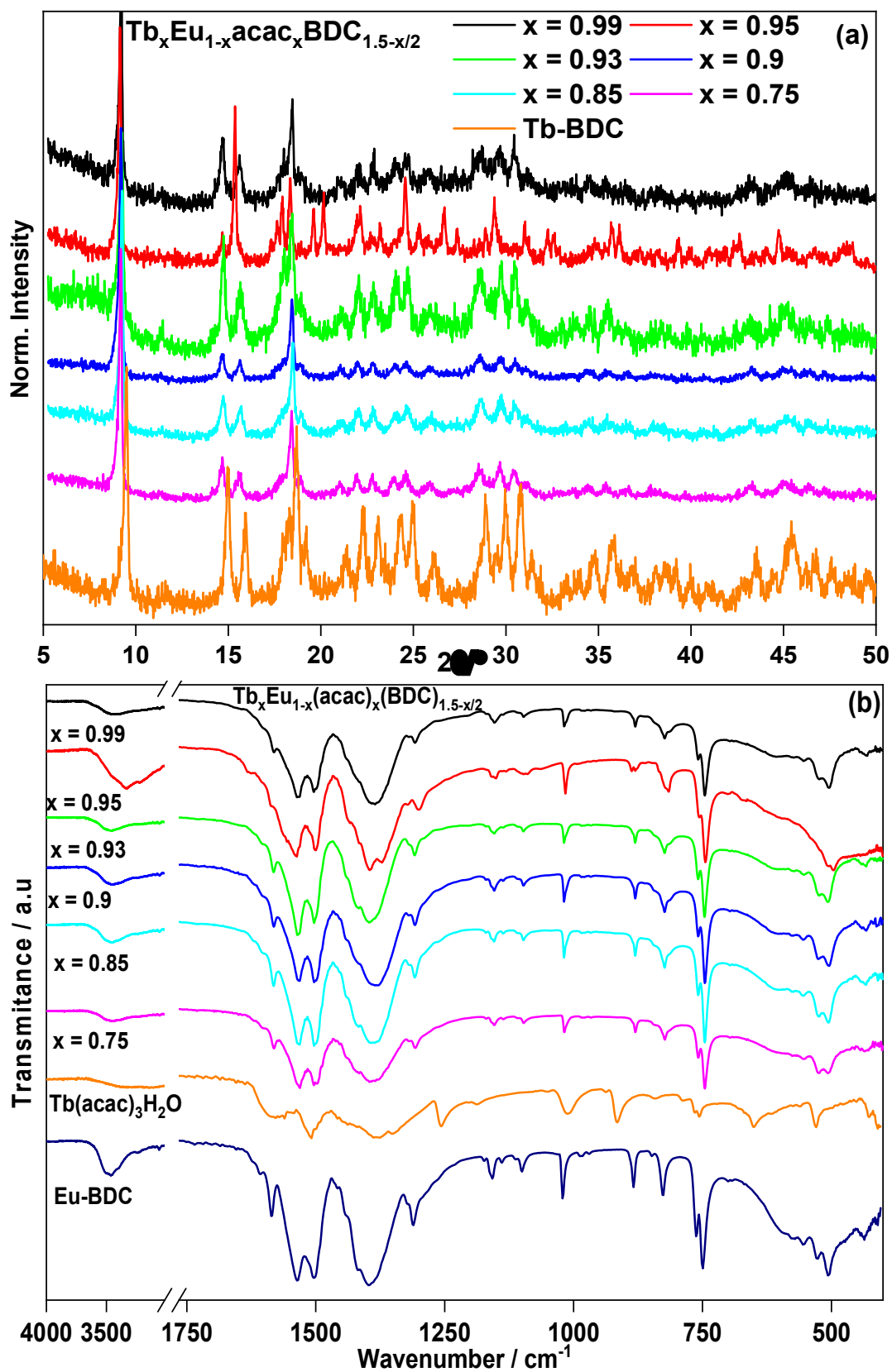


Fig. 26: P-XRD patterns (a) and FT-IR spectra (b) of the compounds represented by $\text{Tb}_x\text{Eu}_{1-x}\text{acac}_x\text{BDC}_{1.5-x/2}$ ($x = 0.99, 0.95, 0.93, 0.9, 0.85$ and 0.75).

4.6.2. Thermal stability

The thermogravimetric analysis was performed in the temperature range 30-1200 °C under nitrogen atmosphere for the compounds where ($x = 0.99, 0.95, 0.93$ and 0.9). It is clear from the thermograms that the compounds undergo a mass loss of about 6-8% in the first step (100-140 °C) corresponding to the elimination of free and coordinated water molecules. After a slow mass loss up to 400 °C, the anhydrous structures start collapsing to achieve the T_{peaks} around 450 °C resulting in a plateau corresponding to ca 50 % of the initial mass value. This value is in perfect agreement with the formation of lanthanide oxycarbonate ($\text{Ln}_2\text{O}(\text{CO}_3)_2$) as final residue.

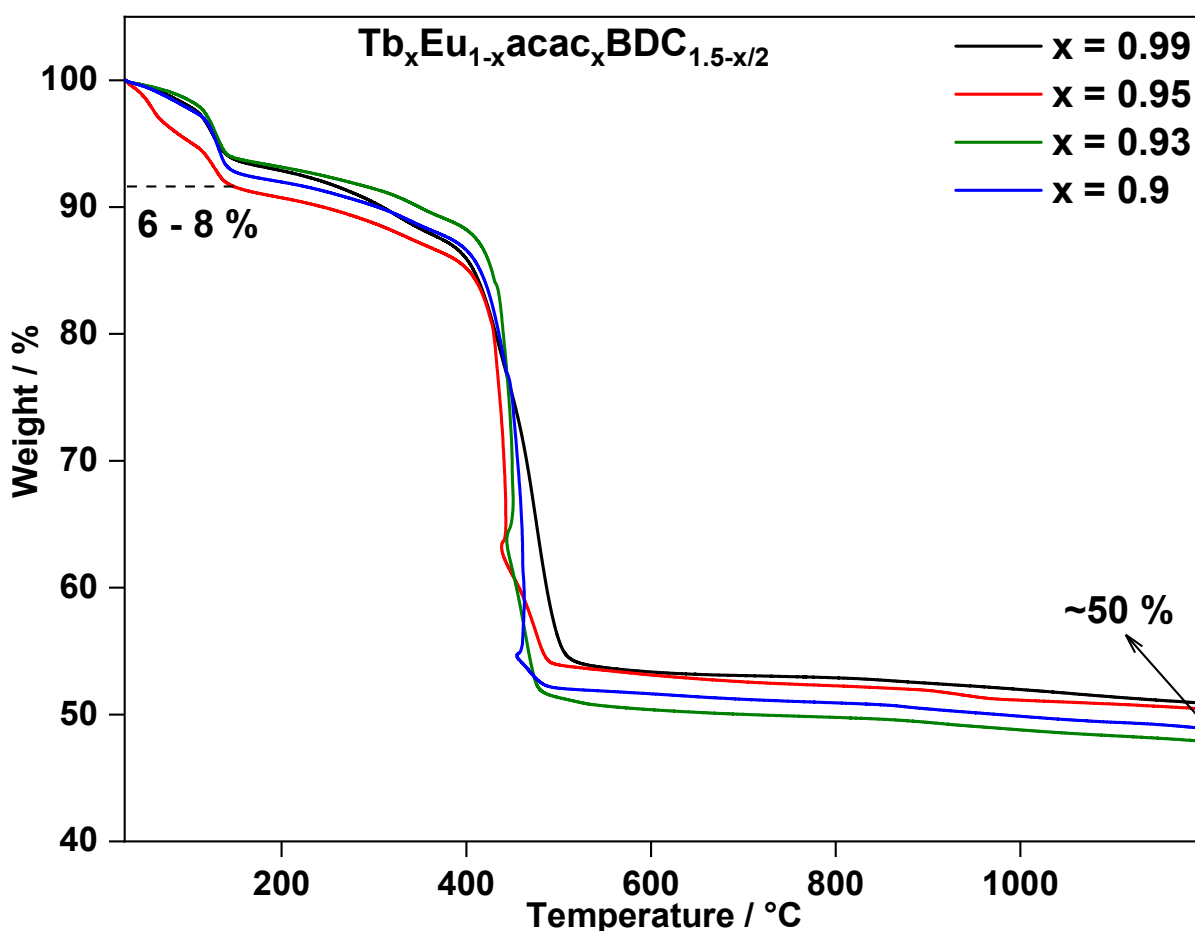


Fig. 27: Thermograms of the compounds represented by $\text{Tb}_x\text{Eu}_{1-x}(\text{acac})_x(\text{BDC})_{1.5-x/2}$ ($x = 0.99, 0.95, 0.93$ and 0.9).

4.6.3. Electronic properties: Diffuse reflectance UV-vis spectroscopy

As shown in Fig. 28, the solid-state UV-vis absorption spectra of the free ligands H_3TCPMB , H_6TDCPMB , H_2BDC and the salts Naacac and Na_2BDC were measured and compared to the spectra of the as-synthesized compounds. All spectra are

characterized by a broad band assigned to singlet-singlet electronic transitions. For H₃TCPMB and H₆TDCPMB, the Gd^{III} coordination results in a slight blue shift of the maxima and a narrowing of the absorption band which can be ascribed to the perturbation induced by the metal ion [110]. Due to their emission following the ligand absorption in the UV range, the spectra of the compound containing Eu^{III} or Tb^{III} show a different profile compared to those containing Gd^{III} ions.

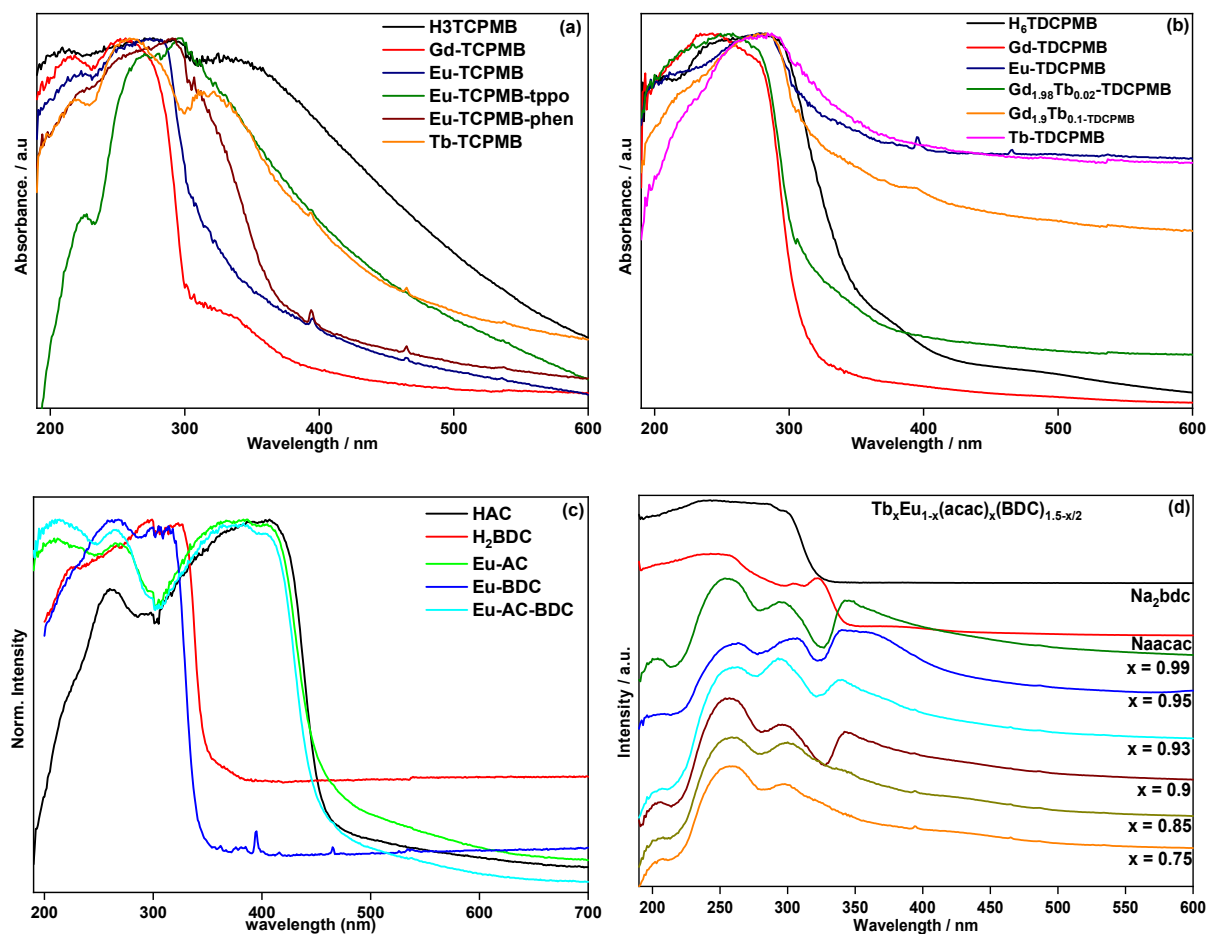


Fig. 28: Representative UV-vis DRS spectra of the compounds synthesized from the ligands H₃TCPMB (a), H₆TDCPMB (b), HAC & H₂BDC (c) and Hacac & H₂BDC (d).

Despite it was proven by P-XRD spectroscopy and thermal analysis that the compound Eu-AC-BDC contains the linker BDC²⁻, its absorption spectrum is quite similar to the absorption spectrum of Eu-AC, thus in agreement with the result obtained in the infrared spectroscopy. Comparing the spectra of the salts Naacac, Na₂BDC to the spectra of the compounds represented by Tb_xEu_{1-x}(acac)_x(BDC)_{1.5-x/2}, it is clear that the absorption band at 340 nm is assigned to the acac⁻ part once its intensity decreases progressively as the fraction of acac⁻ decreases from 0.99 to 0.75.

4.7. Solid-state photophysical properties

4.7.1. Compounds based on the ligand H₃TCPMB

4.7.1.1. Triplet state of H₃TCPMB

As mentioned in the introduction, in lanthanide complexes, the indirect excitation (called sensitization or antennae effect) of the active ion occurs from an energy migration following the ligand centered absorption, mainly, by a singlet to triplet intersystem crossing ($^1S^* \rightarrow ^3T^*$) and finally the triplet to lanthanide energy transfer ($^3T^* \rightarrow Ln^{III}$). The efficiency of this complex energy transfer process involves numerous rate constants and is highly dependent on the energy gap between the lowest ligand triplet state and the Ln^{III} emitting level [111]. In the cases of Eu^{III} and Tb^{III} respectively, the triplet ligand state should be localized sufficiently above the 5D_0 (17,290 cm^{-1}) and 5D_4 (20,500 cm^{-1}) levels, respectively, allowing efficient energy transfer and preventing quenching via the back-energy transfer. Therefore, it becomes an important issue to determine the triplet state energy of the ligand, which can be calculated by referring to the lower wavelength emission edge of the corresponding phosphorescence spectrum obtained at low temperature of the Gd^{III} equivalent compound [42]. When coordinated to the Gd^{III} , the ligand phosphorescence is facilitated by both paramagnetic and heavy-atom effects improving the intersystem crossing from the singlet to the triplet excited state [112] and the absence of energy transfer from the ligand to Gd^{III} ion which has the first excited level ($^6P_{7/2}$) at 32,200 cm^{-1} , thus above the first triplet energy level of all organic ligands [113–115]. Therefore, energy transfer from ligands to the Gd^{III} ion not occurring, photoluminescence of Gd^{III} complexes involving ligands with aromatic rings is due to electronic transitions between perturbed ligand localized states [116]. Furthermore, the cryogenic temperature enhances the phosphorescence emission, which is often weak at room temperature due to thermal and solvent quenching. Fig. 29a shows the excitation and emission spectra of the free ligand H₃TCPMB and the compound Gd-TCPMB collected at 77 K. The emission spectrum of the free ligand shows the phosphorescence represented by three vibrionic bands at 405, 440 and 470 nm but is dominated by the fluorescence band with the maximum at 338 nm (29,586 cm^{-1}) owing to the $^1S \rightarrow ^1S_0$ electronic transitions. The assignments of these bands were based on the photoluminescence spectra of La-TCPMB shown in Fig. 30a and

b, which also shows that the relative intensities of the singlet and triplet states are temperature dependent. Upon excitation at 270 nm and 295 K, the emission band owing from the second singlet is more intense than the triplet state emission (Fig. 30a). Lowering the temperature down to 77 K, the triplet band becomes more intense relatively (Fig. 30b). With a delay of 0.05 ms, the two bands at 300 and 354 nm disappeared indicating that they are owing to allowed singlet to singlet electronic transitions. The more intense phosphorescence regarding the fluorescence can be attributed to the heavy atom effect [117]. After complexation to the Gd^{III} , the fluorescence band is completely attenuated and the vibronic bands are not well defined probably due to the paramagnetic effect which, from the strong interaction between the ligand π -electrons inner 4f electrons of Gd^{III} ion, mixes the triplet and singlet states improving the internal conversion and the intersystem crossing [118]. By the spin-orbit coupling interaction, the triplet state acquires a partially singlet character and the selection rules are relaxed [31].

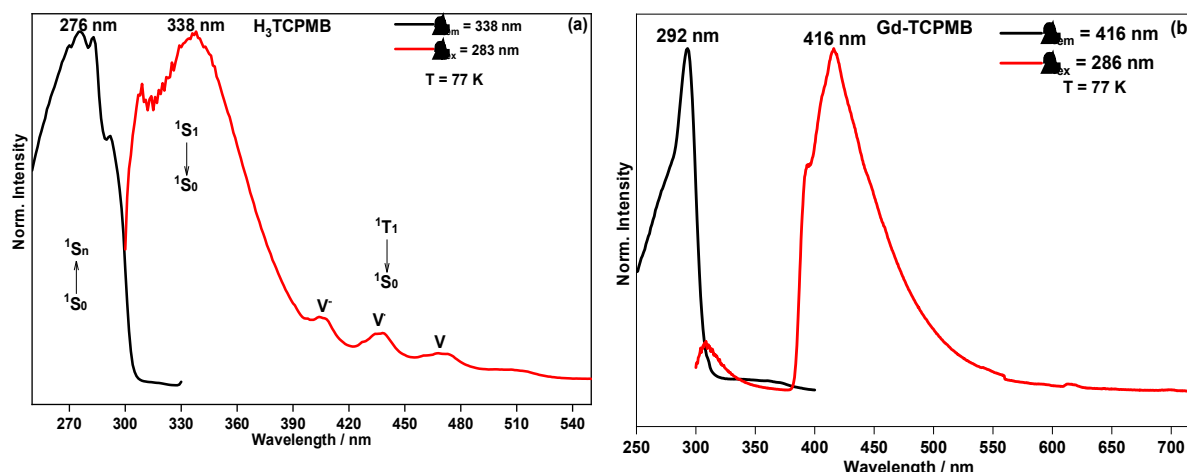


Fig. 29: (a) Excitation (dark) and emission (red) spectra of the free ligand H_3TCPMB at 77 K monitored at $\lambda_{em} = 338$ nm and $\lambda_{ex} = 283$ nm respectively. (b) Excitation (dark) and emission (red) spectra of $Gd-TCPMB$ at 77 K monitored at $\lambda_{em} = 416$ nm and $\lambda_{ex} = 286$ nm respectively.

By assuming the shortest phosphorescence band wavelength to be the 0-0 phonon transition, the triplet state energy was estimated to $26,316\text{ cm}^{-1}$, therefore $9,052$ and $5,816\text{ cm}^{-1}$ above the emitting states of Eu^{III} (5D_0) and Tb^{III} (5D_4), respectively. These results suggest that the ligand may sensitize luminescence of both active ions but is more suitable for the Tb^{III} ion. According to the general antennae effect principle, the ligand to metal energy transfer efficiency depends directly on the energy difference

between the lowest triplet state energy of ligands and the resonant emissive of the optically active ion [119].

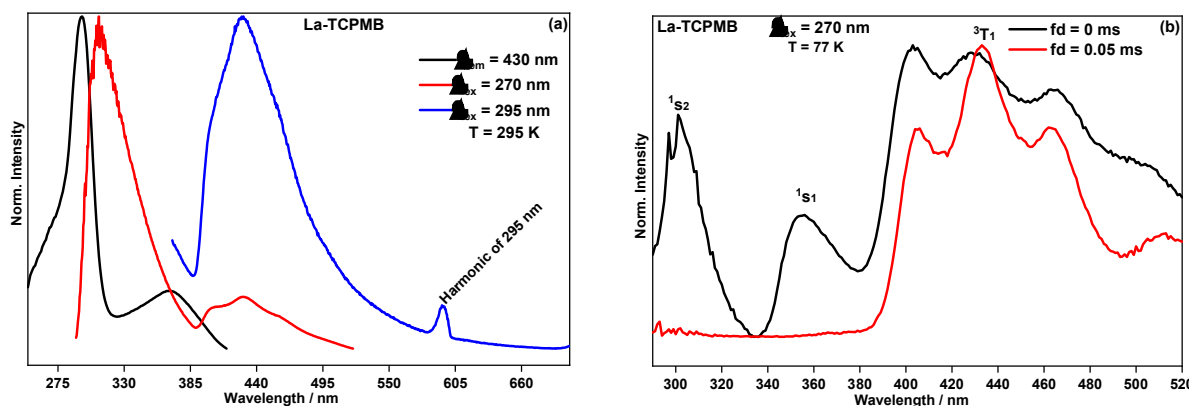


Fig. 30: (a) Photoluminescence study of La-TCPMB at 295 K. Excitation spectrum monitored at $\lambda_{em} = 430$ nm (dark) and emission spectra monitored at $\lambda_{ex} = 270$ nm (red) and at $\lambda_{ex} = 295$ nm (blue). (b) Prompted and delayed emission of La-TCPMB upon excitation at $\lambda_{ex} = 270$ nm and $T = 77$ K.

4.7.1.2. Photoluminescent properties of the compounds containing the optically active ions

The solid-state photophysical properties (excitation and emission spectra and emission lifetime) of the compounds Eu-TCPMB and Tb-TCPMB and Tb_{0.95}Eu_{0.05}-TCPMB were investigated at 77, 110 and 300 K. The photoluminescence of La_{0.95}Eu_{0.05}-TCPMB was also studied by comparison effect. For Eu-TCPMB, the excitation spectra monitored at 616 nm collected at the temperatures of 77 K, 110 K and 300 K (Fig. 31a) exhibit a broad band between 250 and 380 nm attributed to $\pi^* \leftarrow \pi$ transitions of the TCPMB³⁻ trianion [120] indicating that energy transfer occurs from the ligand to the Eu^{III} ions. Apart from this broad band, a series of narrow lines in the longer wavelength region (350 nm to 600 nm) owing to intra-configurational electronic transitions between ⁷F₀ and ⁵L₆ electronic states at 393 nm and transitions between ⁷F_{0,1} and ⁵D_{2,1} electronic state level were also observed. The detection of these intra-configurational bands evidences the poor efficiency of the energy transfer between the ligand and the Eu^{III} ions. Unexpectedly, the intra-configurational transition becomes more intense at room temperature regarding the ligand excitation band. This result suggests an increase of possible deactivation mechanisms of the singlet state at the expense of the intersystem crossing process or an intensification of the vibronic transitions.

The emission spectra of Eu-TCPMB at the three temperatures recorded under ligand and intra-configurational excitation at 290 and 393nm, respectively show the typical Eu^{III} red emission as narrow and well-separated emission bands centered at ~579, 592, 616, 651, and 700 nm, corresponding to electronic transitions from the Eu^{III} centered ⁵D₀ excited state to the ⁷F_J (J = 0–4) ground state multiplet with the hypersensitive ⁵D₀ → ⁷F₂ transition dominating the spectra, thus in agreement with the fact that the Eu^{III} are localized in site with no inversion center. The intensity ratio of 8.32 between the ⁵D₀ → ⁷F₂ forced electric dipole and symmetry sensitive and the ⁵D₀ → ⁷F₁ magnetic dipole allowed transitions is in good agreement with the symmetry of the field around the Europium ion [121,122]. When excited in the intra-configurational band at 393 nm, the ⁵D₀ → ⁷F₁ and ⁵D₀ → ⁷F₂ transitions split into four and seven Stark components respectively (Fig. 31e). The resolved emission band attributed to ⁵D₀ → ⁷F₀ transition remains as an asymmetric and relatively broad one-component band (Fig. 31f) and a different profile of the emission band attributed to ⁵D₀ → ⁷F₄ transition is observed when it is compared to the emission spectrum obtained upon excitation at 290 nm. Such a result probably is an indication that the obtained emission profile upon the intra-configurational excitation may be assigned to the crystal disorder owing from the two different spatial orientations of the coordinated DMF molecules. Such special orientation probably leads to slight differences around the Eu^{III} sites probably due to small distortions and variations in the Eu-O bond lengths (Table 2).

In order to confirm this premise, we tried to substitute the solvent molecules by triphenyl oxide (tppo) or phenanthroline (phen) ligands synthesizing the compounds namely Eu-TCPMB-tppo and Eu-TCPMB-phen. The angle O_D-Eu-O_w of 79.64° is sufficiently large to allow the coordination of the auxiliary ligands. Unfortunately, these syntheses did not result in crystalline compounds. However, the photoluminescence study performed at 293 K gave a few hints. The absence of the narrow band at 317 nm due to its overlapping by the broad excitation part assigned to tppo, indicate the coordination of the auxiliary ligand to Eu^{III}. For Eu-TCPMB-phen, the intra-configurational transition bands are very weak regarding the indirect excitation proving that *phen* is better than *tppo* in the sensitization of Eu^{III} luminescence. Furthermore, Eu-TCPMB and Eu-TCPMB-tppo show a similar excitation profile at 293 K regarding the intensity ratio between the ligand excitation and intra-configuration band at 393 nm.

This fact suggests that the geometry of the Eu^{III} environment did not change with the substitution of the solvent molecules.

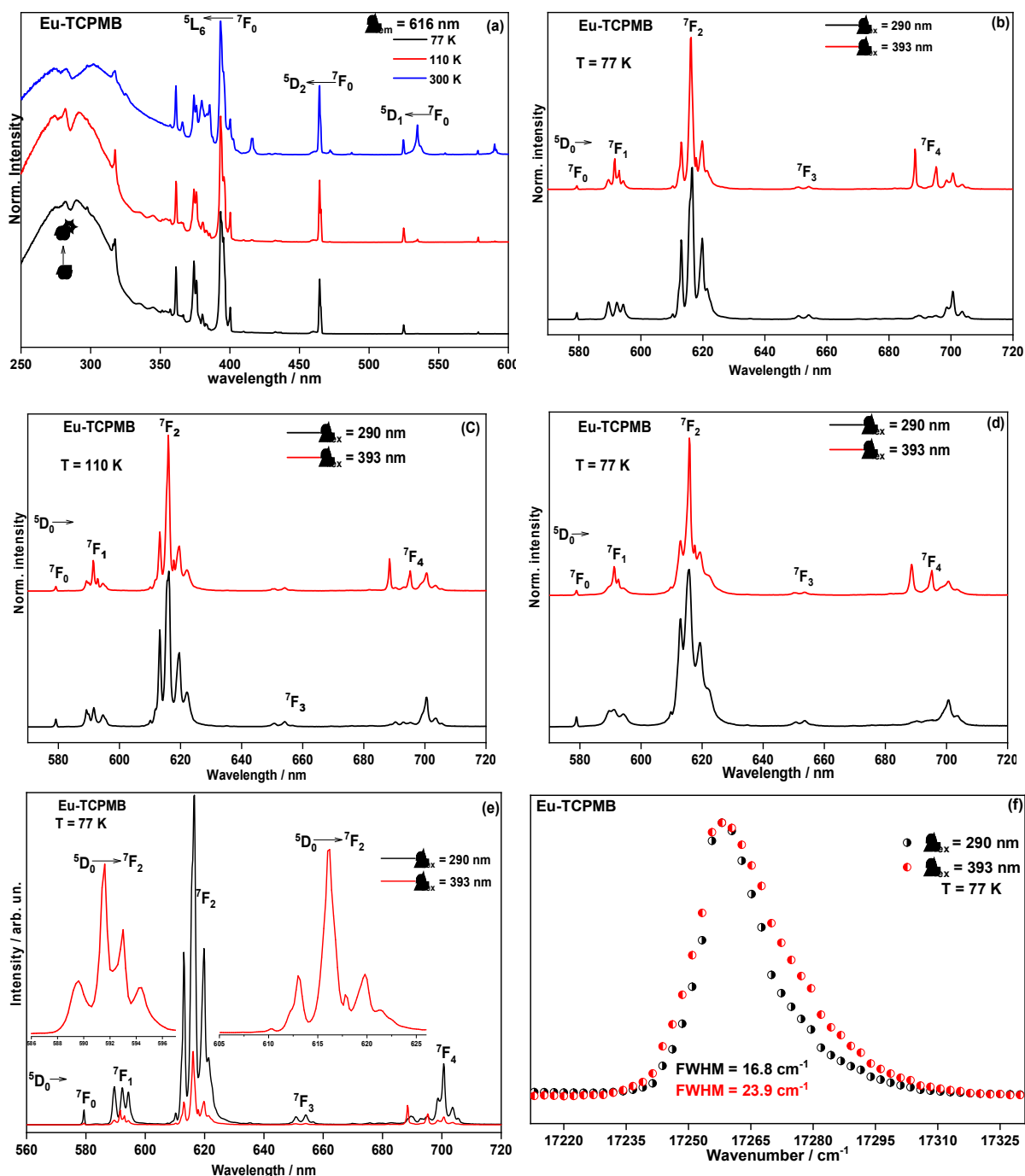


Fig. 31: Normalized excitation spectra obtained at 77 K (dark), 110 K (red) and 300 K (blue) of Eu-TCPMB monitoring at 616 nm (a). Normalized emission spectra of Eu-TCPMB upon excitation at 290 nm (dark) and at 393 nm (red) collected at 77 K (b), 110 K (c) and 300 K (d). Emission spectra of Eu-TCPMB at 77 upon excitation at 290 nm and 393 nm. The Insets show the $^5\text{D}_0 \rightarrow ^7\text{F}_1$ and $^5\text{D}_0 \rightarrow ^7\text{F}_2$ regions magnified (e). High-resolution $^5\text{D}_0 \rightarrow ^7\text{F}_0$ emission band of the Eu-TCPMB coordination network obtained at 77 K upon excitation at 290 and 393 nm (f).

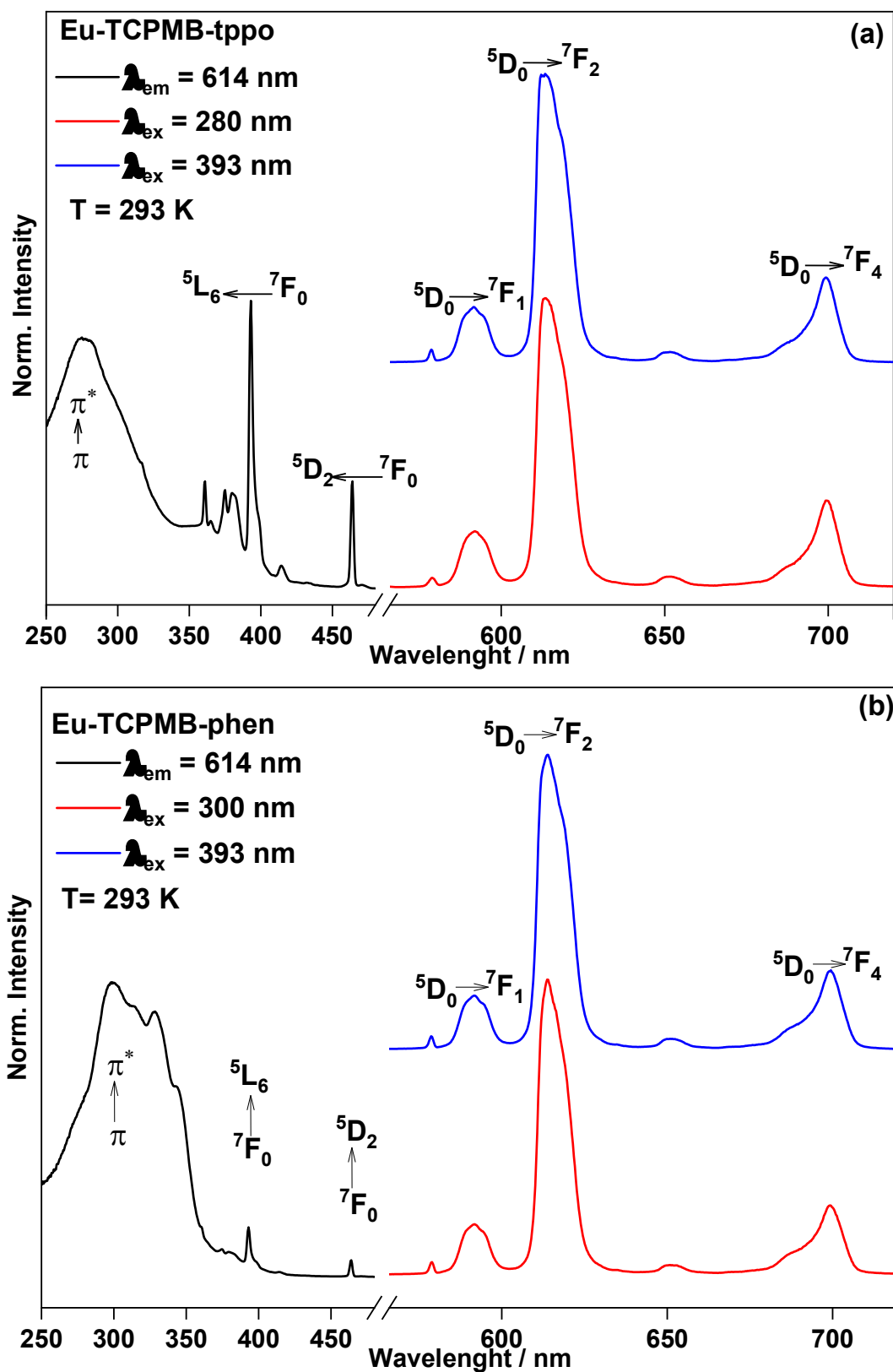


Fig. 32: Normalized excitation and emission spectra monitored at 614 nm and at 280 nm respectively of Eu-TCPMB-tpo (a) and at 614 nm and 300 nm of Eu-TCPMB-phen (b) collected at ca. 293 K

In the case of Tb-TCPMB, the ligand excitation band extend only to 310 nm and enlarges slightly when collected at 300 K (Fig. 33a). The emission spectra, upon excitation at 280 nm are characterized by the Tb^{III} emission bands centered at 489, 542, 586 and 622 nm assigned to the transitions between 5D_4 and 7F_J ($J=6, 5, 4, 3$) states, respectively.

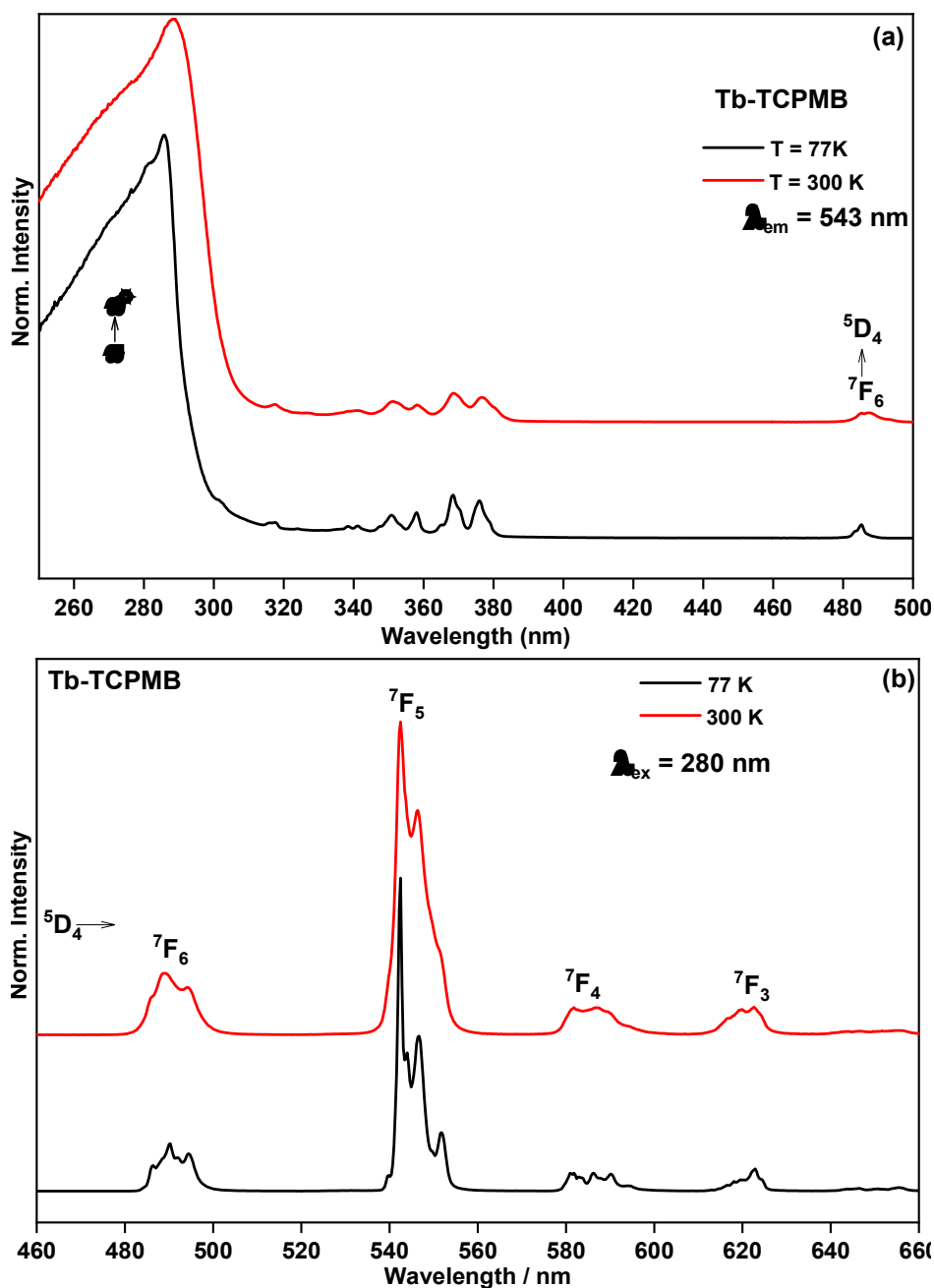


Fig. 33: Normalized excitation (a) and emission (b) spectra of Tb-TCPMB monitored at 543 nm and 280 nm respectively and collected at 77 K (dark) and at 300 K (red).

As evidenced from its photoluminescence spectra presented in Fig. 34a and b, excitation spectra of the mixed Ln^{III} compound Tb_{0.95}Eu_{0.05}-TCPMB monitored both Tb^{III} and Eu^{III} emission show the same profile of Tb-TCPMB. Monitoring at 616 nm, the excitation spectra show the weak narrow band at 488 nm assigned to Tb^{III}, indicating thus, a Tb^{III} → Eu^{III} energy transfer. As expected, the emission spectra show simultaneously the bands assigned to 4f-4f electronic transitions of both Eu^{III} and Tb^{III}.

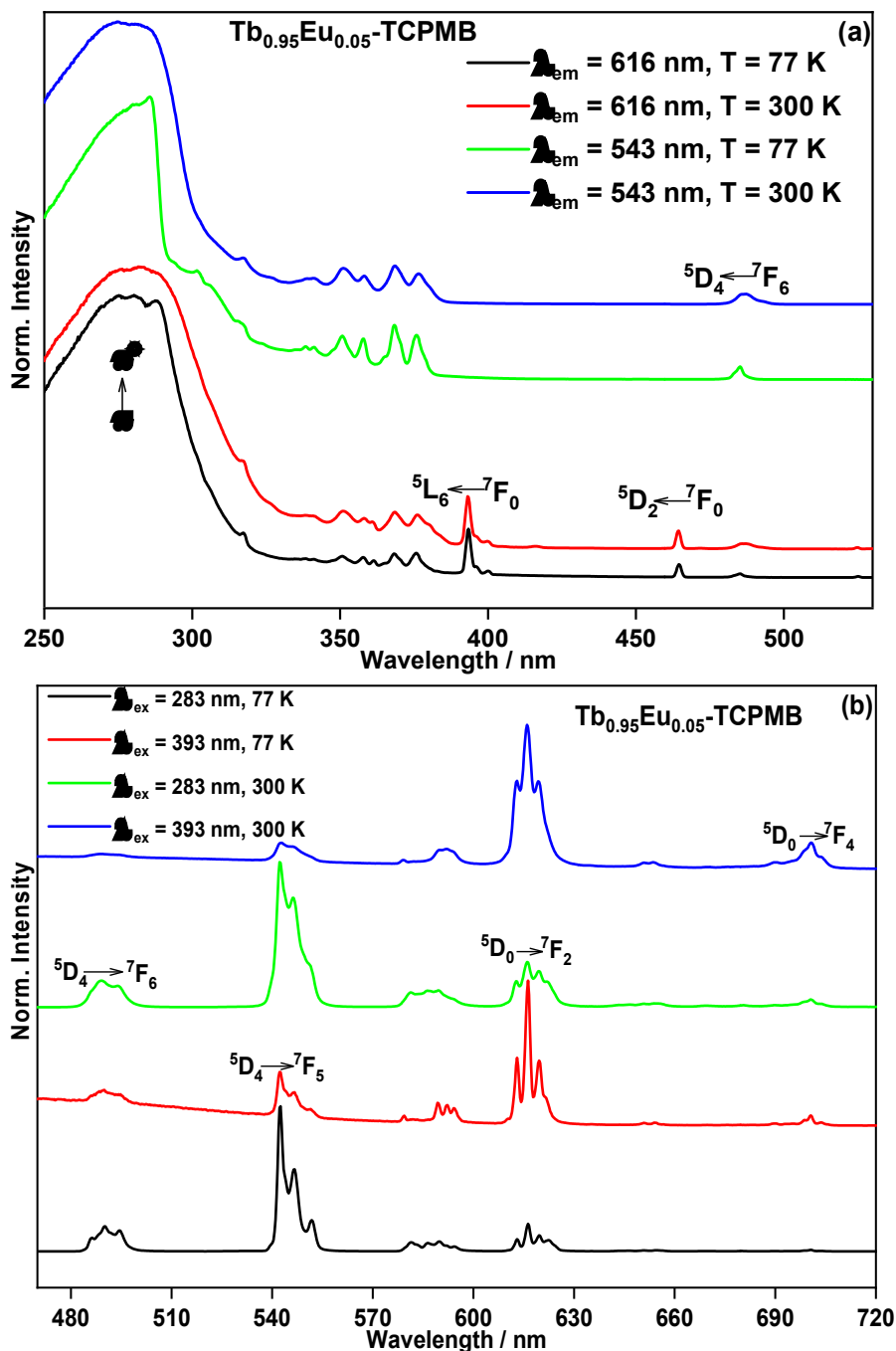


Fig. 34: (a) Normalized excitation of Tb_{0.95}Eu_{0.05}-TCPMB monitored at 616 nm and 543 nm at the temperatures of 77 K and 300 K. (b) normalized emission spectra of Tb_{0.95}Eu_{0.05}-TCPMB excited at 283 nm and at 393 nm at the temperatures of 77 K and 300 K.

The photoluminescence decay curves were collected at the three different temperatures by monitoring the respective strongest emission of both Eu^{III} ($^5\text{D}_0 \rightarrow ^7\text{F}_2$) and Tb^{III} ($^5\text{D}_4 \rightarrow ^7\text{F}_5$) ions. The corresponding curves for Eu-TCPMB upon excitation at 290 nm and 393 nm and for Tb-TCPMB excited at 280 nm are given in Fig. 35. The emission lifetime values, depicted in Fig. 38, were obtained by fitting the decay curves with mono-exponential decay functions, indicating that even with the slight differences in symmetry around the ions due to the crystal disorder, on average the emitting states contribute with just one emission lifetime value. This result is corroborated with the $^5\text{D}_0 \rightarrow ^7\text{F}_0$ band shape obtained at 77 K (Fig. 31f). A similar result was also obtained by Monteiro and co-authors [123]. The observed emission lifetime of Eu-TCPMB and Tb-TCPMB obtained in three different temperatures upon excitation in the broad and also at 393 nm for Eu-TCPMB remain practically invariable in the temperature range of 77–300 K, indicating a rigid stacking of the crystal lattice opening a possibility to prepare NIR emitting network, by changing Tb^{III} and Eu^{III} to Yb^{III} , Er^{III} , or Nd^{III} , for biological applications and upconversion study. A similar result was obtained by Richard and collaborators studying the optical properties Tb^{III} and Eu^{III} containing MOFs constructed from the ligand 3,5-disulfobenzoate anion (DSB) [55]. The slight variations of the emission lifetime values as the temperature increases may probably related to the fact that the efficiency of the ligand to metal energy transfer process improves with temperature increase as shown by the emission spectra of Gd-TCPMB collected at 77 and 300 K (A 33). When collected at 77 K, the spectrum shows only the broad band assigned to the ligand owing from the radiative decay of the triplet state. At 300 K, the ligand emission is completely attenuated, and narrow emission bands attributed to both Tb^{III} and Eu^{III} were observed due to the presence of Eu^{III} and Tb^{III} as impurities in the compound. As can be seen in Table 4, for Eu-TCPMB, the lifetime values obtained exciting at 393 nm are slightly higher than obtained upon excitation in the ligand broad band at 290 nm. The same effect which may be an indication of an increase in the radiative decay rate upon $^5\text{L}_6 \leftarrow ^7\text{F}_0$ intra-configurational excitation was observed for a Europium coordination framework based on the terephthalic acid [124].

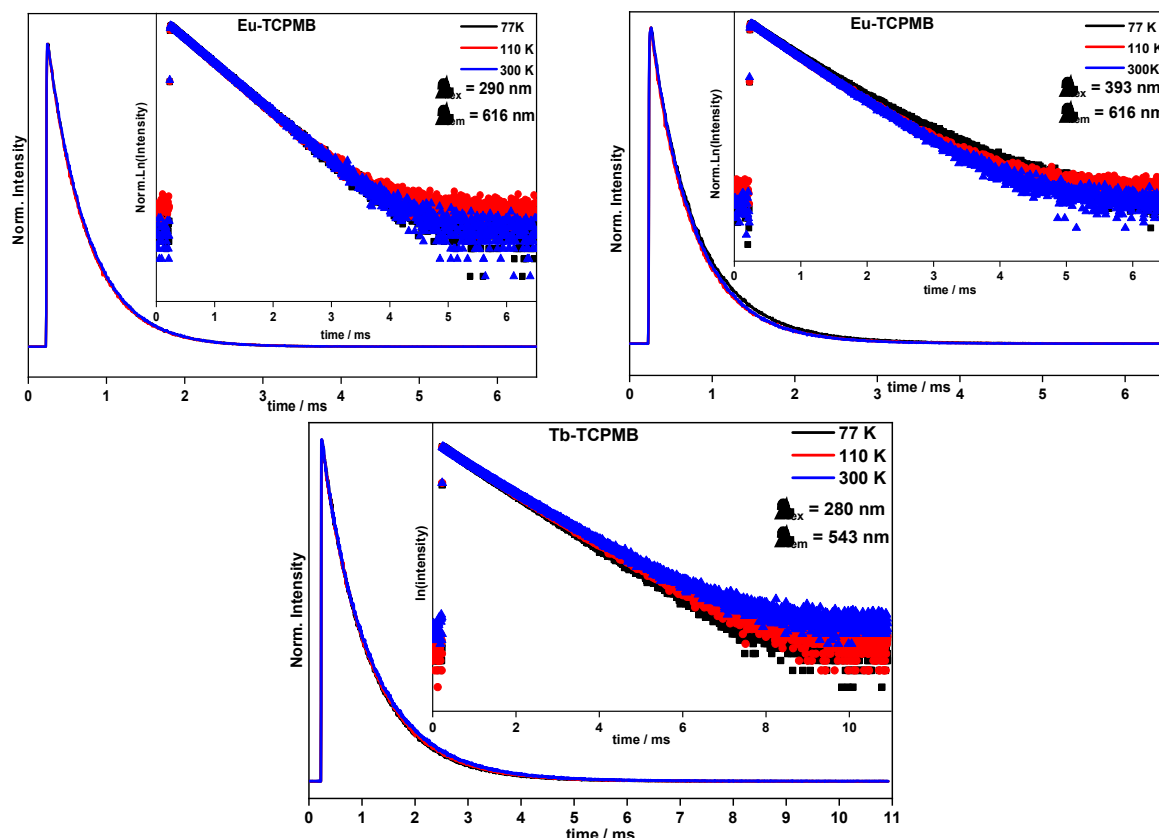


Fig. 35: Luminescence decay curves of Eu-TCPMB and Tb-TCPMB monitored at 616 nm and 543 nm respectively upon excitation at 290 nm and 393 nm for Eu-TCPMB and at 280 nm for Tb-TCPMB at the temperatures of 77K, 110 K and 300 K.

Table 4: Observed emission-lifetime values of the compounds prepared from ligand H₃TCPMB

			77 K	110 K	300 K
	$\lambda_{\text{ex}}/\text{nm}$	$\lambda_{\text{em}}/\text{nm}$	τ/ms	τ/ms	τ/ms
Eu-TCPMB	290	616	0.507 ± 0.001	0.505 ± 0.002	0.514 ± 0.001
Eu-TCPMB	393	616	0.560 ± 0.004	0.526 ± 0.001	0.530 ± 0.001
Tb-TCPMB	280	543	0.888 ± 0.004	0.907 ± 0.001	0.982 ± 0.008
Eu-TCPMB-tpo	393	616	0.602 ± 0.000	0.577 ± 0.001	0.500 ± 0.001
Eu-TCPMB-tpo	290	616	0.616 ± 0.000	0.611 ± 0.001	0.487 ± 0.000
Eu-TCPMB-phen	393	616	0.801 ± 0.000	0.802 ± 0.000	0.662 ± 0.000
Eu-TCPMB-phen	290	616	0.760 ± 0.000	0.774 ± 0.000	0.690 ± 0.000
Tb _{0.95} Eu _{0.05} -TCPMB	283	543	0.260 ± 0.004	0.220 ± 0.003	0.180 ± 0.003
			&	&	&
			0.910 ± 0.002	0.901 ± 0.002	0.890 ± 0.001
Tb _{0.95} Eu _{0.05} -TCPMB	283	700	1.62 ± 0.001	1.58 ± 0.001	1.51 ± 0.001

The emission decay curves of Eu-TCPMB-*tpo* and Eu-TCPMB-*phen*, collected at the same temperatures, are presented in Fig. 36 and 37. They are single exponential decays and as can be seen in Table 4, the luminescence lifetime values are longer than for Eu-TCPMB. Such a fact can be seen as an additional evidence of substitution of the solvent molecules in Eu-TCPMB by *tpo* or *phen* ligand. Water molecules in the first coordination sphere of Eu^{III} provide an efficient route for radiationless deactivation of the excited states [125]. Assuming that the reduction in Tb^{III} emission lifetime is due only to the presence of Eu^{III} ions, the efficiency of the Tb^{III} to Eu^{III} energy transfer process (η_{ET}) may be estimated to 71%, 76% and 80% at 77 K, 110 K, and 300 K respectively using the equation $\eta_{ET} = 1 - \tau_1/\tau_0$ where τ_0 and τ_1 are the Tb^{III} luminescence lifetimes in the absence and presence, respectively, of Eu^{III} ions.

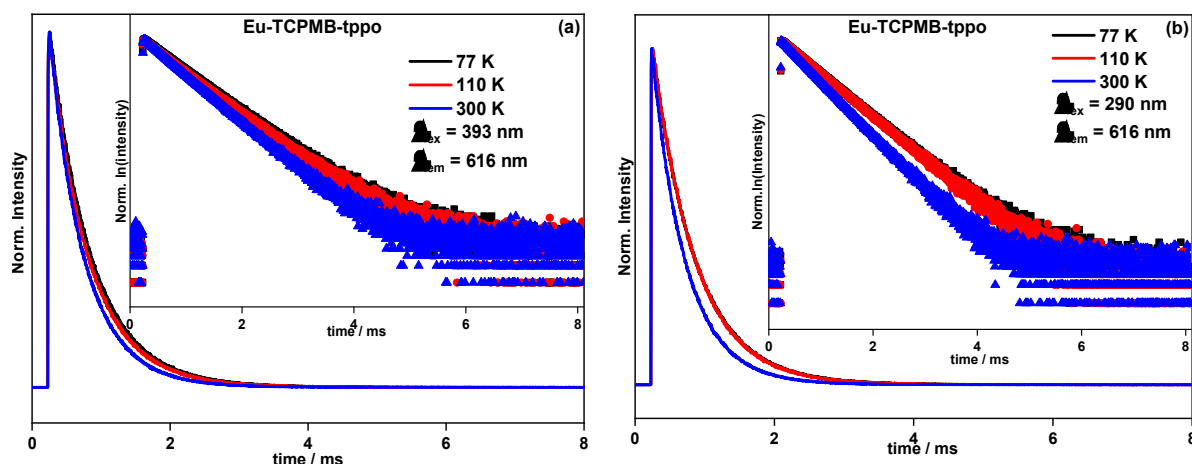


Fig. 36: Emission decay curves of Eu-TCPMB-*tpo* excited at 393 nm (a) and at 290 nm (b) monitored at 616nm at the temperatures of 77 K, 110 K, and 300 K.

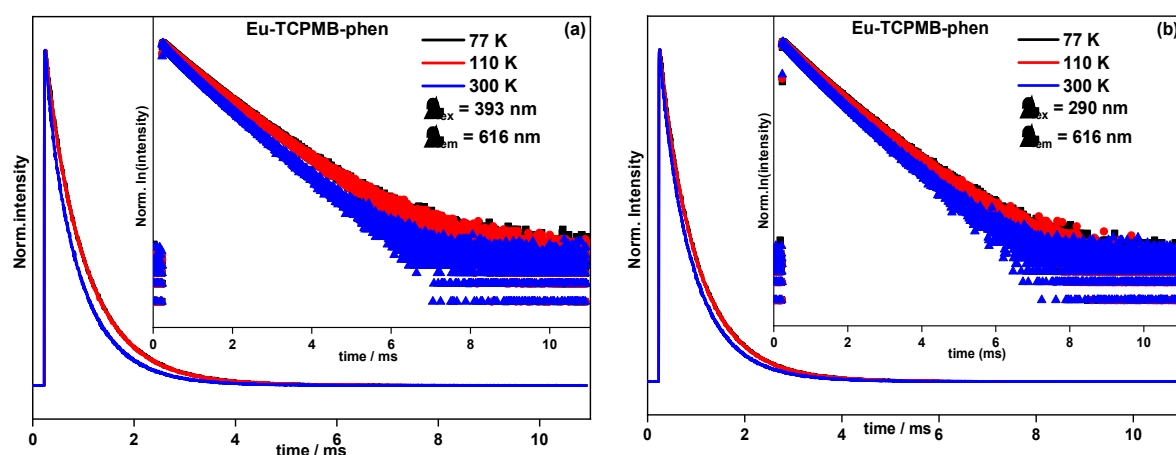


Fig. 37: Emission decay curves of Eu-TCPMB-*phen* excited at 393 nm (a) and at 290 nm (b) monitored at 616nm at the temperatures of 77 K (black), 110 K (red) and 300 K (green).

The lifetime measurements for the Ln^{III} emissions in mixed lanthanide compounds represent an important tool for the demonstration of energy transfer between the Ln^{III} ions. The luminescence lifetimes of Eu^{III} and Tb^{III} are not effectively affected by the temperature increases. While the decay curves monitored in Eu^{III} are mono-exponential, those monitored in Tb^{III} are fitted by biexponential functions resulting in two emission lifetime values, thus confirming the $\text{Tb}^{\text{III}} \rightarrow \text{Eu}^{\text{III}}$ energy transfer. The lifetime value of 0.9 ms has the closest resemblance to the lifetime values found for Tb-TCPMB indicating that the Eu^{III} affects the spectroscopic properties of only a part of the Tb^{III} ions. The observed rise time of Eu^{III} monitored decay curves suggests a slow Tb^{III} to Eu^{III} energy migration, probably due to the intermetallic distance [55]. In terms of the Eu^{III} $^5\text{D}_0$ lifetimes measured for $\text{Tb}_{0.95}\text{Eu}_{0.05}\text{-TCPMB}$, the significant increase in the decay emission observed in comparison to Eu-TCPMB may be explained by the $\text{Tb}^{\text{III}} \rightarrow \text{Eu}^{\text{III}}$ and mainly the reduction of the concentration quenching effect.

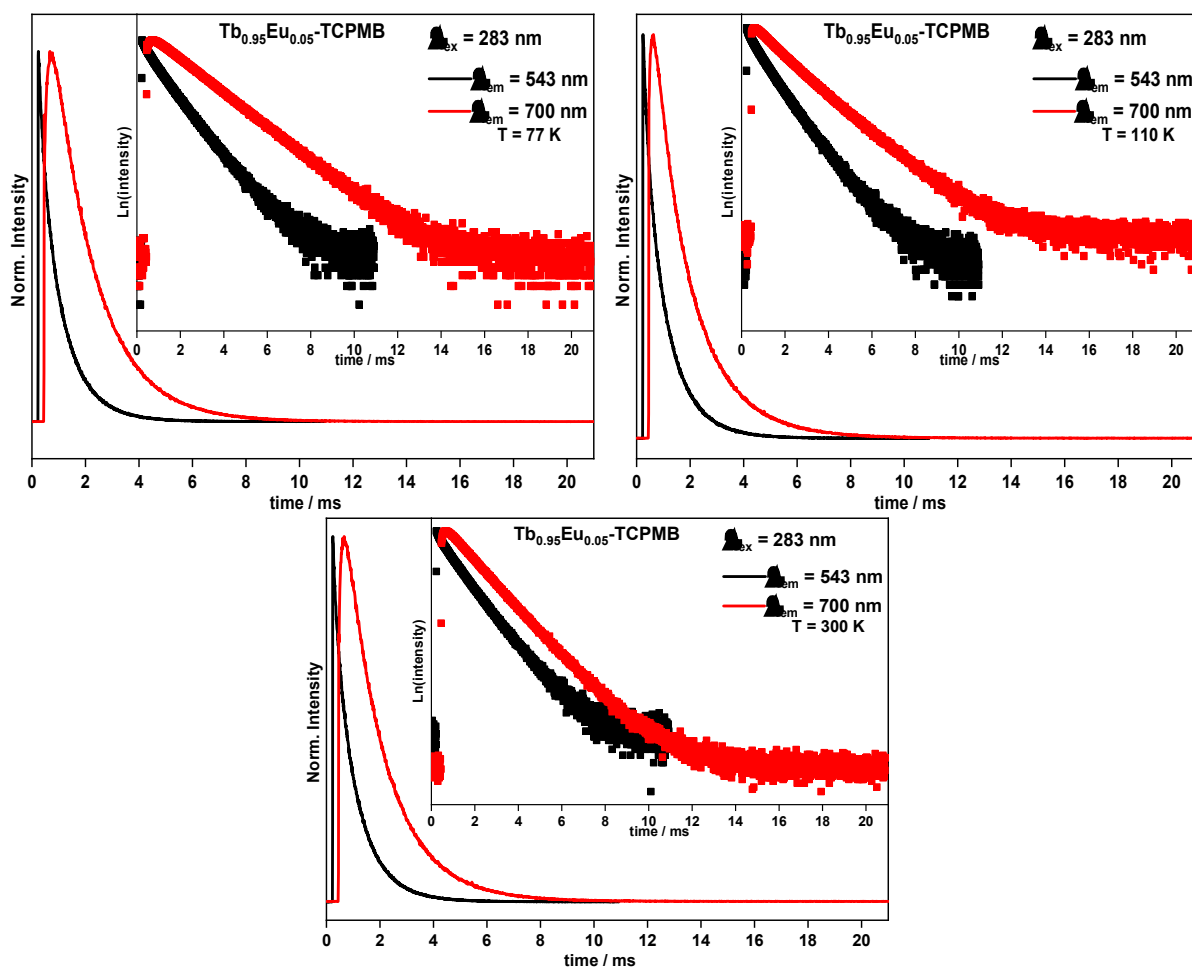


Fig. 38: Emission decay curves of $\text{Tb}_{0.95}\text{Eu}_{0.05}\text{-TCPMB}$ monitored at 543 nm and 700 nm upon excitation at 283 nm at the temperatures of 77K, 110 K and 300 K

4.7.2. Compounds based on the H₆TDCPMB ligand

In the same way, the photophysical properties were investigated for the compounds represented by the general formula Ln-TDCPMB (Ln = Gd^{III}, Eu^{III}, Tb^{III}) in the solid-state at room temperature. Firstly, the time-resolved phosphorescence (Fig. 39a) spectra of the ligand were obtained at 77 K using Gd-TDCPMB in order to discriminate the triplet state emission. The triplet energy was estimated to 25,974 cm⁻¹ and 22,779 cm⁻¹ by the tangent and deconvolution methodologies respectively using the emission spectrum corresponding to the delay of 1.1 ms as shown in Fig. 39b.

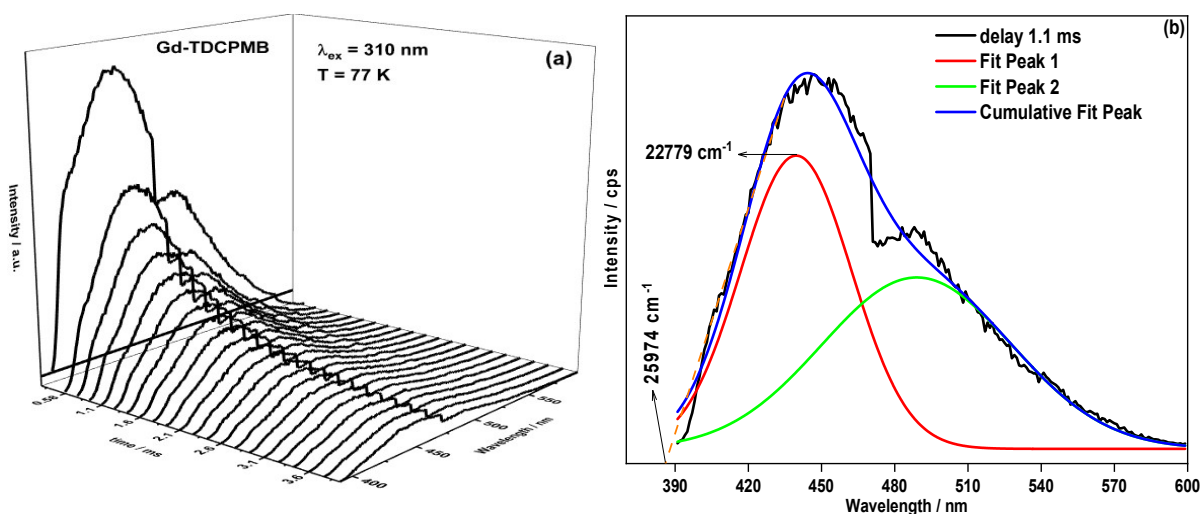


Fig. 39: Time-resolved photoluminescence of Gd-TDCPMB at 77 K excited at 310 nm (a) and triplet energy estimation for H₆TDCPMB using both tangent and deconvolution methodologies (b).

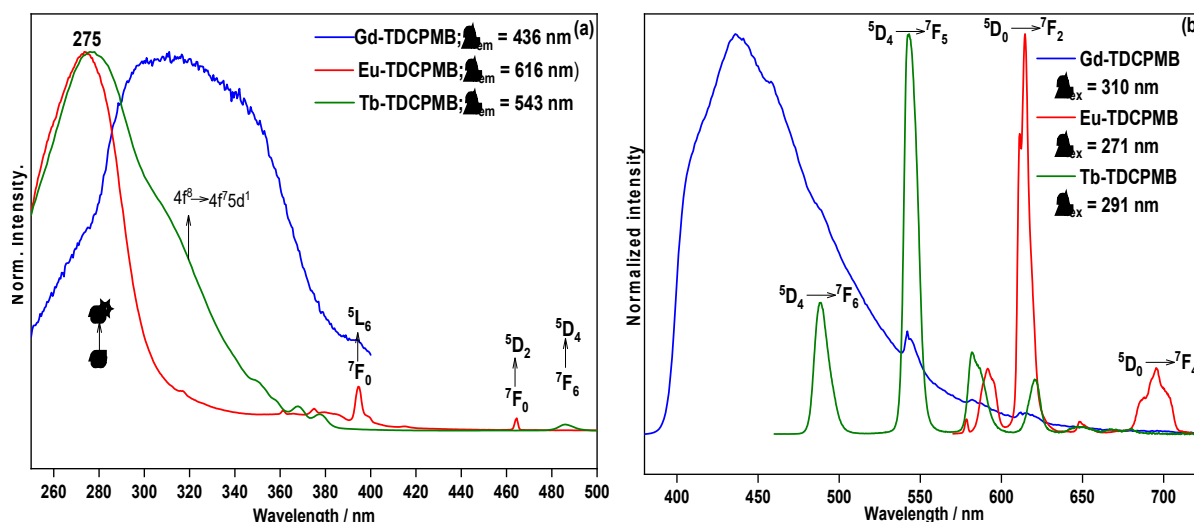


Fig. 40: Excitation (a) and emission (b) spectra of Gd-TDCPMB, Eu-TDCPMB and Tb-TDCPMB measured at 295 K.

The capacity of the TDCPMB⁶⁻ linker to provide efficient sensitization for Eu^{III} and Tb^{III}, excitation and emission spectra of the Ln-TDCPMB (Ln = Gd^{III}, Eu^{III} or Tb^{III}) were examined at room temperature in the solid-state. All the excitation spectra display an intense and broad band in the blue spectral range attributed to $\pi^* \leftarrow \pi$ electron transition of TDCPMB linkers [126]. The shoulder between 300 and 360 nm in the excitation spectrum of Tb-TDCPMB may be assigned to the spin-forbidden interconfigurational $4f^8 \rightarrow 4f^7 5d^1$ transition of Tb^{III} ions [127]. To better investigate this difference in the profile of the excitation spectra, the Gd^{III} compound was doped with Tb^{III} (4 %) and the photoluminescence properties were studied (appendix A 34). Monitoring the Tb^{III} emission at 544 nm, the excitation spectrum exhibits a similar band in comparison to Tb-TDCPMB, while monitored in the range of the ligand phosphorescence at 513 nm, the excitation spectrum shows a two-component band centered at 312 and 424 nm. Interestingly, the excitation at 312 nm results in the Tb^{III} emission. Such observations suggest that the luminescence sensitization occurs from Triplet to Ln^{III} energy transfer and mainly via singlet energy transfer and ligand to metal charge transfer. As shown in Fig. 40b, under excitation in the ligand broad band, the emission spectrum of Gd-TDCPMB displays the typical ligand emission band with the maximum at 436 nm, which was assigned to the triplet state emission based on the time-resolved spectra. Upon excitation in the ligand absorption band, Eu-TDCPMB and Tb-TDCPMB spectra exhibit the characteristic Eu^{III} and Tb^{III} luminescence with narrow and well-separated emission bands. Eu-TDCPMB and Tb-TDCPMB display their respective emission narrow bands centered at 578, 592, 615, 648 and 696 nm for Eu-TDCPMB and at 489, 543, 582 and 621 nm for Tb-TDCPMB attributed to the $^5D_0 \rightarrow ^7F_J$ ($J = 0-4$) and $^5D_4 \rightarrow ^7F_J$ ($J = 6-3$) electronic transitions of Eu^{III} and Tb^{III}, respectively. The absence ligand band in emission spectra of Eu-TDCPMB and Tb-TDCPMB indicates an effective energy transfer from the ligand to both trivalent lanthanide ions. As discussed before, the compound Eu-TDCPMB was synthesized following the solvothermal methodology in order to obtain them in a crystalline phase. By comparing the diverse excitation and emission spectra (appendix A 35) with those of the compound obtained by direct precipitation (Fig. 40), one may note that variations in the Eu-TDCPMB spectra profile were observed when the temperature was increased to 180 °C. As expected, all the Tb^{III} / Eu^{III} doped compounds simultaneously show both the characteristic emissions of the Tb^{III} and Eu^{III} ions.

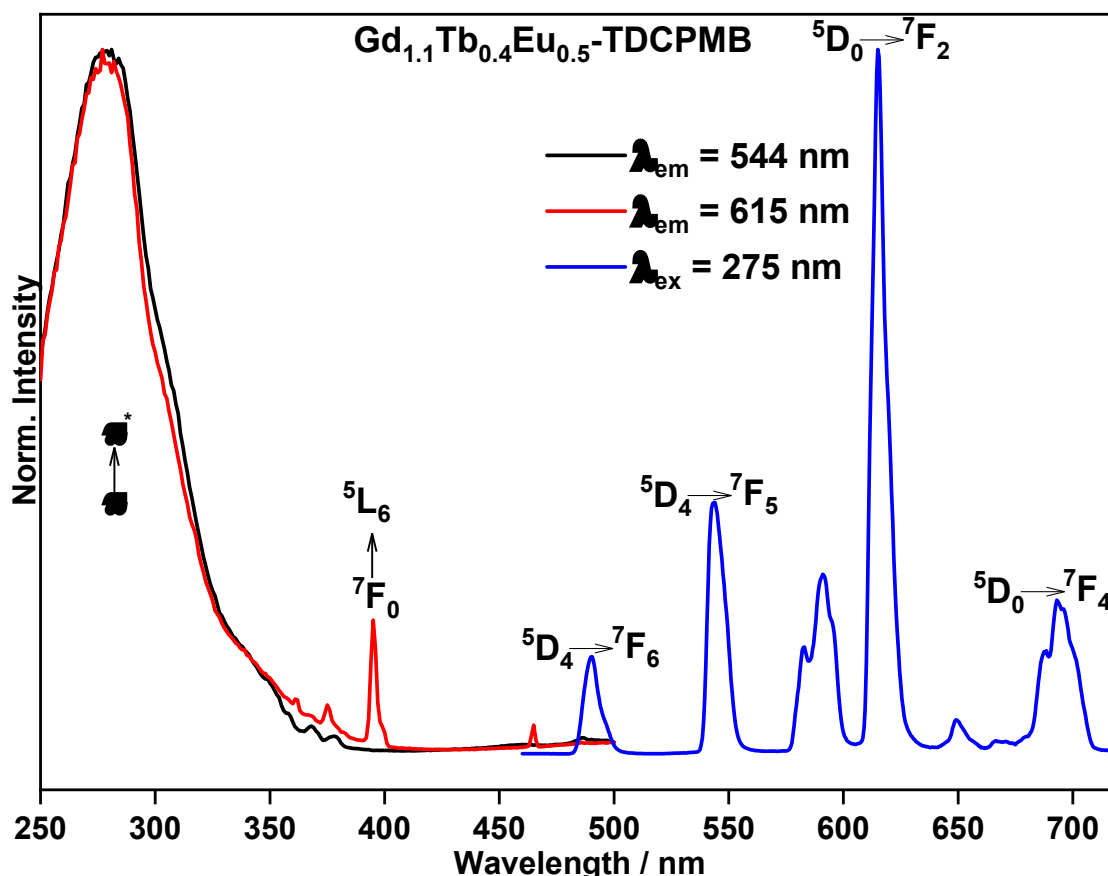


Fig. 41: Excitation and emission spectra of $\text{Gd}_{1.1}\text{Tb}_{0.4}\text{Eu}_{0.5}\text{-TDCPMB}$ obtained at room temperature (293 K).

Typical luminescence decay profiles of the compounds Tb-TDCPMB , Eu-TDCPMB , $\text{Gd}_{1.9}\text{Tb}_{0.1}\text{-TDCPMB}$, and $\text{Gd}_{1.9}\text{Eu}_{0.1}\text{-TDCPMB}$, $\text{Gd}_{1.5}\text{Tb}_{0.4}\text{Eu}_{0.1}\text{-TDCPMB}$, and $\text{Gd}_{1.3}\text{Tb}_{0.4}\text{Eu}_{0.3}\text{-TDCPMB}$ are depicted in Fig. 42. For Tb-TDCPMB and Eu-TDCPMB , the curves can be described by single exponential decay functions thus indicating that the Ln^{III} ions are located in the very similar chemical environments. The luminescence decay time monitoring the transitions $^5\text{D}_4 \rightarrow ^7\text{F}_5$ and $^5\text{D}_0 \rightarrow ^7\text{F}_2$ for Tb-TDCPMB and Eu-TDCPMB were estimated to be 0.98 and 0.63 ms, respectively. The shorter lifetime of $^5\text{D}_0$ may be explained by the presence of the water molecules in the coordination sphere which quenches more effectively the Eu^{III} luminescence regarding Tb^{III} . Relatively efficient coupling of the Eu^{III} excited states occurs to the third vibrational overtone of the O-H oscillators ($\nu_{\text{O-H}} \sim 3300\text{-}3500\text{ cm}^{-1}$) and to the fourth harmonic in the case of Tb^{III} , which is consistent with the less efficient quenching observed for Tb^{III} where the Franck–Condon overlap factor is less favorable [38]. In $\text{Gd}_{1.9}\text{Tb}_{0.1}\text{-TDCPMB}$ and $\text{Gd}_{1.9}\text{Eu}_{0.1}\text{-TDCPMB}$, while the Tb^{III} emission lifetime shows only a higher value (Fig. 42 a-b) due to the reduction of the concentration quenching

in comparison to Tb-TDCPMB, the 5D_0 Eu^{III} decay curve exhibits a biexponential profile and important variations in the lifetime values compared to Eu-TDCPMB indicating the distribution of the ions in at least two different chemical environments. In the Tb/Eu mixed compounds, luminescence decay monitored in both ions show a biexponential profile. The simultaneous decrease and increase in the luminescence lifetimes of 5D_4 of Tb^{III} and 5D_0 of Eu^{III} indicate the existence of energy transfer from Tb^{III} to Eu^{III} [128].

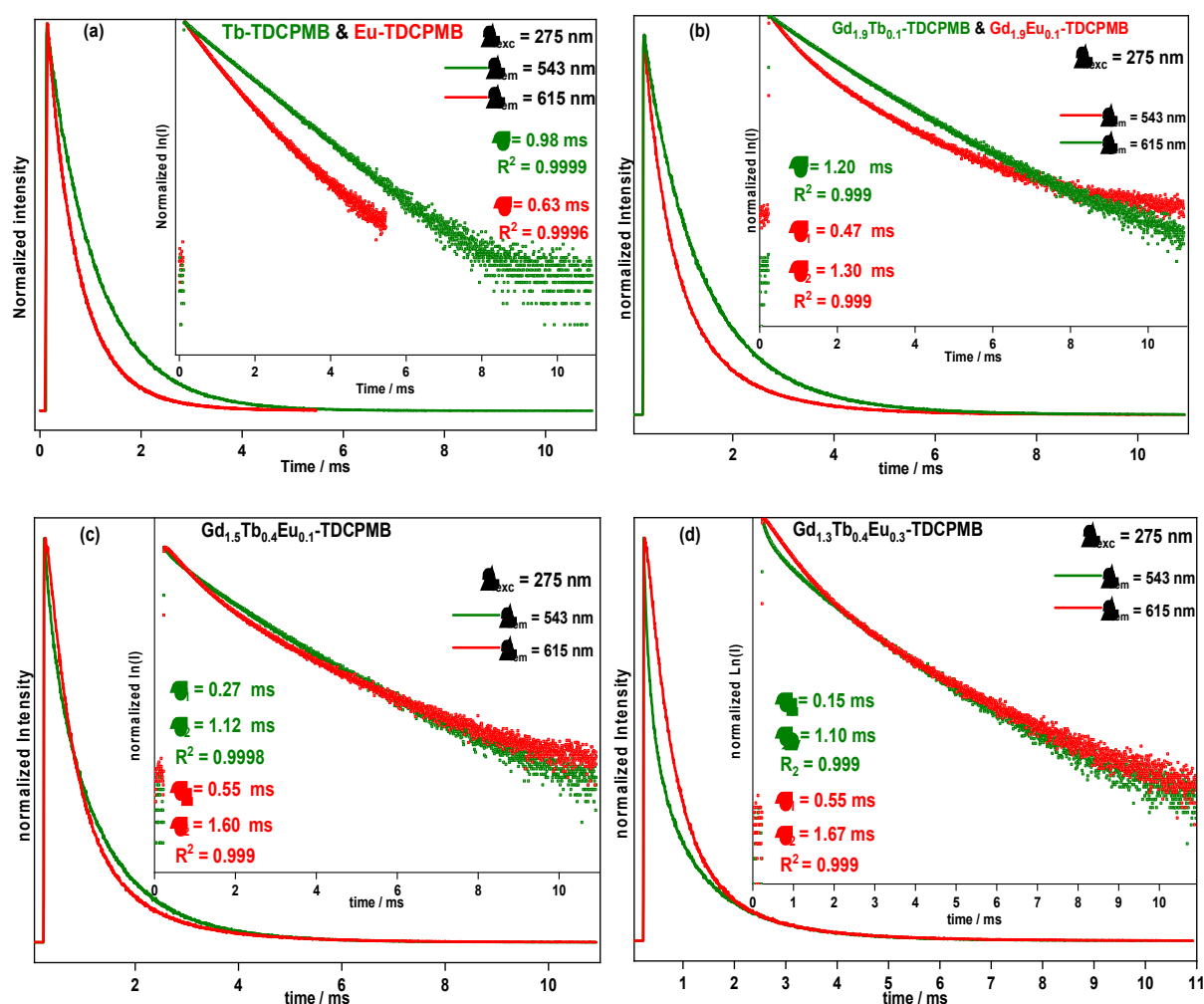


Fig. 42: Luminescence decay profiles of the compounds Tb-TDCPMB and Eu-TDCPMB (a), Gd_{1.9}Tb_{0.1}-TDCPMB and Gd_{1.9}Eu_{0.1}-TDCPMB (b), Gd_{1.5}Tb_{0.4}Eu_{0.1}-TDCPMB (c) and Gd_{1.3}Tb_{0.4}Eu_{0.3}-TDCPMB (d) excited at 275 nm and monitored at 543 nm (Tb^{III}) and at 616 nm (Eu^{III}).

4.7.3. Compounds based on the ligand H₂BDC and HAC

The photoluminescence studies of the compounds synthesized from the ligands H₂BDC and HAC were carried out at room temperature. The energies of the H₂BDC and HAC ligands triplet levels are reported in the literature as 23,256 and 20,200 cm⁻¹ [124,129]. For Eu-BDC and Tb-BDC, the excitation spectra (Fig. 43 a and b) show the intense broadband with two maxima at around 280 and 320 nm which is assigned to the $\pi \rightarrow \pi^*$ transitions of the BDC²⁻ linker, indicating an effective energy transfer from the ligand to the metal (antenna effect). In the region of 350 - 470 nm, the excitation spectrum of Eu-BDC shows the low-intensity narrow bands attributed to the 4f-4f transitions of Eu^{III}. In both cases, exciting in the broad band, the emission spectra of the compounds exhibit only the characteristic narrow and well-separated emission bands of Eu^{III} (Fig. 43a) and Tb^{III} (Fig. 43b) indicating that the BDC²⁻ is an interesting antenna chromophore for sensitizing both Eu^{III} and Tb^{III} ions. The low-lying energy of the triplet state prevents the sensitization of Tb^{III} and Eu^{III} ions, thus the photoluminescence spectra of Eu-AC and Tb-AC (Fig. 44) show only the ligand centered-luminescence.

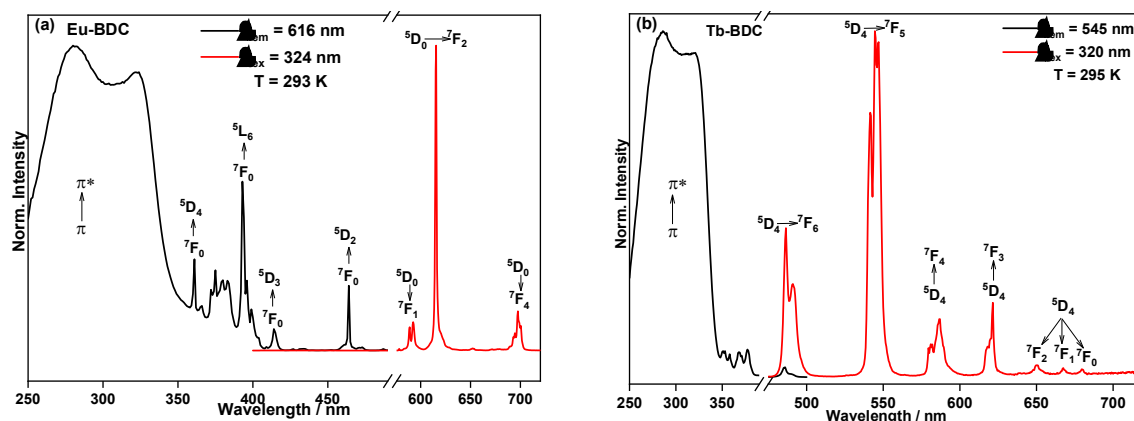


Fig. 43: (a) Excitation spectrum monitored at 616 nm (black) and emission spectrum monitored at 324 nm (red) of Eu-BDC at 295k. (b) (a) excitation spectrum monitored at 545 nm (black) and emission spectrum monitored at 320 nm (red) of Tb-BDC at 295k.

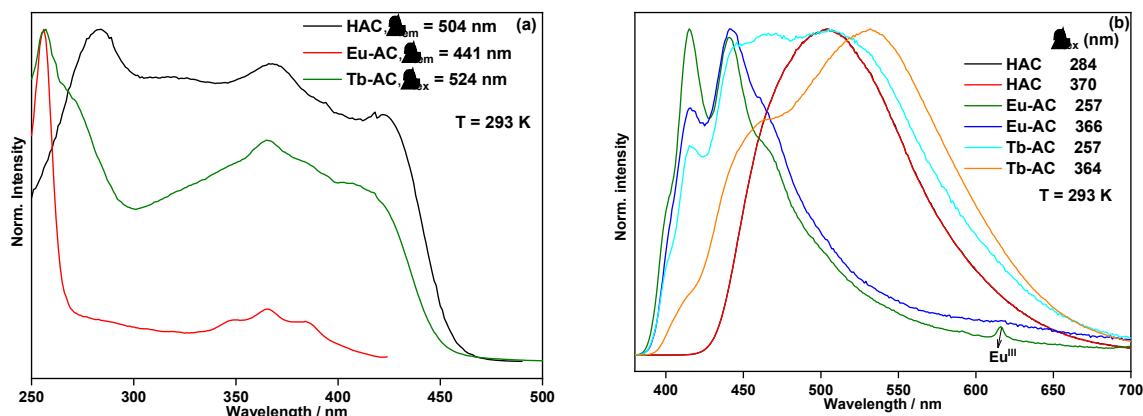


Fig. 44: (a) Excitation spectra of the free ligand HAC and the compounds Eu-AC and Tb-AC monitored at 504, 441 and 524 nm respectively. (b) emission spectra of HAC excited at 284 nm (dark) and 370 nm (red), of Eu-AC, excited at 257 nm (green) and 366 nm (blue) and of Tb-AC excited at 257 nm (cyan) and 364 nm (orange). The spectra were recorded at 293 K.

The steady-state excitation spectra of Ln-BDC-AC ($Ln = Eu^{III}$, Tb^{III}) (Fig. 45) show the same broad band with a blue-shift in comparison to the spectra of the compounds containing only the BDC ligand. Furthermore, the Eu^{III} intra-configurational bands are substantially attenuated suggesting an energy transfer from Eu^{III} ion to the ligand AC^- . The emission spectra exhibit a similar profile of Ln-BDC indicating that the symmetries around the lanthanide ions are the same in both cases.

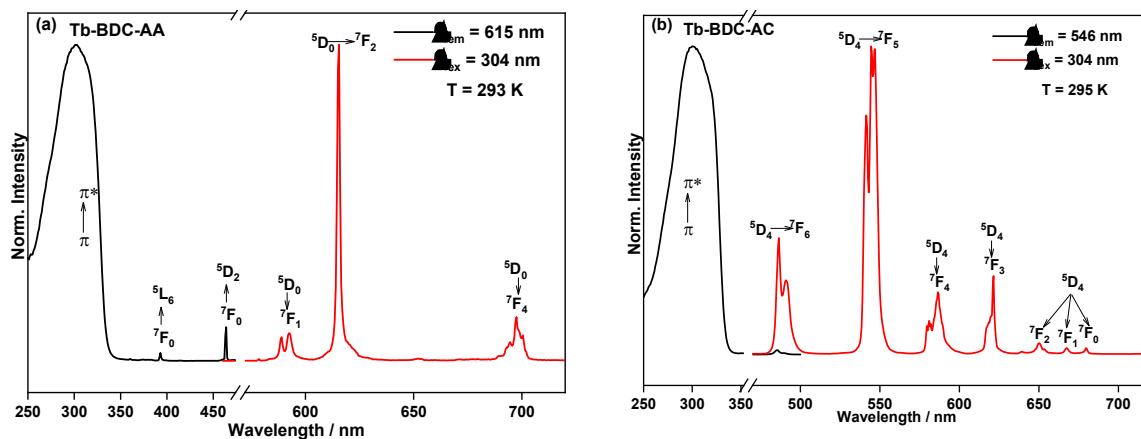


Fig. 45: (a) Excitation spectrum monitored at 615 nm (black) and emission spectrum monitored at 304 nm (red) of Eu-BDC-AC at 295k. (b) (a) excitation spectrum monitored at 546 nm (black) and emission spectrum monitored at 304 nm (red) of Tb-BDC-AC at 295k.

The emission spectra of $Tb_{0.93}Eu_{0.07}$ -BDC-AC and $Tb_{0.993}Eu_{0.007}$ -BDC-AC (Fig. 46a and b) show the emission bands assigned to both Tb^{III} and Eu^{III} ions. Fig. 46a shows that even representing 7 mol% of the Tb^{III}/Eu^{III} mixture, the relative Eu^{III} emission is more intense than the Tb^{III} one. Reducing the Eu^{III} part from 7 to 0.7 mol%, the emission assigned to Tb^{III} becomes the most intense. It is important nothing that

comparing the spectra collected at 80 and 300 K (Fig. 46b), it is important to note the increase and decrease in Eu^{III} and Tb^{III} emissions respectively. Such result may be considered as an indication of Tb^{III} to Eu^{III} energy transfer in the system.

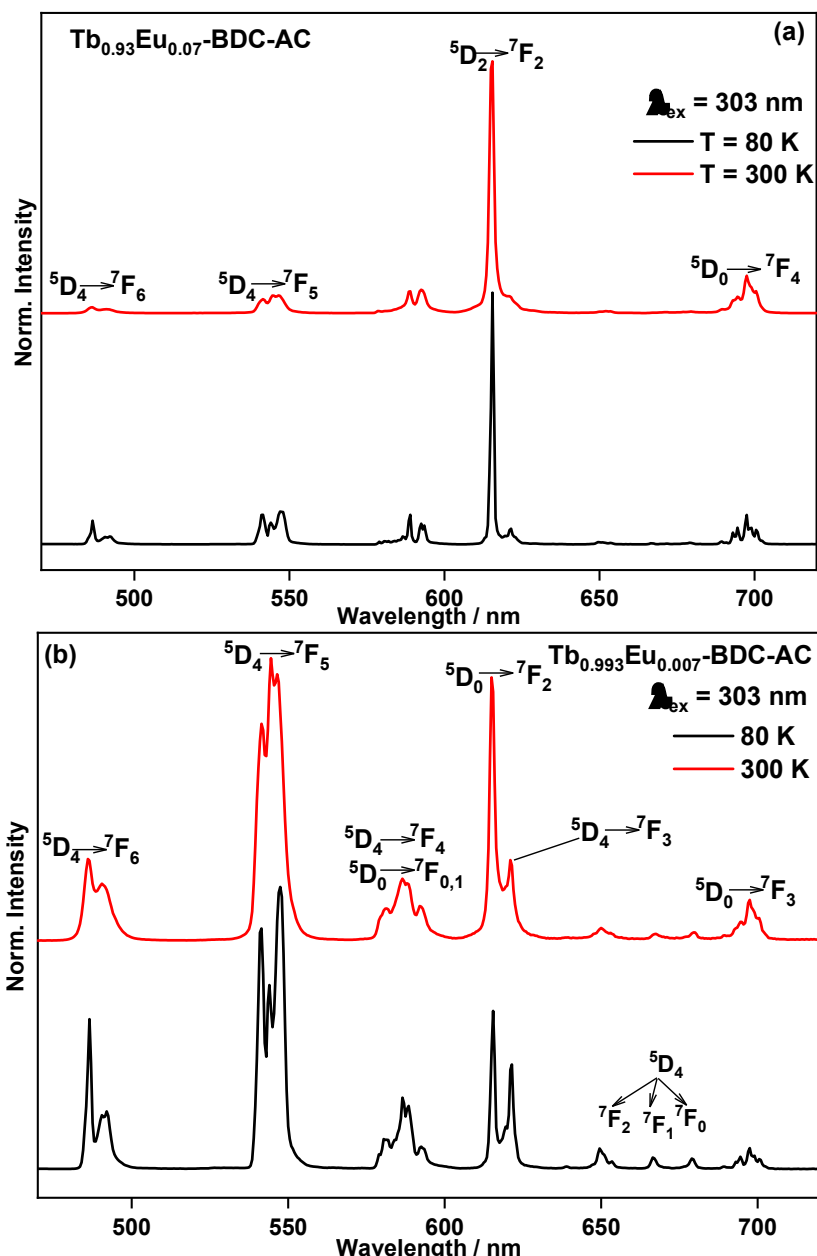


Fig. 46: (a) Normalized emission spectra of $\text{Tb}_{0.93}\text{Eu}_{0.07}\text{-BDC-AC}$ monitored at 303 nm obtained at 80 K (black) and 300 K (red). (b) Normalized emission spectra of $\text{Tb}_{0.993}\text{Eu}_{0.007}\text{-BDC-AC}$ at 80 K (dark) and at 305 (red) upon excitation at 303 nm.

The emission decay curves of the compounds Ln-DBC and Ln-DBC-AC ($\text{Ln} = \text{Tb}^{\text{III}}, \text{Eu}^{\text{III}}$) measured at 295 K (Fig. 47a and b) are single exponential decay functions

pointing to the uniqueness of the chemical ambient of the ions. The lifetime values are given insight to each figure. The fact that the emission lifetime values of the compounds Ln-BDC-AC are smaller in comparison to Ln-BDC suggests a quenching mechanism where the Ln^{III} excited states are depopulated by the ligand AC probably via a Dexter-energy transfer process.

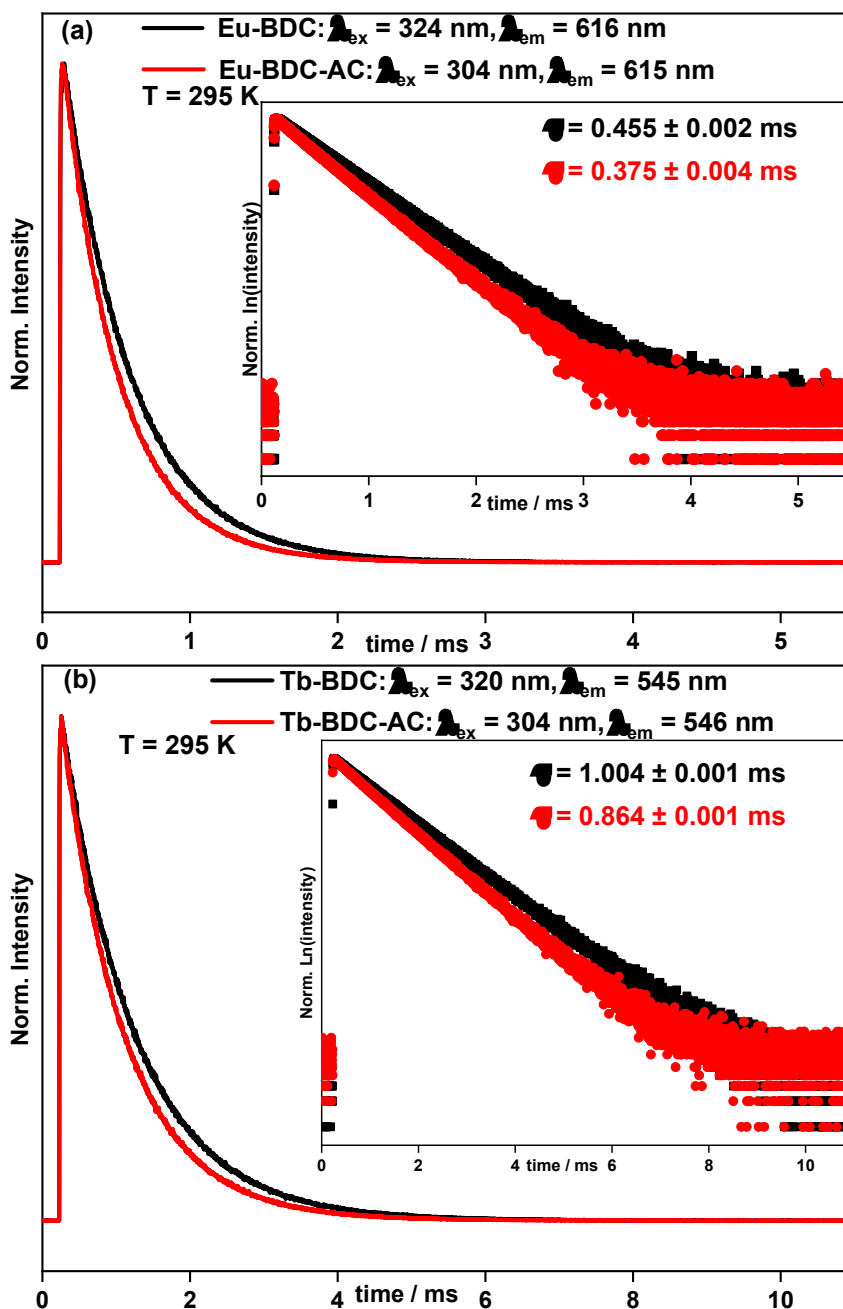


Fig. 47: (a) Emission decay curves of Eu-BDC (black) and Eu-BDC-AC (red) exciting at 324 nm and 304 nm respectively and monitoring at 616 nm and 615 nm respectively. (b) Photoluminescence decay curves of Tb-BDC (black) and Tb-BDC-AC (red) exciting at 320 nm and 304 nm respectively and monitoring at 545 nm and 546 nm respectively.

The luminescence decay curves of $\text{Tb}_{0.93}\text{Eu}_{0.07}\text{-BDC-AC}$ and $\text{Tb}_{0.993}\text{Eu}_{0.007}\text{-BDC-AC}$ (Fig. 48a and b) show an rise time in the $^5\text{D}_0 \text{Eu}^{\text{III}}$ population, thus indicating, one more time, the Tb^{III} to Eu^{III} energy transfer.

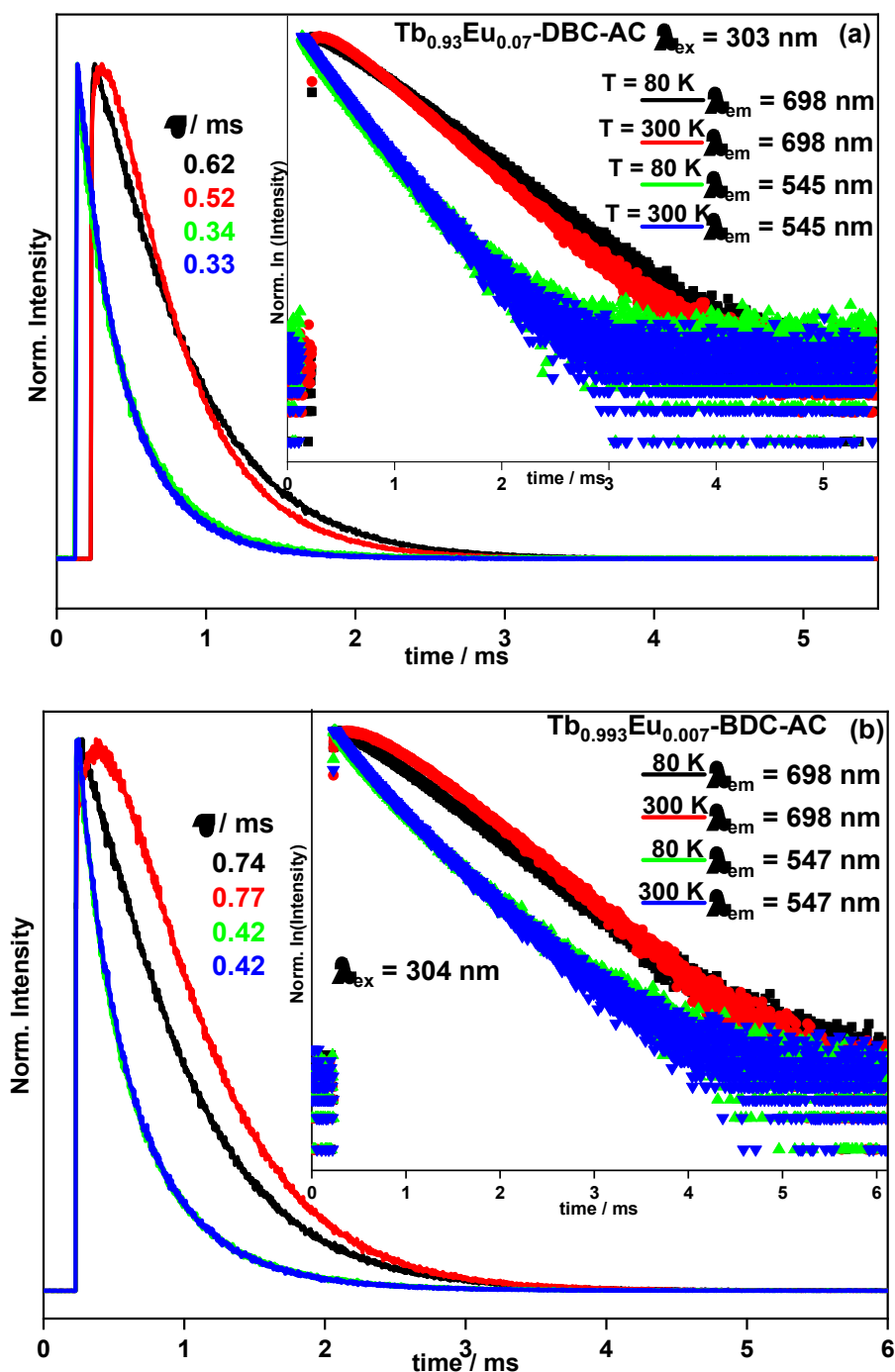


Fig. 48: (a) Emission decay curves of $\text{Tb}_{0.93}\text{Eu}_{0.07}\text{-BDC-AC}$ upon excitation at 303 nm and monitoring at 698 and 545 nm at the temperature of 80 and 300 K. (b) Photoluminescence decay curves of $\text{Tb}_{0.993}\text{Eu}_{0.007}\text{-BDC-AC}$ upon excitation at 304 nm and monitoring at 698 and 545 nm at the temperature of 80 and 300 K.

4.7.4. Compounds based on the ligand H₂BDC and Hacac

The energy of the triplet level of the acac⁻ anion is reported in the literature as 25,310 cm⁻¹ [130]. The photoluminescence spectra of all synthesized compounds are shown in Fig. 49. Monitoring on the Tb^{III} emission at 546 nm or the Eu^{III} emissions at 615 nm and 698 nm (Fig. 49 a-c), the excitation spectra show a two-component band extended from 250 nm to 340 nm which may be assigned to $\pi^* \leftarrow \pi$ electronic transitions in the BDC²⁻ and acac⁻ ions. Similarly, to the compounds based on the ligand BDC²⁻, the maxima are centered at around 280 and 325 nm. The inversion in the relative intensities of two components comparing these excitation spectra to those in Fig. 43 obtained for Eu-BDC and Tb-BDC may be attributed to the presence of the acac⁻ anion which is an excellent antenna for Tb^{III} luminescence. In fact, for the compounds represented by Ln-BDC, the excitation spectra also show a band with two components. However, the component in the higher energy region is relatively more intense, exactly the contrary to the observation in Fig. 49 a-c. Even the acac⁻ not being a good sensitizer for Eu^{III} luminescence, the excitation spectra monitored on Eu^{III} also show the lower energy component more intense indicating a Tb^{III} to Eu^{III} following the ligand excitation. The peculiar behavior of the excitation spectrum of the compound Tb_{0.95}Eu_{0.05}acac_{0.95}BDC_{1.025} may be due to a different orientation of the BDC²⁻ improving and lessening respectively the energy transfer process between the binder BDC²⁻ to Tb^{III} and to Eu^{III}, respectively. This result corroborates with the P-XRD data (Fig. 26 a) which shows that the compound Tb_{0.95}Eu_{0.05}acac_{0.95}BDC_{1.025} is not isostructural to the other ones. Another proof of Tb^{III} to Eu^{III} energy transfer has been confirmed by the presence of the intra-configurational $^5D_4 \leftarrow ^7F_6$ Tb^{III} excitation (Fig. 49c) monitoring the $^5D_0 \rightarrow ^7F_4$ emission band of Eu^{III}. As expected, the emission spectra exhibit emission characteristics of both Tb^{III} and Eu^{III} ions with an increase of Eu^{III} emission as its relative fraction increases.

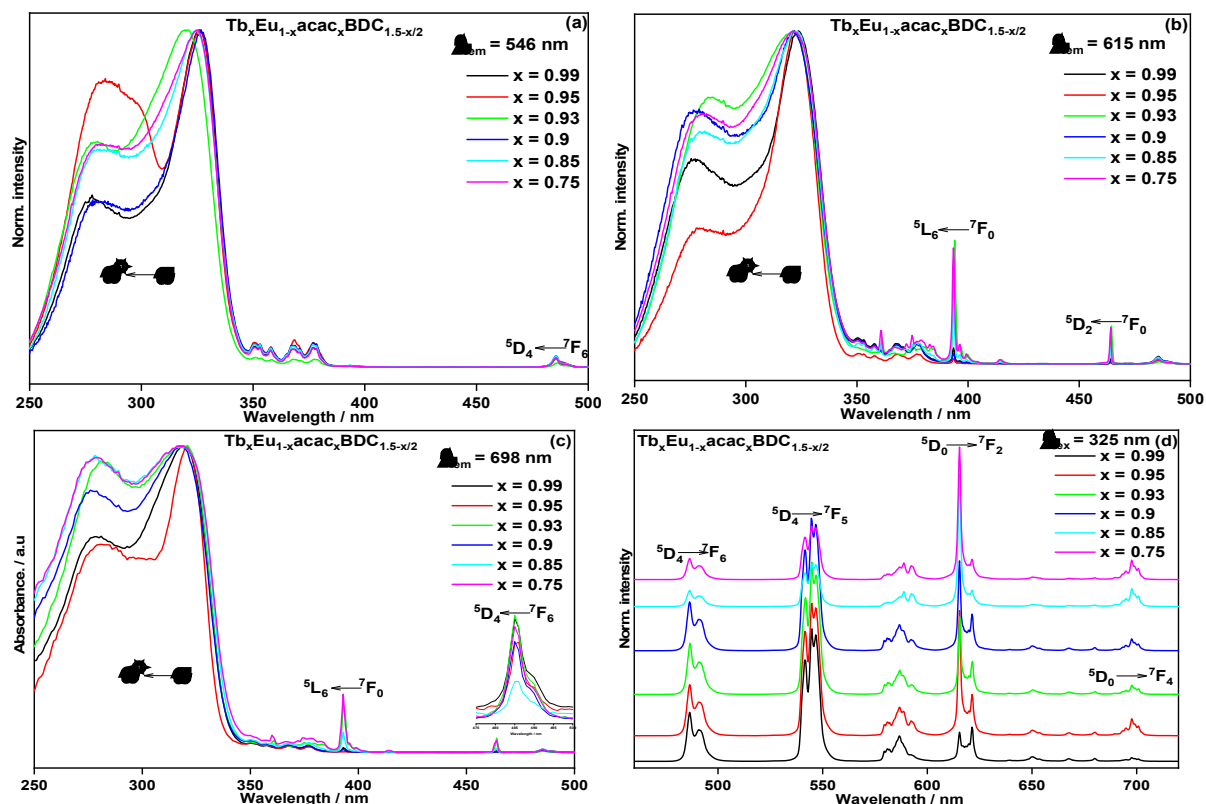


Fig. 49: Excitation spectra monitored at 545 nm (a), at 615 nm (b) and at 698 nm and emission spectra upon excitation at 325 nm (c) of the compound $\text{Tb}_x\text{Eu}_{1-x}\text{acac}_x\text{BDC}_{1.5-x/2}$ collected at room temperature ($x = 0.99, 0.95, 0.93, 0.9, 0.85$ and 0.75).

The emission decay curves of the compounds $\text{Tb}_x\text{Eu}_{1-x}\text{acac}_x\text{BDC}_{1.5-x/2}$ ($x = 0.99, 0.95, 0.9, 0.85$ and 0.75) excited at 325 nm and monitoring the $^5\text{D}_0 \rightarrow ^7\text{F}_4$ Eu^{III} and $^5\text{D}_4 \rightarrow ^7\text{F}_5$ Tb^{III} transitions respectively as shown in Fig. 50a and b. All curves were fitted by single exponential functions. The lifetime values are presented in Table 5.

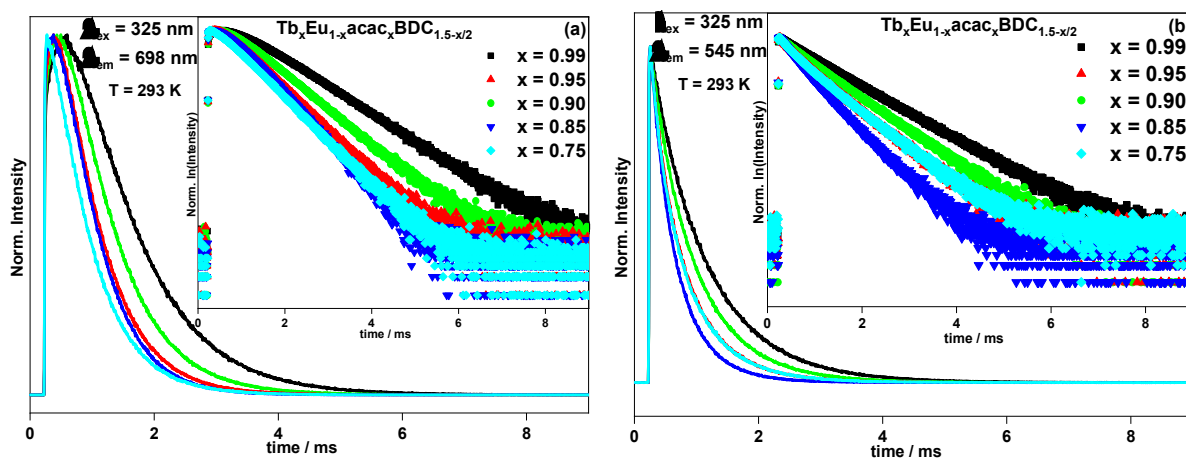


Fig. 50: Emission decay profiles of the compounds $\text{Tb}_x\text{Eu}_{1-x}\text{acac}_x\text{BDC}_{1.5-x/2}$ ($x = 0.99, 0.95, 0.90, 0.85, 0.75$) at 295 K upon excitation at 320 nm and monitored the Eu^{III} emission at 698 nm (a) and the Tb^{III} emission at 545 nm (b).

Table 5: Emission lifetime values of the compounds $\text{Tb}_x\text{Eu}_{1-x}\text{acac}_x\text{BDC}_{1.5-x/2}$ ($x = 0.99, 0.95, 0.90, 0.85, 0.75$) at 295 K

X	Eu ^{III} (698 nm)	Tb ^{III} (545 nm)
0.99	1.227 ± 0.001	0.874 ± 0.000
0.95	0.927 ± 0.001	0.634 ± 0.000
0.90	0.795 ± 0.001	0.730 ± 0.000
0.85	0.755 ± 0.000	0.448 ± 0.000
0.75	0.722 ± 0.001	0.508 ± 0.000

4.8. Temperature-dependent photoluminescence properties

4.8.1. Compounds based on the ligand (H₃TCPMB)

In order to establish their potential as luminescent thermometers, the temperature-dependent photoluminescence properties of Ln-TCPMB (Ln = Eu^{III}, Tb^{III}, and Gd^{III}) and Tb_{0.95}Eu_{0.05}-TCPMB were investigated in terms of emission intensity variation once the emission lifetime values remain constant in the temperature range of 80 to 300 K. As illustrated in Fig. 51a and Fig. 52a, upon excitation at 280 nm, the emission intensity of Eu-TCPMB and Tb-TCPMB decrease substantially in the temperature range 90 - 300 K, which may be attributed to an increase in the rates and thermal activation of nonradiative-decay pathways with temperature increase including vibrational excitation and back-energy transfer (BET) [44]. Fig. 51b and Fig. 52b show the temperature-dependence of the area of the emission bands assigned to the $^5\text{D}_0 \rightarrow ^7\text{F}_2$ and $^5\text{D}_4 \rightarrow ^7\text{F}_5$ transitions in Eu-TCPMB and Tb-TCPMB spectra, respectively. When compared at 90 K and 300 K, unexpectedly the emission intensities of Eu-TCPMB and Tb-TCPMB decrease almost equally to the same fraction of the respective initial values (33% and 35%, respectively). This result suggests that the decrease in the Eu-TCPMB emission intensity is due mainly to nonradiative deactivation of the emitting level by the oscillators in the organic part. The thermal quenching process for achieving temperature sensing properties is dependent on the energy gap between the emitting level and the highest accepting level in 4f–4f transitions. Harmonic energy matching of the vibrational overtone of typical C–H or O–H vibrational frequency in Eu^{III} containing complexes promotes effective vibrational relaxation [131]. The energy gap of $12,290\text{ cm}^{-1}$ between the $^5\text{D}_0$ and $^7\text{F}_6$ states is well-matched with the overtone of C–H and O–H vibrational frequencies. Their effective overtone matching frequencies promote a decrease in the emission quantum yield, resulting in temperature-dependent luminescence. For Tb-TCPMB, besides the deactivation of the $^5\text{D}_4$ by the oscillators,

the luminescence quenching is probably due mainly to a significant increase in the Tb^{III} to ligand energy back-transfer with temperature increasing. The energy gap between the triplet state energy level of the ligand (26,316 cm⁻¹) and the Eu^{III} emitting level ⁵D₀ (17,290 cm⁻¹) in Eu-TCPMB is much larger than one between the triplet state energy level of the ligand and the Tb^{III} emitting level ⁵D₄ (20,500 cm⁻¹) in Tb-TCPMB making more effective the nonradiative depopulation of ⁵D₄ Tb^{III} level by energy back transfer. In this case, the non-radiative deactivation of the exciting state by oscillator vibrations is less probable due to the fact that the energy gap of 14,800 cm⁻¹ between the ⁵D₄ and ⁷F₀ in Tb^{III} is larger, compared to Eu^{III}, leading to reduction of the vibrational relaxation. Thus, in Tb^{III} based complexes, the luminescence quenching by energy migration is the key factor to control the thermosensitive photophysical properties [132]. The green solid line in Fig. 51b is the temperature calibration curve between 90 and 220 K, which shows a linear temperature emission intensity relationship with the relative sensitivity varying from 0.23 to 1.21% K⁻¹ for Eu-TCPMB. For Tb-TCPMB, the relative sensitivity varies in the range 0.003 – 1.2% K⁻¹.

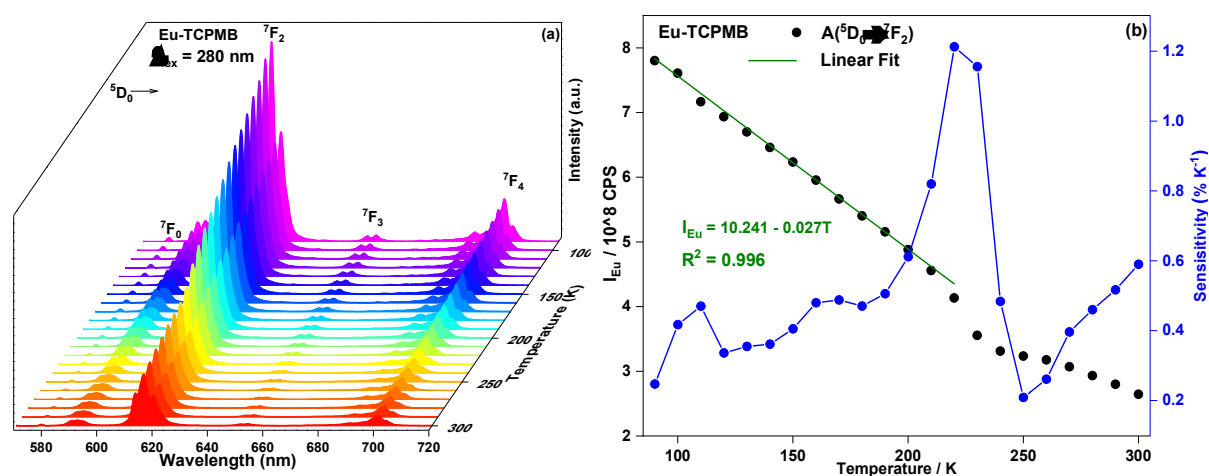


Fig. 51: (a) Solid-state emission spectra of Eu-TCPMB recorded between 80 and 300 K upon excitation at 280 nm. (b) Temperature-dependent area of the band assigned to ⁵D₀ → ⁷F₂ transition of Eu-TCPMB (dark dot), the linear fit of the area of ⁵D₀ → ⁷F₂ transition versus temperature in the temperature of 90-220 K, relative sensitivity versus temperature (blue).

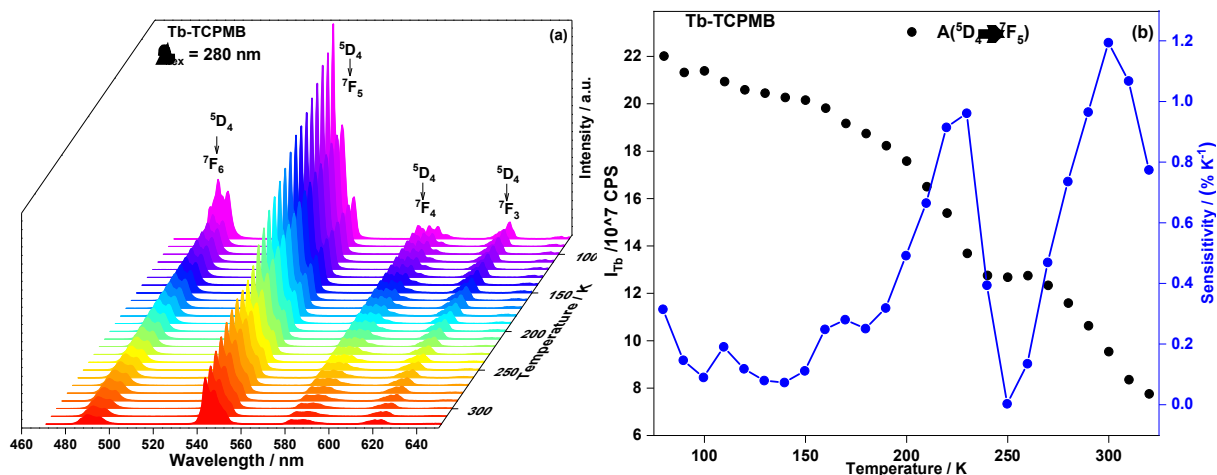


Fig. 52: (a) Solid-state emission spectra of Tb-TCPMB recorded between 80 and 300 K upon excitation at 280 nm. (b) Temperature-dependent area of the band assigned to $^5D_4 \rightarrow ^7F_5$ transition of Tb-TCPMB (dark dot), relative sensitivity versus temperature (blue).

The co-doped $Tb_{0.95}Eu_{0.05}$ -TCPMB shows a similar profile of temperature-dependent luminescence. In the emission spectrum of a Tb^{III} / Eu^{III} mixed compound, usually, the $^5D_0 \rightarrow ^7F_2$ Eu^{III} emission band overlaps with the $^5D_4 \rightarrow ^7F_3$ Tb^{III} transition. Thus, the intensity of the $^5D_0 \rightarrow ^7F_2$ transition is less indicated for being chosen as an experimental parameter to reflect luminescence changes in Eu^{III} emission [82]. Therefore, in view of there being no overlap of the $^5D_0 \rightarrow ^7F_4$ transition with any Tb^{III} transition, the correlation between temperature and emission intensity ratios was defined in terms of both $^5D_4 \rightarrow ^7F_5 / ^5D_0 \rightarrow ^7F_2$ and $^5D_4 \rightarrow ^7F_5 / ^5D_0 \rightarrow ^7F_4$ used as thermometric parameters (I_{Tb} / I_{Eu}). As illustrated in Fig. 53a and b, with the temperature increasing from 90 to 300 K, the areas of emission bands assigned to the $^5D_4 \rightarrow ^7F_5$ of the Tb^{III} ion and to $^5D_0 \rightarrow ^7F_2$ and $^5D_0 \rightarrow ^7F_4$ of the Eu^{III} ion decrease at the same rate (Fig. 53b). Consequently, $Tb_{0.95}Eu_{0.05}$ -TCPMB is not reliable as a luminescent ratiometric thermal probe in this temperature range, once the Tb^{III}/Eu^{III} ratios (Fig. 53b) remain practically constant as shown in Fig. 53c.

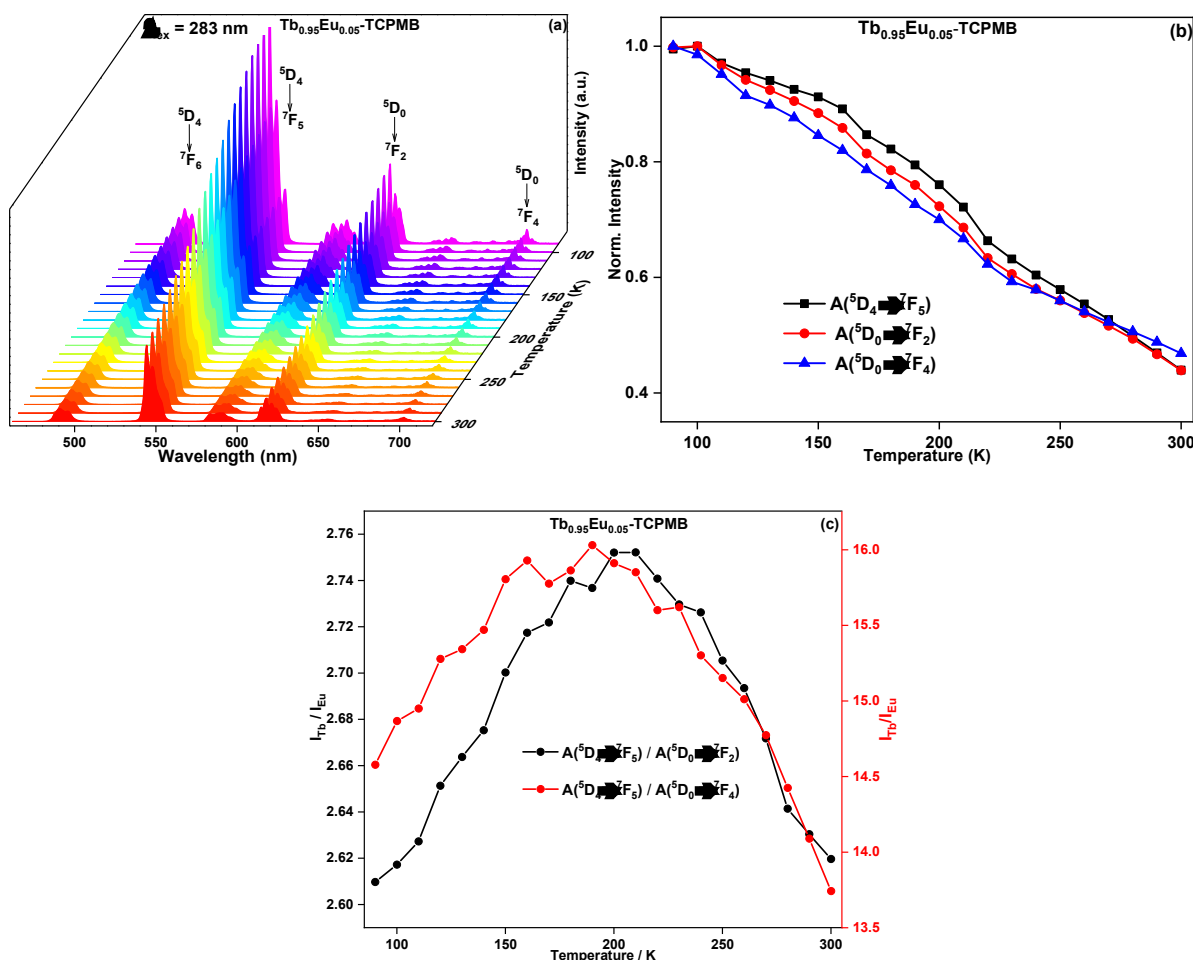


Fig. 53: (a) Solid-state emission spectra of Tb_{0.95}Eu_{0.05}-TCPMB recorded between 80 and 300 K upon excitation at 280 nm. (b) Temperature-dependent area of the bands assigned to $^5D_4 \rightarrow ^7F_5$, $^5D_0 \rightarrow ^7F_2$ and $^5D_0 \rightarrow ^7F_4$. (c) temperature dependence of the intensity ratio of Tb^{III} to Eu^{III}.

Tb_{0.95}Eu_{0.05}-TCPMB was also tested as ratiometric probe for higher temperature using the Peltier and the Linkam accessories in the temperature ranges 278 – 348 K and 298 -393 K, respectively. The results are presented in Fig. 54 and Fig. 55. Heating from 278 to near 340 K, the intensity ratios show no substantial variations corroborating thus, the result obtained with the cryostat (Fig. 53). In a narrow temperature (340 -350 approximatively) the Tb^{III} and Eu^{III} show an abrupt drop and an increase, respectively resulting probably in the highest value of relative thermal sensitivity reported in the literature. Such behavior is probably due to the loss of water molecules as shown by the thermogravimetric curves and a substantial increase in the Tb^{III} to Eu^{III} energy transfer.

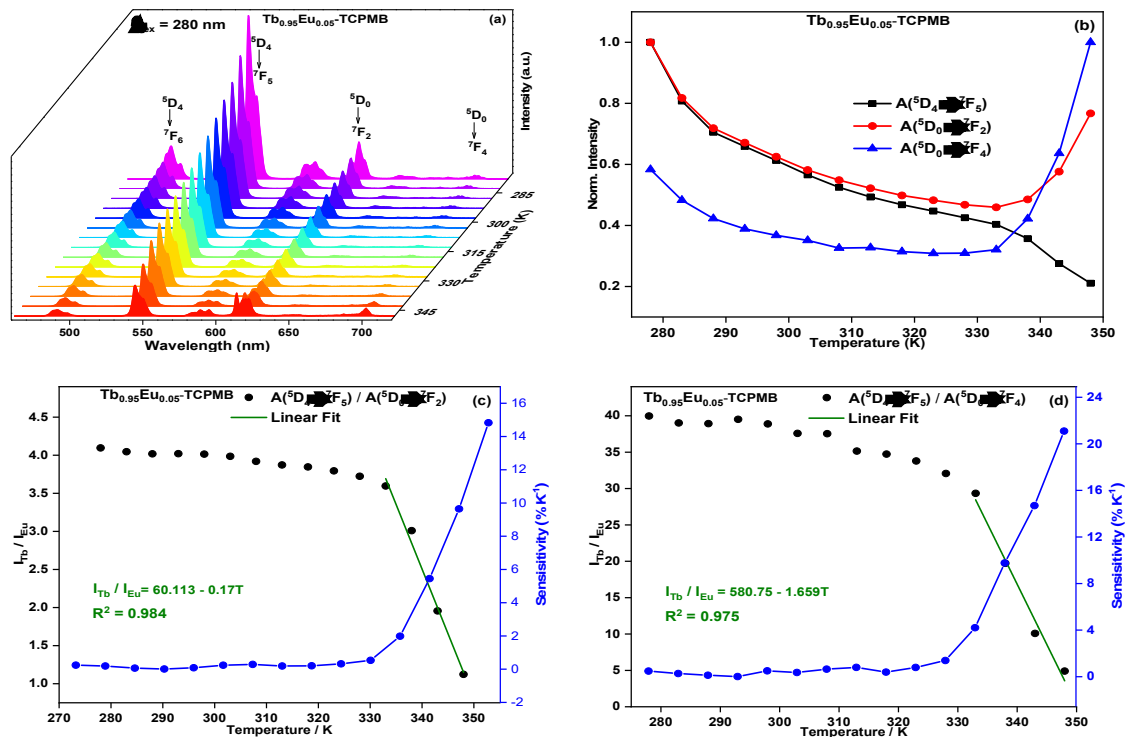


Fig. 54: (a) Temperature-dependent of Tb_{0.95}Eu_{0.05}-TCPMB recorded between 278 and 348 K with the excitation wavelength fixed at 280 nm. (b) Corresponding temperature dependence of normalized I_{Tb} and I_{Eu} . (c) and (d) Corresponding temperature dependence of I_{Tb}/I_{Eu} .

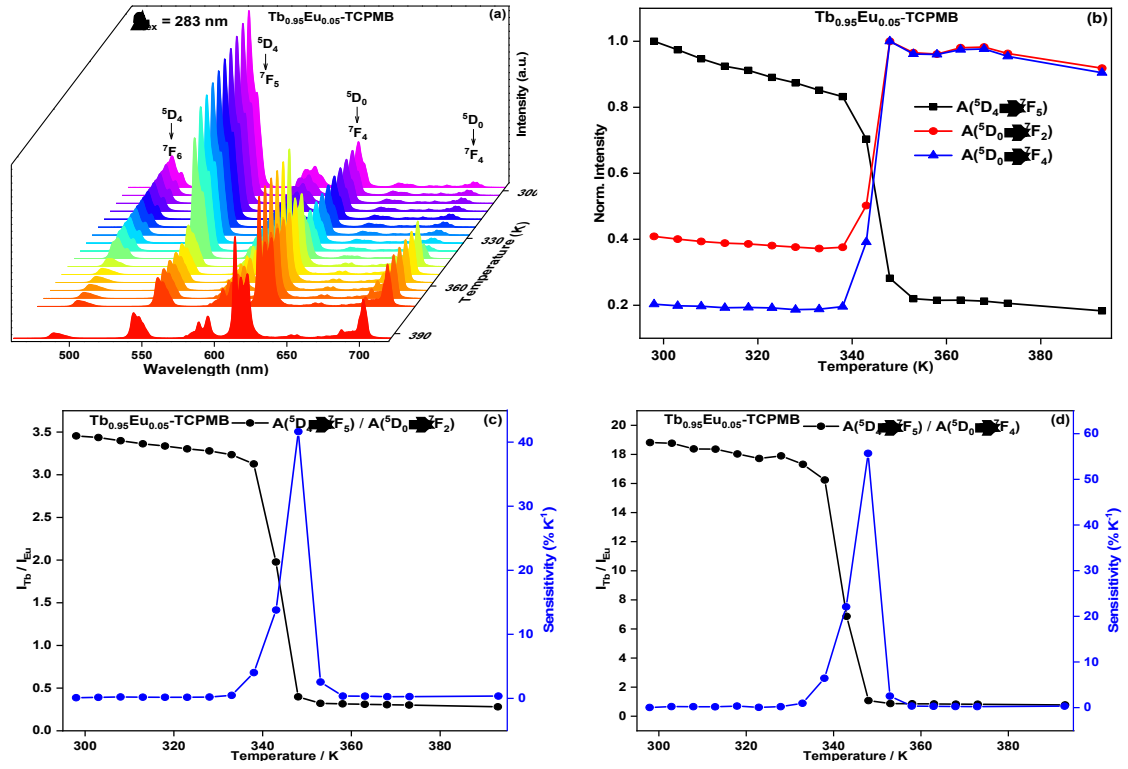


Fig. 55: (a) Temperature-dependent of Tb_{0.95}Eu_{0.05}-TCPMB recorded between 298 and 393 K with the excitation wavelength fixed at 283 nm. (b) Corresponding temperature dependence of normalized I_{Tb} and I_{Eu} . (c) and (d) Corresponding temperature dependence of I_{Tb}/I_{Eu} .

$\text{Tb}_{0.95}\text{Eu}_{0.05}\text{-TCPMB}$ was also investigated as a thermal sensor under the laser excitation. Upon laser excitation at 488 nm, the emission spectra collected in the range 80 – 320 K are presented in Fig. 56a. Differently from the $^5\text{D}_0 \rightarrow ^7\text{F}_4$ band, the intensity of the $^5\text{D}_0 \rightarrow ^7\text{F}_2$ Eu^{III} shows a similar profile regarding the $^5\text{D}_4 \rightarrow ^7\text{F}_5$ Tb^{III} (Fig. 56b) transition suggesting a considerable contribution of the $^5\text{D}_4 \rightarrow ^7\text{F}_3$ Tb^{III} . The increase in the Tb^{III} luminescence intensity between 80 and 140 K (Fig. 56b black curve) may be considered as an indication of the important role of the vibrational component in the direct excitation of the trivalent lanthanide. The $^5\text{D}_4 \rightarrow ^7\text{F}_5$ / $^5\text{D}_0 \rightarrow ^7\text{F}_2$ (Fig. 56c) and $^5\text{D}_4 \rightarrow ^7\text{F}_5$ / $^5\text{D}_0 \rightarrow ^7\text{F}_4$ (Fig. 56d) intensity ratios indicate the range 80 – 200 K where the probe is potentially applicable. It is interesting to note the similarity between the $^5\text{D}_0 \rightarrow ^7\text{F}_4$ band in $\text{Tb}_{0.95}\text{Eu}_{0.05}\text{-TCPMB}$ (Fig. 56a) and in Eu-TCPMB (Fig. 31) upon intra-configurational excitation at 488 and 393 nm respectively.

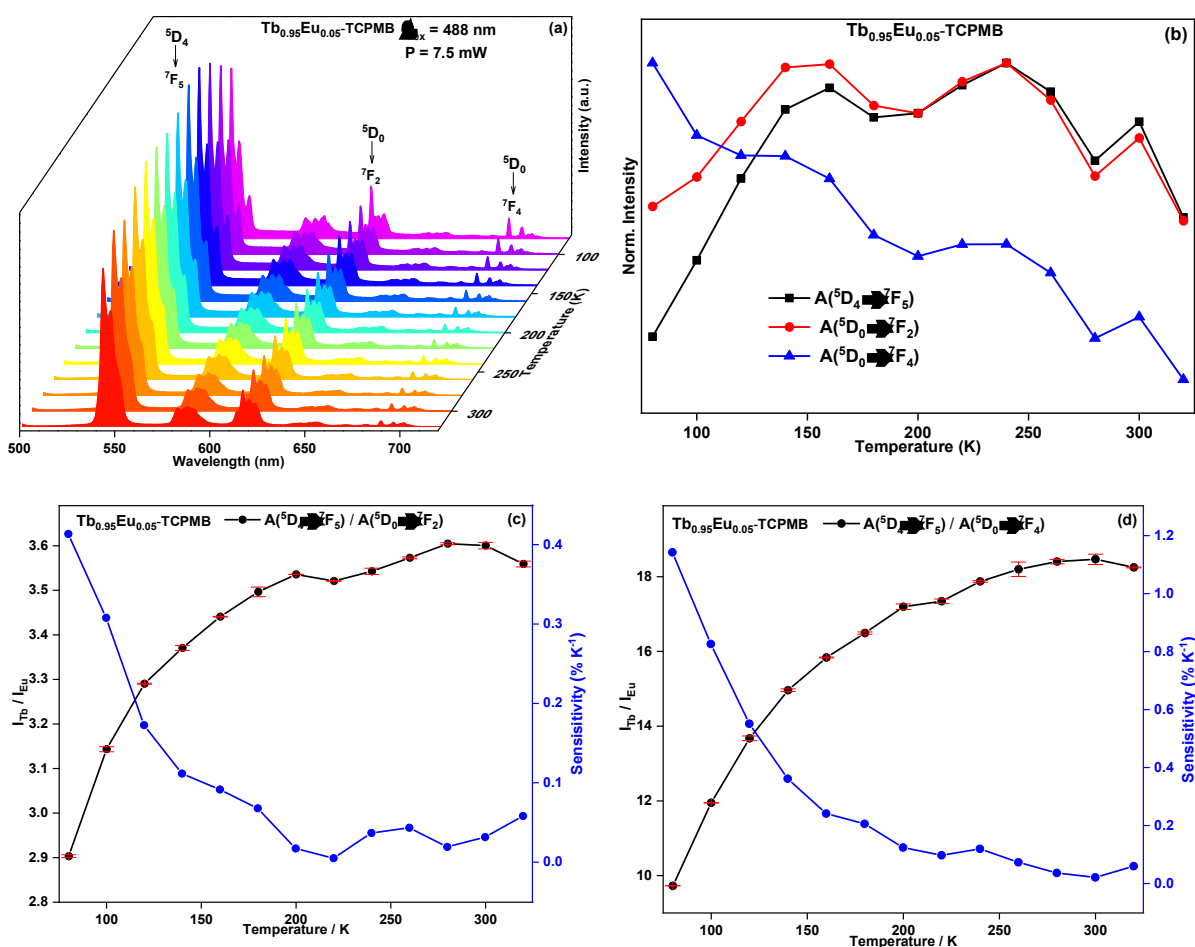


Fig. 56: (a) Temperature-dependent of $\text{Tb}_{0.95}\text{Eu}_{0.05}\text{-TCPMB}$ recorded between 80 and 320 K with upon laser excitation at 488 nm. (b) Corresponding temperature dependence of normalized I_{Tb} and I_{Eu} . (c) and (d) Corresponding temperature dependence of $I_{\text{Tb}} / I_{\text{Eu}}$.

A scientific curiosity enables to investigate the Gd^{III} containing isostructural coordination network which was prepared from a $\text{Gd}(\text{NO}_3)_3$ contaminated by Tb^{III} and Eu^{III} . As can be seen in Fig. 57a, the emission spectra in the 80 – 210 K show the corresponding triplet broad emission and the f-f transitions of both optically active ions. The integrated intensities in the spectral ranges 370 – 536 nm, 536 – 558 nm and 606 – 632 nm for the triplet ligand and $^5\text{D}_4 \rightarrow ^7\text{F}_6$ Tb^{III} , $^5\text{D}_4 \rightarrow ^7\text{F}_5$ Tb^{III} and $^5\text{D}_0 \rightarrow ^7\text{F}_2$ Eu^{III} emissions respectively as functions of the temperature are presented in Fig. 57b. With the temperature increasing, the triplet emission intensity decreases exponentially. The triplet emission intensity at 210 K represented only 5 % of the phosphorescence intensity at 80 K. In the cases of Eu^{III} and Tb^{III} , it was observed an intensity emission increasing by 48 % up 130 K where it starts decreasing. The Eu^{III} and Tb^{III} emission intensities at 210 K presented 74 and 65%, respectively, of the emission intensities at 130 K. The temperature-dependence of the $I_{\text{triplet}} / I_{\text{Eu}}$ and $I_{\text{triplet}} / I_{\text{Tb}}$ (Fig. 57c-d) can be approximated by mono-exponential functions with correlation factor near 1 and here it is interesting to call attention to the fact that the relative thermal sensitivities values on the whole temperature range vary on the ranges 1.2 – 4.4% K^{-1} and 0.8 – 2.8% K^{-1} for $I_{\text{triplet}} / I_{\text{Eu}}$ and $I_{\text{triplet}} / I_{\text{Tb}}$, respectively. Finally, the $I_{\text{Tb}} / I_{\text{Eu}}$ ratio versus the temperature (Fig. 57e) shows only slight variations between 1.4 and 1.6 corroborating thus the result obtained for $\text{Tb}_{0.95}\text{Eu}_{0.05}\text{-TCPMPB}$ in the temperature range 80 – 300 K (Fig. 53c). It is worth noting that, by allowing the combination of the three basic colors provided by the ligand blue emission and the red and green emissions of Eu^{III} and Tb^{III} , respectively, these compounds may be a simple alternative to attempt almost any color, including white emission, by an intelligent variation of the molar ratios of the lanthanide salts used as precursors in the synthesis.

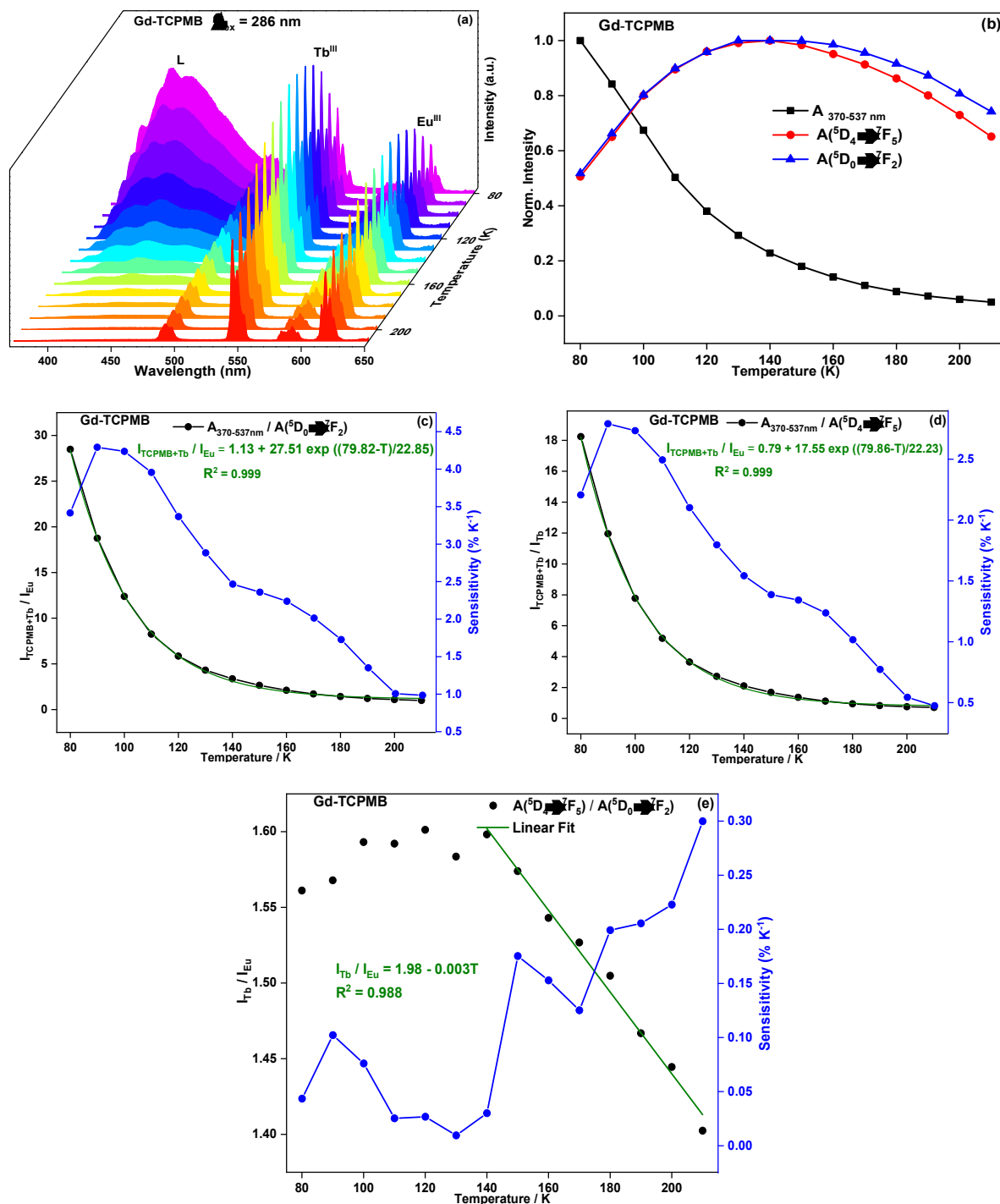


Fig. 57: (a) Temperature-dependent of Gd-TCPMB recorded between 80 and 210 K with the excitation wavelength fixed at 286 nm. (b) Temperature dependence of the integrated intensities in the spectral range of the triplet and the $^5D_4 \rightarrow ^7F_5$ and $^5D_0 \rightarrow ^7F_2$ emissions. Temperature dependence of the $I_{\text{triplet}} / I_{\text{Eu}}$ (c), $I_{\text{triplet}} / I_{\text{Tb}}$ (d) and $I_{\text{Tb}} / I_{\text{Eu}}$ (e).

4.8.2. Compounds based on the ligand (H₆TDCPMB)

The temperature-dependent photophysical properties of the coordination polymers constructed from the ligand H₆TDCPMB were investigated in terms of emission intensity and, in the case of Gd_{1.5}Tb_{0.4}Eu_{0.1}-TDCPMB, also in terms of emission lifetime. Firstly, to investigate the temperature-dependence of the Tb^{III} and Eu^{III} ions diluted in a Gd^{III}-based matrix, photoluminescent spectra of the compounds Gd_{1.9}Ln_{0.1}-TDCPMB (Ln = Eu^{III} and Tb^{III}) were recorded in the temperature range 77 – 300 K (Fig. 58a and b).

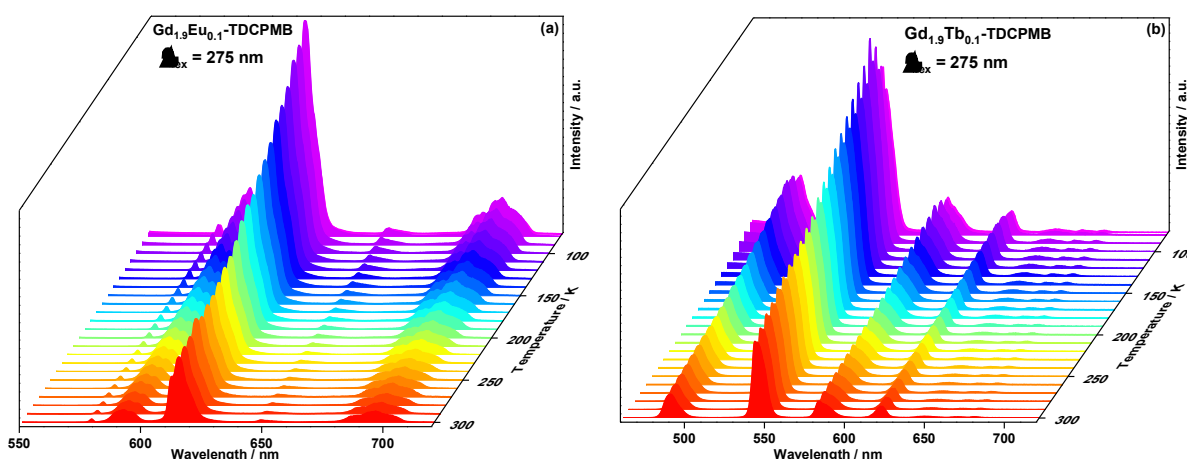


Fig. 58: Emission spectra of Gd_{1.9}Eu_{0.1}-TDCPMB (a) and Gd_{1.9}Tb_{0.1}-TDCPMB (b) recorded between 77 K and 300 K upon excitation at 275 nm and 280 nm, respectively.

Fig. 59a and b show the integrated areas of the emission bands assigned to the $^5D_0 \rightarrow ^7F_2$ (I_{Eu}) and $^5D_4 \rightarrow ^7F_5$ (I_{Tb}) transitions in Gd_{1.9}Eu_{0.1}-TDCPMB and Gd_{1.9}Tb_{0.1}-TDCPMB, respectively. In both cases, the luminescence intensity of the optically active ions decreases substantially with the temperature increase which indicates an effective activation of the nonradiative deactivation pathways on the emitting states of both ions [6]. The emission intensities of Eu^{III} and Tb^{III} decrease to 31% and 41% of their initial values, respectively, as the temperature increases from 77 to 300 K demonstrating that the luminescence of both compounds is temperature-sensitive. The difference in the intensity decrease can be explained in two ways: firstly it can be assigned to the fact that, in comparison to the 5D_4 Tb^{III} emitting state, the emitting state 5D_0 of Eu^{III} is more susceptible to be quenching by structural oscillator [133]. Alternatively, the energy difference of 8,620 cm⁻¹ between the triplet state of the ligand H₆TDCPMB (25,510

cm^{-1}) and the Eu^{III} emitting level $^5\text{D}_0$ ($17,290 \text{ cm}^{-1}$) in $\text{Gd}_{1.9}\text{Eu}_{0.1}\text{TDCPMB}$ is larger than that of the $5,010 \text{ cm}^{-1}$ in the case of Tb^{III} in $\text{Gd}_{1.9}\text{Tb}_{0.1}\text{TDCPMB}$ making more effective the ligand to Tb^{III} energy transfer process with temperature increasing. It is important nothing that for the central ions, the luminescence decreases with the temperature following a near linear profile with the sensitivity values varying from 0.17 to 11.20 and from 0 to $1.24\% \text{ K}^{-1}$ for $\text{Gd}_{1.9}\text{Eu}_{0.1}\text{TDCPMB}$ and $\text{Gd}_{1.9}\text{Tb}_{0.1}\text{TDCPMB}$, respectively probably because the susceptibility of the $^5\text{D}_0$ Eu^{III} to be deactivated by C-H vibrations.

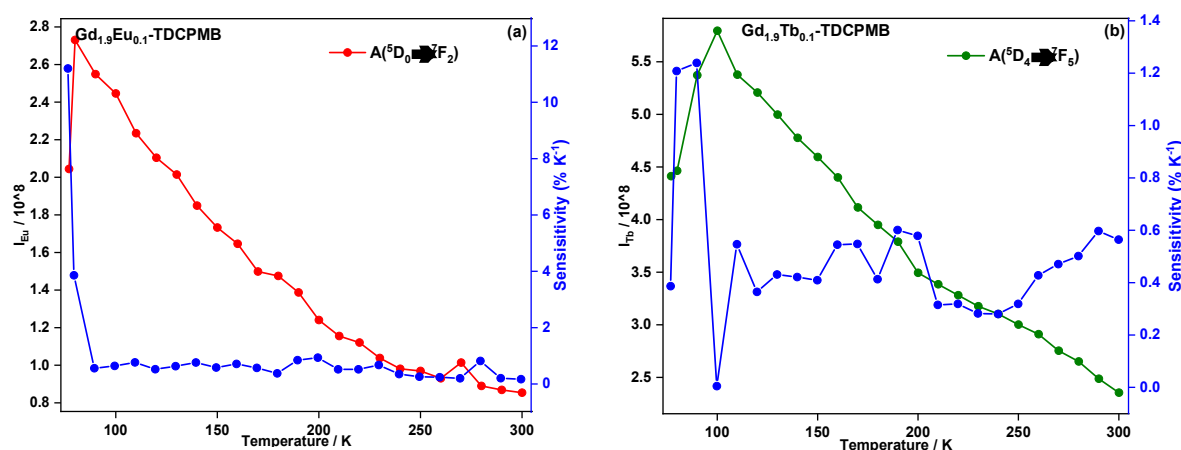


Fig. 59: Relative thermal sensitivities and temperature-dependent of the areas of the bands assigned to the $^5\text{D}_0 \rightarrow ^7\text{F}_2$ and $^5\text{D}_4 \rightarrow ^7\text{F}_5$ transitions for $\text{Gd}_{1.9}\text{Eu}_{0.1}\text{-TDCPMB}$ (a) and $\text{Gd}_{1.9}\text{Tb}_{0.1}\text{-TDCPMB}$ (b) between 77 and 300 K

4.8.2.1. Ratiometric thermometers based on the $\text{Gd}_{1.6-x}\text{Tb}_{0.4}\text{Eu}_x\text{-TDCPMB}$, $x = 0.1, 0.2, 0.3, 0.4, 0.5$) mixed Ln-Cps

The temperature-dependence of the luminescence shown by the compounds $\text{Gd}_{1.9}\text{Eu}_{0.1}\text{TDCPMB}$ and $\text{Gd}_{1.9}\text{Tb}_{0.1}\text{TDCPMB}$ suggest that the Gd^{III} / Tb^{III} / Eu^{III} contained coordination polymers may be potentially used as ratiometric luminescent thermometers. Thus, amounts of Eu^{III} ions were inserted in a Gd-CP with 20 % of Tb^{III} to obtain the multicenter systems ($\text{Gd}_{1.6-x}\text{Tb}_{0.4}\text{Eu}_x\text{TDCPMB}$, $x = 0.1, 0.2, 0.3, 0.4, 0.5$). Their temperature-dependent photoluminescence was recorded in the temperature ranges 77 - 300 K and 273 - 373 K using the liquid nitrogen VNF-100 Cryostat and the F-3004 Peltier Sample Cooler accessories, respectively. As expected, emission spectra of all ternary systems upon excitation in the broad band show emission bands characteristic of both Eu^{III} and Tb^{III} ions. In the investigation of their potential as

radiometric thermal probes, we started with $\text{Gd}_{1.5}\text{Tb}_{0.4}\text{Eu}_{0.1}\text{-TDCPMB}$. Although the excitation spectra of the Tb / Eu mixed compounds exhibit the maxima at 275 nm, the shoulder in the excitation spectrum of Tb-TDCPMB comparing to Eu-TDCPMB (Fig. 40) encouraged us to study the behavior of the emission intensity of the multicenter systems upon excitation in the region where the ligand to Tb^{III} ions energy transfer is better than to Eu^{III} ones. In this case, we expected that being mainly due to an energy transfer from Tb^{III} , the luminescence of Eu^{III} should increase as the temperature increases while the Tb^{III} emission intensity decreases. Such behavior should result in high-sensitive thermometer. The temperature-dependence of the photoluminescence of $\text{Gd}_{1.5}\text{Tb}_{0.4}\text{Eu}_{0.1}$ upon excitation at 330 nm collected in the range 77–300 K in terms of emission intensity is shown in Fig. 60a. Contrary to our expectation, both Eu^{III} and Tb^{III} emission intensity show the same decrease rate in the range 77–300 K (Fig. 60b). Similarly to the observed of the compounds $\text{Gd}_{1.9}\text{Ln}_{0.1}\text{-TDCPMB}$, the luminescence intensity at 300 K is about 40 % of the initial value at 77 K. Therefore, $\text{Gd}_{1.5}\text{Tb}_{0.4}\text{Eu}_{0.1}$ is not a reliable radiometric luminescent thermal sensor in these conditions.

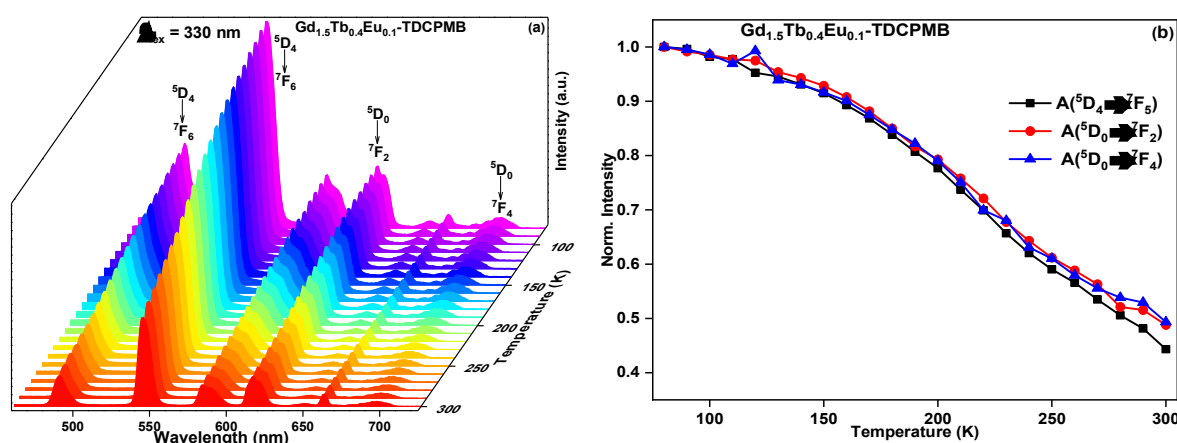


Fig. 60: (a) Temperature-dependent of $\text{Gd}_{1.5}\text{Tb}_{0.4}\text{Eu}_{0.1}\text{-TDCPMB}$ recorded between 77 and 300 K with the excitation wavelength at 330 nm. (b) Corresponding temperature dependence of normalized I_{Tb} and I_{Eu} .

Excited at 275 nm (maximum of the excitation band), the luminescence owing from both Eu^{III} and Tb^{III} ions, between 77 K and 300 K, show a similar decrease rate up to 137 K where the Tb^{III} emission decrease becomes more quickly than Eu^{III} emission probably due to an improvement of the Tb^{III} to Eu^{III} energy transfer as the temperature increases. Such a statement should be supported by the fact that in the compounds $\text{Gd}_{1.9}\text{Ln}_{0.1}\text{-TDCPMB}$, the temperature increasing affects more effectively

the intensity of Eu^{III} ions. The temperature and the ${}^5\text{D}_4 \rightarrow {}^7\text{F}_5 / {}^5\text{D}_0 \rightarrow {}^7\text{F}_2$ and ${}^5\text{D}_4 \rightarrow {}^7\text{F}_5 / {}^5\text{D}_0 \rightarrow {}^7\text{F}_4$ intensity ratios (Fig. 61 c and d) are linearly related with the relative thermal sensitivity ranging from 0.05 to 0.94% K^{-1} and 0.00 to 0.48% K^{-1} respectively. The absolute sensitivity values were estimated to be 0.3 and 1.1% K^{-1} considering, as thermographic parameter, the intensity ratios ${}^5\text{D}_4 \rightarrow {}^7\text{F}_5 / {}^5\text{D}_0 \rightarrow {}^7\text{F}_2$ and ${}^5\text{D}_4 \rightarrow {}^7\text{F}_5 / {}^5\text{D}_0 \rightarrow {}^7\text{F}_4$, respectively.

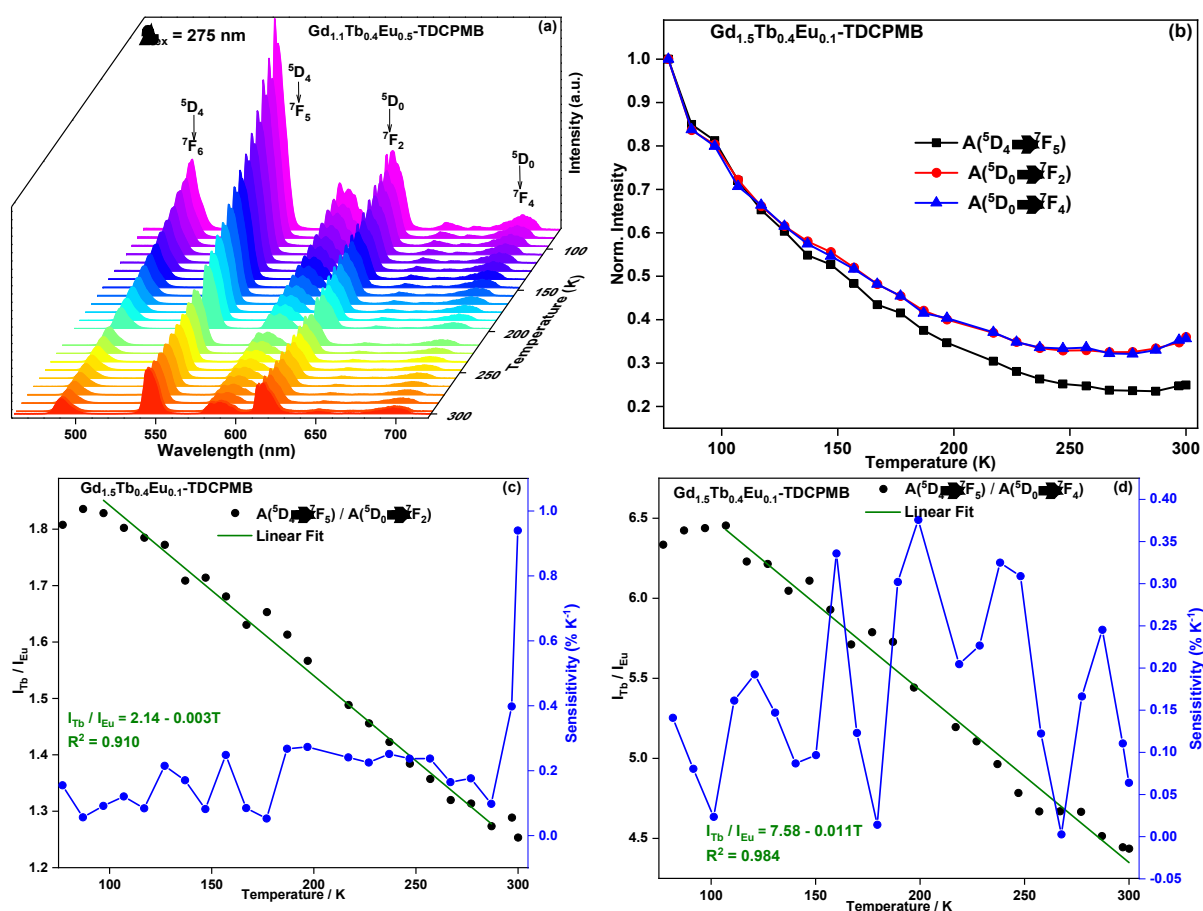


Fig. 61: (a) Temperature-dependent of $\text{Gd}_{1.5}\text{Tb}_{0.4}\text{Eu}_{0.1}\text{-TDCPMB}$ recorded between 77 and 300 K with the excitation wavelength at 275 nm. (b) Corresponding temperature dependence of normalized I_{Tb} and I_{Eu} . (c e d) Corresponding temperature dependence of $I_{\text{Tb}}/I_{\text{Eu}}$.

The variation profile of the emission intensity of both ions with the temperature encourages us to investigate the potential of $\text{Gd}_{1.5}\text{Tb}_{0.4}\text{Eu}_{0.1}$ for high-temperature sensing. Fig. 61a shows the photoluminescence of $\text{Gd}_{1.5}\text{Tb}_{0.4}\text{Eu}_{0.1}\text{-TDCPMB}$ excited at 275 nm, between 273 -373 K. As the temperature increases, the Tb^{III} emission decreases in higher rate, probably due to a Tb^{III} to Eu^{III} energy transfer [92] or / and an increase in the Tb^{III} to ligand back- energy migration with the temperature increasing

as suggested previously. Interestingly, the intensity ratios as functions of the temperature show a very good linear relationship, which can be fitted as linear functions with correlation coefficients R^2 higher than 0.99 and the relative sensitivity between 0.40 and 0.90% K^{-1} (Fig. 62 (c and d)). Furthermore, as can be seen in Fig. 62 c and d, the absolute sensitivities of 1.4 and 4.9% K^{-1} are higher than the values obtained in the temperature range of 77 – 300 K. Thus, those plots suggest that $Gd_{1.5}Tb_{0.4}Eu_{0.1}$ -TDCPMB is promising as probes in luminescent thermometers for high-temperature sensing.

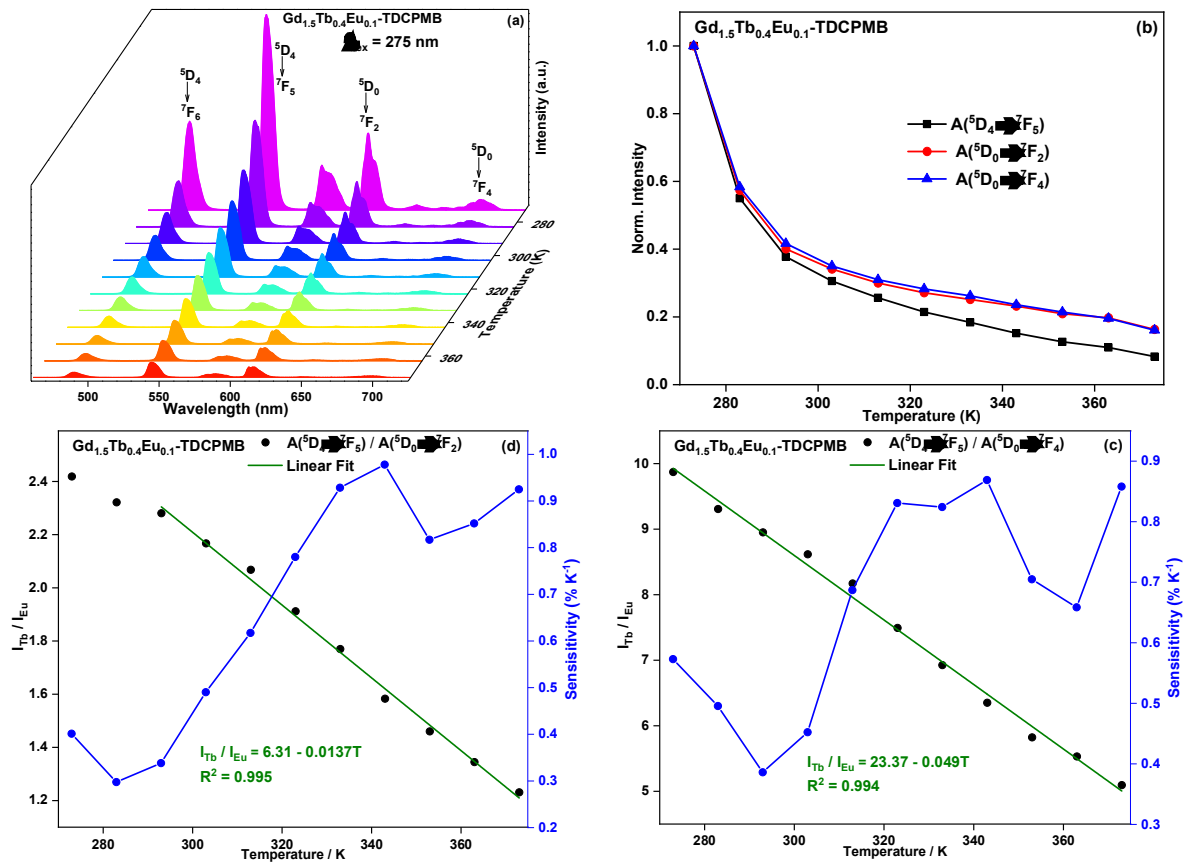


Fig. 62: (a) Temperature-dependent of $Gd_{1.5}Tb_{0.4}Eu_{0.1}$ -TDCPMB recorded between 273 and 373 K with the excitation wavelength at 275 nm. (b) Corresponding temperature dependence of normalized I_{Tb} and I_{Eu} . (c and d) Corresponding temperature dependence of I_{Tb} / I_{Eu} .

To better understand the effect of the temperature on the energy-transfer process occurring in $Gd_{1.5}Tb_{0.4}Eu_{0.1}$ -TDCPMB, the emission lifetime measurement was performed in both temperature ranges 77 - 300K and 273 - 373K as shown in Fig. 63a-b and Fig. 64a-b respectively. The emission lifetime values are listed in Table 6

and Table 7. The emission decay curves of both Tb^{III} or Eu^{III} ions were better fitted by biexponential functions. As can be seen in Fig. 63 (a), the emission lifetimes of Eu^{III} remain practically constant, whereas, the Tb^{III} emission lifetime decreases slightly as the temperature increases. This phenomenon suggests that in the range of 77 – 300 K, the energy transfer rate from ligand to Eu^{III} is not influenced by temperature variations but the Tb^{III} to ligand back-energy transfer rate increase as the temperature increases.

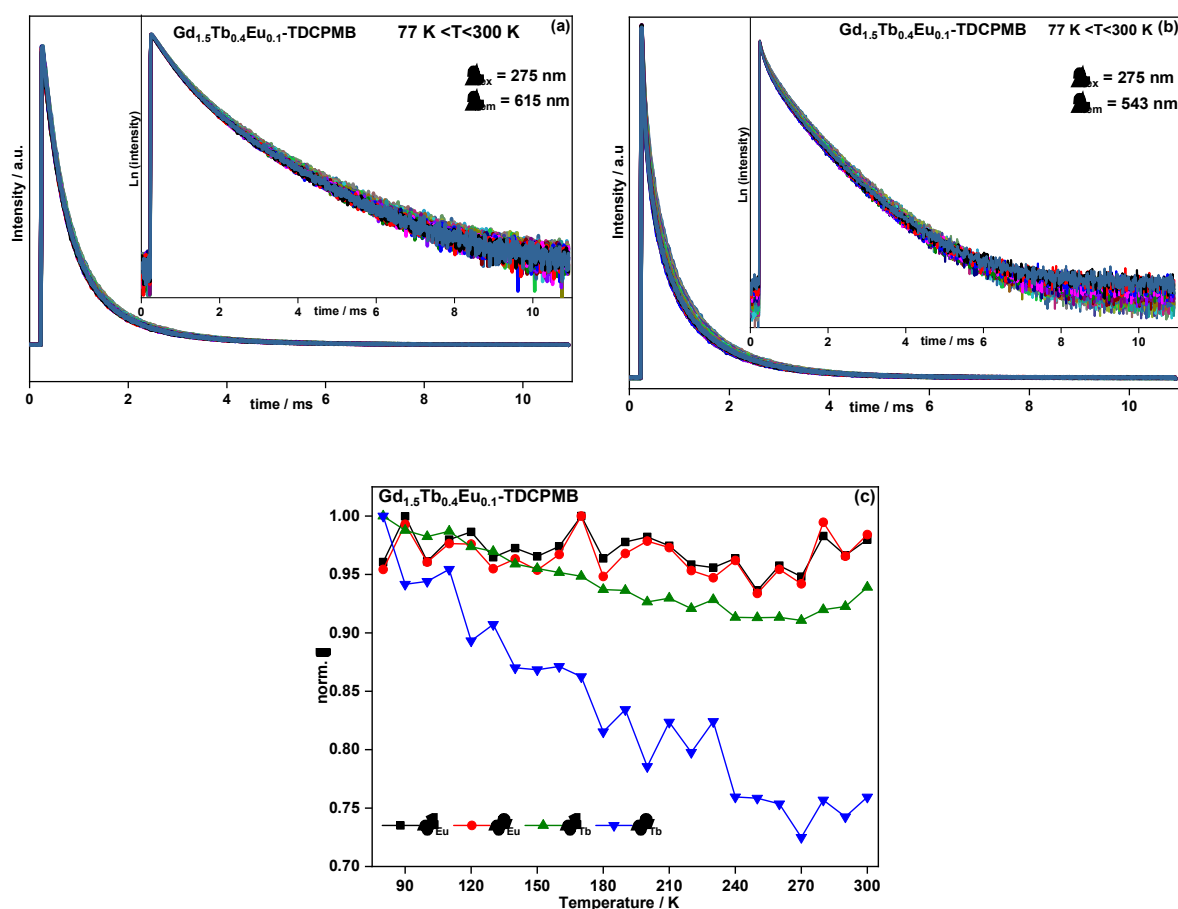


Fig. 63: Emission decay curves of $\text{Gd}_{1.5}\text{Tb}_{0.4}\text{Eu}_{0.1}\text{-TDCPMB}$ excited at 275 nm and monitoring at 615 nm (a) and 543 nm (b) and variation profile of the luminescence lifetime values (c) between 80 and 300 K.

Table 6: Temperature-dependence luminescent decay times (τ) of $\text{Gd}_{1.5}\text{Tb}_{0.4}\text{Eu}_{0.1}\text{I}$ monitored at 543 nm and 615 nm in the temperature range of 77 - 300 K.

Temperature (K)	decay time / ms			
	$\tau^1\text{Eu}$	$\tau^2\text{Eu}$	$\tau^1\text{Tb}$	$\tau^2\text{Tb}$
80	0.45	1.32	0.21	1.01
90	0.47	1.38	0.20	1.00
100	0.45	1.33	0.20	0.99
110	0.46	1.35	0.20	1.00
120	0.46	1.35	0.19	0.98
130	0.45	1.32	0.19	0.98
140	0.46	1.34	0.19	0.97
150	0.45	1.32	0.18	0.96
160	0.46	1.34	0.19	0.96
170	0.47	1.39	0.18	0.96
180	0.45	1.32	0.17	0.95
190	0.46	1.34	0.18	0.95
200	0.46	1.36	0.17	0.93
210	0.46	1.35	0.17	0.94
220	0.45	1.32	0.17	0.93
230	0.45	1.36	0.18	0.94
240	0.45	1.33	0.16	0.92
250	0.44	1.30	0.16	0.92
260	0.45	1.32	0.16	0.92
270	0.45	1.31	0.15	0.92
280	0.46	1.38	0.16	0.93
290	0.45	1.34	0.16	0.93
300	0.46	1.36	0.16	0.95

By varying the temperature between 273 and 373 K, the Eu^{III} emission lifetime decreases until 323 K probably due to the thermal activation of nonradiative deactivation pathways [6]. The increase in the lifetime values after 323 K indicates a better effectivity of the ligand to Eu^{III} energy transfer.

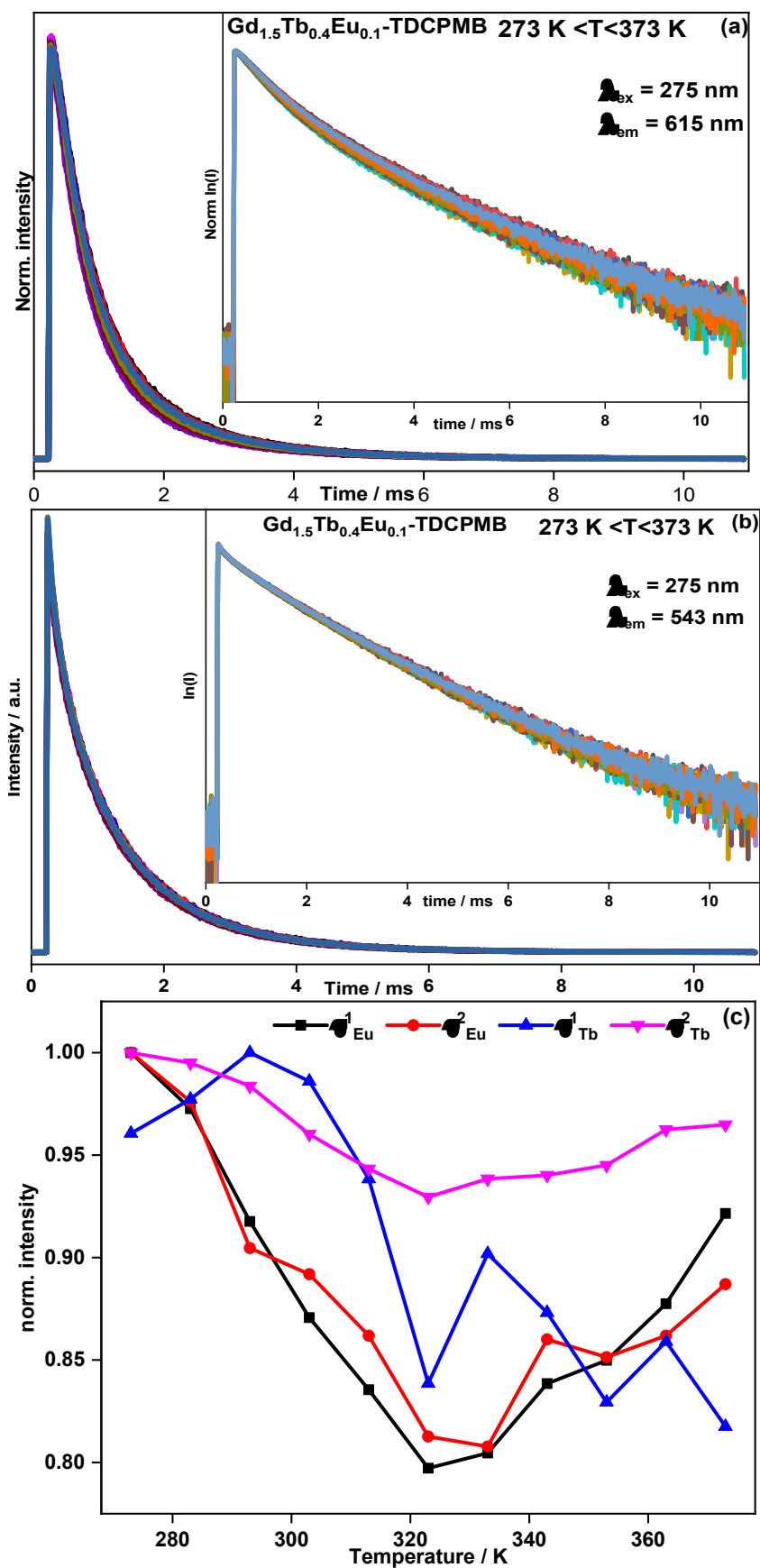


Fig. 64: Emission decay curves of $\text{Gd}_{1.5}\text{Tb}_{0.4}\text{Eu}_{0.1}\text{-TDCPMB}$ upon excitation at 275 nm and monitoring at 615 nm (a) and 543 nm (b) and variation profile of the luminescence lifetime values (c) between 273 and 373 K.

Table 7: Temperature-dependence emission lifetimes (τ) of Gd_{1.5}Tb_{0.4}Eu_{0.1}-TDCPMB monitored at 543 nm and 614 nm in the temperature range of 273 to 373 K

Temperature (K)	Decay time (ms)			
	$\tau^1\text{Eu}$	$\tau^2\text{Eu}$	$\tau^1\text{Tb}$	$\tau^2\text{Tb}$
273	0.67	1.98	0.25	1.16
283	0.65	1.94	0.25	1.16
293	0.61	1.80	0.26	1.15
303	0.58	1.77	0.26	1.12
313	0.56	1.7	0.24	1.10
323	0.53	1.61	0.22	1.10
333	0.54	1.60	0.23	1.10
343	0.56	1.71	0.23	1.10
353	0.56	1.69	0.22	1.10
363	0.59	1.71	0.22	1.12
373	0.62	1.76	0.21	1.12

The temperature sensing properties of all other H₆TDCPMB-based co-doped CPs were investigated in terms of emission intensity ratio. Fig. 65 a-d and Fig. 66 a-d show the investigation of the potential of Gd_{1.3}Tb_{0.4}Eu_{0.3}-TDCPMB as a self-referencing luminescent thermometer in the temperature ranges of 77-300 K and 273 – 373 K, respectively. As can be seen in Fig. 65b, with temperature increasing from 100 to 300 K, the emission intensity of Tb^{III} decreases while increases the Eu^{III} emission intensity. The plots of the emission intensity ratios $^5\text{D}_4 \rightarrow ^7\text{F}_5 / ^5\text{D}_0 \rightarrow ^7\text{F}_2$ and $^5\text{D}_4 \rightarrow ^7\text{F}_5 / ^5\text{D}_0 \rightarrow ^7\text{F}_4$ as functions of the temperature (Fig. 65c and Fig. 65d, respectively) have been fitted by linear functions with a coefficient correlation R^2 of 0.99 and absolute thermal sensitivities of 0.17 and 0.56% K⁻¹ respectively. The correlation coefficient suggests Gd_{1.3}Tb_{0.4}Eu_{0.3}-TDCPMB as um accurate self-referenced optical thermal probe in the temperature 100 – 300 K. However, in the investigation carried out in the range 278 – 373 K, the $I_{\text{Tb}}/I_{\text{Eu}}$ ratio shows an increase in the temperature range up to 300 K, thus an opposite behavior regarding to the observed when the study was carried out in the range 77 – 300 K. The self-calibrated ratiometric parameters $I_{\text{Tb}}/I_{\text{Eu}}$ and temperature relationships were fitted by linear functions with correlation coefficient R^2 near unity (Fig. 66 c-d) in the temperature ranging from 323 to 373 K. The measurements realized for the CPs Gd_{1.2}Tb_{0.4}Eu_{0.4}-TDCPMB and Gd_{1.1}Tb_{0.4}Eu_{0.5}-TDCPMB are exhibited in Fig. 67-70. In general, it was observed that the variations of the emission intensities and consequently the emission intensity ratios are strongly dependent on the molar fractions of the trivalent lanthanide ions in the co-doped systems. Relatively low

values were obtained for the thermal sensitivities as a consequence of the fact that emission intensities of both Eu^{III} and Tb^{III} decrease simultaneously as the temperature increases.

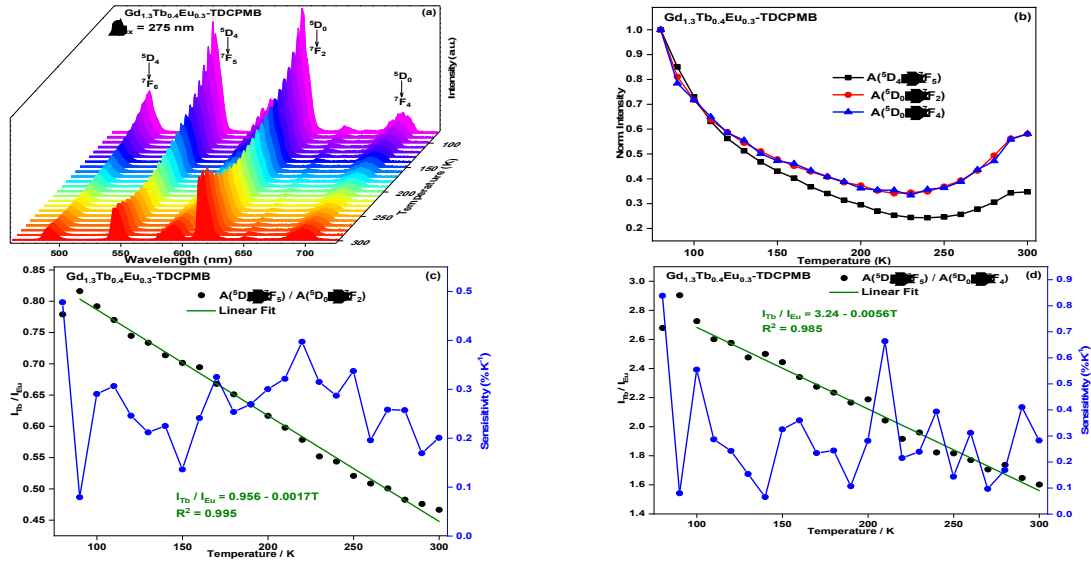


Fig. 65: (a) Temperature-dependent of $\text{Gd}_{1.3}\text{Tb}_{0.4}\text{Eu}_{0.3}\text{-TDCPMB}$ recorded between 77 and 300 K with the excitation wavelength at 275 nm. (b) Corresponding temperature dependence of normalized I_{Tb} and I_{Eu} . (c) Corresponding temperature dependence of $I_{\text{Tb}} / I_{\text{Eu}}$.

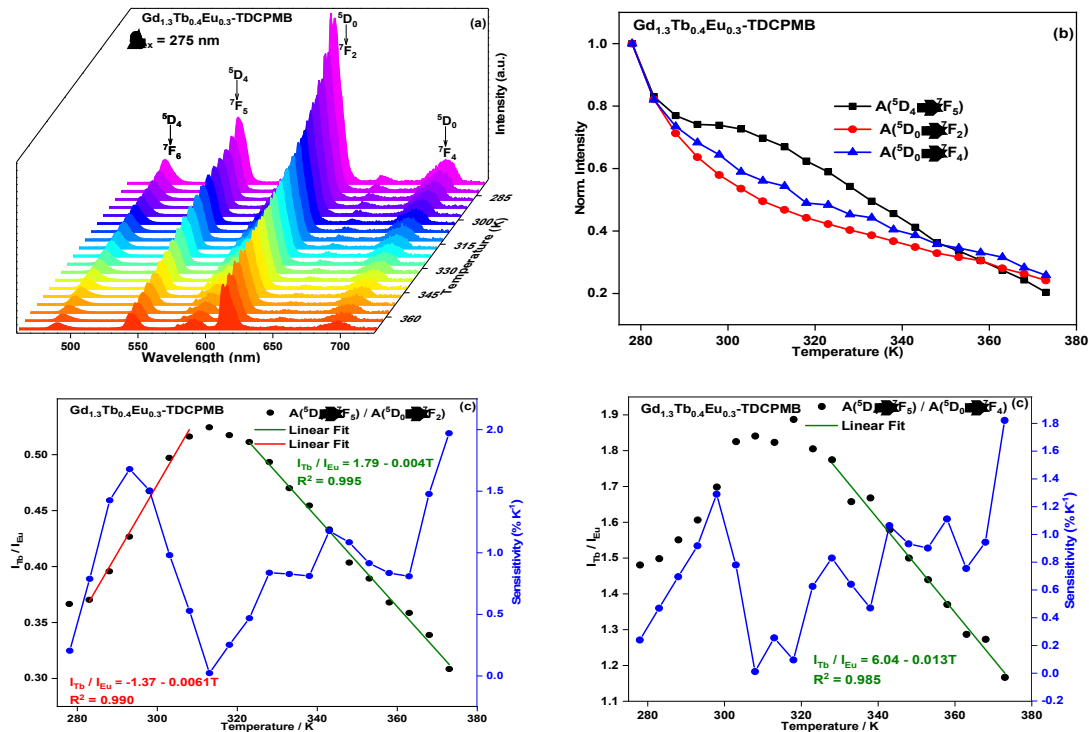


Fig. 66: (a) Temperature-dependent of $\text{Gd}_{1.3}\text{Tb}_{0.4}\text{Eu}_{0.3}\text{-TDCPMB}$ recorded between 278 and 373 K with the excitation wavelength at 275 nm. (b) Corresponding temperature dependence of normalized I_{Tb} and I_{Eu} . (c) Corresponding temperature dependence of $I_{\text{Tb}} / I_{\text{Eu}}$.

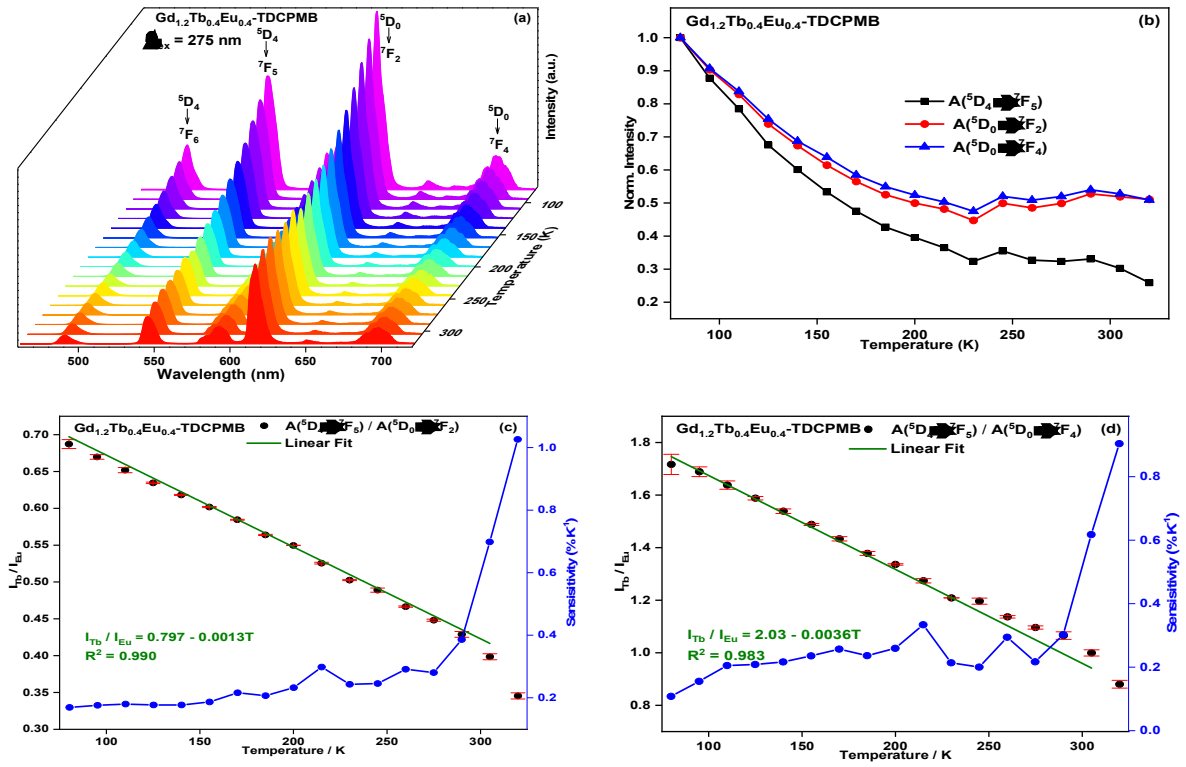


Fig. 67: (a) Temperature-dependent of $\text{Gd}_{1.2}\text{Tb}_{0.4}\text{Eu}_{0.4}\text{-TDCPMB}$ recorded between 77 and 320 K with the excitation wavelength at 275 nm. (b) Corresponding temperature dependence of normalized I_{Tb} and I_{Eu} . (c) Corresponding temperature dependence of $I_{\text{Tb}} / I_{\text{Eu}}$.

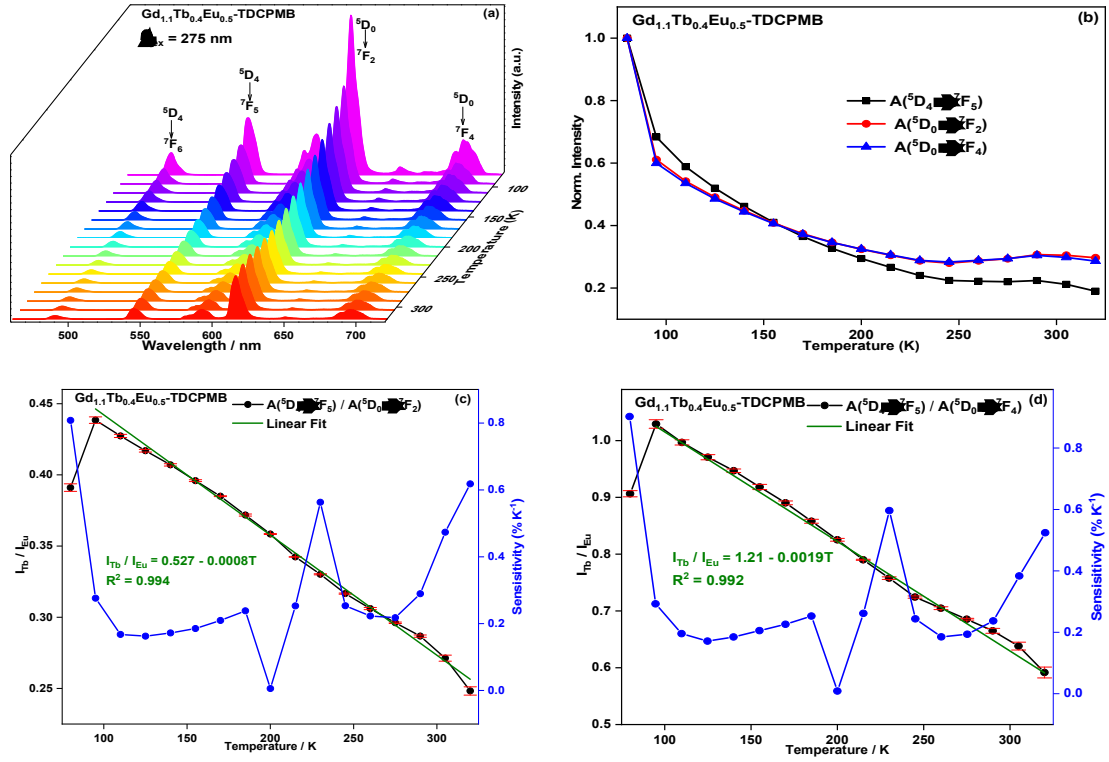


Fig. 68: (a) Temperature-dependent of $\text{Gd}_{1.1}\text{Tb}_{0.4}\text{Eu}_{0.5}\text{-TDCPMB}$ recorded between 77 and 320 K with the excitation wavelength at 275 nm. (b) Corresponding temperature dependence of normalized I_{Tb} and I_{Eu} . (c) and (d) Corresponding temperature dependence of $I_{\text{Tb}} / I_{\text{Eu}}$.

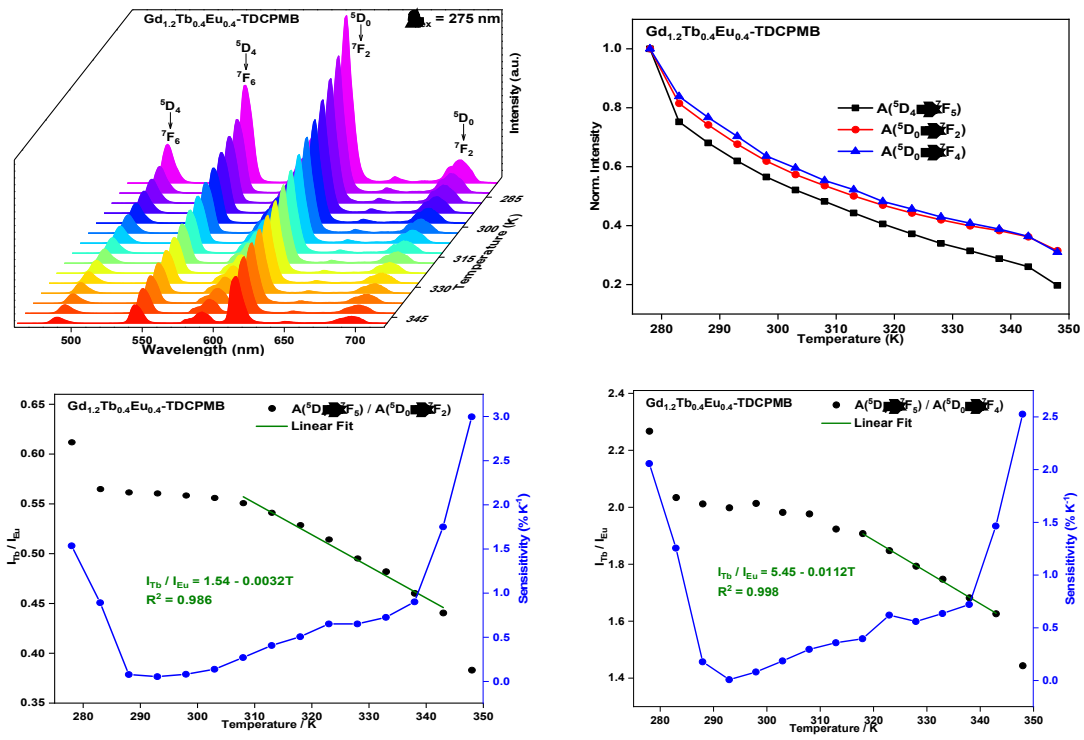


Fig. 69: (a) Temperature-dependent of $\text{Gd}_{1.2}\text{Tb}_{0.4}\text{Eu}_{0.4}\text{-TDCPMB}$ recorded between 278 and 348 K with the excitation wavelength at 275 nm. (b) Corresponding temperature dependence of normalized I_{Tb} and I_{Eu} . (c) and (d) Corresponding temperature dependence of $I_{\text{Tb}}/I_{\text{Eu}}$

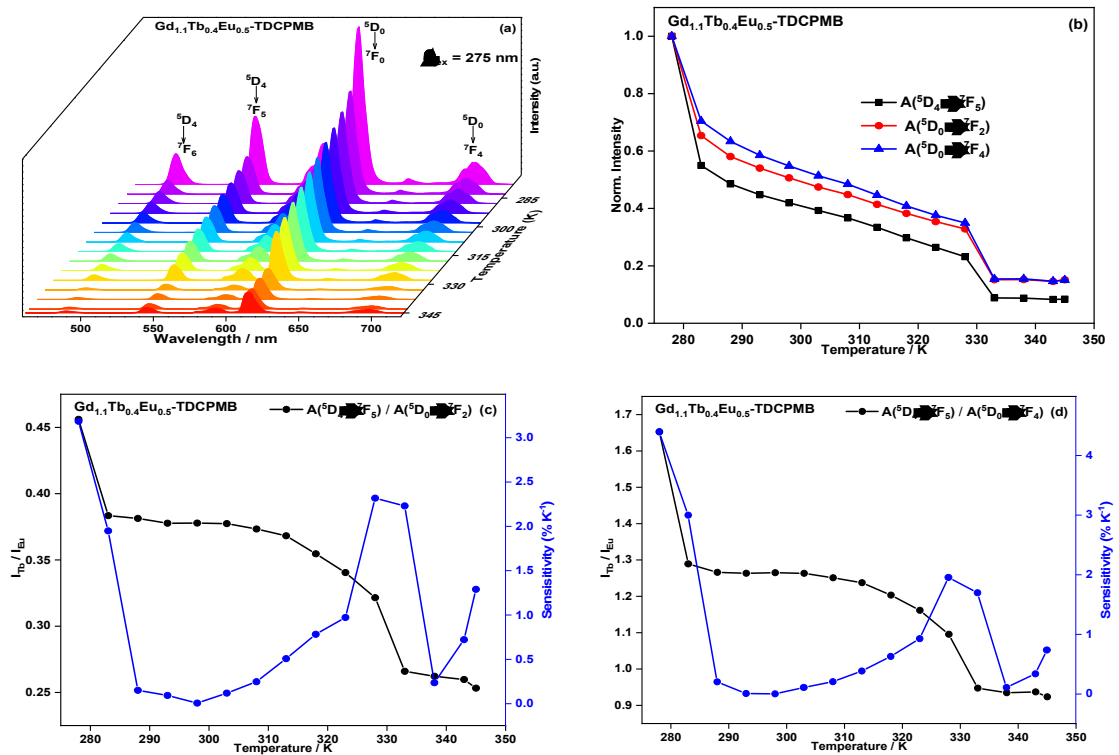


Fig. 70: (a) Temperature-dependent of $\text{Gd}_{1.1}\text{Tb}_{0.4}\text{Eu}_{0.5}\text{-TDCPMB}$ recorded between 278 and 345 K with the excitation wavelength at 280 nm. (b) Corresponding temperature dependence of normalized I_{Tb} and I_{Eu} . (c) and (d) Corresponding temperature dependence of $I_{\text{Tb}}/I_{\text{Eu}}$

4.8.3. Compounds based on the ligand H₂BDC and HAC

Temperature-dependent photoluminescence was investigated for both compounds Tb_{0.93}Eu_{0.07}-BDC-AC and Tb_{0.993}Eu_{0.007}-BDC-AC. Tb_{0.93}Eu_{0.07}-BDC-AC exhibits a significantly different temperature-dependent luminescence behavior with respect to the emissions of Eu^{III} and Tb^{III} ions. With the increase in temperature from 80 to 300 K, the intensity of the Tb^{III} emission band assigned to the ⁵D₄ → ⁷F₅ transition decreases progressively by about 72%. The intensities of the Eu^{III} emission bands attributed to the transitions ⁵D₀ → ⁷F₂ and ⁵D₀ → ⁷F₄ increase slightly by about 3% in the temperature range 80 – 155 K (Fig. 71b). However, between 155 and 300 K, the emissions from Eu^{III} starts decreasing to about 30%. Such results suggest the occurrence of energy transfer from Tb^{III} to Eu^{III} but also an effective non-radiative deactivation of the emitting states by thermal activation. As depicted in Fig. 71a-d, the temperature can be readily correlated to the emission intensity ratios (I_{Tb} / I_{Eu}). In particular, it shows a linear relationship with temperature from 80 to 180 K with correlation factor near unity and relative thermal sensitivities ranging from 0.1 to 0.6% K⁻¹ proving the potential of Tb_{0.93}Eu_{0.07}-BDC-AC as a ratiometric probe for low-temperature sensing.

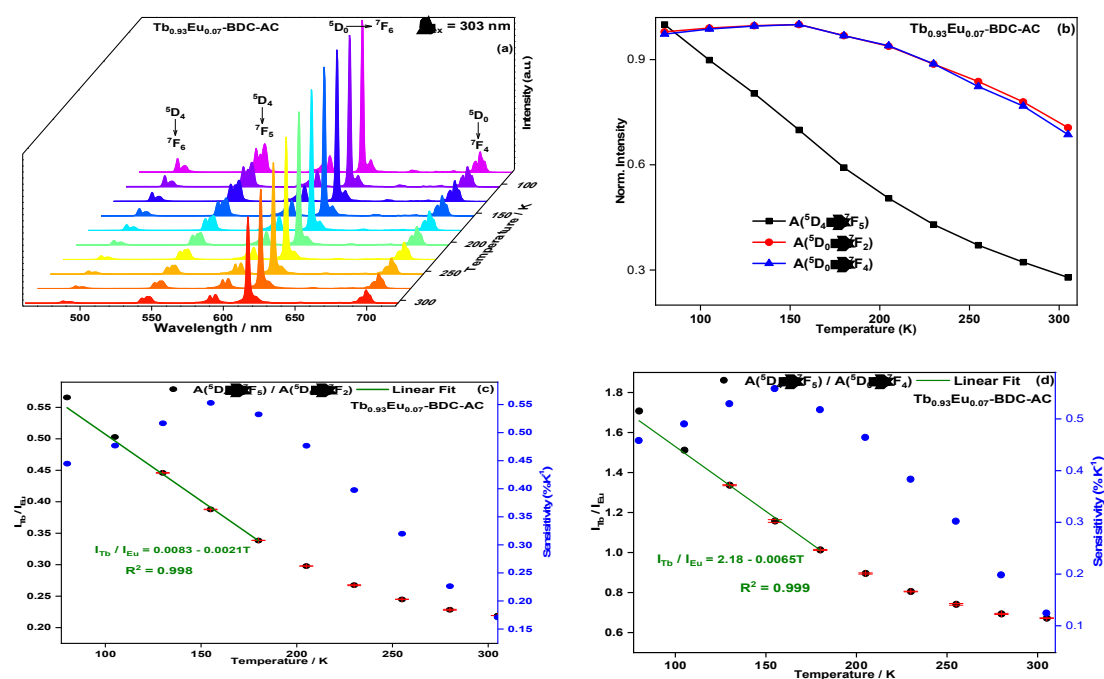


Fig. 71: (a) Solid-state emission spectra of Tb_{0.93}Eu_{0.07}-BDC-AC recorded between 80 -300 K. (b) Temperature-dependent areas of the ⁵D₀ → ⁷F₂, ⁵D₀ → ⁷F₄ and ⁵D₄ → ⁷F₅ transitions. (c and d) Temperature-dependent intensity ratio ⁵D₄ → ⁷F₅ / ⁵D₀ → ⁷F₂ and ⁵D₄ → ⁷F₅ / ⁵D₀ → ⁷F₄ between 80 and 300 K.

The significantly temperature-dependent luminescence behaviors of both Tb^{III} and Eu^{III} in Tb_{0.993}Eu_{0.007}-BDC-AC enable us to investigate the performance as a ratiometric thermal of Tb_{0.993}Eu_{0.007}-BDC-AC. The temperature-dependence of the photoluminescence, the variations of the areas of the $^5D_0 \rightarrow ^7F_2$, $^5D_0 \rightarrow ^7F_4$, and $^5D_4 \rightarrow ^7F_5$ transition bands, and the intensity ratios are shown in Fig. 72. As can be seen in Fig. 72b, the variations of the emission intensities are different compared to Tb_{0.93}Eu_{0.07}-BDC-AC indicating a significant change in the rates of energy migration processes. The linear correlation between temperature and intensity ratios extends over a large temperature range in comparison to Tb_{0.93}Eu_{0.07}, however with lower values of the relative sensitivity which ranges between 0.1 and 0.36% K⁻¹. It is important to detach the higher value of absolute sensitivity (4.8%) when the thermographic parameter is defined as the ratio between the $^5D_0 \rightarrow ^7F_4$ Eu^{III} and $^5D_4 \rightarrow ^7F_5$ Tb^{III} emissions.

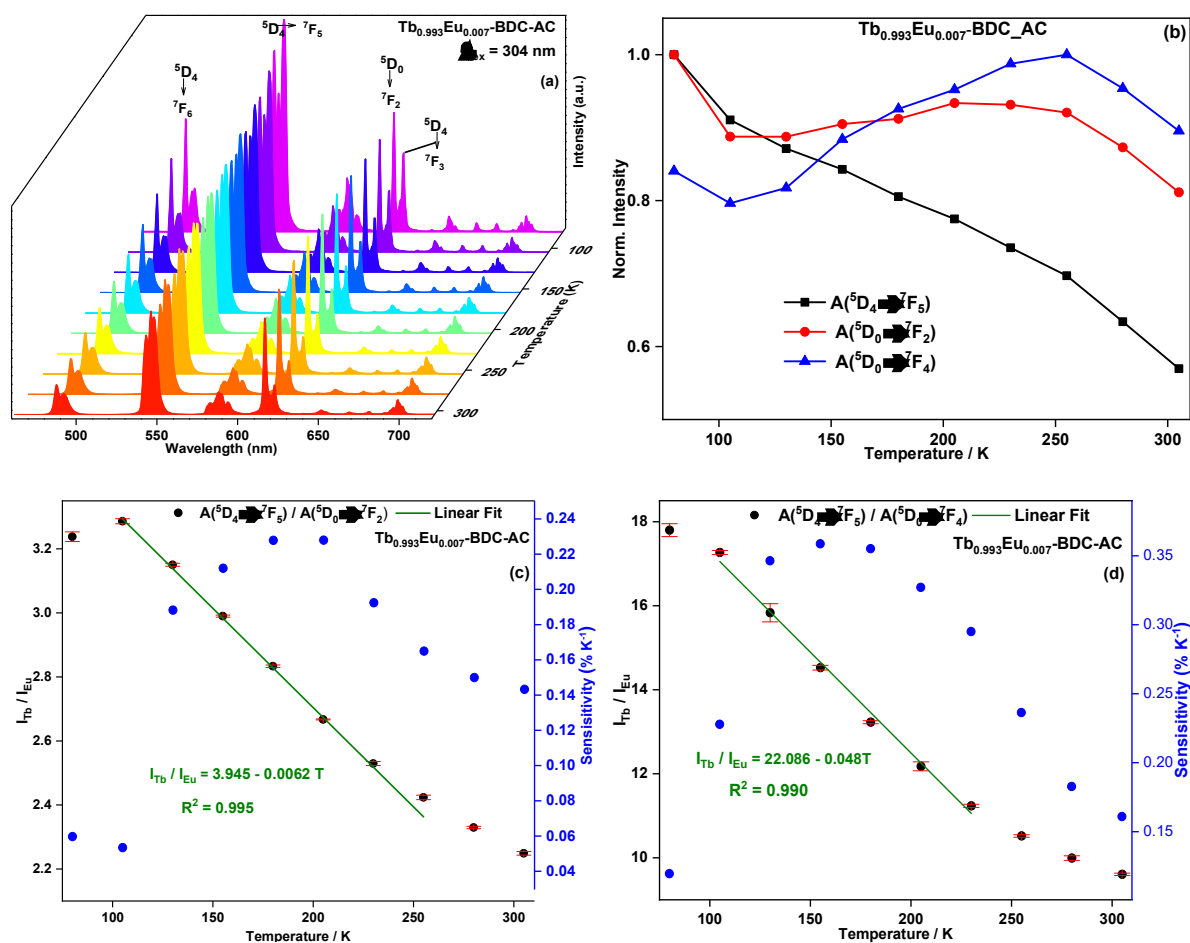


Fig. 72: (a) Solid-state emission spectra of Tb_{0.993}Eu_{0.007}-BDC-AC recorded between 80 -305 K. (b) Temperature-dependent areas of the $^5D_0 \rightarrow ^7F_2$, $^5D_0 \rightarrow ^7F_4$ and $^5D_4 \rightarrow ^7F_5$ transitions. (c and d) Temperature-dependent intensity ratio $^5D_4 \rightarrow ^7F_5 / ^5D_0 \rightarrow ^7F_2$ and $^5D_4 \rightarrow ^7F_5 / ^5D_0 \rightarrow ^7F_4$ between 80 and 305 K.

4.8.4. Compounds based on the ligand H₂BDC and Hacac

The temperature-dependent photophysical properties were investigated for all compounds represented by $\text{Tb}_x\text{Eu}_{1-x}\text{acac}_x\text{BDC}_{1.5-x/2}$ in terms of intensity. The temperature dependence of the emission spectra recorded between 80 and 300 K, the integrated intensities of the $^5\text{D}_4 \rightarrow ^7\text{F}_5$ (Tb^{III}), $^5\text{D}_0 \rightarrow ^7\text{F}_2$ (Eu^{III}) and $^5\text{D}_0 \rightarrow ^7\text{F}_4$ (Eu^{III}) and the intensity ratios are shown in Fig. 73 - Fig. 77 for $x = 0.99, 0.95, 0.90, 0.85$ and 0.75 , respectively. The temperature dependences of the luminescence intensities of both Tb^{III} and Eu^{III} exhibit different behaviors as their relative fractions change indicating a dependence of ions-ions energy transfer rates with the relative molar fractions. Another important fact to be noted is the significant temperature-dependent behavior of the $^5\text{D}_0 \rightarrow ^7\text{F}_2$ and $^5\text{D}_0 \rightarrow ^7\text{F}_4$ Eu^{III} transitions. Such discrepancy which decreases as the Eu^{III} fraction increases may be explained considering the Tb^{III} emission at 621 nm whose is more important where Eu^{III} is in smaller fractions. In general, for all mixed compounds, the Eu^{III} emission intensity increases while that of Tb^{III} decreases with the temperature increasing. Such a fact may be interpreted as an indication of an energy migration from the Tb^{III} to Eu^{III} ions, probably, based on the phonon-assisted Förster energy transfer mechanism [134]. The energy gaps of 4,800 and 2,700 cm^{-1} respectively, between the Tb^{III} emitting level $^5\text{D}_4$ and the excited triplet states of the ligands acac^- and BDC^{2-} respectively, suggest that the quenching of the Tb^{III} luminescence with increasing temperature may be partly assigned to a Tb^{III} to BDC^{2-} energy back-transfer.

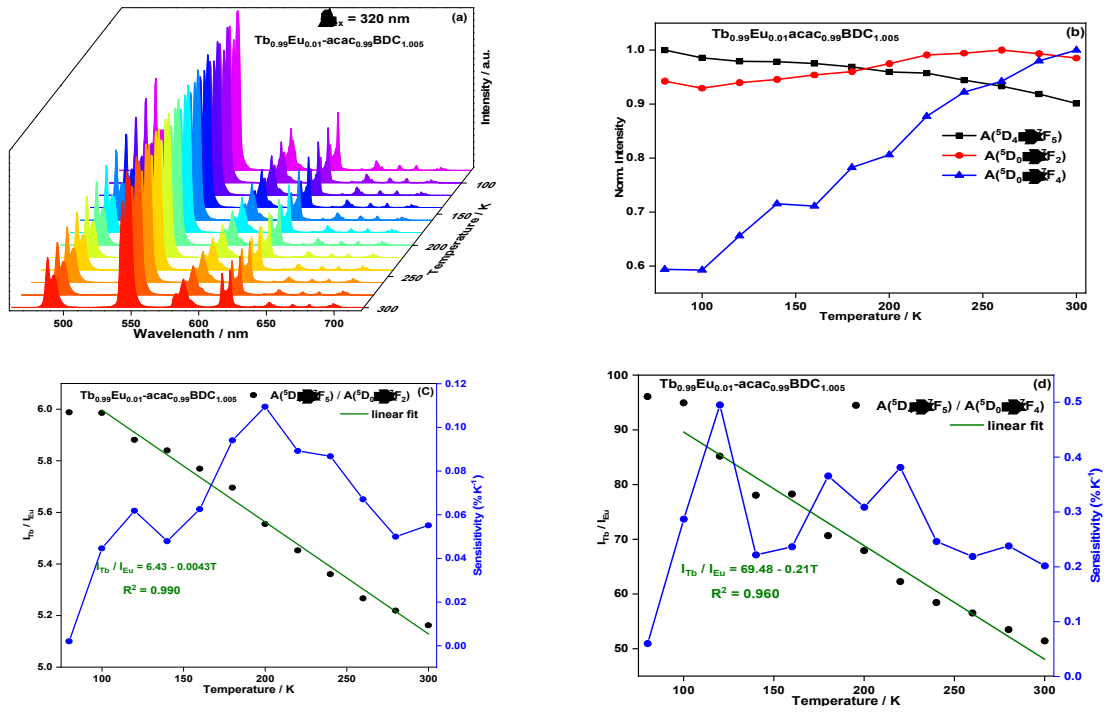


Fig. 73: (a) Emission spectra of $\text{Tb}_{0.99}\text{Eu}_{0.01}\text{acac}_{0.99}\text{BDC}_{1.005}$ recorded between 80 and 300 K upon excitation at 320 nm. (b) temperature dependence of the normalized integrated intensities of the $^5\text{D}_4 \rightarrow ^7\text{F}_5$, $^5\text{D}_0 \rightarrow ^7\text{F}_2$ and $^5\text{D}_0 \rightarrow ^7\text{F}_4$ (c) and (d) Temperature dependence of the integrated intensity ratio of Tb^{III} and Eu^{III}. The green and the blue curves represent the linear fitting of the intensity ratios and the relative sensitivities respectively.

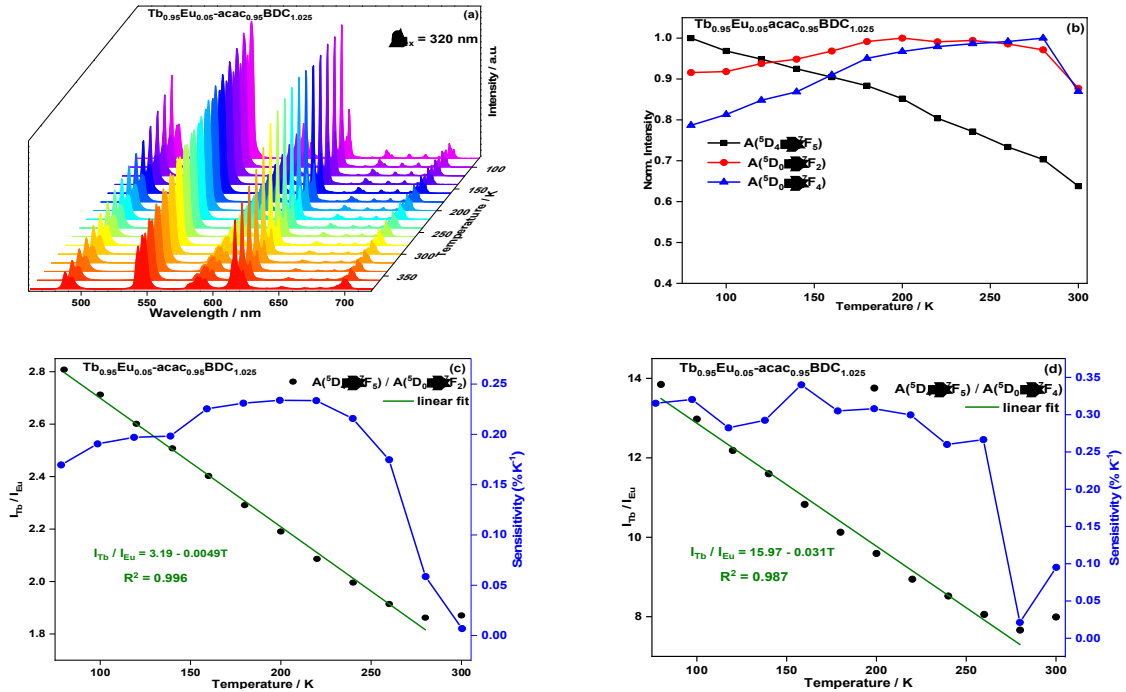


Fig. 74: (a) Emission spectra of $\text{Tb}_{0.95}\text{Eu}_{0.05}\text{acac}_{0.95}\text{BDC}_{1.025}$ recorded between 80 and 300 K upon excitation at 320 nm. (b) temperature dependence of the normalized integrated intensities of the $^5\text{D}_4 \rightarrow ^7\text{F}_5$, $^5\text{D}_0 \rightarrow ^7\text{F}_2$ and $^5\text{D}_0 \rightarrow ^7\text{F}_4$ (c) and (d) Temperature dependence of the integrated intensity ratio of Tb^{III} and Eu^{III}. The green and the blue curves represent the linear fitting of the intensity ratios and the relative sensitivities respectively.

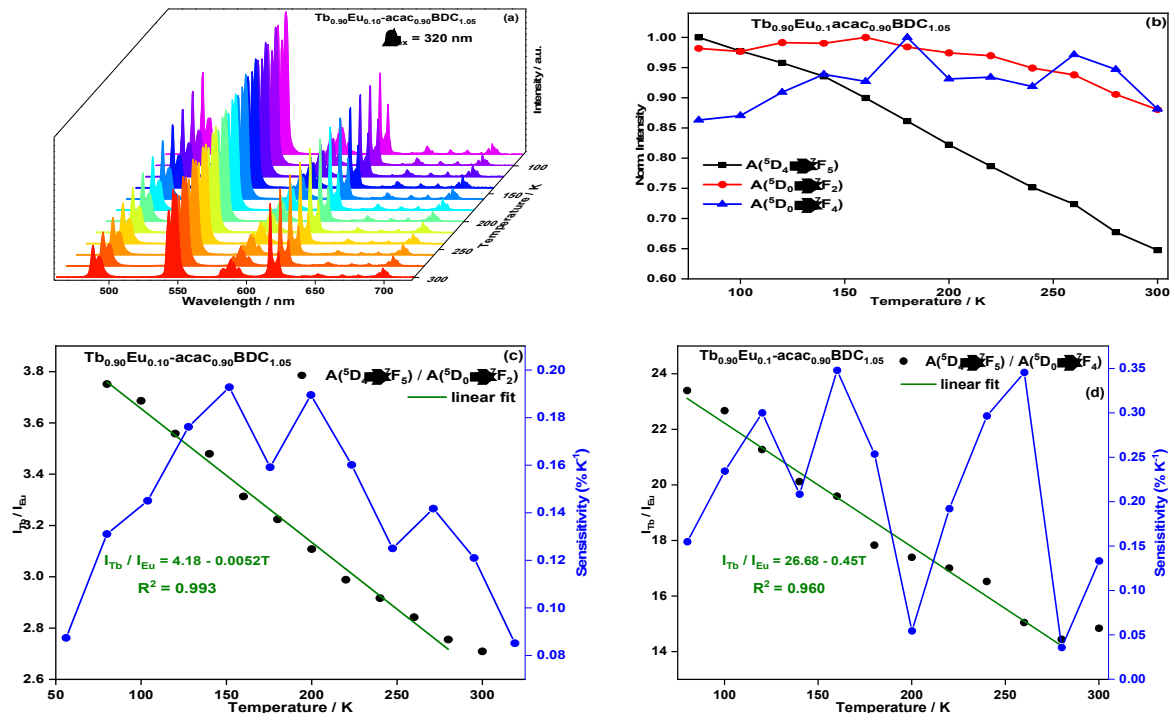


Fig. 75: (a) Emission spectra of $\text{Tb}_{0.90}\text{Eu}_{0.10}\text{acac}_{0.90}\text{BDC}_{1.05}$ recorded between 80 and 300 K upon excitation at 320 nm. (b) temperature dependence of the normalized integrated intensities of the $^5\text{D}_4 \rightarrow ^7\text{F}_5$, $^5\text{D}_0 \rightarrow ^7\text{F}_2$ and $^5\text{D}_0 \rightarrow ^7\text{F}_4$ (c) and (d) Temperature dependence of the integrated intensity ratio of Tb^{III} and Eu^{III}. The green and the blue curves represent the linear fitting of the intensity ratios and the relative sensitivities respectively.

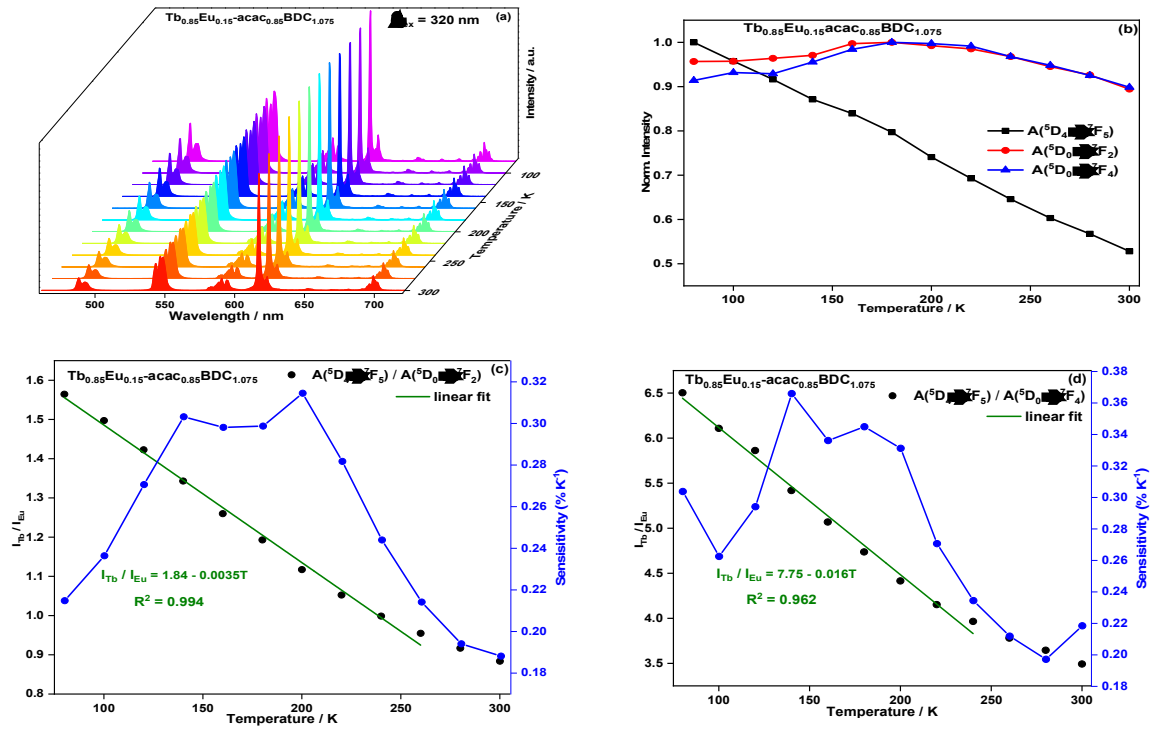


Fig. 76: (a) Emission spectra of $\text{Tb}_{0.85}\text{Eu}_{0.15}\text{acac}_{0.90}\text{BDC}_{1.05}$ recorded between 80 and 300 K upon excitation at 320 nm. (b) temperature dependence of the normalized integrated intensities of the $^5\text{D}_4 \rightarrow ^7\text{F}_5$, $^5\text{D}_0 \rightarrow ^7\text{F}_2$ and $^5\text{D}_0 \rightarrow ^7\text{F}_4$ (c) and (d) Temperature dependence of the integrated intensity ratio of Tb^{III} and Eu^{III}. The green and the blue curves represent the linear fitting of the intensity ratios and the relative sensitivities respectively.

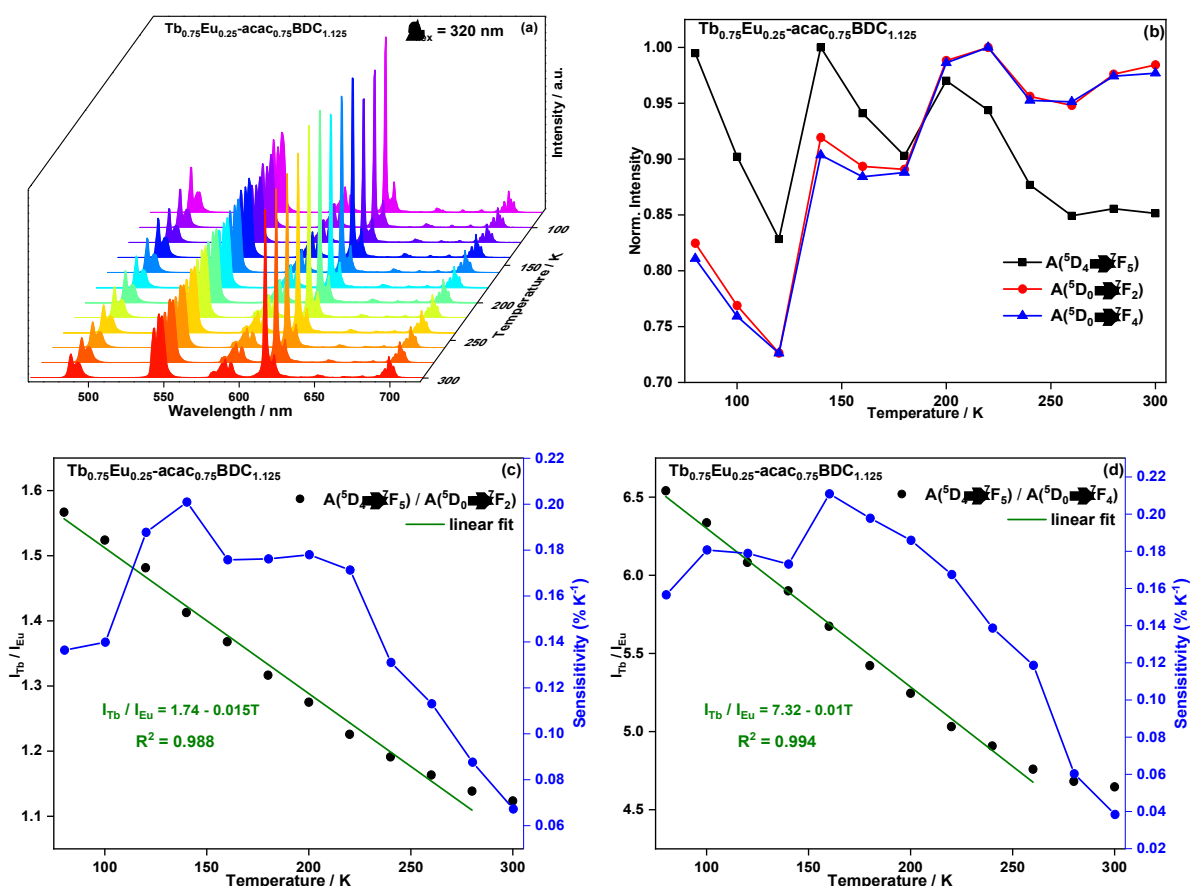


Fig. 77: (a) Emission spectra of $\text{Tb}_{0.75}\text{Eu}_{0.25}\text{-acac}_{0.75}\text{BDC}_{1.125}$ recorded between 80 and 300 K upon excitation at 320 nm. (b) temperature dependence of the normalized integrated intensities of the $^5\text{D}_4 \rightarrow ^7\text{F}_5$, $^5\text{D}_0 \rightarrow ^7\text{F}_2$ and $^5\text{D}_0 \rightarrow ^7\text{F}_4$ (c) and (d) Temperature dependence of the integrated intensity ratio of Tb^{III} and Eu^{III}. The green and the blue curves represent the linear fitting of the intensity ratios and the relative sensitivities respectively.

It is worth noting that, for all investigated compounds, the temperature can be readily correlated to the emission intensity ratios $^5\text{D}_4 \rightarrow ^7\text{F}_5 / ^5\text{D}_0 \rightarrow ^7\text{F}_2$ and $^5\text{D}_4 \rightarrow ^7\text{F}_5 / ^5\text{D}_0 \rightarrow ^7\text{F}_2$ in the whole temperature range of 80 – 280 K with interesting sensing performance quantified by the absolute thermal sensitivities values. Considering the $^5\text{D}_4 \rightarrow ^7\text{F}_5 / ^5\text{D}_0 \rightarrow ^7\text{F}_2$ intensity ratio, the absolute thermal sensitivity values obtained for $x = 0.99; 0.95; 0.90; 0.85$ and 0.75 were: 0.43, 0.49, 0.52, 0.35, 1.5% K⁻¹, respectively and when based on the $^5\text{D}_4 \rightarrow ^7\text{F}_5 / ^5\text{D}_0 \rightarrow ^7\text{F}_2$ the S_a values were determined to be: 21, 3.1, 45, 1.6, 10% K⁻¹, respectively. These values are much larger than the 0.14 obtained for $\text{Tb}_{0.99}\text{Eu}_{0.01}(\text{BDC})_{1.5}(\text{H}_2\text{O})_2$ investigated as a luminescent thermometer in the physiological range (300 – 320 K) [84]. Furthermore, the maxima relative thermal sensitivity values (Table 8) are, in general, much higher than the 0.14% K⁻¹ reported for $\text{Tb}_{0.99}\text{Eu}_{0.01}(\text{BDC})_{1.5}(\text{H}_2\text{O})_2$ comparable to the estimated one for

Tb_{0.99}Eu_{0.01}acac_{0.99}BDC_{1.005} varying up to 0.11 % K⁻¹ and 0.5% K⁻¹ for ⁵D₄ → ⁷F₅ / ⁵D₀ → ⁷F₂ and ⁵D₄ → ⁷F₅ / ⁵D₀ → ⁷F₄, respectively. The fact that the temperature can be linearly related to the intensity ratio and the relatively high values of absolute sensitivities considering the fitting curves suggest these compounds are promising as ratiometric temperature probes.

To make easier the comparison between all the investigated systems, their operating range, absolute and maximum relative thermal sensitivities are compiled in Table 8.

Table 8: Composition, working ranges, absolute sensitivity values (S_a) and maximum relative sensitivity values (max S_r) of the CPs studied as ratiometric thermal probes.

Ligand	CPs	Range / K	S_a / %K ⁻¹	Max S_r / %K ⁻¹	T_{MaxSr} / K	I_{Tb} / I_{Eu}
H₃TCPMB	Tb _{0.95} Eu _{0.05} -TCPMB	333-348	17.00	14.8	348	⁵ D ₄ → ⁷ F ₅ / ⁵ D ₀ → ⁷ F ₂
			165.90	21.1		⁵ D ₄ → ⁷ F ₅ / ⁵ D ₀ → ⁷ F ₄
		338-348	27.2	41.60		⁵ D ₄ → ⁷ F ₅ / ⁵ D ₀ → ⁷ F ₂
			152.00	55.70		⁵ D ₄ → ⁷ F ₅ / ⁵ D ₀ → ⁷ F ₄
H₆TDCPMB	Gd _{1.5} Tb _{0.4} Eu _{0.1} -TDCPMB	97- 287	0.30	0.94	300	⁵ D ₄ → ⁷ F ₅ / ⁵ D ₀ → ⁷ F ₂
		107-300	1.10	0.38	197	⁵ D ₄ → ⁷ F ₅ / ⁵ D ₀ → ⁷ F ₄
		293-373	1.40	0.98	343	⁵ D ₄ → ⁷ F ₅ / ⁵ D ₀ → ⁷ F ₂
		273-373	4.90	0.87		⁵ D ₄ → ⁷ F ₅ / ⁵ D ₀ → ⁷ F ₄
	Gd _{1.3} Tb _{0.4} Eu _{0.3} -TDCPMB	90-300	0.17	0.48	80	⁵ D ₄ → ⁷ F ₅ / ⁵ D ₀ → ⁷ F ₂
		100-300	0.56	0.84		⁵ D ₄ → ⁷ F ₅ / ⁵ D ₀ → ⁷ F ₄
		283-308	0.61	1.68	293	⁵ D ₄ → ⁷ F ₅ / ⁵ D ₀ → ⁷ F ₂
		323-373	0.40	1.97	373	⁵ D ₄ → ⁷ F ₅ / ⁵ D ₀ → ⁷ F ₂
		328-373	1.30	1.82		⁵ D ₄ → ⁷ F ₅ / ⁵ D ₀ → ⁷ F ₄
	Gd _{1.2} Tb _{0.4} Eu _{0.4} -TDCPMB	80-305	0.13	1.00	320	⁵ D ₄ → ⁷ F ₅ / ⁵ D ₀ → ⁷ F ₂
			0.36	0.90		⁵ D ₄ → ⁷ F ₅ / ⁵ D ₀ → ⁷ F ₄
		308-343	0.32	3.00	348	⁵ D ₄ → ⁷ F ₅ / ⁵ D ₀ → ⁷ F ₂
		318-343	1.12	2.52		⁵ D ₄ → ⁷ F ₅ / ⁵ D ₀ → ⁷ F ₄
	Gd _{1.1} Tb _{0.4} Eu _{0.5} -TDCPMB	95-320	0.08	0.81	80	⁵ D ₄ → ⁷ F ₅ / ⁵ D ₀ → ⁷ F ₂
			0.20	0.90		⁵ D ₄ → ⁷ F ₅ / ⁵ D ₀ → ⁷ F ₄
H₂BDC / HAC	Tb _{0.93} Eu _{0.07} -BDC-AC	80-180	0.21	0.55	155	⁵ D ₄ → ⁷ F ₅ / ⁵ D ₀ → ⁷ F ₂
			0.65	0.56		⁵ D ₄ → ⁷ F ₅ / ⁵ D ₀ → ⁷ F ₄
	Tb _{0.993} Eu _{0.007} -BDC-AC	105-255	0.62	0.23	205	⁵ D ₄ → ⁷ F ₅ / ⁵ D ₀ → ⁷ F ₂
		105-230	4.8	0.36	155	⁵ D ₄ → ⁷ F ₅ / ⁵ D ₀ → ⁷ F ₄
H₂BDC / Hacac	X = 0.99	100-300	0.43	0.11	200	⁵ D ₄ → ⁷ F ₅ / ⁵ D ₀ → ⁷ F ₂
		120-300	21	0.50	120	⁵ D ₄ → ⁷ F ₅ / ⁵ D ₀ → ⁷ F ₄
	X = 0.95	80-280	0.49	0.23	220	⁵ D ₄ → ⁷ F ₅ / ⁵ D ₀ → ⁷ F ₂
			3.10	0.34	160	⁵ D ₄ → ⁷ F ₅ / ⁵ D ₀ → ⁷ F ₄
	X = 0.90	80-280	0.53	0.19	160	⁵ D ₄ → ⁷ F ₅ / ⁵ D ₀ → ⁷ F ₂
			45	0.35	160 and 260	⁵ D ₄ → ⁷ F ₅ / ⁵ D ₀ → ⁷ F ₄
	X = 0.85	80-260	0.35	0.32	200	⁵ D ₄ → ⁷ F ₅ / ⁵ D ₀ → ⁷ F ₂
		80-240	1.6	0.37	140	⁵ D ₄ → ⁷ F ₅ / ⁵ D ₀ → ⁷ F ₄
	X = 0.75	80-280	1.5	0.20	140	⁵ D ₄ → ⁷ F ₅ / ⁵ D ₀ → ⁷ F ₂
		80-260	1.0	0.21	160	⁵ D ₄ → ⁷ F ₅ / ⁵ D ₀ → ⁷ F ₄

5. Conclusions

In summary, a series of new mixed lanthanide-containing coordination polymers were synthesized, by solvothermal and precipitation method, basing of the co-doping approach and tested as ratiometric luminescent probes for temperature sensing. The compounds built by combining lanthanide cations with H₃TCPMB, under solvothermal conditions, were proven to share the same crystalline structure with remarkable structural and luminescence properties including temperature-independent luminescence lifetime in the temperature range 77 – 300 K. For Eu-TCPMB, the ligand to Eu^{III} energy migration is unexpectedly less effective with temperature increase and it was observed that the luminescence lifetimes of all Ln-TCPMB compounds are temperature independent in the temperature range 77 – 300 K which might be the grounds for another research, such as preparation of Yb / Er CPs for up-conversion study and to develop nanothermometers for bio-applications and nanomedicine: Nanostructures whose emission and absorption bands lie within the so-called biological windows (650 – 950 nm and 1000 –1350 nm) where tissue scattering and absorption are minimized. The solvothermal method using NaOH was identified as a promising way to obtain H₆TDCPMB in a crystalline phase. Compounds synthesized from the H₂BDC / Hacac and H₂DBC / HAC-mixed ligands excepted for x = 0.95 in the former case are isostructural. The spectroscopy study of the compounds shows that the efficiency ligand to lanthanide energy transfer depends strongly on the complex geometry and structure. Except for the ones based only on the HAC ligand, all compounds show intense lanthanide-centered luminescence bands because of the excellent light-harvesting used linkers a large π -conjugated system, an efficient energy transfer to Tb^{III} and Eu^{III}. The different temperature-dependent photoluminescence behaviors between Tb^{III} and Eu^{III} within the same compound enable many of the prepared systems to be applicable for self-referencing temperature. Owing to the higher triplet state energy of the H₆TDCPMB ligand, the ternary mixed Ln-CPs exhibit a sensitive response to temperature in wide ranges making them promising luminescence as ratiometric temperature sensors. The use of mixed-ligand systems to improve the temperature-sensing properties provides a new strategy to explore lanthanide-based coordination polymers in the luminescence-based thermometry. For all investigated systems, it was observed that the temperature-dependence of the

emission intensity ratios is due not only to the thermal relaxation process but also to the different energy migration processes. As shown in the text, the design and construction of mixed lanthanide-based coordination polymers approach have opened up a new interesting strategy for designing dual-emitting for temperature sensing. Although in its geneses, the current reports have shown that it is a very promising and active research field attempting to translate these promising materials into real sensor devices.

References

- [1] K. M. McCabe and M. Hernandez, **Molecular thermometry**, *Pediatr. Res.* 67 (2010) 469–475. doi:10.1203/PDR.0b013e3181d68cef.
- [2] X. D. Wang, O.S. Wolfbeis, R.J. Meier, **Luminescent probes and sensors for temperature**, *Chem. Soc. Rev.* 42 (2013) 7834–7869. doi:10.1039/c3cs60102a.
- [3] A. Ćirić, and S. Stojadinović, **Time-integrated luminescence thermometry of Eu³⁺ and Dy³⁺ doped YVO₄**, *Sensors and Actuators A: Physical.* 295 (2019) 450–455. doi:10.1016/j.sna.2019.06.035.
- [4] G. P. Morriss, and L. Rondoni, **Definition of temperature in equilibrium and nonequilibrium systems**, *Phys. Rev. E.* 59 (1999) 5–8. doi:org/10.1103/PhysRev-E.59.R5.
- [5] P. R. N. Childs, J. R. Greenwood, and C. A. Long, **Review of temperature measurement**, *Rev. Sci. Instrum.* 2959 (2003). doi:10.1063/1.1305516.
- [6] C. D. S. Brites, P. P. Lima, N. J. O. Silva, A. Millán, V. S. Amaral, F. Palacio and L. D. Carlos, **Lanthanide-based luminescent molecular thermometers**, *New. J. Chem.* 35 (2011) 1177–1183. doi:10.1039/c0nj01010c.
- [7] A. W. V. HERWAARDEN and P. M. SARRO, **Sensors based on the seebeck effect**, *Sensors & Actuators.* 10 (1986) 321–346. doi:org/10.1016/0250-6874(86)80053-1.
- [8] D. Jaque and F. Vetrone, **Luminescence nanothermometry**, *Nanoscale.* 4 (2012) 4301–4326. doi:10.1039/c2nr30764b.
- [9] Y. Cui, F. Zhu and G. Qian, **Metal-organic frameworks for luminescence thermometry**, *Chem. Commun.* 51 (2015) 7420–7431. doi:10.1039/C5CC00718F.
- [10] C. Gota, K. Okabe, T. Funatsu, Y. Harada and S. Uchiyama, **Hydrophilic fluorescent nanogel thermometer for intracellular thermometry**, *J. Am. Chem. Soc.* 131 (2009) 2766–2767. doi:10.1021/ja807714j.
- [11] Y. Cui, R. Song, J. Yu, M. Liu, Z. Wang, C. Wu, Y. Yang, Z. Wang, B. Chen and G. Qian, **Dual-emitting MOF-dye composite for ratiometric temperature sensing**, *Adv. Mater.* 27 (2015) 1420–1425. doi:10.1002/adma.201404700.
- [12] G. Kucsko, P. C. Maurer, N. Y. Yao, M. Kubo, H. J. Noh, P. K. Lo, H. Park and M. D. Lukin, **Nanometre-scale thermometry in a living cell**, *Nat.* 500 (2013) 54–8. doi:10.1038/nature12373.
- [13] T. Hayashi, N. Fukuda, S. Uchiyama and N. Inada, **A cell-permeable fluorescent polymeric thermometer for intracellular temperature mapping in mammalian cell lines**, *PLoS One.* 10 (2015) 1–18. doi:10.1371/journal.pone.0117677.
- [14] K. Okabe, N. Inada, C. Gota, Y. Harada, T. Funatsu, and S. Uchiyama, **Intracellular temperature mapping with a fluorescent polymeric thermometer and fluorescence lifetime imaging microscopy**, *Nat. Commun.* 3 (2012) 705. doi:10.1038/ncomms1714.
- [15] C. D. S. Brites, P. P. Lima, N. J. O. Silva, A. Millán, V.S. Amaral, F. Palacio and L.D. Carlos, **Thermometry at the nanoscale**, *Nanoscale.* 4 (2012) 4799–4829. doi:10.1039/c2nr30663h.

- [16] B. Valeur and M. N. Berberan-Santos, **A brief history of fluorescence and phosphorescence before the emergence of quantum theory**, J. Chem. Educ. 88 (2011) 731–738. doi:10.1021/ed100182h.
- [17] J. N. Demas and B. A. DeGraff, **Interactions of transition-metal-complex photosensitizers with polymers and organized media**, J. Macromol. Sci. Part A - Chem. 25 (1988) 1189–1214. doi:10.1080/00222338808053416.
- [18] X. Hu, Y. Li, T. Liu, G. Zhang and S. Liu, **Intracellular Cascade FRET for Temperature Imaging of Living Cells with Polymeric Ratiometric Fluorescent Thermometers**, ACS Appl. Mater. Interfaces. 7 (2015) 15551–15560. doi:10.1021/acsami.5b04025.
- [19] E. J. McLaurin, L. R. Bradshaw and D. R. Gamelin, **Dual-Emitting Nanoscale Temperature Sensors**, Chem. Mater. 25 (2013) 1283–122. doi:10.1021/cm304034s.
- [20] K. Miyata, Y. Konno, T. Nakanishi, A. Kobayashi, M. Kato, K. Fushimi and Y. Hasegawa, **Chameleon Luminophore for Sensing Temperatures: Control of Metal-to-Metal and Energy Back Transfer in Lanthanide Coordination Polymers** Angew., (2013) 6413–6416. doi:10.1002/anie.201301448.
- [21] F. Vetrone, R. Naccache, A. Zamarrón, A. Juarranz de la Fuente, F. Sanz-rodríguez, L. M. Maestro, E. M. Rodriguez, D. Jaque, J. G. Solé and J. A. Capobianco, **Temperature Sensing Using Fluorescent Nanothermometers**, ACS Nano. 4 (2010) 3254–3258. doi: org/10.1021/nn100244a
- [22] **Static & Dynamic Characteristics of measurement systems**,. <http://mediatoget.blogspot.in/2012/01/static-dynamic-characteristics-of.html> (accessed August 22, 2019).
- [23] C. J. Liang, Z. R. Hong, X. Y. Liu, D. X. Zhao, D. Zhao, W. L. Li, J. B. Peng, J. Q. Yu, C. S. Lee and S. T. Lee, **Organic electroluminescent devices using europium complex as an electron-transport emitting layer**, Thin Solid Films. 359 (2000) 14–16. doi:org/10.1016/S0040-6090(99)00713-0
- [24] H. Q. Ye, Z. Li, Y. Peng, C. C. Wang, T. Y. Li, Y. X. Zheng, Sapelkin, G. Adamopoulos, Hernández, P.B. Wyatt and W. P. Gillin, **Organo-erbium systems for optical amplification at telecommunications wavelengths**, Nat. Mater. 13 (2014) 382–6. doi:10.1038/nmat3910.
- [25] J. C. G. Bünzli, **On the design of highly luminescent lanthanide complexes**, Coord. Chem. Rev. 293–294 (2015) 19–47. doi:10.1016/j.ccr.2014.10.013.
- [26] R. Tian, S. Zhao, G. Liu, H. Chen, L. Ma, H. You and C. Liu, Z. Wang, **Construction of lanthanide-doped upconversion nanoparticle-Uelx Europaeus Agglutinin-I bioconjugates with brightness red emission for ultrasensitive in vivo imaging of colorectal tumor**, Biomaterials. 212 (2019) 64–72. doi:10.1016/j.biomaterials.2019.05.010.
- [27] Y. Hasegawa and T. Nakanishi, **Luminescent lanthanide coordination polymers for photonic applications**, RSC Adv. 5 (2015) 338–353. doi:10.1039/C4RA09255D.
- [28] O. L. Malta, H. F. Brito, J. F. S. Menezes, F. R. Gonçalves e Silva, S. A. Junior and A. V. M. De Andrade, **Spectroscopic properties of a new lighth-converting device Eu(thenoyltrifluoro-acetone)₃.2(dibenzylsulfoxide): A theoretical analysis based on structural data obtained from a sparkle model**, Journal of luminescence. 75 (1997) 255–268. doi: org/10.1016/S0022-2313(97)00107-5
- [29] J. Claude G. Bünzli, **The europium(III) ion as spectroscopic probe in bioinorganic chemistry**, Inorganica Chim. Acta. 139 (1987) 219–222. doi:10.1016/S0020-1693(00)84084-0.

- [30] S. V. Eliseeva and J. C. G. Bünzli, **Lanthanide luminescence for functional materials and bio-sciences**, Chem. Soc. Rev. 39 (2010) 189–227. doi:10.1039/b905604c.
- [31] K. Binnemans, **Lanthanide-Based Luminescent Hybrid Materials**, Chem. Rev. 109 (2009) 4283–4374. doi:10.1021/cr8003983.
- [32] J. C. G. Bünzli and C. Piquet, **Taking advantage of luminescent lanthanide ions**, Chem. Soc. Rev. 34 (2005) 1048–1077. doi:10.1039/b406082m.
- [33] E. Pershagen, K. E. Borbas, **Designing reactivity-based responsive lanthanide probes for multicolor detection in biological systems**, Coord. Chem. Rev. 273–274 (2014) 30–46. doi:10.1016/j.ccr.2013.10.012.
- [34] G. S. Ofelt, **Intensities of Crystal Spectra of RareEarth Ions**, J. Chem. Phys. 511 (1972) 511–520. doi:10.1063/1.1701366.
- [35] B. R. Judd, **Optical Absorption Intensities of Rare-Earth Ions**, Phys. 197 (1962) 750–761.
- [36] O. L. Malta, **Ligand—rare-earth ion energy transfer in coordination compounds. A theoretical approach**, J. Lumin. 71 (1997) 229–236. doi:10.1016/S0022-2313(96)00126-3.
- [37] Y. Hasegawa, M. Yamamuro, Y. Wada, N. Kanehisa, Y. Kai and S. Yanagida, **Luminescent polymer containing the Eu(III) complex having fast radiation rate and high emission quantum efficiency**, J. Phys. Chem. A. 107 (2003) 1697–1702. doi:10.1021/jp022397u.
- [38] R. Ilmi and K. Iftikhar, **Optical emission studies of new europium and terbium dinuclear complexes with trifluoroacetylacetone and bridging bipyrimidine. Fast radiation and high emission quantum yield**, Polyhedron. 102 (2015) 16–26. doi:10.1016/j.poly.2015.07.046.
- [39] D. Parker, **Luminescent lanthanide sensors for pH, pO₂ and selected anions**, Coord. Chem. Rev. 205 (2000) 109–130. doi:10.1016/s0010-8545(00)00241-1.
- [40] A. Młkonkowski, S. Lis, Z. Hnatejko, K. Czarnobaj, M. Pietraszkiewicz and M. Elbanowski, **Improvement of emission intensity in luminescent materials based on the antenna effect**, J. Alloys Compd. (2000) 55–60. doi:org/10.1016/S0925-8388(99)00712-4
- [41] S.I. Weissman, **Intramolecular Energy Transfer The Fluorescence of Complexes of Europium**, J. Chem. Phys. 10 (1942) 214–217. doi:10.1063/1.1723709.
- [42] B. Yan, H. Zhang, S. Wang and J. Ni, **Intramolecular energy transfer mechanism between ligands in ternary rare earth complexes with aromatic carboxylic acids and 1,10-phenanthroline**, J. Photochem. Photobiol. A Chem. 116 (1998) 209–214. doi:10.1016/S1010-6030(98)00307-4.
- [43] A. D'Aléo, F. Pointillart, L. Ouahab, C. Andraud and O. Maury, **Charge transfer excited states sensitization of lanthanide emitting from the visible to the near-infra-red**, Coord. Chem. Rev. 256 (2012) 1604–1620. doi:10.1016/j.ccr.2012.03.023.
- [44] S. Katagiri, Y. Tsukahara, Y. Hasegawa and Y. Wada, **Energy-Transfer Mechanism in Photoluminescent Terbium(III) Complexes Causing Their Temperature-Dependence**, Bull. Chem. Soc. Jpn. 80 (2007) 1492–1503. doi:10.1246/bcsj.80.1492.
- [45] M. Latvaa, H. Takalob, V. Mukkala, C. Matachescuc, J.C. Rodriguez-ubisd and J. Kankarea, **Correlation between the lowest triplet state energy level of the ligand and lanthanide(III) luminescence quantum yield**, Journal of luminescence. 75 (1997)

- 149–169. doi:org/10.1016/S0022-2313(97)00113-0.
- [46] S. SeethaLekshmi, A. R. Ramy, M. L. P. Reddy and S. Varughese, **Lanthanide complex-derived white-light emitting solids: A survey on design strategies**, J. Photochem. Photobiol. C Photochem. Rev. 33 (2017) 109–131. doi:10.1016/j.jphotochemrev.-2017.11.001.
- [47] L. C. Courrol, F. R. de Oliveira Silva, L. Gomes and N. D. Vieira Júnior, **Energy transfer study of europium-tetracycline complexes**, J. Lumin. 122–123 (2007) 288–290. doi:10.1016/j.jlumin.2006.01.143.
- [48] P. P. Lima, F. A. A. Paz, C. D. S. Brites, W. G. Quirino, C. Legnani, M. Costa e Silva, R. A. S. Ferreira, S. A. Júnior, O. L. Malta, M. Cremona and L. D. Carlos, **White OLED based on a temperature sensitive $\text{Eu}^{3+}/\text{Tb}^{3+}$ β -diketonate complex**, Org. Electron. 15 (2014) 798–808. doi:10.1016/j.orgel.2014.01.009.
- [49] B. S. Richards, **Luminescent layers for enhanced silicon solar cell performance: Down-conversion**, Sol. Energy Mater. Sol. Cells. 90 (2006) 1189–1207. doi:10.1016/j.solmat.2005.07.001.
- [50] S. R. Batten, N. R. Champness, X. Chen, J. Garcia-martinez, S. Kitagawa and L. Öhrström, **Coordination polymers , metal – organic frameworks and the need for terminology guidelines**, Cryst. Eng. Commun. 14 (2012) 3001–3004. doi:10.1039/c2ce06488j.
- [51] S. R. Batten, N. R. Champness, X. M. Chen, J. G. Martinez, S. Kitagawa, L. Öhrström, M. O’Keeffe, M. Paik Suh and J. Reedijk, **Terminology of metal–organic frameworks and coordination polymers (IUPAC Recommendations 2013)**, Pure Appl. Chem. 85 (2013) 1715–1724. doi:10.1351/PAC-REC-12-11-20.
- [52] O. M. Yaghi, M. O’Keeffe, N. W. Ockwig, H. K. Chae, M. Eddaoudi and J. Kim, **Reticular synthesis and the design of new materials**, Nature. 423 (2003) 705–714. doi:10.1038/nature01650.
- [53] K. S. Asha, K .M. Ranjith, A. Yogi, R. Nath and S. Mandal, **Magnetic properties of manganese based one-dimensional spin chains**, Dalt. Trans. 44 (2015) 19812–19819. doi:10.1039/c5dt03080c.
- [54] A. Schoedel, M. Li, D. Li, M. O’Keeffe and O. M. Yaghi, **Structures of Metal-Organic Frameworks with Rod Secondary Building Units**, Chem. Rev. 116 (2016) 12466–12535. doi:10.1021/acs.chemrev.6b00346.
- [55] R. F. D’Vries, S. Álvarez-García, N. Snejko, L. E. Bausá, E. Gutiérrez-Puebla, A. De Andrés and M. Á. Monge, **Multimetal rare earth MOFs for lighting and thermometry: Tailoring color and optimal temperature range through enhanced disulfobenzoic triplet phosphorescence**, J. Mater. Chem. C. 1 (2013) 6316–6324. doi:10.1039/c3tc30858h.
- [56] X. Liu, S. Akerboom, M. De Jong, I. Mutikainen, S. Tanase, A. Meijerink and E. Bouwman, **Mixed-Lanthanoid Metal-Organic Framework for Ratiometric Cryogenic Temperature Sensing**, Inorg. Chem. 54 (2015) 11323–11329. doi:10.1021/acs.inorgchem.5b01924.
- [57] Y. Li, S. Zhang and D. Song, **A luminescent metal-organic framework as a turn-on sensor for DMF vapor**, Angew. Chemie - Int. Ed. 52 (2013) 710–713. doi:10.1002/anie.201207610.
- [58] N. B. Shustova, A. F. Cozzolino, S. Reineke, M. Baldo and M. Dincă, **Selective turn-on ammonia sensing enabled by high-temperature fluorescence in metal-organic**

- frameworks with open metal sites**, J. Am. Chem. Soc. 135 (2013) 13326–13329. doi:10.1021/ja407778a.
- [59] Y. H. Zhang, X. Li and S. Song, **White light emission based on a single component Sm(III) framework and a two component Eu(III)-doped Gd(III) framework constructed from 2,2'-diphenyl dicarboxylate and 1H-imidazo[4,5-f][1,10]-phenanthroline**, Chem. Commun. 49 (2013) 10397–10399. doi:10.1039/c3cc46397d.
- [60] J. M. Zhou, W. Shi, N. Xu and P. Cheng, **Highly selective luminescent sensing of fluoride and organic small-molecule pollutants based on novel lanthanide metal-organic frameworks**, Inorg. Chem. 52 (2013) 8082–90. doi:10.1021/ic400770j.
- [61] Z. Dou, J. Yu, Y. Cui, Y. Yang, Z. Wang, D. Yang and G. Qian, **Luminescent metal-organic framework films as highly sensitive and fast-response oxygen sensors**, J. Am. Chem. Soc. 136 (2014) 5527–5530. doi:10.1021/ja411224j.
- [62] C. Sanchez, K.J. Shea and S. Kitagawa, **Luminescent multifunctional lanthanides-based metal-organic frameworks**, Chem. Soc. Rev. 40 (2011) 926–940. doi:10.1039/c0cs00130a.
- [63] D. Zhao, Y. Cui, Y. Yang and G. Qian, **Sensing-functional luminescent metal-organic frameworks**, CrystEngComm. 18 (2016) 3746–3759. doi:10.1039/C6CE00545D.
- [64] B. Li, H. M. Wen, Y. Cui, G. Qian and B. Chen, **Multifunctional lanthanide coordination polymers**, Prog. Polym. Sci. 48 (2015) 40–84. doi:10.1016/j.prog-polymsci.2015.04.008.
- [65] Y. Cui, B. Chen and G. Qian, **Lanthanide metal-organic frameworks for luminescent sensing and light-emitting applications**, Coord. Chem. Rev. 273–274 (2014) 76–86. doi:10.1016/j.ccr.2013.10.023.
- [66] Y. Cui, H. Xu, Y. Yue, Z. Guo, J. Yu, Z. Chen, J. Gao, Y. Yang, G. Qian and B. Chen, **A Luminescent Mixed-Lanthanide Metal-Organic Framework Thermometer**, J. Am. Chem. Soc. 2012, 134, 3979–3982. doi: org/10.1021/ja2108036
- [67] C. Pagis, M. Ferbinteanu, G. Rothenberg and S. Tanase, **Lanthanide-Based Metal Organic Frameworks: Synthetic Strategies and Catalytic Applications**, ACS Catal. 6 (2016) 6063–6072. doi:10.1021/acscatal.6b01935.
- [68] D. Ma, X. Li and R. Huo, **A high-efficiency white light-emitting lanthanide-organic framework assembled from 4,4'-oxybis(benzoic acid), 1,10-phenanthroline and oxalate**, J. Mater. Chem. C. 2 (2014) 9073–9076. doi:10.1039/C4TC01409J.
- [69] M. L. Cable, J. P. Kirby, H. B. Gray and A. Ponce, **Enhancement of Anion Binding in Lanthanide Optical Sensors**, accounts of chemical research 46, 11 (2013) 2576–2584. doi: 10.1021/ar400050t
- [70] B. Chen, L. Wang, F. Zapata, G. Qian and E. B. Lobkovsky, **A Luminescent Microporous Metal - Organic Framework for the Recognition**, J. Am. Chem. Soc. 130 (2008) 6718–6719. doi:org/10.1021/ja802035e
- [71] B. Chen, L. Wang, Y. Xiao, F. R. Fronczek, M. Xue, Y. Cui and G. Qian, **A luminescent metal-organic framework with Lewis basic pyridyl sites for the sensing of metal ions**, Angew. Chemie - Int. Ed. 48 (2009) 500–503. doi:10.1002/anie.200805101.
- [72] B. Chen, Y. Yang, F. Zapata, G. Lin, G. Qian and E.B. Lobkovsky, **Luminescent open metal sites within a metal-organic framework for sensing small molecules**, Adv. Mater. 19 (2007) 1693–1696. doi:10.1002/adma.200601838.

- [73] X. Meng, S. Y. Song, X. Z. Song, M. Zhu, S. N. Zhao, L. L. Wu and H. J. Zhang, **A Eu/Tb-codoped coordination polymer luminescent thermometer**, *Inorg. Chem. Front.* 1 (2014) 757–760. doi:10.1039/C4QI00122B.
- [74] A. Cornia and M. Mannini, **Molecular Nanomagnets and Related Phenomena**, Springer Berlin Heidelberg, Beijing, 2015. doi:10.1007/430_2014_150.
- [75] H. F. Brito, J. F. S. Menezes, F. R. G. Silva, S. A. Junior, F. S. F. Junior, A. V. M. De Andrade, **A theoretical analysis based on structural data obtained from a sparkle model**, *J. Lumin.* 75. 75 (1997) 255–268.
- [76] Y. Li, Y. Fang, N. Hirotsaki, R. Xie, L. Liu, T. Takeda and X. Li, **Crystal and Electronic Structures, Photoluminescence Properties of Eu²⁺-Doped Novel Oxynitride Ba₄Si₆O_{16-3x/2}N_x**, *Materials (Basel)*. 3 (2010) 1692–1708. doi:10.3390/ma3031692.
- [77] Z. Wang, Y. Yang, Y. Cui, Z. Wang and G. Qian, **Color-tunable and white-light emitting lanthanide complexes based on (Ce_xEu_yTb_{1-x-y})₂(BDC)₃(H₂O)₄**, *J. Alloys Compd.* 510 (2012) L5–L8. doi:10.1016/j.jallcom.2011.08.082.
- [78] X. Rao, T. Song, J. Gao, Y. Cui, Y. Yang, C. Wu, B. Chen and G. Qian, **A highly sensitive mixed lanthanide metal-organic framework self-calibrated luminescent thermometer**, *J. Am. Chem. Soc.* 135 (2013) 15559–15564. doi:10.1021/ja407219k.
- [79] J. Rocha, C. D. S. Brites, L. D. Carlos, **Lanthanide Organic Framework Luminescent Thermometers**, *Chem. - A Eur. J.* (2016) 1–15. doi:10.1002/chem.201600860.
- [80] D. Zhao, D. Yue, K. Jiang, L. Zhang, C. Li and G. Qian, **Isostructural Tb 3+ /Eu 3+ Co-Doped Metal-Organic Framework Based on Pyridine-Containing Dicarboxylate Ligands for Ratiometric Luminescence Temperature Sensing**, *Inorg. Chem.* 58 (2019) 2637–2644. doi:10.1021/acs.inorgchem.8b03225.
- [81] Y. Cui, H. Xu, Y. Yue, Z. Guo, J. Yu, Z. Chen, J. Gao, Y. Yang, G. Qian and B. Chen, **A luminescent mixed-lanthanide metal-organic framework thermometer**, *J. Am. Chem. Soc.* 134 (2012) 3979–82. doi:10.1021/ja2108036.
- [82] Y. Wei, R. Sa, Q. Li and K. Wu, **Highly stable and sensitive LnMOF ratiometric thermometers constructed with mixed ligands**, *Dalt. Trans.* 44 (2015) 3067–3074. doi:10.1039/c4dt03421j.
- [83] Y. Han, C. Tian, Q. Li and S. Du, **Highly chemical and thermally stable luminescent Eu_xTb_{1-x} MOF materials for broad-range pH and temperature sensors**, *J. Mater. Chem. C Mater. Opt. Electron. Devices.* 2 (2014) 8065–8070. doi:10.1039/C4TC013-36K.
- [84] A. Cadiou, C. D. S. Brites, P. M. F. J. Costa, R. A. S. Ferreira, J. Rocha and L. D. Carlos, **Ratiometric nanothermometer based on an emissive Ln³⁺-organic framework**, *ACS Nano.* 7 (2013) 7213–7218. doi:10.1021/nn402608w.
- [85] Z. Wang, D. Ananias, A. Carné-Sánchez, C. D. S. Brites, I. Imaz, D. Maspoch, J. Rocha, and L.D. Carlos, **Lanthanide-Organic Framework Nanothermometers Prepared by Spray-Drying**, *Adv. Funct. Mater.* (2015) n/a-n/a. doi:10.1002/adfm.201500518.
- [86] X. Lian, D. Zhao, Y. Cui, Y. Yang and G. Qian, **A near infrared luminescent metal-organic framework for temperature sensing in the physiological range**, *Chem. Commun.* 51 (2015) 17676–17679. doi:10.1039/c5cc07532g.
- [87] F. Sebastian, W. Seichter, E. Weber, **Synthesis and Structures of Three- and Hexa-armed Benzene Derivatives Featuring Lateral Benzoic Ester and Benzoic Acid Functions**, *Z. Naturforsch.* 66b (2011) 939 – 946.

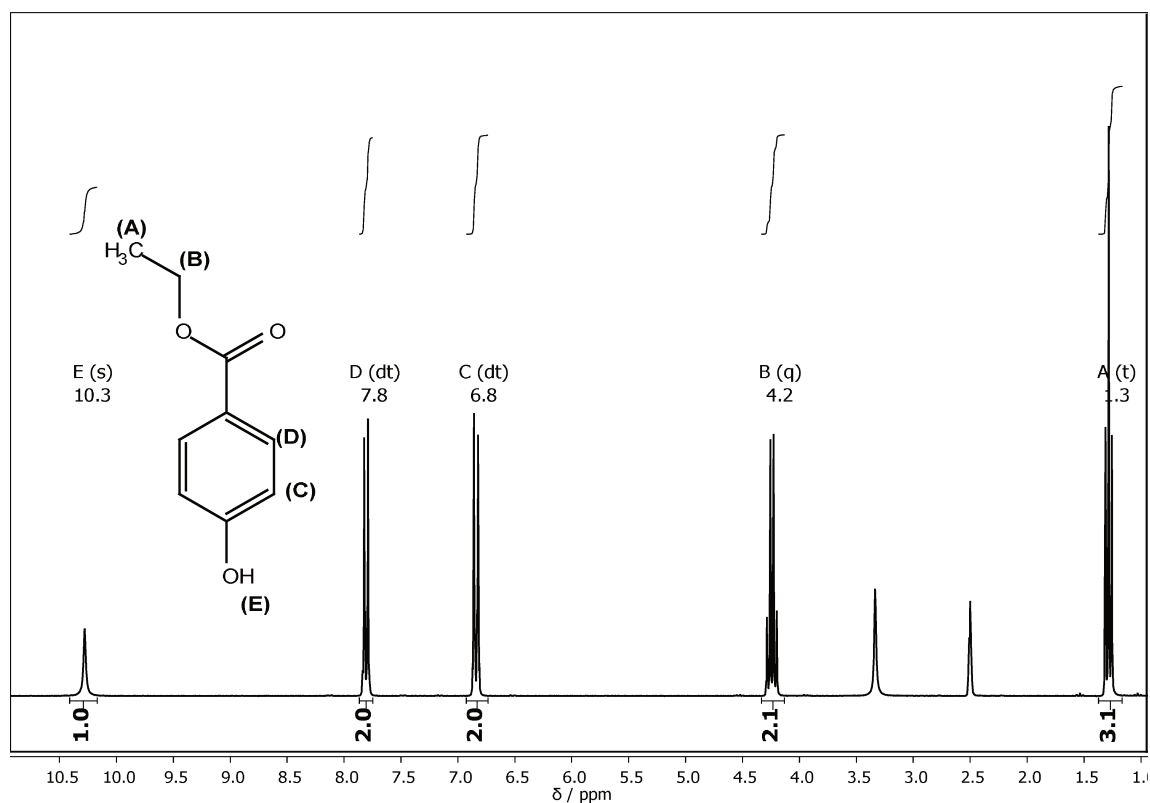
- [88] Chunhui Huang et al., **RARE EARTH COORDINATION CHEMISTRY: Fundamentals and applications**, 2010.
- [89] E. E. S. Teotonio, H. F. Brito, M. C. F. C. Felinto, L. C. Thompson, V. G. Young and O. L. Malta, **Preparation, crystal structure and optical spectroscopy of the rare earth complexes ($RE^{3+} = \text{Sm, Eu, Gd and Tb}$) with 2-thiopheneacetate anion**, J. Mol. Struct. 751 (2005) 85–94. doi:10.1016/j.molstruc.2005.05.001.
- [90] G. M. Sheldrick, **A short history of SHELX**, Acta Crystallogr. Sect. A Found. Crystallogr. 64 (2008) 112–122. doi:10.1107/S0108767307043930.
- [91] R. H. D. Hosangad and D. Bhaskar, **An Efficient General Method for Esterification of Aromatic Carboxylic Acids**, Tetrahedron Lett. 37 (1996) 6375–6378. doi:10.1016/0040-4039(96)01351-2.
- [92] H. Wang, D. Zhao, Y. Cui, Y. Yang and G. Qian, **A Eu / Tb-mixed MOF for luminescent high-temperature sensing**, J. Solid State Chem. 246 (2017) 341–345. doi:10.1016/j.jssc.2016.12.003.
- [93] B. M. Ociepa, D. Michalska and A. Pietraszko, **Structures and vibrational spectra of indolecarboxylic acids. 5-Methoxyindole-2-carboxylic acid**, J. Mol. Struct. 688 (2004) 87–94. doi:10.1016/j.molstruc.2003.09.029.
- [94] J. S. Gromiuk, I. Rusinek, Ł. Kurach and Z. Rzączyńska, **Thermal and spectroscopic (IR, XPS) properties of lanthanide(III) benzene-1,3,5-triacetate complexes**, J. Therm. Anal. Calorim. 126 (2016) 327–342. doi:10.1007/s10973-016-5521-8.
- [95] E. G. Palacios, G. J. López and A. J. Monhemius, **Infrared spectroscopy of metal carboxylates: II. Analysis of Fe(III), Ni and Zn carboxylate solutions**, Hydrometallurgy. 72 (2004) 139–148. doi:10.1016/S0304-386X(03)00137-3.
- [96] J. R. V. D. L. Pavia, G. M. Lampman and G. S. Kriz, **Introduction to Spectroscopy**, 4th ed., Brooks/Cole, Cengage Learning, Belmont, USA, 2009.
- [97] L. Shi, H. Y. Liu, H. Shen, J. Hu, G. L. Zhang, H. Wang, L. N. Ji, C. K. Chang and H. F. Jiang, **Fluorescence properties of halogenated mono-hydroxyl corroles: the heavy-atom effects**, J. Porphyr. Phthalocyanines. 13 (2010) 1221–1226. doi:10.1142/s1088424609001546.
- [98] O. Karagiari, W. Bury, A. A. Sarjeant, J.T. Hupp and O. K. Farha, **Synthesis and Characterization of Functionalized Metal-organic Frameworks**, J. Vis. Exp. (2014) 1–9. doi:10.3791/52094.
- [99] J. K. Molloy, C. Lincheneau, M. M. Karimdjy, F. Agnese, L. Mattera, C. Gateau, P. Reiss, D. Imbert and M. Mazzanti, **Sensitisation of visible and NIR lanthanide emission by InPZnS quantum dots in bi-luminescent hybrids**, Chem. Commun. 52 (2016) 4577–4580. doi:10.1039/c6cc01182a.
- [100] X. Q. Zhao, B. Zhao, S. Wei and P. Cheng, **Synthesis, structures, and luminescent and magnetic properties of Ln-Ag heterometal-Organic frameworks**, Inorg. Chem. 48 (2009) 11048–11057doi:10.1021/ic901291b.
- [101] J. Rong, W. Zhang and J. Bai, **Highly thermostable lanthanide(III) MOFs constructed from 4,4',4''-s-triazine-2,4,6-triyl-tribenzoate ligand**, synthesis, structure, and tunable white-light emission, CrystEngComm. 18 (2016) 7728–7736. doi:10.1039/C6CE01-585A.
- [102] E. Kusrini, R. Adnan, M. I. Saleh, L. K. Yan and H. K. Fun, **Synthesis and structure of dimeric anthracene-9-carboxylato bridged dinuclear erbium(III) complex, $[\text{Er}_2(9-$**

- AC)₆(DMF)₂(H₂O)₂], Spectrochim. Acta - Part A Mol. Biomol. Spectrosc. 72 (2009) 884–889. doi:10.1016/j.saa.2008.12.011.**
- [103] P. C. C. Durgaprasad and D.N. Sathyanarayana, **Infrared Spectra and Normal Vibrations of N,N-Dimethylformamide and N,N-Dimethylthioformamide**, Bull. Chem. Soc. Jpn. 44 (1971) 316–322.
- [104] M. Nara, H. Torii and M. Tasumi, **Correlation between the Vibrational Frequencies of the Carboxylate Group and the Types of Its Coordination to a Metal Ion: An *ab Initio* Molecular Orbital Study**, J. Phys. Chem. 100 (1996) 19812–19817. doi:10.1021/jp9615924.
- [105] J. Xu, W. Su and M. Hong, **A series of lanthanide secondary building units based metal-organic frameworks constructed by organic pyridine-2,6-dicarboxylate and inorganic sulfate**, Cryst. Growth Des. 11 (2011) 337–346. doi:10.1021/cg101343k.
- [106] L. M. D'Assunção, M. Ionashiro, D. E. Rasesa and I. Giolito, **Thermal decomposition of the hydrated basic carbonates of lanthanides and yttrium in CO₂ atmosphere**, Thermochim. Acta. 219 (1993) 225–233. doi:10.1016/0040-6031(93)80500-A.
- [107] H. A. Azab, S. A. El-Korashy, Z. M. Anwar, B. H. M. Hussein and G. M. Khairy, **Synthesis and fluorescence properties of Eu-anthracene-9-carboxylic acid towards N-acetyl amino acids and nucleotides in different solvents**, Spectrochim. Acta - Part A Mol. Biomol. Spectrosc. 75 (2010) 21–27. doi:10.1016/j.saa.2009.09.008.
- [108] W. R. Busing, **Infrared spectra and structure of NaOH and NaOD**, J. Chem. Phys. 23 (1955) 933–936. doi:10.1063/1.1742150.
- [109] R. J. P. G. B. Deacon, **Relationships between the carbon-oxygen stretching frequencies of carboxylate complexes and the type of carboxylate coordination**, Coord. Chem. Rev. 33 (1980) 227–250. doi:10.1016/S0010-8545(00)80455-5.
- [110] L. Yang, S. Zhang, X. Qu, Q. Yang, X. Liu, Q. Wei, G. Xie and S. Chen, **Synthesis, crystal structure and photoluminescence property of Eu/Tb MOFs with mixed polycarboxylate ligands**, J. Solid State Chem. 231 (2015) 223–229. doi:10.1016/j.jssc.2015.08.037.
- [111] A. Beeby, S. Faulkner, D. Parker and J. A. G. Williams, **Sensitised luminescence from phenanthridine appended lanthanide complexes: analysis of triplet mediated energy transfer processes in terbium, europium and neodymium complexes**, J. Chem. Soc. Perkin Trans. 2. (2001) 1268–1273. doi:10.1039/b009624p.
- [112] M. Kleinerman, **Energy Migration in Lanthanide Chelates**, J. Chem. Phys. 51 (1969) 2370. doi:10.1063/1.1672355.
- [113] W.T. Carnal, C. Hannah and H. M. Crosswhite, **Energy Level Structure and Transition Probabilities in the Spectra of the Trivalent Lanthanides in LaF₃**, OSTI.GOV, 1978, doi: 10.2172/6417825.
- [114] S. Tobita, M. Arakawa and I. Tanaka, **Electronic relaxation processes of rare-earth chelates of benzoyltrifluoroacetone**, J. Phys. Chem. 88 (1984) 2697–2702. doi:10.1021/j150657a006.
- [115] S. Tobita, M. Arakawa and I. Tanaka, **The paramagnetic metal effect on the ligand localized S₁ → T₁ intersystem crossing in the rare-earth-metal complexes with methyl salicylate**, J. Phys. Chem. 89 (2005) 5649–5654. doi:10.1021/j100272a015.
- [116] A. I. Baba, J. R. Shaw, J. A. Simon, R. P. Thummel and R. H. Schmehl, **The photophysical behavior of d₆ complexes having nearly isoenergetic MLCT and**

- ligand localized excited states**, *Coord. Chem. Rev.* 171 (1998) 43–59. doi:org/10.1016/S0010-8545(98)90009-1
- [117] H. Xu, R. Chen, Q. Sun, W. Lai, Q. Su, W. Huang and X. Liu, **Recent progress in metal-organic complexes for optoelectronic applications**, *Chem. Soc. Rev.* 43 (2014) 3259–302. doi:10.1039/c3cs60449g.
- [118] I.T. Tanaka, S. Tobita and M. Arakawa, **The Paramagnetic Metal Effect on the Ligand Localized $S_1 \rightarrow T_1$ Intersystem Crossing In the Rare-Earth-Metal Complexes with Methyl Salicylate**, *J. Phys. Chem.* 89 (1985) 5649–5654. doi:10.1021/j100272a015.
- [119] J. Z. N. Bing Yan, H. J. Zhang and S. B. Wang, **Photophysical Properties of Some Binary and Ternary Complexes of Rare Earth Ions with Aminobenzoic Acids and 1,10-Phenanthroline**, *Monatshefte Für Chemie.* 129 (1998) 151–158.
- [120] S. Wang, H. Wu, L. You, G. Xiong, Y. He, F. Ding and Y. Sun, **Synthesis , structure and photoluminescence of 3D lanthanide coordination polymers based on 2-(3, 5-dicarboxybenzyloxy) benzoic acid**, *Inorganica Chim. Acta.* 485 (2019) 49–53. doi:10.1016/j.ica.2018.09.083.
- [121] F. Chen, Z. Bian, Z. Liu, D. Nie, Z. Chen and C. Huang, **Highly Efficient Sensitized Red Emission from Europium(III) in Ir-Eu Bimetallic Complexes by 3MLCT Energy Transfer**, *Inorg. Chem.* 47 (2008) 2507–2513. doi:org/10.1021/ic701817n
- [122] Z. J. Li, X. Y. Li, Y. T. Yan, L. Hou, W. Y. Zhang and Y. Y. Wang, **Tunable Emission and Selective Luminescence Sensing in a Series of Lanthanide Metal-Organic Frameworks with Uncoordinated Lewis Basic Triazolyl Sites**, *Cryst. Growth Des.* 18 (2018) 2031–2039. doi:10.1021/acs.cgd.7b01453.
- [123] J. H. S. K. Monteiro, R. D. Adati, M. R. Davolos, J. R. M. Vicenti, R. A. Burrow, **Correlation between structural data and spectroscopic studies of a new β -diketonate complex with trivalent europium and gadolinium**, *New J. Chem.* 35 (2011) 1234. doi:10.1039/c0nj00831a.
- [124] J. F. S. do Nascimento, B. S. Barros, J. K. J. Bosco, L. Oliveira, A. K. P. Leite and R. S. Oliveira, **Influence of synthesis time on the microstructure and photophysical properties of Gd-MOFs doped with Eu^{3+}** , *Mater. Chem. Phys.* 190 (2017) 166–174. doi:10.1016/j.matchemphys.2017.01.024.
- [125] K. Binnemans, P. Lenaerts, K. Driesen, C. Görrler-Walrand, **A luminescent tris(2-thenoyltrifluoroacetato)europium(III) complex covalently linked to a 1,10-phenanthroline-functionalised sol–gel glass**, *J. Mat. Chem.* 14 (2004) 191–195. doi:10.1039/B311128H
- [126] L. M. Becerra, M.C. F. Jiménez, J.M. H. Álcantara, E. Camarillo, C. F. Guajardo, R. V. Arreguín and H. M. Sanchez, **Structural and luminescent analysis of hafnium-doped yttrium oxide and yttrium-doped hafnium oxide powders and doped with trivalent europium and terbium ions**, *J. Nanophotonics.* 12 (2018) 1. doi:10.1117/1.jnp.-12.036013.
- [127] Z. Wang, D. Ananias, A. C. Sánchez, C.D.S. Brites, I. Imaz, D. MasPOCH, J. Rocha and L.D. Carlos, **Lanthanide-organic framework nanothermometers prepared by spray-drying**, *Adv. Funct. Mater.* 25 (2015) 2824–2830. doi:10.1002/adfm.201500518.
- [128] L. L. Wu, J. Zhao, H. Wang and J. Wang, **A lanthanide(III) metal–organic framework exhibiting ratiometric luminescent temperature sensing and tunable white light emission**, *CrystEngComm.* 18 (2016) 4268–4271. doi:10.1039/C5CE02444G.
- [129] B. Casanovas, S. Speed, O. Maury, M.S. El Fallah, M. Font-Bardía and R. Vicente,

- Dinuclear Ln^{III} Complexes with 9-Anthracenecarboxylate Showing Field-Induced SMM and Visible/NIR Luminescence**, *Eur. J. Inorg. Chem.* 2018 (2018) 3859–3867. doi:10.1002/ejic.201800624.
- [130] A. N. Gusev, M. Hasegawa, T. Shimizu, T. Fukawa, S. Sakurai, G. A. Nishchymenko, V. F. Shul'gin, S. B. Meshkova and W. Linert, **Synthesis, structure and luminescence studies of Eu(III), Tb(III), Sm(III), Dy(III) cationic complexes with acetylacetone and bis(5-(pyridine-2-yl)-1, 2, 4-triazol-3-yl)propane**, *Inorganica Chim. Acta.* 406 (2013) 279–284. doi:10.1016/j.ica.2013.04.006.
- [131] P. Kolodner and J.A. Tyson, **Remote thermal imaging with 0.7- μ m spatial resolution using temperature-dependent fluorescent thin films**, *Appl. Phys. Lett.* 42 (1983) 117–119. doi:10.1063/1.93766.
- [132] Y. Hasegawa and Y. Kitagawa, **Thermo-sensitive luminescence of lanthanide complexes, clusters, coordination polymers and metal–organic frameworks with organic photosensitizers**, *J. Mater. Chem. C.* 7 (2019) 7494–7511. doi:10.1039/c9tc00607a.
- [133] K. Binnemans, **RARE-EARTH BETA-DIKETONATES**, in: J.-C.G.B. and V.K.P. K.A. Gschneidner, Jr. (Ed.), *Handb. Phys. Chem. Rare Earths*, 2005: pp. 107–166. doi:10.1016/S0168-1273(05)35003-3.
- [134] M. O. Rodrigues, J. Diogo, L. Dutra, L. Anto, O. Nunes, G. F. De Sa, W. M. De Azevedo, F. A. A. Paz, R. O. Freire and S. A. Ju, **Tb³⁺ \rightarrow Eu³⁺ Energy Transfer in Mixed-Lanthanide-Organic Frameworks**, *J. Phys. Chem. C.* 116 (2012) 19951–19957. doi:org/10.1021/jp3054789
- [135] D. A. Wilson, G. Lisa, D. Scutaru and N. Hurduc, **Synthesis and thermal analysis of some ferrocene derivatives**, *J. Iran. Chem. Soc.* 8 (2011) 782–793. doi:10.1007/BF0-3245909.

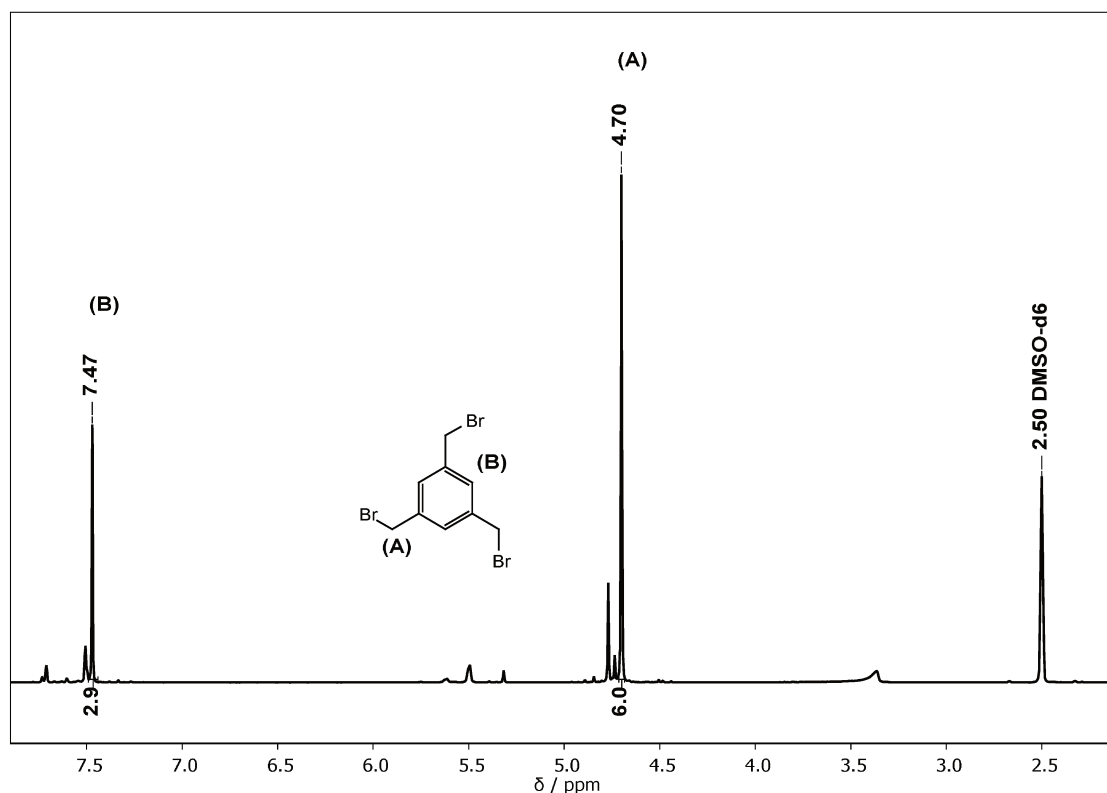
6. Appendix



A 1: The 400-MHz ¹H-nuclear magnetic resonance spectrum of the 4-hydroxy(ethoxycarbonylbenzene) in DMSO-d₆.

A 2: Spectral conditions of the ¹H-NMR spectrum of the 4-hydroxy(ethoxycarbonylbenzene)

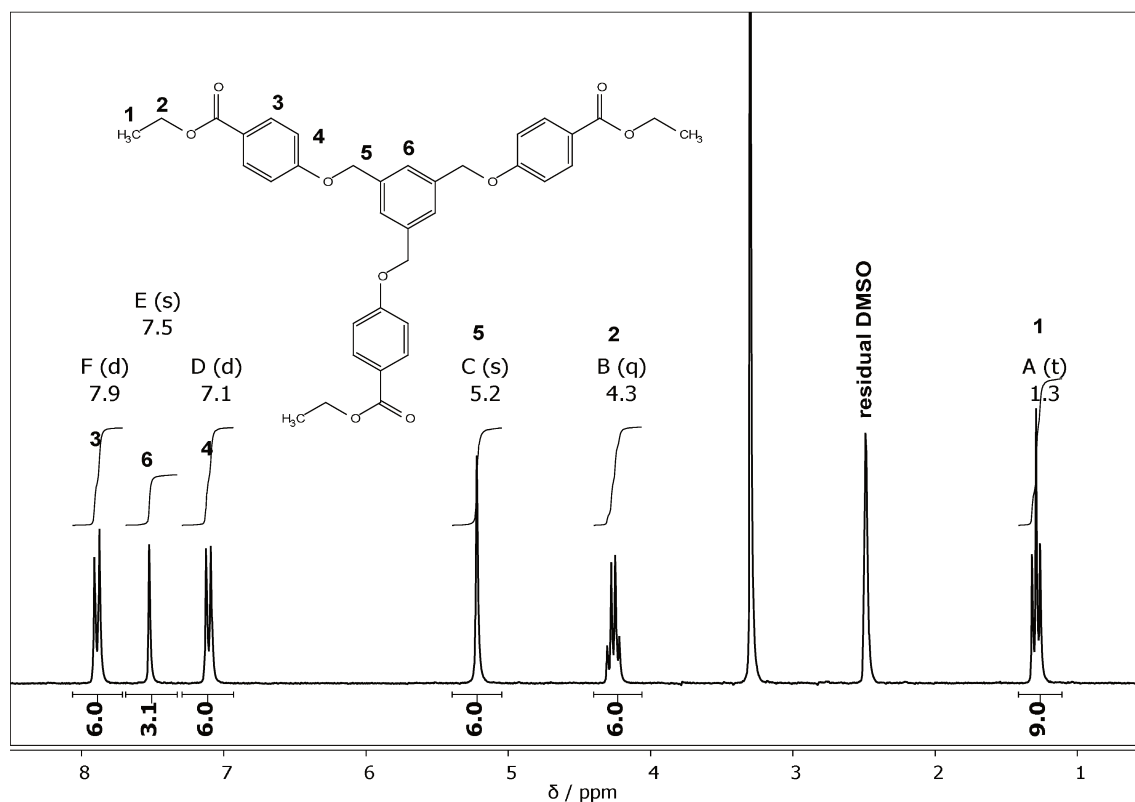
Parameter	Value
Solvent	DMSO
Temperature	298.2
Pulse Sequence	zg30
Probe	5 mm QNP 1H/ 13C/ 31P/ 19F Z3055/ 0065
Number of Scans	16
Receiver Gain	724.1
Relaxation Delay	1.0000
Pulse Width	14.2000
Acquisition Time	3.1654
Spectrometer Frequency	250.13
Spectral Width	5176.0
Lowest Frequency	-1040.1
Nucleus	1H
Acquired Size	16384
Spectral Size	65536



A 3: The 400-MHz ¹H-nuclear magnetic resonance spectrum of the 1,3,5- tris(bromomethyl)benzene in DMSO-d₆

A 4: Spectral conditions of the ¹H-NMR spectrum of the 1,3,5- tris(bromomethyl)benzene

Parameter	Value
Solvent	DMSO
Temperature	298.3
Pulse Sequence	zg30
Probe	5 mm PABBI 1H/ D-BB Z-GRD Z820201/ 0179
Number of Scans	16
Receiver Gain	203.0
Relaxation Delay	1.0000
Pulse Width	8.5000
Acquisition Time	2.0447
Spectrometer Frequency	400.18
Spectral Width	8012.8
Lowest Frequency	-1538.3
Nucleus	¹ H
Acquired Size	16384
Spectral Size	65536



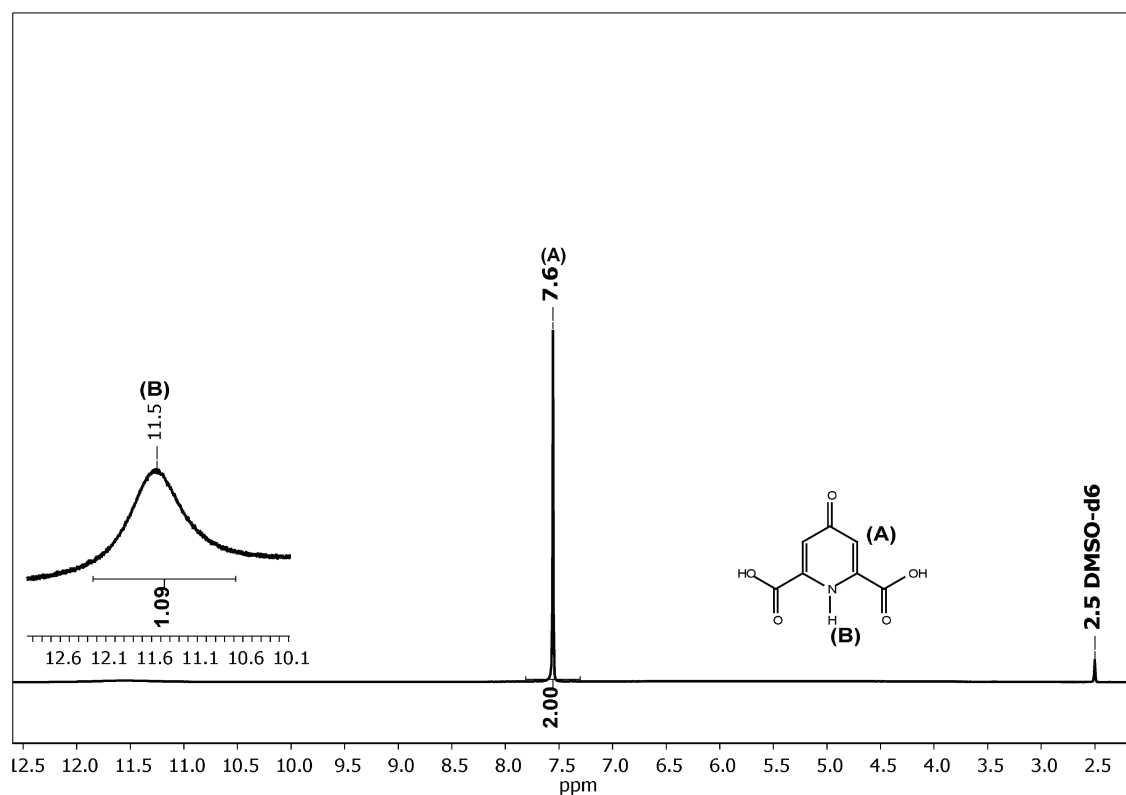
A 5: The 400-MHz ^1H -nuclear magnetic resonance spectrum of the triethyl 1,3,5-tris(4-ethoxycarbonylphenoxy)methylbenzene in DMSO-d_6 .

A 6: Spectral conditions of the ^1H -NMR spectrum of the triethyl 1,3,5-tris(4-ethoxycarbonylphenoxy)methylbenzene

Parameter	Value
Solvent	DMSO
Temperature	298.2
Pulse Sequence	zg30
Probe	5 mm QNP 1H/ 13C/ 31P/ 19F Z3055/ 0065
Number of Scans	16
Receiver Gain	1448.2
Relaxation Delay	1.0000
Pulse Width	14.2000
Acquisition Time	3.1654
Spectrometer Frequency	250.13
Spectral Width	5176.0
Lowest Frequency	-1043.3
Nucleus	^1H
Acquired Size	16384
Spectral Size	65536

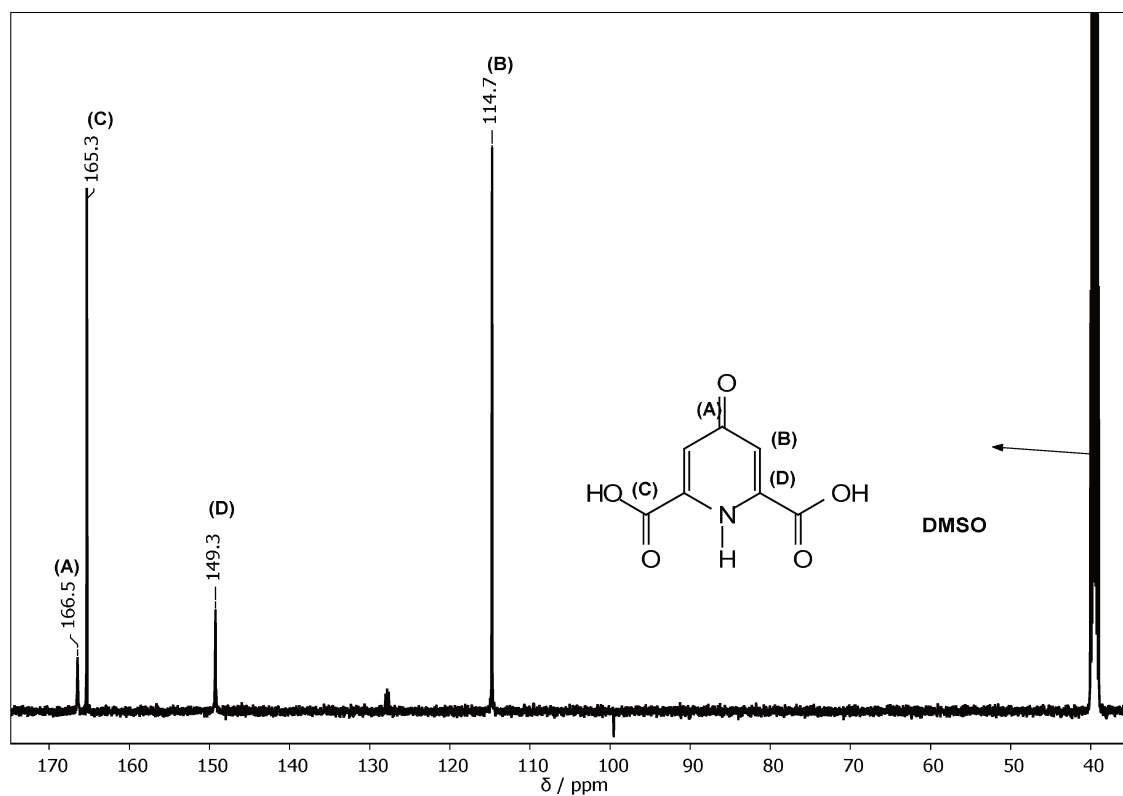
A 7: Spectral conditions of the ^1H -NMR spectrum of the H₃TCPMB ligand

Parameter	Value
Solvent	DMSO
Temperature	298.2
Pulse Sequence	zg30
Probe	5 mm PABBI 1H/ D-BB Z-GRD Z820201/ 0179
Number of Scans	16
Receiver Gain	90.5
Relaxation Delay	1.0000
Pulse Width	8.5000
Acquisition Time	2.0447
Spectrometer Frequency	400.18
Spectral Width	8012.8
Lowest Frequency	-1538.8
Nucleus	^1H
Acquired Size	16384
Spectral Size	65536

A 8: The 500-MHz ^1H -nuclear magnetic resonance spectrum of the 2,6-dicarboxypyridine-4-(1H)-one in DMSO- d_6 .

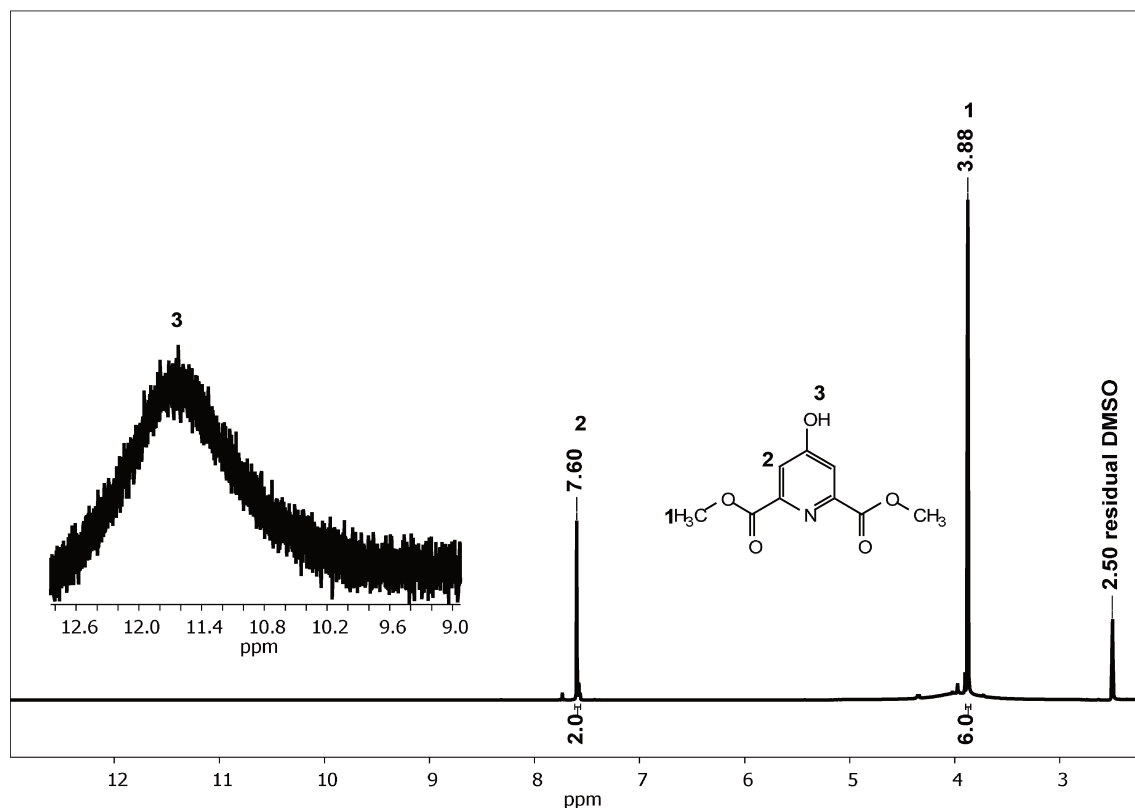
A 9: Spectral conditions of the ^1H -NMR spectrum of the 2,6-dicarboxypyridine-4-(1H)-one

Parameter	Value
Solvent	DMSO
Temperature	298.2
Pulse Sequence	zg30
Probe	5 mm PABBO BB/ 19F-1H/ D Z-GRD Z113652/ 0120
Number of Scans	16
Receiver Gain	128.0
Relaxation Delay	1.0000
Pulse Width	11.7500
Acquisition Time	1.6384
Spectrometer Frequency	499.87
Spectral Width	10000.0
Lowest Frequency	-1921.6
Nucleus	^1H
Acquired Size	16384
Spectral Size	65536

A 10: The 500-MHz ^{13}C -nuclear magnetic resonance spectrum of the 2,6-dicarboxypyridine-4-(1H)-one in DMSO-d_6

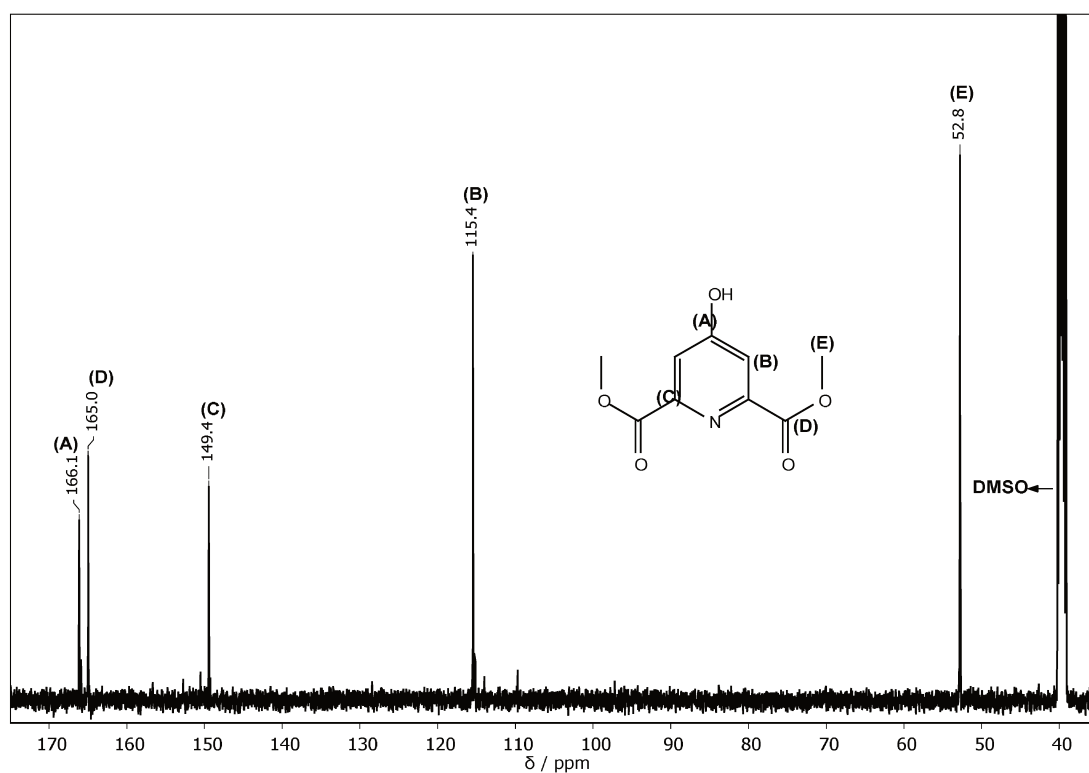
A 11: Spectral conditions of the ^{13}C -NMR spectrum of the 2,6-dicarboxypyridine-4-(1H)-one

Parameter	Value
Solvent	DMSO
Temperature	298.1
Pulse Sequence	zgpg30
Probe	5 mm PABBO BB/ 19F-1H/ D Z-GRD Z113652/ 0120
Number of Scans	1707
Receiver Gain	2050.0
Relaxation Delay	2.0000
Pulse Width	10.0000
Acquisition Time	0.5505
Spectrometer Frequency	125.70
Spectral Width	29761.9
Lowest Frequency	-2367.3
Nucleus	^{13}C
Acquired Size	16384
Spectral Size	32768

A 12: The 500-MHz ^1H -nuclear magnetic resonance spectrum of the dimethyl 4-hydroxypyridine-2,6-dicarboxylate in $\text{DMSO}-d_6$. Inset: magnification of the resonance signal attributed to the proton 3.

A 13: Spectral conditions of the ^1H -NMR spectrum of the dimethyl 4-hydroxypyridine-2,6-dicarboxylate

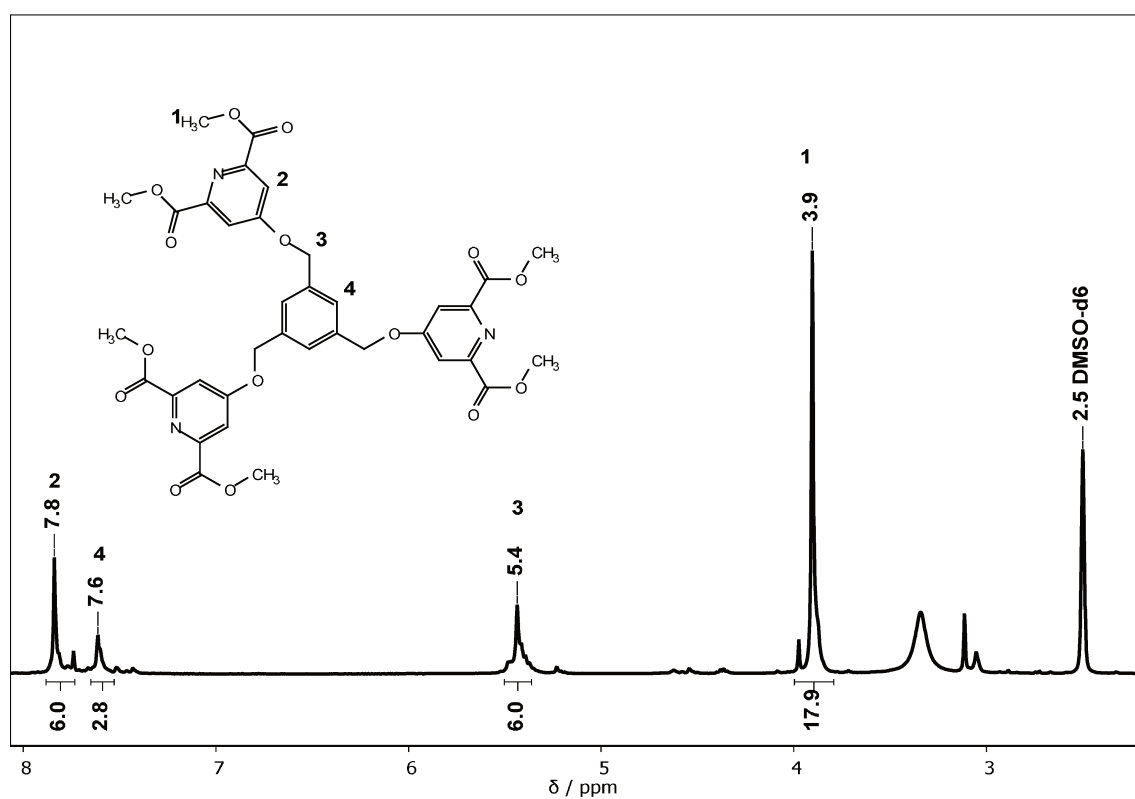
Parameter	Value
Solvent	DMSO
Temperature	298.1
Pulse Sequence	zg30
Experiment	1D
Probe	5 mm PABBO BB/ 19F-1H/ D Z-GRD Z113652/ 0120
Number of Scans	16
Receiver Gain	128.0
Relaxation Delay	1.0000
Pulse Width	11.7500
Acquisition Time	1.5903
Spectrometer Frequency	499.87
Spectral Width	10302.2
Lowest Frequency	-2073.2
Nucleus	^1H
Acquired Size	16384
Spectral Size	65536



A 14: The 500-MHz ^{13}C -nuclear magnetic resonance spectrum of the dimethyl 4-hydroxypyridine-2,6-dicarboxylate in DMSO-d_6

A 15: Spectral conditions of the ^{13}C -NMR spectrum of the dimethyl 4-hydroxypyridine-2,6-dicarboxylate

Parameter	Value
Solvent	DMSO
Temperature	298.1
Pulse Sequence	zgpg30
Experiment	1D
Probe	5 mm PABBO BB/ 19F-1H/ D Z-GRD Z113652/ 0120
Number of Scans	640
Receiver Gain	2050.0
Relaxation Delay	2.0000
Pulse Width	10.0000
Acquisition Time	0.4981
Spectrometer Frequency	125.71
Spectral Width	32894.7
Lowest Frequency	-2658.3
Nucleus	^{13}C
Acquired Size	16384
Spectral Size	32768



A 16: The 500-MHz ^1H -nuclear magnetic resonance spectrum of the 1,3,5-tris(2,6-dimethoxycarbonyl)pyridine-4-ylmethylbenzene in DMSO-d_6

A 17: Spectral conditions of the ^1H -NMR spectrum of the 1,3,5-tris(2,6-dimethoxycarbonyl-pyridine-4-oxy methyl)benzene

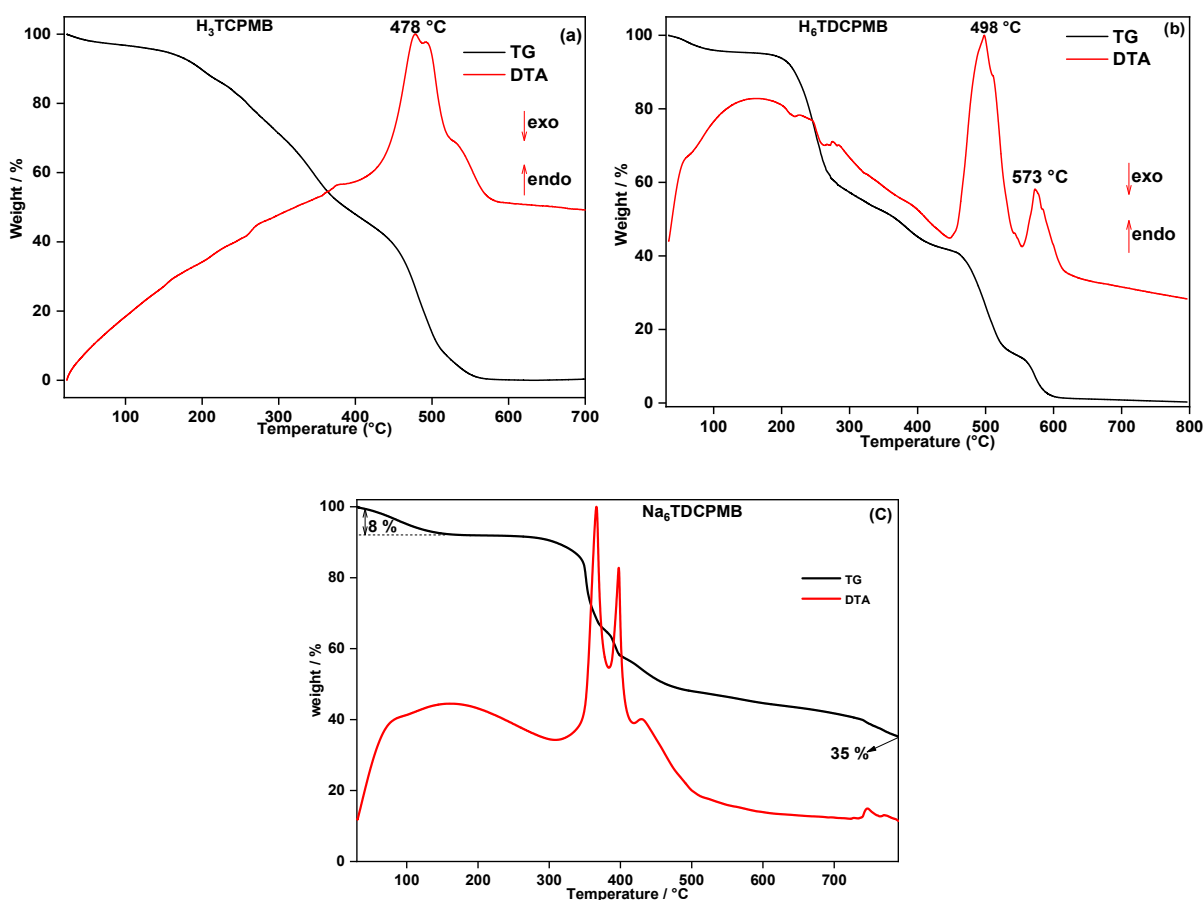
Parameter	Value
Solvent	DMSO
Temperature	298.2
Pulse Sequence	zg30
Experiment	1D
Probe	5 mm PABBI 1H/ D-BB Z-GRD Z820201/ 0179
Number of Scans	32
Receiver Gain	203.0
Relaxation Delay	1.0000
Pulse Width	8.5000
Acquisition Time	2.0447
Spectrometer Frequency	400.18
Spectral Width	8012.8
Lowest Frequency	-1538.7
Nucleus	^1H
Acquired Size	16384
Spectral Size	65536

A 18: Spectral conditions of the ^1H -NMR spectrum of the Na_6TDCPMB ligand salt

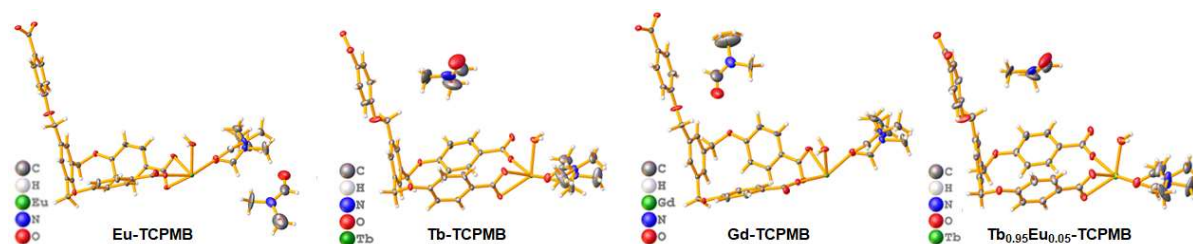
Parameter	Value
Solvent	D_2O
Temperature	298.4
Pulse Sequence	zgpr
Experiment	1D
Probe	5 mm PABBI 1H/ D-BB Z-GRD Z820201/ 0179
Number of Scans	256
Receiver Gain	32.0
Relaxation Delay	1.0000
Pulse Width	8.5000
Acquisition Time	2.0447
Spectrometer Frequency	400.18
Spectral Width	8012.8
Lowest Frequency	-2089.7
Nucleus	^1H
Acquired Size	16384
Spectral Size	65536

A 19: Spectral conditions of the ^{13}C -NMR spectrum of the Na_6TDCPMB ligand salt

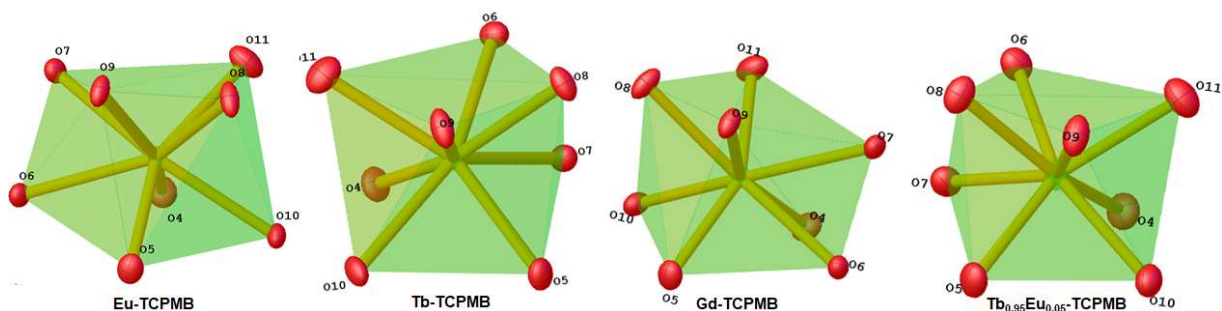
Parameter	Value
Solvent	D_2O
Temperature	296.9
Pulse Sequence	zgpg30
Experiment	1D
Probe	5 mm PABBI 1H/ D-BB Z-GRD Z820201/ 0179
Number of Scans	7168
Receiver Gain	203.0
Relaxation Delay	1.0000
Pulse Width	14.1000
Acquisition Time	0.6816
Spectrometer Frequency	100.64
Spectral Width	24038.5
Lowest Frequency	-1669.6
Nucleus	^{13}C
Acquired Size	16384
Spectral Size	32768

A 20: TG (black) and DTA (red) curves of H_3TCPMB (a), H_6TDCPMB (b) and Na_6TDCPMB (c)

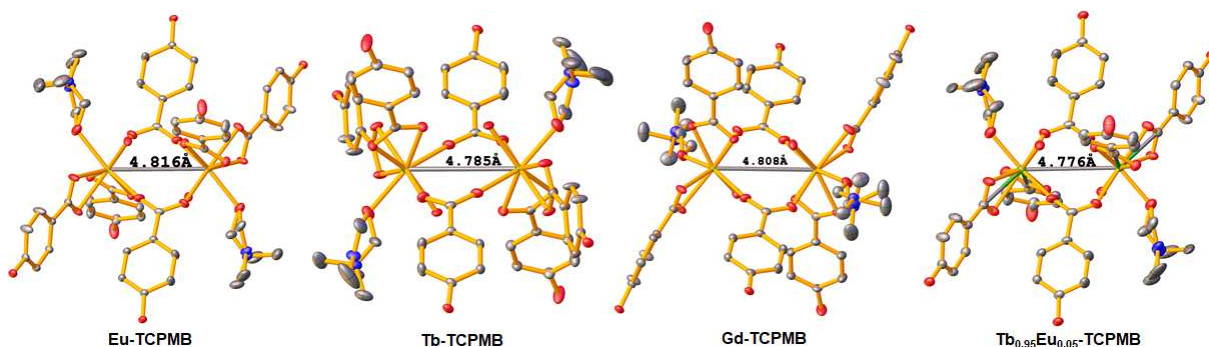
A 21: Asymmetric units and coordination geometries of the central ions for Eu-TCPMB, Tb-TCPMB, Gd-TCPMB and Tb_{0.95}Eu_{0.05}-TCPMB.



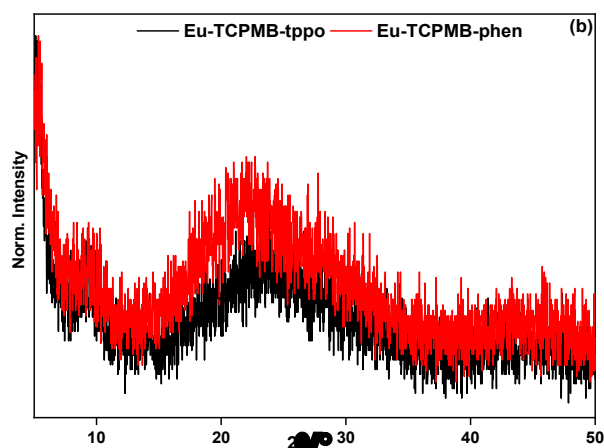
A 22: Matt drawing of the asymmetric units of Eu-TCPMB, Tb-TCPMB, Gd-TCPMB and Tb_{0.95}Eu_{0.05}-TCPMB.



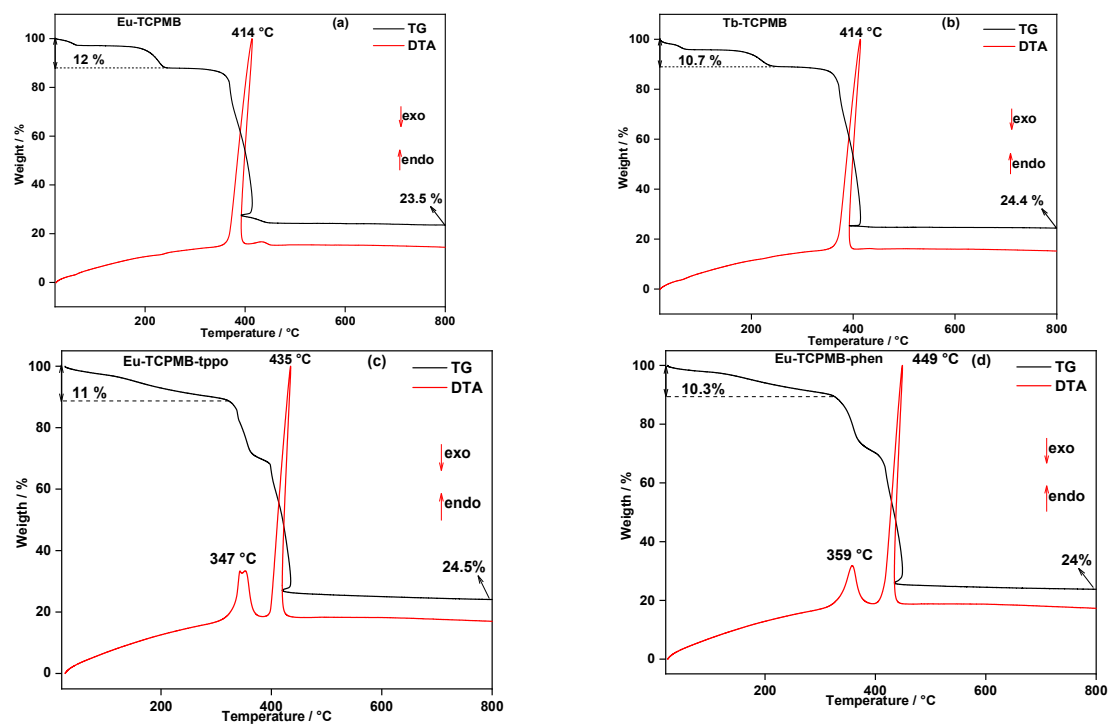
A 23: The coordination geometries of Eu^{III}, Tb^{III}, Gd^{III} and Tb^{III} ions in Eu-TCPMB, Tb-TCPMB, Gd-TCPMB and Tb_{0.95}Eu_{0.05}-TCPMB resulting in a distorted D_{4d} symmetry site for the central ions



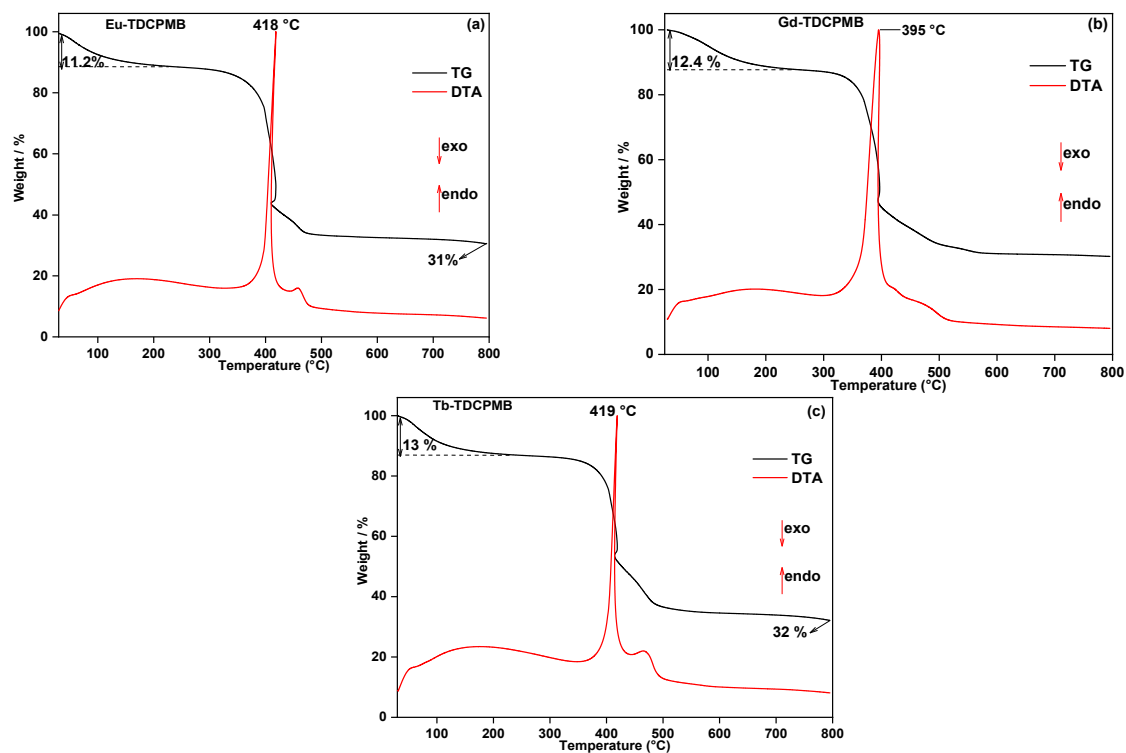
A 24: The connection mode of the Ln^{III} ions in the binuclear units of Eu-TCPMB, Tb-TCPMB, Gd-TCPMB, Tb_{0.95}Eu_{0.05}-TCPMB.



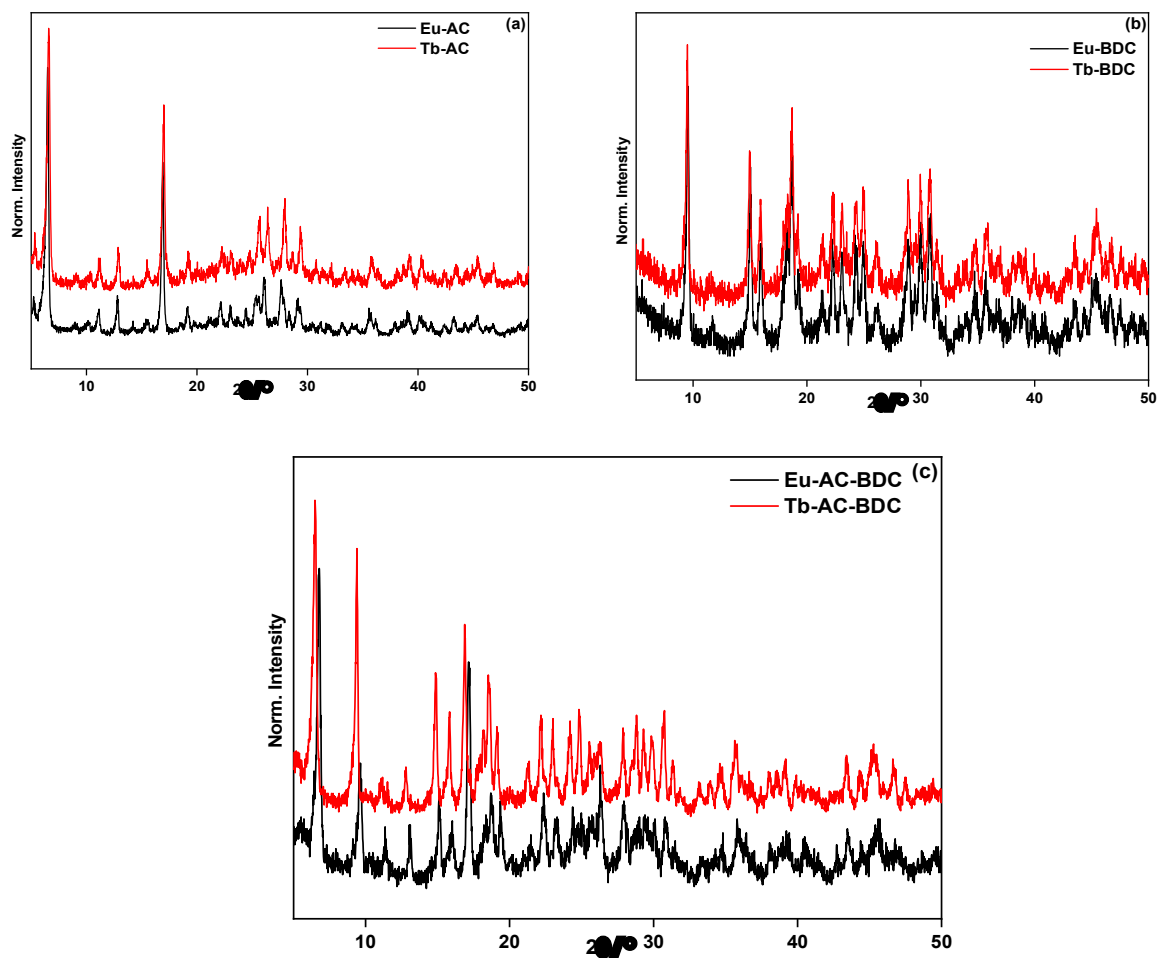
A 25: Experimental XRD patterns of Eu-TCPMB-tpo (dark) and Eu-TCPMB-phen.



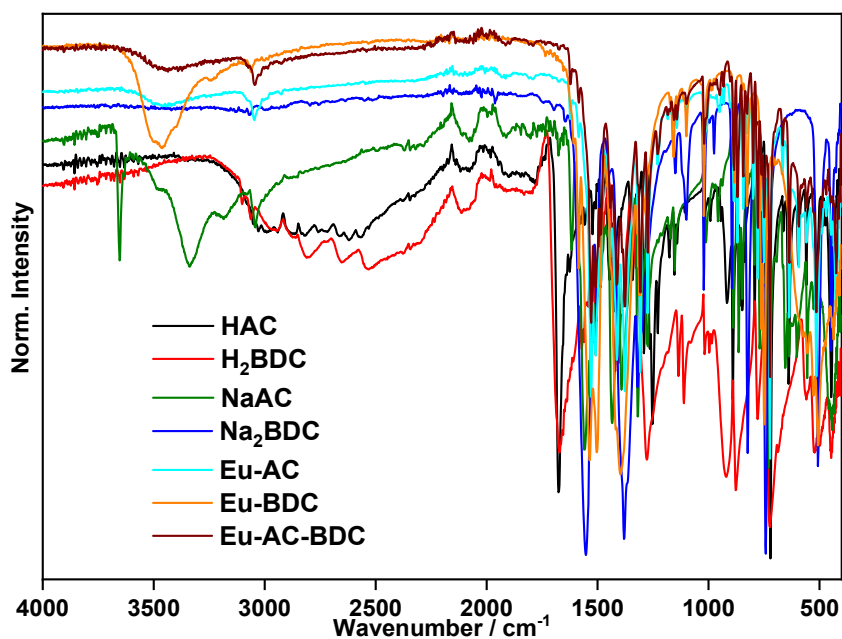
A 26: TG and DTA curves of Eu-TCPMB (a), Tb-TCPMB (b), Eu-TCPMB-tpo (c) and Eu-TCPMB-phen (d)



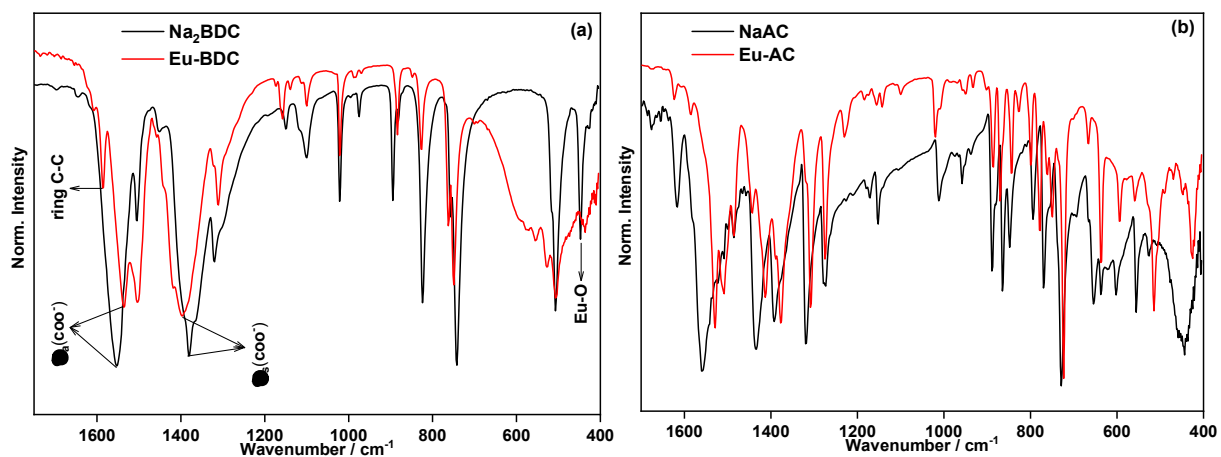
A 27: TG and DTA curves of Eu-TDCPMB (a), Gd-TDCPMB (b) and Tb-TDCPMB (c).



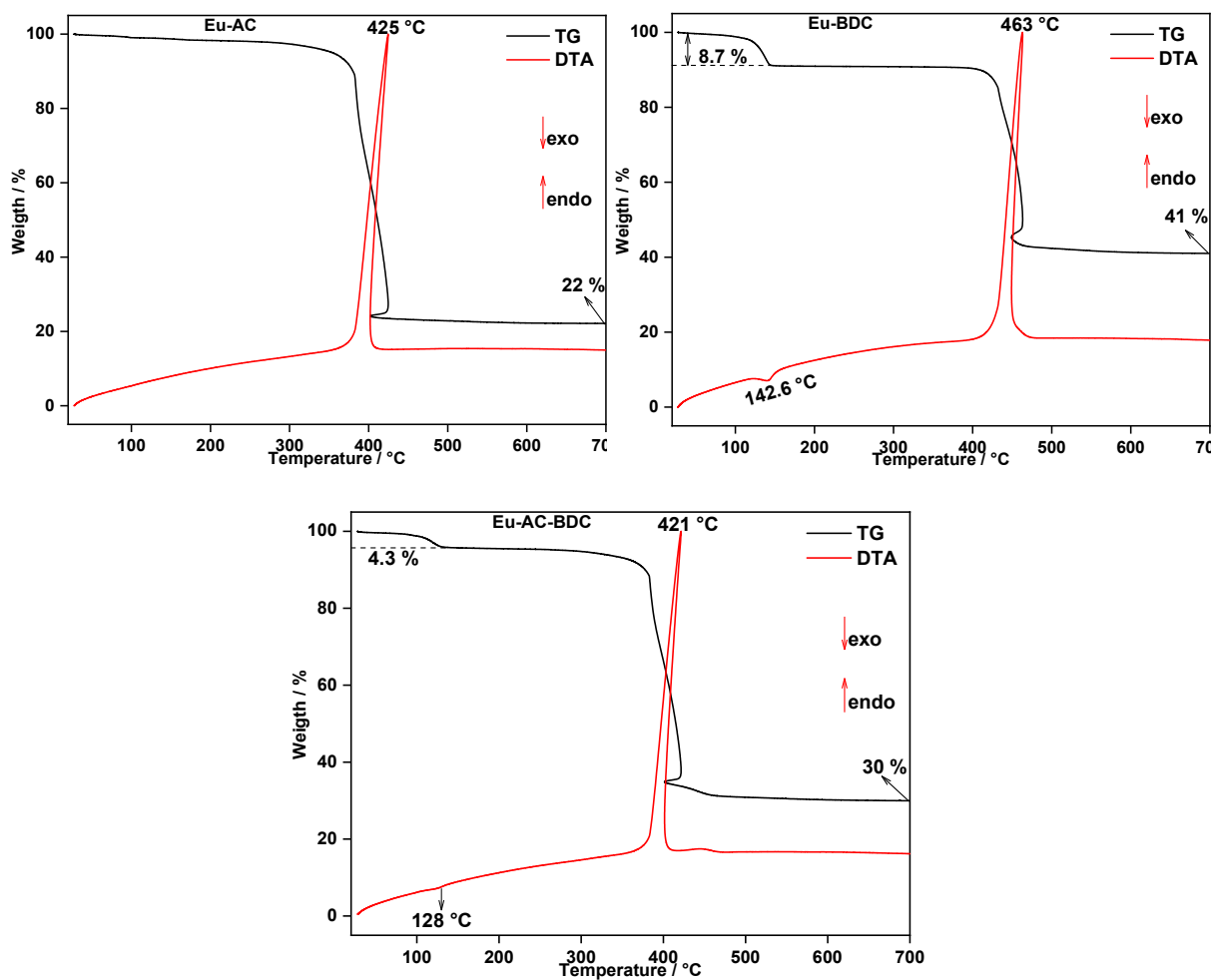
A 28: Diffractograms of the compounds constructed from HAC only (a), H₂BDC only (b) and the mixing ligands (c).



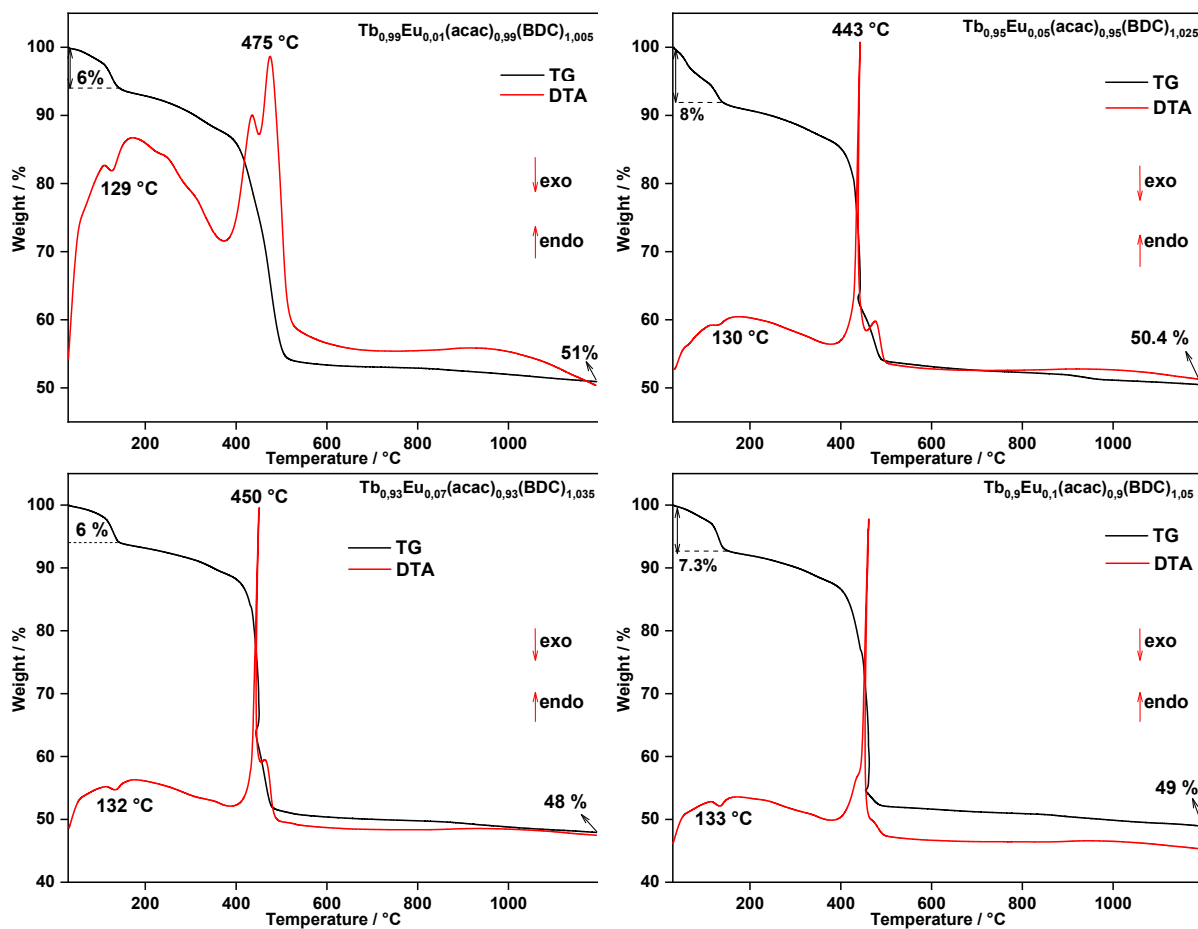
A 29: FT-IR spectra of HAC, H₂BDC, NaAC, Na₂BDC, Eu-AC, Eu-BDC, Eu-AC-BDC.



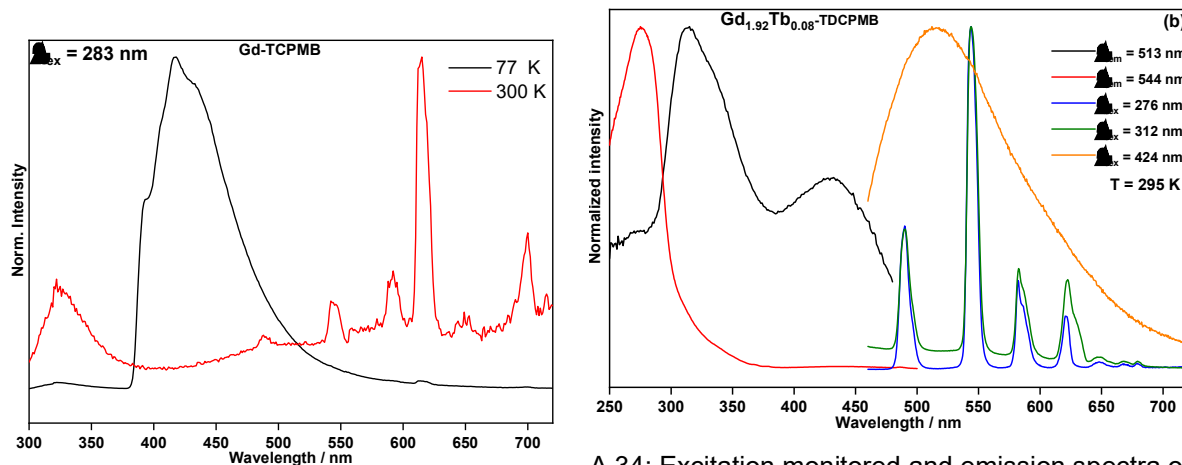
A 30: FT-IR spectra of Na₂BDC and Eu-BDC (a) and of NaAC, Eu-AC (b) the range 1700 – 400 cm⁻¹.



A 31: TG and DTA curves of Eu-AC, Eu-BDC and Eu-AC-BDC

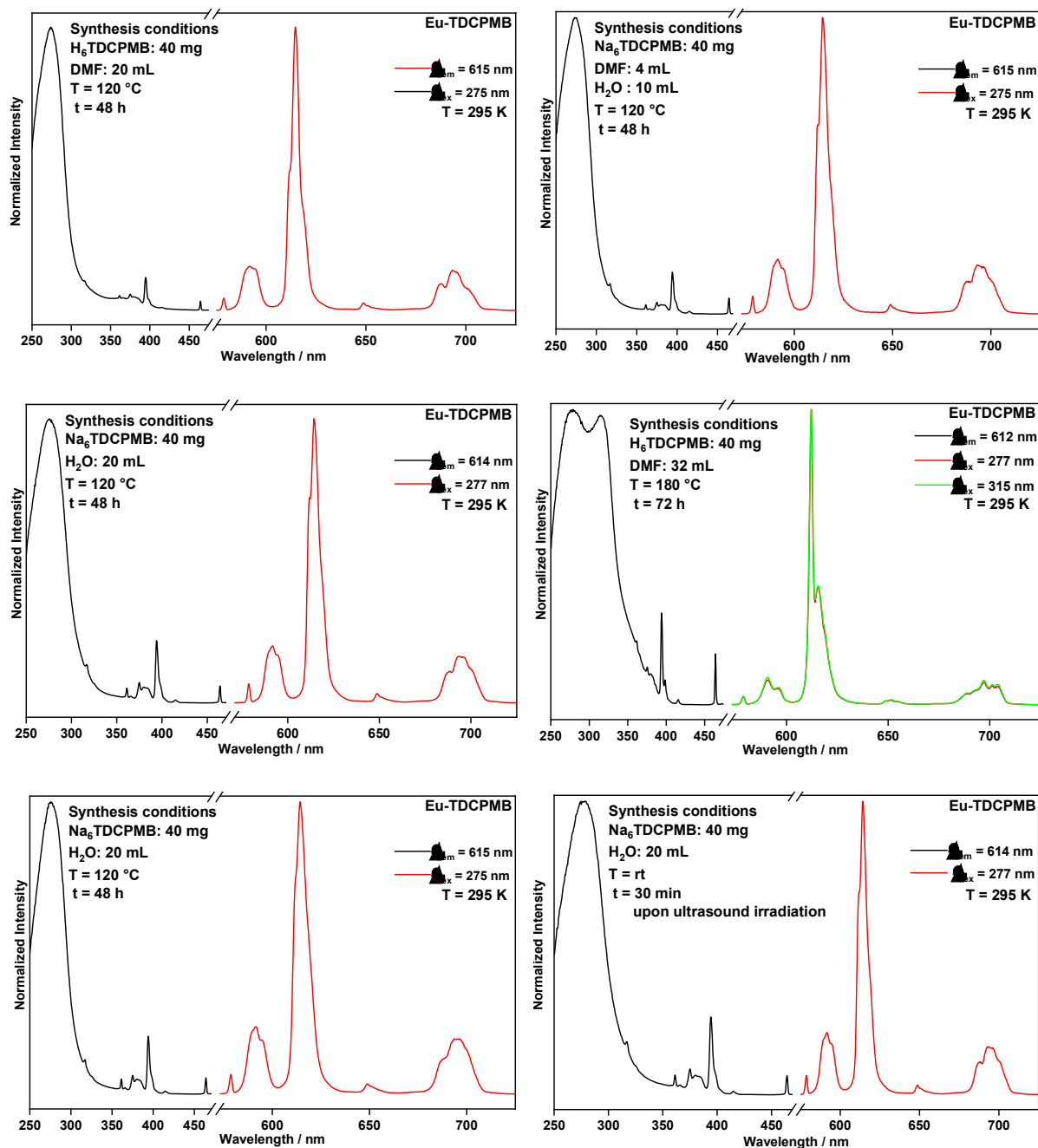


A 32: TG and DTA curves of the compound represented by $\text{Tb}_x\text{Eu}_{1-x}(\text{acac})_x(\text{BDC})_{1.5-x/2}$ ($x = 0.99, 0.95, 0.93$ and 0.9).



A 33: Emission GdL at 77 K and 300 K upon excitation at 283 nm

A 34: Excitation monitored and emission spectra of $\text{Gd}_{1.92}\text{Tb}_{0.08}\text{-TDCPMB}$ at room temperature.



A 35: Excitation and emission spectra of Eu-TDCPMB obtained using diverse synthetic methodologies. The conditions of each synthesis are described in the inset.

A 36: List of used ligands.

